Physical modelling of junction fabrication processes on FDSOI substrate for the 10 nm node and below

Anthony Payet

To cite this version:

Anthony Payet. Physical modelling of junction fabrication processes on FDSOI substrate for the 10 nm node and below. Micro and nanotechnologies/Microelectronics. Université Grenoble Alpes, 2017. English. NNT : 2017GREAY034 . tel-01699426

HAL Id: tel-01699426
https://theses.hal.science/tel-01699426v1
Submitted on 2 Feb 2018

Communauté
UNIVERSITÉ Grenoble Alpes

THÈSE

Pour obtenir le grade de

DOCTEUR DE LA COMMUNAUTÉ UNIVERSITÉ GRENOBLE ALPES

Spécialité : **Physique appliquée**

Arrêté ministériel : 7 Août 2006

Présentée par

Anthony PAYET

Thèse dirigée par **Patrice GERGAUD**
et codirigée par **Ignacio MARTIN-BRAGADO**

préparée au sein **CEA LETI**
et de **Ecole doctorale de Physique**

Modélisation physique des procédés de fabrication des jonctions FDSOI pour le nœud 10 nm et en-deçà

Thèse soutenue publiquement le **18 Mai 2017**,
devant le jury composé de :

M. Alain CLAVERIE
Directeur de recherche, CNRS CEMES, Président
Mme Lourdes PELAZ
Professeur, Université de Valladolid (Espagne), Rapporteur
Mme Evelyne LAMPIN
Chargée de recherche, CNRS IEMN, Rapporteur
M. Frédéric LANÇON
Docteur, CEA INAC, Examinateur

Acknowledgements

First and foremost, I would like to thank all of my advisors, beginning with my directors, Patrice Gergaud and Ignacio Martin-Bragado who have followed me during these three years. Next, it is unthinkable not to mention my supervisors, Jean-Charles Barbé, Clément Tavernier and Roberto Gonella for their insightful comments in their respective field. Finally, a great thanks to Benoît Sklénard, who not only paved the way for my PhD as a former student but also thoroughly accompanied me on it as a supervisor.

I am also greatly grateful to all of the TCAD team members in STMicroelectronics. First, to recognise me as a part of the team even if I was rarely present. Thanks to Sébastien Gallois-Garreignot, Floria Blanchet, Denis Rideau, Frédéric Monsieur Olivier Nier as well as the new team members and of course all of the PhD students I met there.

In CEA laboratory, I would like to express my gratitude to all the LETI/LSM members to have introduced me to the TCAD field. These years — almost four — along you were insightful as they shaped my future. Big thanks to all of you: Estelle Brague, Olga Cueto, Pierrette Rivallin, Sébastien Martinie, Benoit Mathieu, Philippe Blaise, François Triozon, Joris Lacord, Marie-Anne Jaud, Hélène Jacquinot, Luca Lucci, Patrick Martin, Marina Reyboz, Pascal Scheiblin and Anne-Sophie Royet. Of course I would like to thank people I have encountered during my various errands and experiments and who helped me: Perrine Batude, Christophe Licitra, Anne-Marie Papon, Flavia Piegas Luce, Caroline Curfs, Samuel Tardif and so much more! Thanks to you all.

Going on, I would like to thank all the PhD students — and encourage those who are still — whom I have met during these years. Huge thanks to Leo Bourdet, Gabriel Mugny, Yvan Denis, Fabio Pereira, Clément Sart, Anouar Idrissi-Eloudrhiri, Luca Pasini, Aurore Bonnevialle. And of couse special mentions to Kevin Morot and Pierre Dorion who have endured me throughout these years. Quick thanks to Zaiping Zeng and Eamon McDermott who are not PhD students but shared some quality tea time with us.

I would like to courteously thank my reading committee members Lourdes Pelaz and Evelyne Lampin for their time and interest in my PhD, as well as Alain Claverie and Frédéric Lançon to be part of my defense commitee.

Last, but by no means least, thanks to my family, their love and encouragement during these years, you made me who I am. As we say in Reunion Island “*Merci zot tout’* ”.

Anthony Payet

Research is to see
what everybody else has seen,
and to think
what nobody else has thought.

ALBERT SZENT-GYÖRGYI

Contents

List of Figures

List of Tables

Chapter I

Context and goals of this work

Contents

1 Technological context

1.1 Devices scaling throughout the years

The semiconductor industry is in a steady evolution since the beginning of the electronic computer, the Electronic Numerical Integrator Analyser and Computer, or ENIAC, until now. These regular evolutions have been condensed into the now famous Moore's law, stating that the density of transistor is relatively doubling every two years. The industry followed this trend until the middle of the 2010 decade, where the International Technology

Roadmap for Semiconductors predicted a decrease in this trend[1] and one of the industry leader, Intel, has slowed down its research and development cycles as the device scale approach the 10 nm gate length[2].
Another way to see the steady evolution of the semiconductor industry is introduced by Koomey *et al.* [Koomey *et al.* 2011]. In the publication, the team concludes that the number of computations per energy dissipated has been doubling around every 1.57 years. This trend, named Koomey's law, has been surprisingly well followed since the beginning of electronic computers, as it can be seen in Figure I.1, contrary to the Moore's law [3], which seems to slow down.

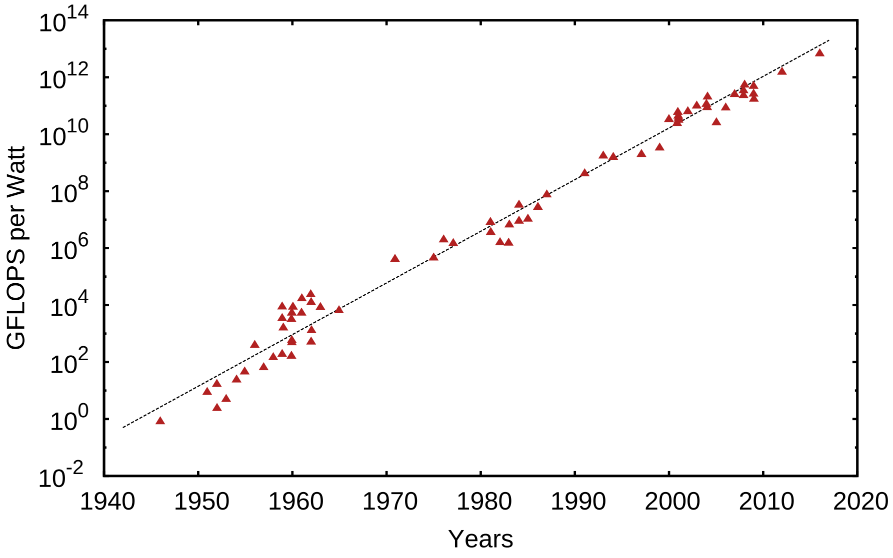

Figure I.1: Number of computations per joule dissipated. The Koomey's law states that the efficiency doubles every 1.57 years. Data from [Koomey *et al.* 2011], [Dong *et al.* 2014] and the first CPU-only based supercomputer on the Green 500 list, the ZettaScaler-1.6

The industry is approaching the limits of the Complementary Metal Oxide Semiconductor (CMOS) technology in term of gate length. The advanced nodes below 20 nm are technically very challenging to process as several issues have been encountered, such as short channel effect, gate and junctions leakages. To overcome these issues, several architectures have been proposed. From bulk CMOS, planar Fully Depleted Silicon on Insulator (FDSOI), TriGate or FinFET architectures have been introduced to cope the aforementioned issues [Ferain *et al.* 2011] (see Figure I.2). As an example, to increase the electrostatic control of the gate, two possibilities exist. First, from bulk CMOS, the introduction of a depleted silicon layer over an oxide in FDSOI structures greatly enhances the electrostatic control [Weber *et al.* 2008]. This method can be seen in Figure I.2a. Another way to increase this control is to create a larger contact area between the gate

---

[1] `http://bit.ly/2jXtu2S`
[2] `http://bit.ly/1LGd3ly`
[3] `http://bit.ly/2jw14ym`

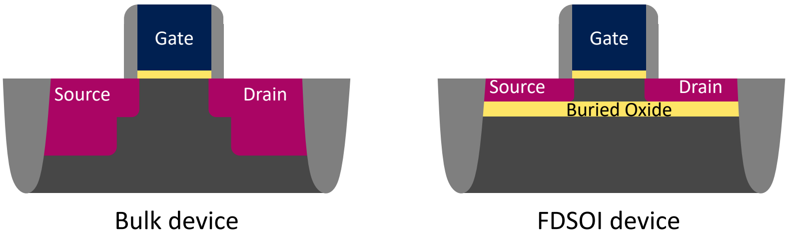

(a) 2D sketches of bulk and FDSOI devices

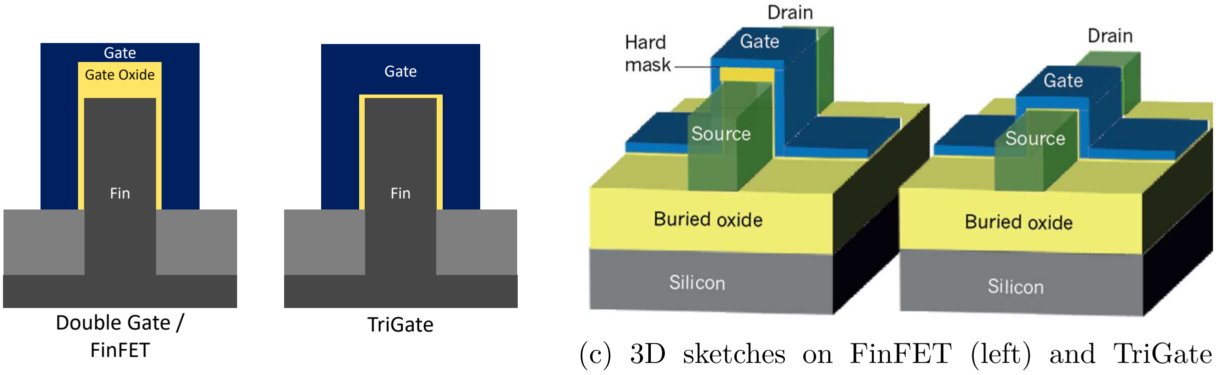

(b) 2D sketches of FinFET and TriGate devices based on bulk base

(c) 3D sketches on FinFET (left) and TriGate (right) devices based on a FDSOI substrate. Adapted from [Ferain *et al.* 2011]

Figure I.2: The different CMOS transistor technologies

and the channel. Three dimensional transistors thus appeared. Sketches of these 3D transistors, either TriGate or FinFET are drawn in Figure I.2b. Ultimately, one of the best electrostatic control can be achieved by combining the two former methods. This results in 3D transistors with a FDSOI base as in Figure I.2c.

1.2 New approach: 3D sequential integration

The fact that the transistors are now very efficient, thus producing less heat, allowed a new approach to device scaling. It is indeed possible to stack transistors in order to virtually double the transistors density with the same footprint and thus continuing the Moore's law. This technique is called 3D integration.

3D integration is usually invoked for a parallel 3D integration where two parts are processed separately and bonded together with Through Silicon Vias (TSV). This technology is used to improve integration density and lower interconnect delay and latency issues between several circuits. A basic scheme of this technology is shown in Figure I.3.

However, this technique cannot be used to front-end processing with transistors as the alignment of the two wafers during bonding is not fine enough to allow high performances.

A new approach to effectively double the transistor density and overcome the alignment issue has been introduced. The technique is called 3D sequential integration and consists of sequentially processing two layers of transistors and connect them in a last step. Both top and bottom transistors are based on the FDSOI architecture. The process integration scheme is summarised in Figure I.4.

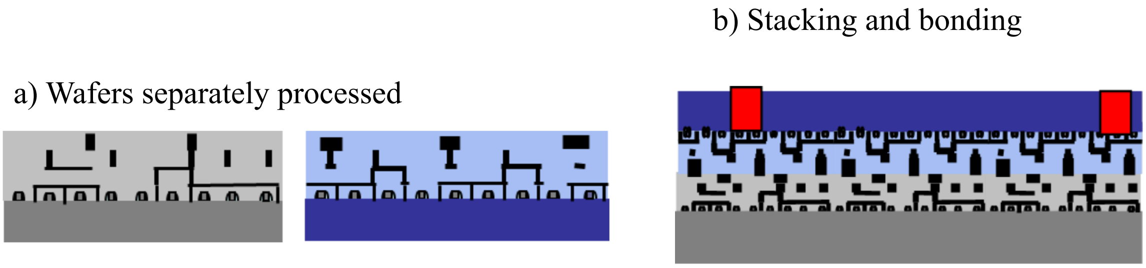

Figure I.3: Parallel integration process flow: a) two wafers are separately processed and b) contacted afterwards

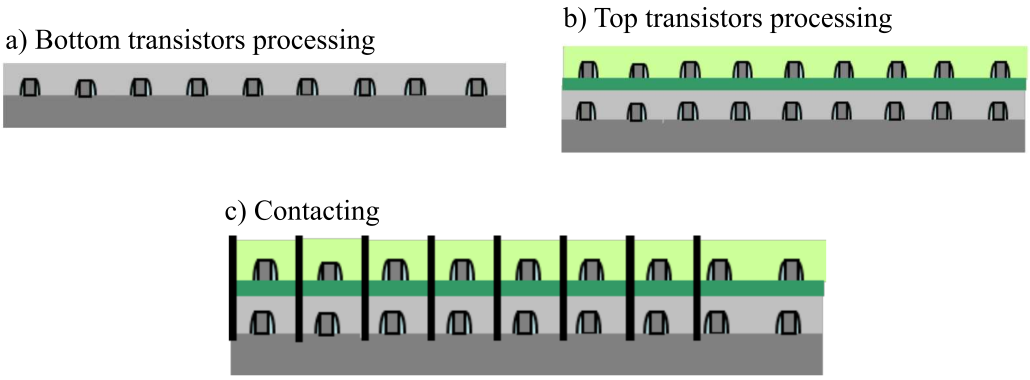

Figure I.4: 3D integration process flow: a) bottom transistors are processed, b) top transistors are processed, c) contacts are made

The 3D sequential integration technique possesses its own challenges in order to compete with the more traditional integration techniques, *id est* FinFET, TriGate or FDSOI integrations. Indeed, the allowed thermal budget for the top layer must be reduced to a minimum in order to keep the bottom transistor from any degradations. These degradations, reduced salicide stability, gate oxide growth, dopant diffusion and deactivation, can severely hinder the performance of the bottom transistors [Batude *et al.* 2011a, Batude *et al.* 2013]. A simple scheme of the 3D integration process can be seen in Figure I.5. First, the bottom transistor is processed with a conventional high temperature thermal budget. Secondly, a SOI substrate is bonded via a low temperature (200°C) molecular bonding, thus allowing a full transfer of the crystalline layer. A Transmission Electron Microscopy (TEM) cross-section image of the process result [Batude *et al.* 2011b] can be seen in Figure I.6.

For the technological process considered in this work, several thermal budgets have been considered. Figure I.7 shows the thermal budgets (TB) that yield a stable FET. The maximal aimed thermal budget is therefore 500°C-5h for the top layer. One of the challenge is to sufficiently activate the dopants with such a low thermal budget, particularly when it is compared with conventional ones that are around 1100°C. It is

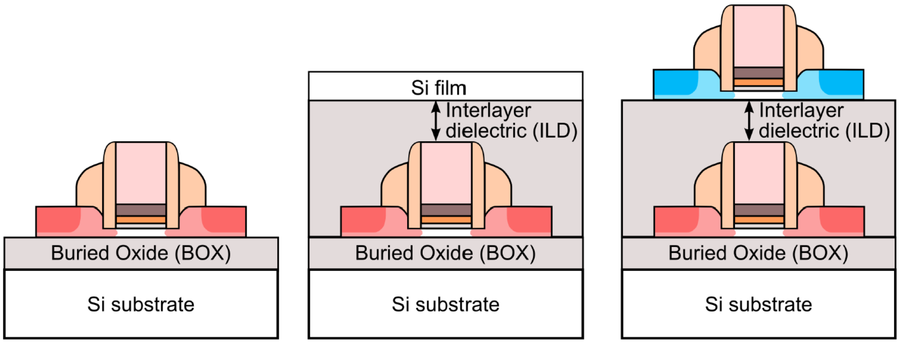

Figure I.5: Description of the 3D integration process flow at the transistor level. The bottom transistor is processed with a high temperature budget, an interlayer is deposited and the top transistor is processed with a low temperature budget

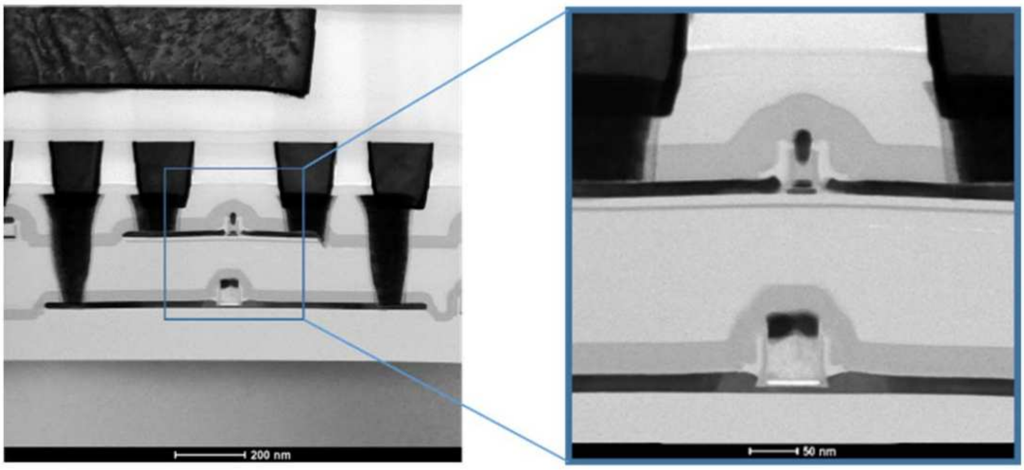

Figure I.6: TEM images of two stacked transistors fabricated according to the 3D integration process [Brunet *et al.* 2016]

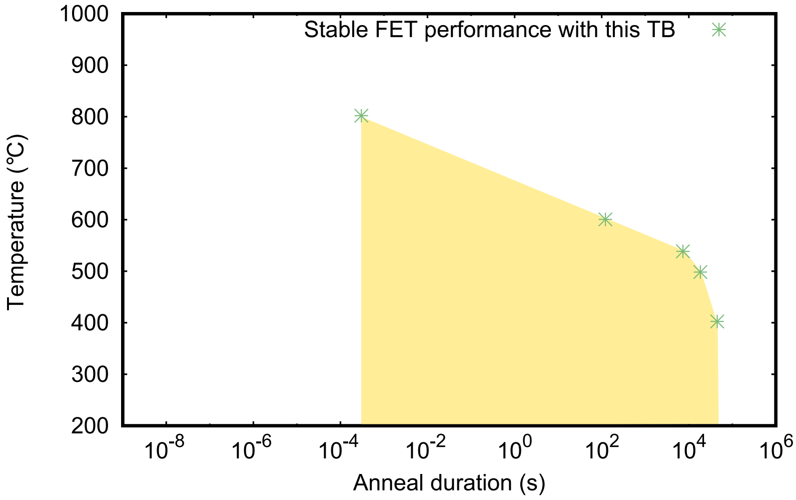

Figure I.7: Stable thermal budgets for FET fabrication using the CoolCube^{TM} integration [Batude *et al.* 2015] therefore not possible to use conventional process — rapid thermal anneal (RTA) — to activate the dopants. Fortunately, there are other processes that can activate dopants with a low thermal budget. Very short anneal enabled by dynamic surface anneal, an annealing technique using a nanosecond LASER, appears to be a promising candidate to activate the top transistor [Batude *et al.* 2015, Cristiano *et al.* 2016]. This technique uses a Liquid Phase Epitaxial Regrowth reaction or LPER, where the amorphous phase is liquefied using nanosecond LASER pulses but not the cristalline one.

The Solid Phase Epitaxial Regrowth (SPER) can also place doping atoms into the lattice sites, thus activating them, with a thermal budget in accordance with the limitations of 3D sequential integration. In the 3D integration, the top transistor is thus processed using SPER for dopant activation. Contrary to the LPER, both phases stay solid in the SPER reaction. After a SPER process, a very high concentration of electrically active dopants is achieved far above equilibrium [Solmi *et al.* 1990]. In this work, the latter option will be investigated.

1.3 New material: Silicon-germanium alloys

Along with the formerly introduced new architectures, silicon-germanium (SiGe) alloys have been considered by the semiconductor industry as a replacement of only silicon-based transistors, in order to furtherly increase transistor performance. This performance increase can be achieved in two ways. First, with a silicon channel, compressive strained SiGe source and drain increase the hole mobility in the channel, as in [Ghani *et al.* 2003]. Second, by growing directly a compressive SiGe alloy layer for the whole junction, source - channel -drain, as in [Cheng *et al.* 2012].

By compressively straining a Si, Ge or SiGe alloy channel, light and heavy bands split. Light holes are thus more populated and the hole mobility is increased. Moreover, as the germanium holes have lighter masses, the use of strained SiGe alloys, instead of only strained silicon, combines the performance boost of strain and germanium inclusions [Cheng *et al.* 2015]. The hole mobility incremental performance boost can be seen in Figure I.8. Ultimately the device performances are boosted as it can be seen in Figure I.9. In the 3D sequential integration, a strained SiGe-based transistor is used, as it offers the best performances possible in conjunction with an FDSOI architecture.

1.4 The 3D sequential integration process and its challenges

The former sections introduced the architecture — FDSOI — and material — strained SiGe alloys — that are used within a 3D sequential integration. However, this integration raises numerous challenges. They will be presented in the following sections.

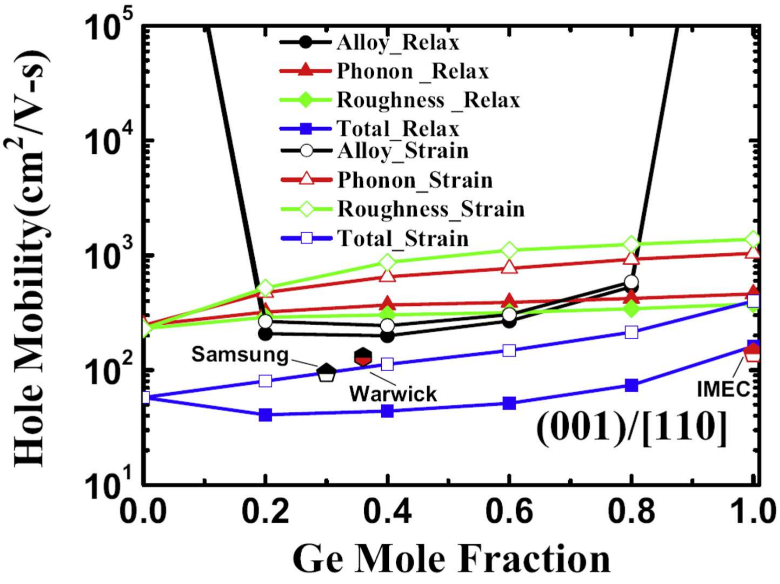

Figure I.8: Hole mobility incremental performance boost by adding compressive strain and germanium. From [Cheng *et al.* 2015]

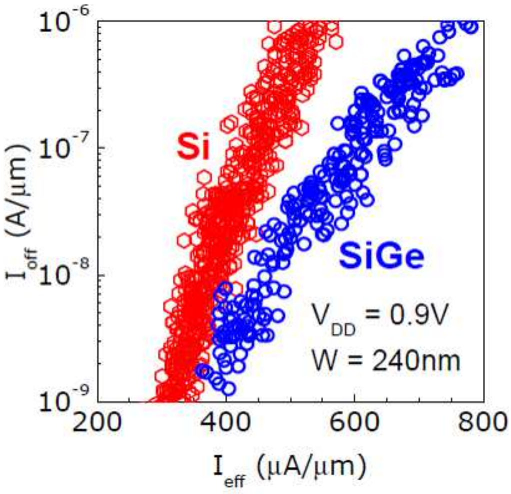

Figure I.9: Transistor performances increase due to inclusion of a compressively strained SiGe alloy channel. From [Cheng *et al.* 2012]

1.4.1 Strained SiGe layer manufacturing

The manufacturing of strained SiGe layer is rather difficult and could be the object of an entire chapter. The work presented here will not focus on this issue but will only highlight the difficulties of such a process.

SiGe alloys have their own lattice constants for each germanium concentration. The lattice constant can be roughly approximated by a linear interpolation as a function of the germanium content between the pure silicon lattice constant (5.43 Å) and the pure germanium one (5.66 Å). When epitaxially grown on a silicon substrate, the SiGe alloys has to match the lattice constant of the substrate, as it can be seen in Figure I.10. This results in a biaxially compressive strained SiGe layer.

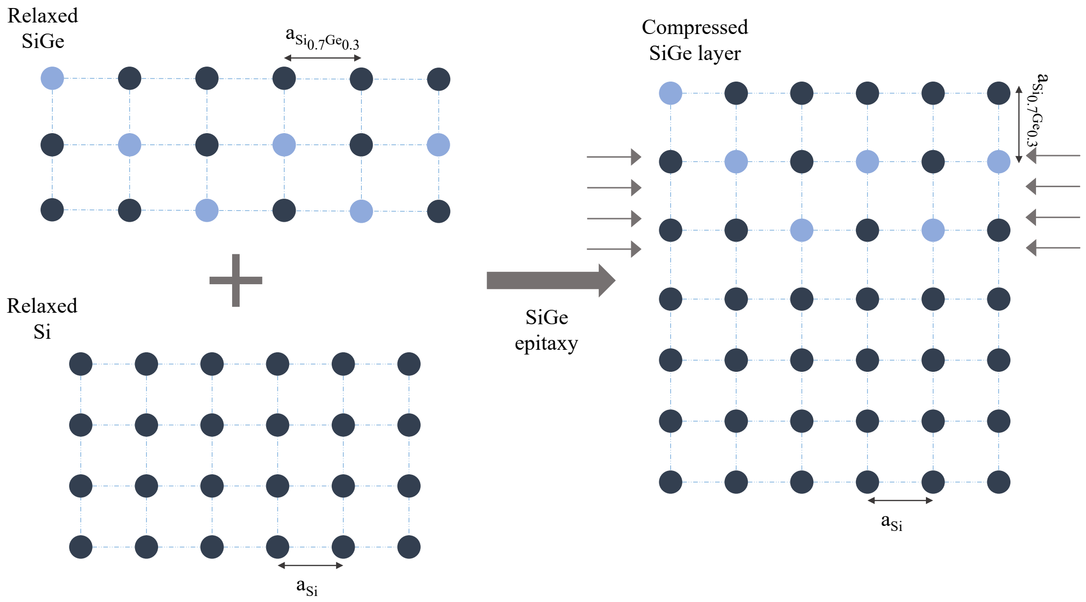

Figure I.10: Strained SiGe manufacturing by epitaxial growth on a relaxed silicon layer.

The strain resulting from the lattice mismatch is elastically stored in the grown layer and more grown thickness means more elastic energy. However, the grown thickness must be kept below a critical thickness to prevent the grown layer to relax via the formation of misfit dislocations. This issue has been thoroughly investigated in the following works [Matthews & Blakeslee 1974, People & Bean 1985, Paine *et al.* 1991, Hartmann *et al.* 2011]. *In fine* up to 40 nm SiGe layer containing up to 40% of germanium can be epitaxially grown on a silicon substrate. These limits match with the 3D sequential integration requirements, where a layer with less than 30 nm is grown.

1.4.2 Amorphisation and SPER

A low thermal budget — fixed below 500°C-5h — has been introduced in the transistor processes in order to stay within the constraints imposed by the 3D sequential integration process. The solid phase epitaxial regrowth verifies the 3D sequential constraints and activate the dopant. Dopant activation via SPER can be resumed into three steps. Firstly damage is created to a crystalline substrate for it to become amorphous, *i.e* a disordered phase. This step is called the pre-amorphisation implant (PAI). Secondly, the dopant is implanted. Finally, the substrate is annealed and the amorphous phase previously generated recovers its crystallinity, through the aforementioned SPER process. This step also places the dopant into the lattice positions, thus activating them and will be presented in the following section. Figure I.11 presents the two main steps in a) and b), where the PAI and dopant implantation are merged into step a). This is possible only in the case where the dopant has a high enough mass to amorphise the substrate. In the case of light atoms, such as boron, two implantations are made, one to amorphise the substrate and one to place the boron atoms.

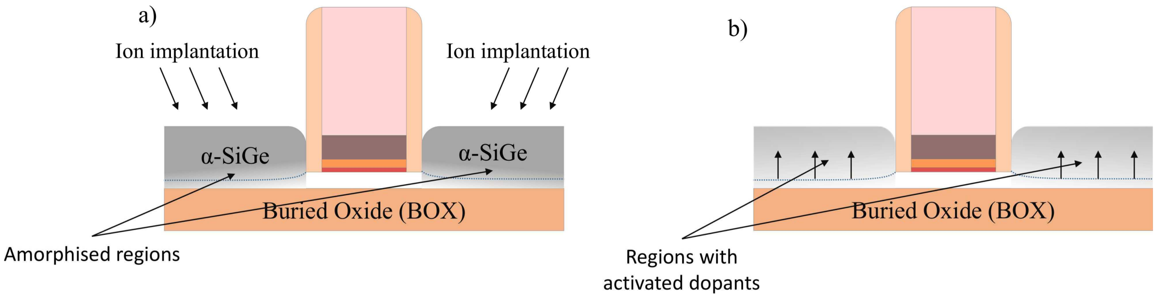

Figure I.11: Junction formation steps with SPER technique: a) source and drain are amorphised, b) the SPER reaction is activated by an anneal and subsequently activates the source and drain regions

Amorphous silicon or silicon-germanium layers can be achieved with high energy implantation into crystalline layers. Upon implantation, each ion collides with lattice atoms and expels them from their lattice sites, thus creating interstitial and vacancy point defects. Each lattice atom that has been expelled possesses a kinetic energy given by the collision with the implanting ion. These expelled atoms can thus in turn collide with other lattice atom, creating successive collision events, called a cascade. Such an event can be seen in Figure I.12. During the implantation, the point defects may recombine if there is enough lattice vibration. This substrate healing, called dynamic annealing, is directly linked to the temperature during implantation. When the lattice is heavily damaged, it will reorganise itself into small amorphous pockets.

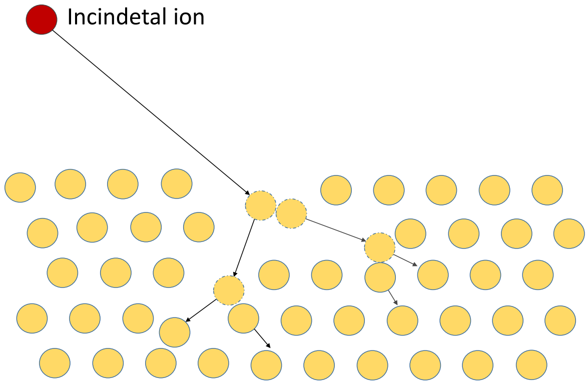

Figure I.12: Sketch of a single atomic collision and the resulting cascade. Vacancy and interstitial defects are the result of a single cascade

The amount of damage produced by the implantation is proportional to the mass, dose and energy of the incoming atoms. Higher masses and energies yield a higher inertia for the incoming atom, thus giving it a higher damage power. The dose, how many atoms are implanted by units of area, increases the probability of amorphisation of the volume.

With high enough doses and dose rates, the small amorphous pockets grow large and finally form a continuous amorphous layer on top of the crystalline phase. These steps are sketched in Figure I.13.

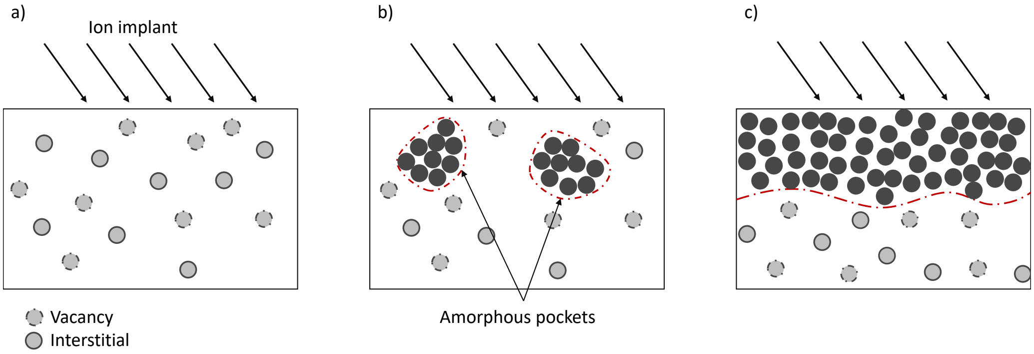

Figure I.13: Continuous cascades leading to a continuous amorphous layer

In the 3D sequential integration, the amorphisation process is challenging. Indeed, a non-damaged crystalline seed is required for the subsequent recrystallisation. As the transistor architecture is FDSOI with a material thickness below 30 nm, as it can be noted in Figure I.6, the amorphisation control is difficult. Too little amorphisation and the transistor will not perform well due to less active dopants. A too deep amorphisation and the device performs even worse as the single crystal is destroyed. Indeed, without a proper crystalline seed, the SPER cannot happen. In this particular case, Random Nucleation Growth (RNG) happens and yields a polycrystal. Due to its poor electrical performances, a polycrystal must be avoided with utmost importance, reinforcing the need of precision during PAI. The interested reader can consult [Spinella *et al.* 1998]. The differences between these reactions are highlighted in Figure I.14. The process window is therefore tiny. Fortunately, this window can be revealed with careful upstream preparation with atomistic simulations that have been consistent with experimental data on the whole SiGe alloy spectrum [Payet *et al.* 2016a].

2 The amorphous to crystalline transition

2.1 Phase structures

2.1.1 Crystalline silicon

Under pressure and temperature conditions encountered during semiconductor processes — from -3 to +3 GPa and below 1600K — the lowest energy phase of crystalline silicon (c-Si) is the diamond structure [Kaczmarski *et al.* 2005], as seen in Figure I.15a. The diamond structure is often described as an interlacing of two face-centred cubic system

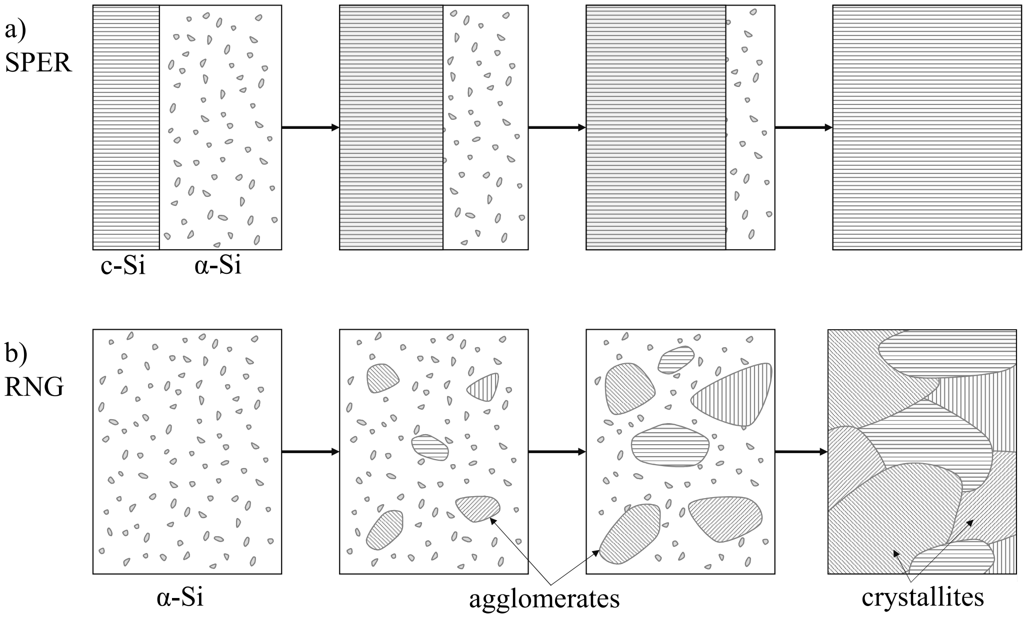

Figure I.14: Sketch revealing the difference between a) SPER and b) random nucleation growth (RNG)

that are shifted between each other by one fourth of the lattice unit in [100], [010] and [001] orientation. The diamond structure can also be described as a Zincblende structure with a unique atom instead of a two-atom alternation, as it can be seen in Figure I.15a. In this structure, each silicon atom are covalently bonded with 4 other atoms. A single silicon atom has an electronic structure of [Ne]$3s^2 3p^2$, but in order to minimise the atom total energy, $3s$ and $3p$ orbitals hybridise into a sp^3 orbital. The covalent bonds form therefore a regular tetrahedron with an angle of 109° between each bond.
The silicon unit cell contains 8 atoms, as seen in Figure I.15a, with a lattice parameter of a_{Si}=5.43072 Å at 300K [Pichler 2004], giving a concentration of 5×10^{22} cm^{-3}. At room temperature, the bond length between two atoms is $a_{Si} \cdot \sqrt{3}/4 = 2.352$ Å. Each silicon atom has 4 first neighbours at a distance of $a_{Si} \cdot \sqrt{3}/4$, 12 unique second neighbours at a distance of $a_{Si} \cdot \sqrt{2}/2$ and 12 unique third neighbours at a distance of $a_{Si} \cdot \sqrt{11}/4$. Two dimensional projections of the silicon lattice along [100], [110] and [111] can be seen in Figure I.15b, Figure I.15c and Figure I.15d, respectively.

The structure of SiGe alloys is the same as pure silicon, as germanium and silicon atoms possess the same outer shell electronic configuration. However, the germanium atom is bigger and the alloy lattice constant can be approximated by the Vegard's law. The Vegard's law is an empirical rule stating that a linear relation exists, at constant temperature, between the crystal lattice constant of an alloy and the concentrations its pure elements. More precisely in the case of SiGe alloys, the Vegard's law is not *stricto sensu* followed as experimental data [Dismukes *et al.* 1964, Kasper *et al.* 1995] and first principle calculations [de Gironcoli *et al.* 1991] have shown.

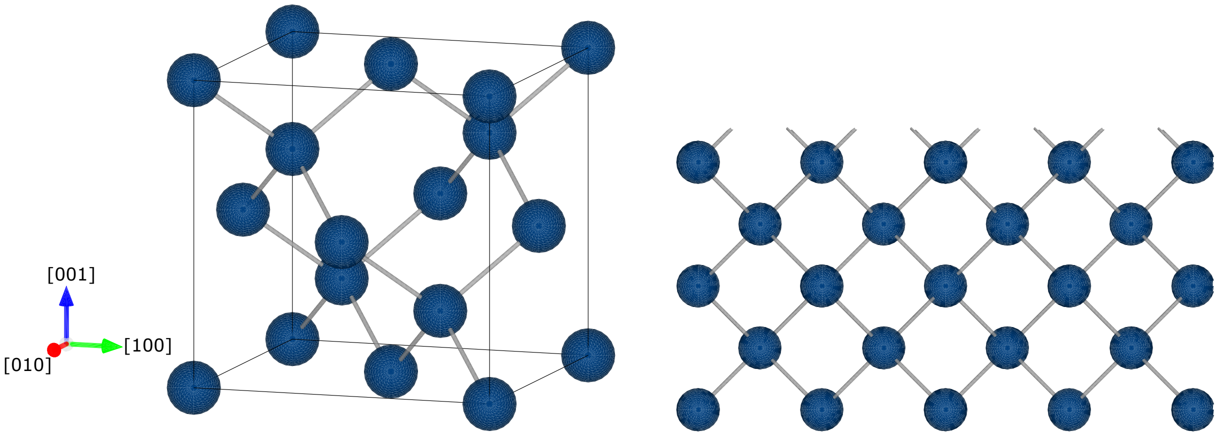

(a) Three dimensional view

(b) View in <100> direction

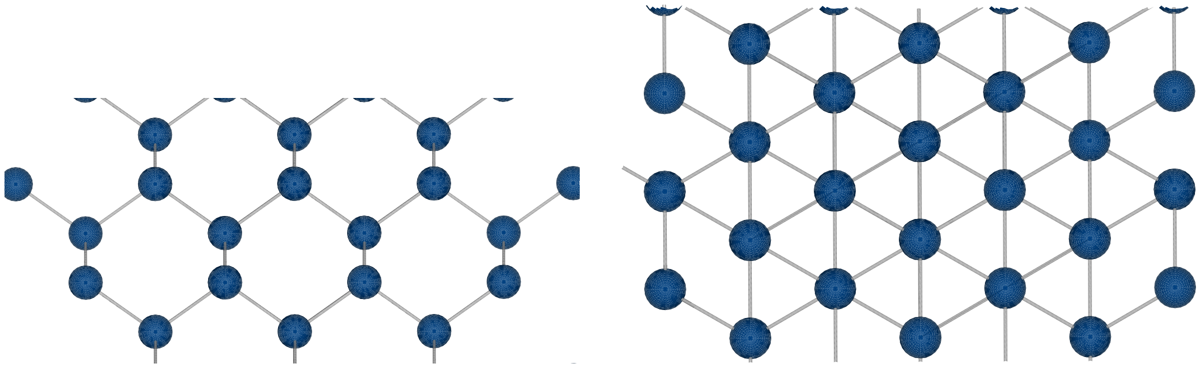

(c) View in <110> direction

(d) View in <111> direction

Figure I.15: The diamond structure. Views generated by `VESTA` [Momma & Izumi 2011]

2.1.2 Amorphous silicon

The amorphous phase is often described as a continuous random network (CRN). The structure of amorphous silicon (α-Si)— or a SiGe alloy — shares some properties with the crystalline phase. Atoms are still covalently bond to four nearest neighbours with bond lengths that do not significantly differ between the two phases. In SiGe alloys as well as pure silicon or germanium, amorphous phases are always less dense (∼2%) than crystalline ones [Custer *et al.* 1994, Laaziri *et al.* 1995]. Bond angles however deviate from the crystalline phase. Experimental data from high energy X-ray diffraction of amorphous silicon present an average of the bond angle distortion ($\Delta\theta$) between 9-10° [Laaziri *et al.* 1999]. These two properties can be viewed with the partial distribution function $g(r)$ (PDF) comparison between the two phases. This function describes the probability to find an atom at a given distance from the centre of another atom. Mathematically, $g(r)$ is defined as [Takeshi & Billinge 2012a]:

$$g(r) = \frac{1}{4N\pi r^2 \rho_0} \sum_{i,j} \delta\Big(r - |R_i - R_j|\Big) \tag{I.1}$$

where N is the number of total atoms, ρ_0 is the material density — here 0.049 at/Å^3 [Laaziri *et al.* 1995] — and $|R_i - R_j|$ is the distance between atoms i and j. A high value means the presence of atoms whereas a low value means a void. As a diamond lattice crystal is well ordered, neighbour peaks are easily identifiable. The PDF of amorphous and crystalline silicon can be seen at Figure I.16. Experimental data are derived from the radial distribution function $R(r)$ (RDF) of [Laaziri *et al.* 1999]. The link between the PDF $g(r)$ and the RDF $R(r)$ is $R(r) = 4\pi r^2 \rho_0 g(r)$ [Takeshi & Billinge 2012b].

Both phases share the same order at close range as one can see the first and second peaks that symbolize the first and second nearest neighbours presences. However, amorphous silicon loses long range order as the function shows no more peaks after 4 Å. The bond length is also preserved as the first peak coincides between the two curves. Due to this loss of order, amorphous silicon or germanium possesses a lower melting point than their crystalline counterparts, as seen by [Donovan *et al.* 1985].
Furthermore, amorphous phases host several defects. The first defect experimentally seen was an undercoordinated atom, called the dangling bond defect, due to its detectability by the Electron Spin Resonance (ESR) method [Brodsky & Title 1969]. From ESR measurements, the concentration of dangling bonds in amorphous silicon is around 2×10^{20} cm^{-3}. Later [Pantelides 1986] introduced an overcoordinated defect, called floating bond. Finally, tight-binding approach confirmed the presence of neutral dangling bonds, positively and negatively charged dangling bonds and floating bonds in amorphous silicon [Knief & von Niessen 1999]. Contrary to the dangling bonds, floating bonds are not susceptible to

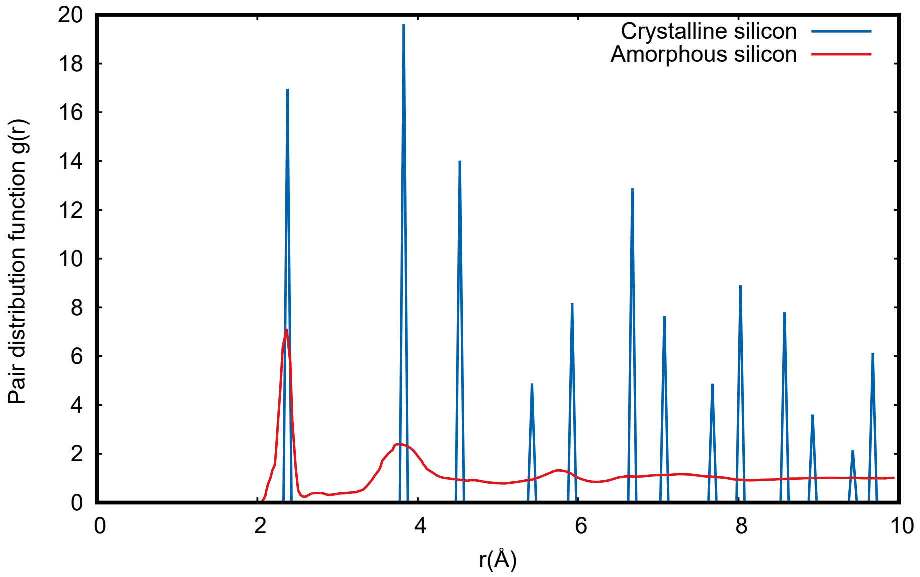

Figure I.16: Partial distribution function $g(r)$ comparison between crystalline and amorphous silicon. The amorphous curve is derived from experimental work of [Laaziri *et al.* 1999]

the ESR method hence their concentration is not known.

2.2 Recrystallisation thermodynamics and kinetics

Due to this loss of its long-range order, the α-Si or α-Ge has a higher Gibbs free energy than its crystalline counterpart. The recrystallisation reaction is therefore thermodynamically favourable as the difference in Gibbs free energy between an amorphous and a crystalline atom, $\Delta G_{\alpha c} \equiv G_\alpha - G_c$, is positive. This free energy can be written:

$$\Delta G_{\alpha c}(T) = \Delta H_{\alpha c}(T) - T\Delta S_{\alpha c}(T), \tag{I.2}$$

where $\Delta H_{\alpha c}$ and $\Delta S_{\alpha c}$ are the recrystallisation enthalpy and entropy, respectively. Enthalpies and entropies can be extracted via Differential Scanning Calorimetry (DSC) by determining the specific heat capacity of the recrystallisation. Donovan *et al.* [Donovan *et al.* 1985] determined a crystallization enthalpy of 11.9 ± 0.7 kJ/mol (at 960 K) and 11.6 ± 0.7 kJ/mol (at 750 K) for silicon and germanium respectively of ion-implantation generated amorphous layers.

The amorphous to crystalline transition has been established as thermodynamically favourable reaction. However, the reaction has to be thermally activated, as it can be seen in Figure I.17. This graphical representation shows that even if the reaction is thermodynamically favourable ($\Delta G_{\alpha c} > 0$), an energetic barrier ΔG^* has to be overcome. The growth rate of the recrystallisation or the rate of the moving amorphous-crystalline interface, can be written [Olson & Roth 1988, Lu *et al.* 1991], within the Transition State

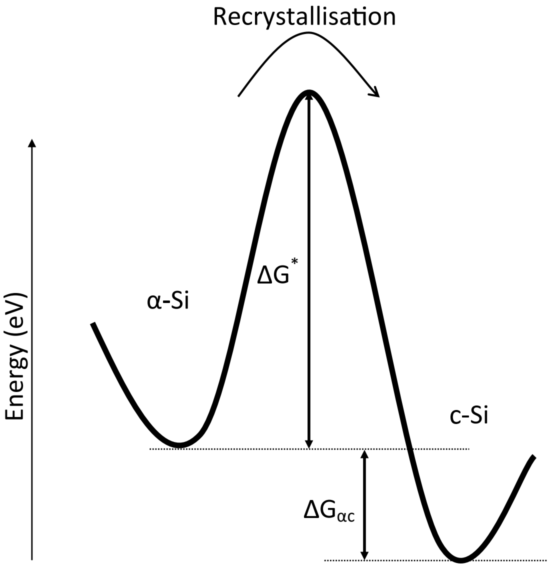

Figure I.17: Energetic representation of the SPER reaction

Theory of thermally activated growth [Christian 1965]:

$$v = \frac{k_B T}{h} f\lambda \left[1 - \exp\left(-\frac{\Delta G_{\alpha c}}{k_B T} \right) \right] \times \exp\left(-\frac{\Delta G^*}{k_B T} \right) \tag{I.3}$$

where $k_B T/h$ is the lattice vibration frequency, f is the fraction of sites where the atomic rearrangement can occur, λ is the distance that the interface moves during a unique rearrangement. Finally, ΔG^* is the SPER activation free energy.
$\Delta G^* \equiv \Delta H^* - T\Delta S^*$, where ΔH^* is the activation enthalpy and ΔS^* is the activation entropy. Furthermore, within the framework of the transition state theory for a bimolecular reaction, the relationship between the activation energy and the activation enthalpy can be written as follow [Atkins 2009]:

$$E^* = \Delta H^* + k_B T \tag{I.4}$$

Moreover, in the case of the SPER reaction, $\Delta H^* \gg k_B T$, yielding $\Delta G^* \cong E^* - T\Delta S^*$. The Equation I.3 can now be rewritten:

$$v = v_0 \times \exp\left(-\frac{\Delta E^*}{k_B T} \right) \tag{I.5}$$

With v_0

$$v_0 = \frac{k_B T}{h} f\lambda \left[1 - \exp\left(-\frac{\Delta G_{\alpha c}}{k_B T} \right) \right] \times \exp\left(\frac{\Delta S^*}{k_B} \right) \tag{I.6}$$

At 600 °C, $0.137 < \Delta G_{\alpha c} < 0.217 eV$ [Donovan *et al.* 1985, Roorda *et al.* 1991] thus yielding $\exp(-\Delta G_{\alpha c}/k_B T) \approx 1$. As the temperature dependence of v_0 can be dropped, the

Equation I.5 can be rewritten under the form of an Arrhenius equation [Arrhenius 1889] $v = A \times \exp(-E^*/k_BT)$. The activation energy for the SPER reaction can be extracted via temperature dependent experiments with $E^* \equiv -k_B\partial(\log v)/\partial(T^{-1})$. Examples are given in Figure I.18 where the regrowth rates of silicon on several substrate orientations are plotted. The regrowth rate is extracted by measuring the α-c position over time. Two main experimental techniques are used, either Rutherford Backscattering Spectrometry (RBS) or *in situ* Time Resolved Reflectometry (TRR). Several authors have extracted the activation energy for pure silicon SPER, as seen in Table I.1. The activation energy for pure silicon SPER is now widely admitted to be 2.7 eV. For germanium, similar experiments have been done, with results are compiled in Table I.2. For pure germanium, the value of 2.17 eV is widely used. Finally, the case of SiGe alloys will be introduced later in this work.

Reference	Temperature range (°C)	E^* (eV)
[Csepregi *et al.* 1978]	450-575	2.35 ± 0.1
[Olson & Roth 1988]	500-1000	2.68 ± 0.05
[Roth *et al.* 1990]	500-750	2.70 ± 0.02
[McCallum 1996]	480-660	2.7

Table I.1: Experimental extractions of the activation energy for pure silicon SPER

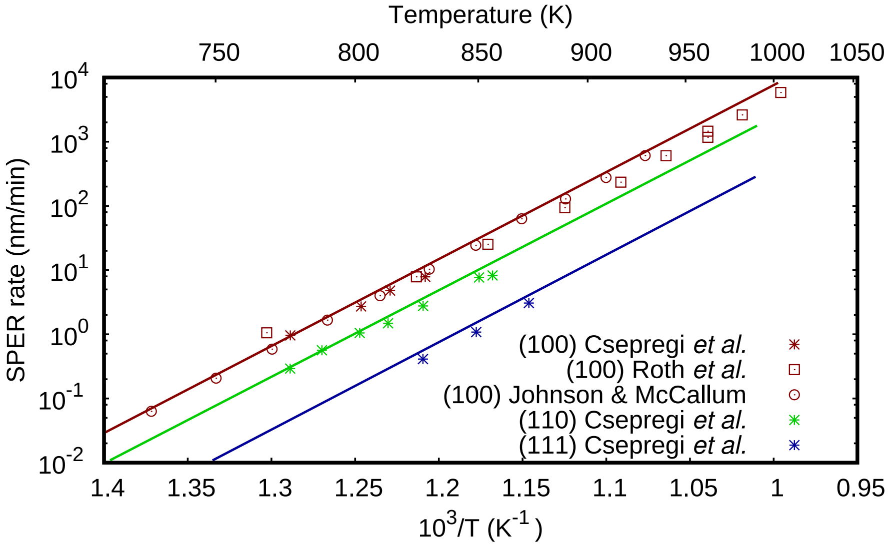

Figure I.18: Arrhenius plot of the SPER rate of silicon on three substrate orientations. Data from [Csepregi *et al.* 1978], [Roth *et al.* 1990] and [Johnson & McCallum 2007]

Reference	Temperature range (°C)	E^* (eV)
[Csepregi *et al.* 1977b]	310–370	2.0
[Donovan *et al.* 1985]	417–457	2.17
[Lu *et al.* 1991]	300-365	2.17 ± 0.2
[Kringhøj & Elliman 1994]	290-430	2.02 ± 0.015
[Haynes *et al.* 1995]	290-390	2.19 ± 0.02
[Johnson *et al.* 2008]	300-540	2.15 ± 0.04
[Claverie *et al.* 2010]	300-540	2.16

Table I.2: Experimental extractions of the activation energy for pure germanium SPER

2.3 Its numerous dependencies

2.3.1 Substrate orientation

As it can be seen in Figure I.18, the silicon regrowth rates differ upon the substrate orientation. Measurements of the regrowth rate along different orientations confirmed this trend, as seen in Figure I.19. The SPER rate heavily depends on the substrate orientation on silicon [Csepregi *et al.* 1978] and germanium [Darby *et al.* 2013]. However, even with these changes of the SPER rate, the activation energy is still 2.7 eV for silicon. The orientation impacts only the pre-exponential factor of the Arrhenius equation [Csepregi *et al.* 1978].

To understand this phenomenon, Csepregi *et al.* suggested that the layer-by-layer recrystallisation occurs at kink sites on <110> ledges on {111} orientations terraces [Csepregi *et al.* 1978]. The substrate orientation dependence thus comes from the density of <110> available ledges. Furthermore, Spaepen [Spaepen 1978] noted that the recristallisation mechanism involves a bond that has to be broken. Finally, these two concepts were refined in a model based on the bond density that are available to be broken at the α-c interface [Custer 1992]. The model of Custer yields very good agreement with the substrate orientation dependence of silicon, as it is shown in Figure I.19.

This bond breaking model has been reviewed as the most propable mechanism [Aziz 1992] amongst other proposed mechanisms for SPER. The model relies on the generation of dangling bonds at the α-c interface caused by breaking a bond. The dangling bonds furthermore migrate along the interface and reconstruct it along their way.

2.3.2 Hydrostatic pressure and non-hydrostatic stress

In the previous section, the SPER rate has been shown to follow an Arrhenius behaviour, in Equation I.3 with an energy barrier of ΔG^* furtherly reduced to an activation energy. However, if we fully expand the Gibbs free-energy, it yields:

$$\Delta G^* = \Delta E^* - T\Delta S^* + P\Delta V^* \tag{I.7}$$

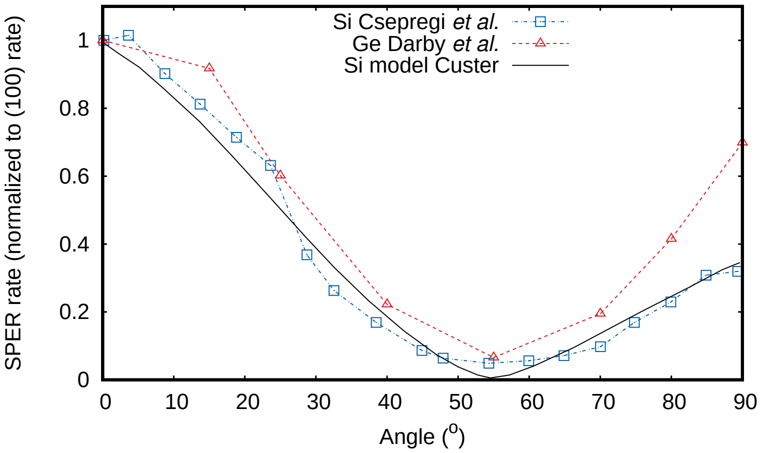

Figure I.19: Regrowth rates for silicon and germanium SPER showing their substrate orientation dependences. Experimental data from [Csepregi *et al.* 1978] and [Darby *et al.* 2013]. Model from [Custer 1992]

where ΔE^* is the activation energy, ΔS^* the entropy change and ΔV^* the volume change upon recrystallisation. The SPER thus have also a pressure dependence. Using the same approximations as before, Equation I.5 becomes:

$$v = v_0 \times \exp\left(-\frac{\Delta E^* + P\Delta V^*}{k_B T}\right) \tag{I.8}$$

ΔV^* is also called activation volume to parallel the activation energy. This activation volume can be extracted during an isothermal pressure-dependent experiment with $\Delta V^* = -k_B T \partial(\log v)/\partial P$. Lu *et al.* [Lu *et al.* 1991] measured an exponential increase of the SPER rate with the hydrostatic pressure, giving a negative activation volume. They extracted $\Delta V^* = -0.28 \pm 0.03\Omega_{Si}$ with $\Omega_{Si} = 12.1\text{cm}^3/\text{mol}$ for silicon and $\Delta V^* = -0.46\Omega_{Ge}$ with $\Omega_{Ge} = 13.6\text{cm}^3/\text{mol}$.

Aziz *et al.* [Aziz *et al.* 1991] expanded the notion of activation volume for non-hydrostatic pressure by introducing a second order tensor: ΔV^*_{ij}. Assuming that the SPER reaction is bounded by a single process and extending the transition state theory a non-hydrostatic stress represented by a second order strain tensor σ_{ij} yields:

$$v(\sigma) = v(\sigma = 0) \times \exp\left(\frac{\sigma_{ij}\Delta V^*_{ij}}{k_B T}\right) \tag{I.9}$$

The activation volume is therefore extended to an activation strain tensor ΔV^*_{ij}. Aziz *et al.* conducted experiments on silicon <100> SPER with an in–plane uniaxial stress over the range of ±600MPa. Their results show a SPER rate decrease with a tensile uniaxial stress and an increase with a compressive uniaxial stress. More recent experiments conducted by Rudawski *et al.* [Rudawski *et al.* 2008] on silicon <100> SPER with an extended range (±1.5GPa) show a decrease with tensile stress but no increase with compressive stress. This behaviour of the SPER rate regarding an uniaxial stress has been previously modelled into a Kinetic Monte Carlo model by Sklénard *et al.* [Sklénard *et al.* 2013]. The model states that the SPER reaction can be divided into two parts. First is a nucleation of an island and second its growth along <110> ledges. The SPER reaction can therefore be seen as a Frank–van der Merwe epitaxial growth mode. Under tensile or compressive stress, the nucleation rate is insignificantly change. However, the ledge recrystallisation rate is severely hindered under compressive stress whereas not hindered under tensile stress. Further details of the model and its implementation can be found in [Sklénard *et al.* 2013]. The model as well as the experimental data from Rudawski *et al.* are shown in Figure I.20.

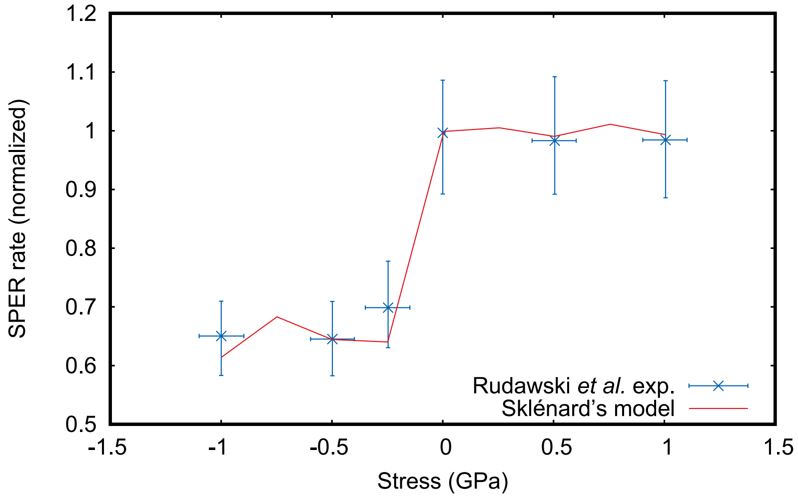

Figure I.20: SPER rates under uniaxial stresses, [Rudawski *et al.* 2008] results and [Sklénard *et al.* 2013]'s model

2.3.3 Impurities

In the 3D integration structures, the SPER process aims to improve the dopant activation. SPER rate is strongly enhanced in presence of dopants. Csepregi *et al.* have seen that group III and V atoms implanted into <100> silicon tremendously enhances the SPER rate. The enhancement is dependent on the atom used, as it can be seen in Figure I.21.

This trend has been confirmed within numerous others investigations [Olson & Roth 1988, McCallum 1999, Johnson & McCallum 2004]. However, at high concentration, the dopant can be pushed towards the surface during the SPER. This phenomenon called snow plough has been observed during arsenic SPER [Hopstaken *et al.* 2004, Demenev *et al.* 2012] and fluorine too [Mastromatteo *et al.* 2010]. High boron concentration does not lead to dopant redistribution. However [Gouyé *et al.* 2010] has experience a limit to the SPER rate increase due to doping. Indeed, above 3×10^{20} /cm^3 boron concentration, the SPER rate

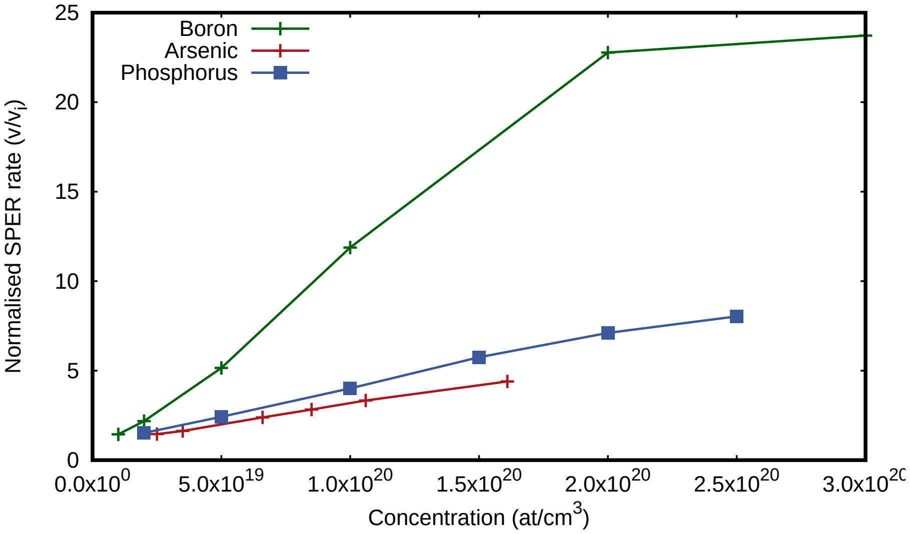

Figure I.21: SPER rate enhancement regarding several doping impurities, data from [Johnson & McCallum 2007]

does not increase anymore. Finally, aluminium and carbon, nitrogen or oxygen are known to decrease the SPER rate, even at moderate concentrations ($< 1 \times 10^{20}$ at./cm^3) [Johnson & McCallum 2007, Chevacharoenkul *et al.* 1991, Strane *et al.* 1996, Narayan 1982]. Lietoila *et al.* co-implanted both group III and V atoms at the same concentration and investigated the impact of this co-implantation during silicon SPER [Lietoila *et al.* 1982]. The co-implantation shows no SPER increase thus affirming that an electrostatic influence is the cause of the SPER enhancement with doping impurities.

A model for the impact of doping impurities on the SPER rate has been developped and refined [Williams & Elliman 1983, Lu *et al.* 1991, Johnson & McCallum 2007, Johnson *et al.* 2012]. This model is based on the assumption that the SPER rate is proportional to the concentration of defects responsible for the SPER. This defect concentration is also proportional to the Fermi level. As the substitutional doping impurities shift the Fermi level, the defect concentration will increase thus increasing the SPER rate. This model, called Generalised Fermi Level Shifting (GFLS), will be presented in-depth in chapter III. The interesting case of the germanium concentration influence during SiGe alloys SPER will be in-depth studied in chapter IV.

3 Simulation context: atomistic simulations

Technology Computer Aided Design (TCAD) is a division of Electronic Design Automation aimed to model and simulate all aspects of a device fabrication. This includes the modelling of process fabrication of a transistor, to the behaviour of several logic gates together. In the front-end processing of transistors, TCAD simulations are used in order

to simulate the process steps of the junction formation. The goal is to know the characteristics, such as defect concentration, dopant activation, stress distribution, of the junction for a specific parameter set and thus find the fittest set of parameters.
TCAD tools span over several timescales and length scales, as it can be seen in Figure I.22. Continuum models, sets of differential equations, can model macroscopic behaviours for large scales. However they lack the physical comprehension of the underlying mechanism generating the behaviour. Atomistic models compromise the simulation scales for a better grasp of the mechanisms occurring during the reaction. Atomistic simulations can be sorted into three different classes that will be explained in the following sections.

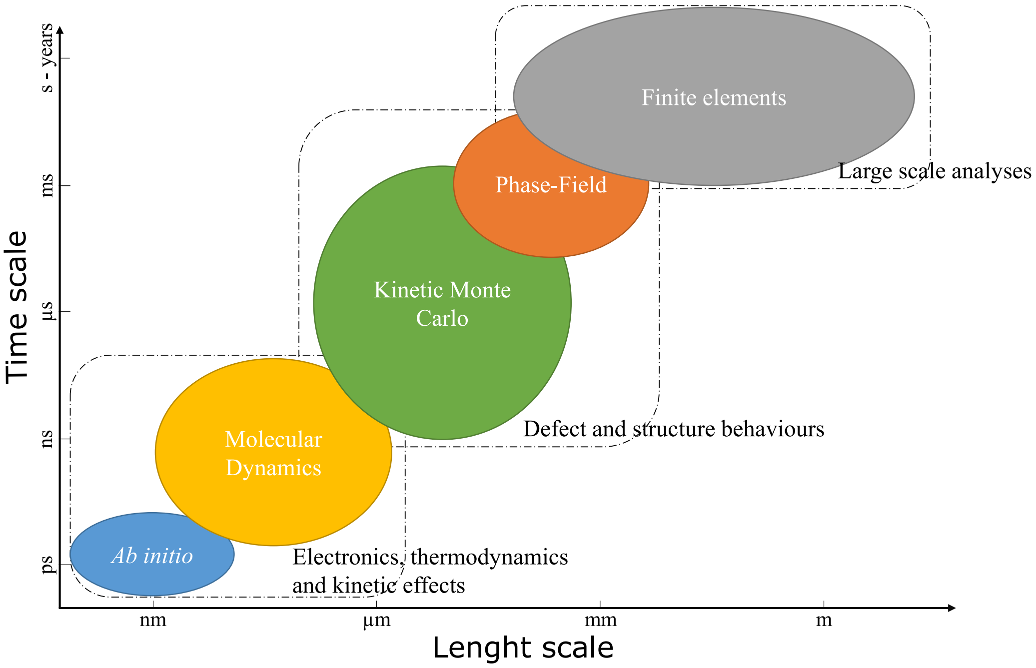

Figure I.22: Time and length scales of the several modelling possibilities and their respective application fields

3.1 *Ab initio* methods

Ab initio methods are non-empirical quantum mechanical methods used to investigate the fundamental properties of materials. These methods use the full Schrödinger equation to investigate many-body systems. However, several approximations have to be introduced in order to be able to solve the Schrödinger equation.
As the *ab initio* methods are more often used to compute material properties of formation energies, the Schrödinger equation can be written within time-independent, non-relativistic Born-Oppenheimer approximation:

$$\mathcal{H}\Psi = [T + V_{ext} + U]\Psi = E\Psi \tag{I.10}$$

where T is the kinetic energy, V_{ext} the external potential seen by the electrons and U the electron-electron interaction. $\mathcal{H}$ is the Hamiltonian of the structure and Ψ its wave function.

There are numerous ways to define the wave function of a system. The simplest one is the Hartree-Fock method. However this method needs a huge computational effort. The wave function computation has been greatly simplified by the Hohenberg & Kohn theorem that states that the electron density is sufficient to describe the fundamental state of the system [Hohenberg & Kohn 1964]. This method is called the Density Functional Theory, or DFT, and has been widely used in materials science to investigate the ground state of a system. From the ground state of between several systems, formation energies of a certain defect can be deducted. *Ab initio* simulations are usually done with cells containing less than 1000 atoms and require large amount of computational time. However, they allow in-depth analyses of material properties.

3.2 Molecular Dynamics methods

Molecular dynamics (MD) method is a deterministic computer simulation used for investigating the movement of vast numbers of particles. The molecular dynamics method can be used to investigate the motion of a system towards its lowest free energy state. The method originates from the late 1950s [Alder & Wainwright 1959]. The position and movement of an atom i in a system containing n atoms are governed by the Newton's equations of motion:

$$m_i \frac{d^2 r_i}{dt^2} = F_i(r_1, r_2, ..., r_n) \tag{I.11}$$

where m_i is the mass of the atom i, r_i its position and F_i the forces upon it.

The force F_i computation is done with an interatomic potential. Several types of potential can be used, depending on the reaction and accuracy wanted. For example, when electron density of states or excited states are needed, potentials derived from *ab initio* methods are to be used but are extremely computationally demanding. Empirical potential alleviate the computation costs but are bounded to certain atom type and must be carefully adjusted. For silicon SPER MD calculations, several many-body potentials can be used: Tersoff [Tersoff 1989], Environment Dependent Interatomic Potential (EDIP) [Bazant & Kaxiras 1996, Bazant *et al.* 1997, Justo *et al.* 1998], Stillinger-Weber [Stillinger & Weber 1985] or the Bond Order Potential (BOP) [Gillespie *et al.* 2007].

Figure I.23 succintly presents the algorithm for MD calculations. At the beginning, the atoms positions and velocities are initialised. Then the forces applied to each atom are calculated and the new atomic positions and velocities are calculated according the Newton's equation. This step can be solved using the Verlet integration [Verlet 1967]. This loops is repeated until a certain time limit.

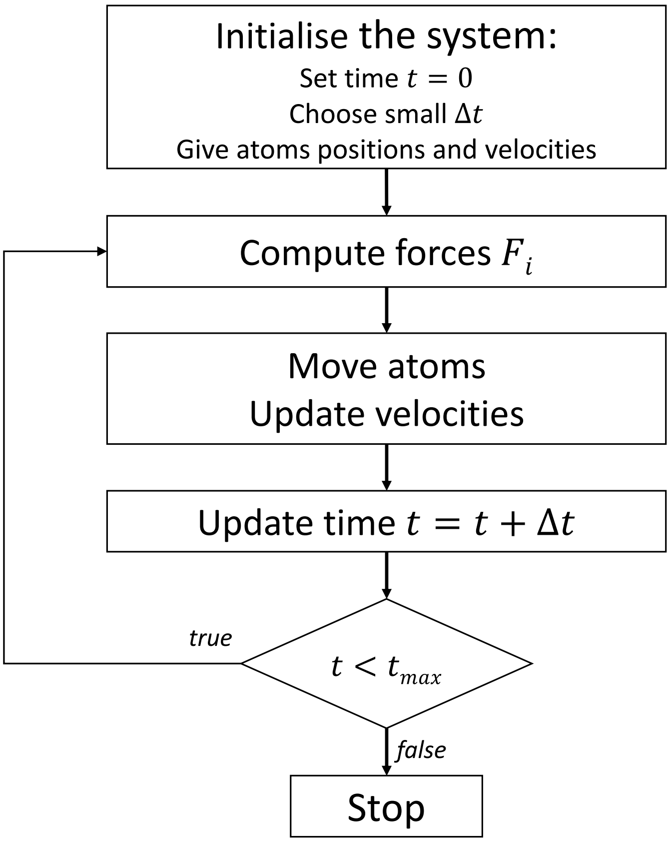

Figure I.23: Flow chart of the Molecular Dynamics algorithm

For silicon Molecular Dynamics, cells containing less than 50000 atoms have been used and the simulated time rarely exceeds 50 ns. This atomistic simulation method computational cost is directly linked to number of atoms in the cells and the simulated time. For the numbers discussed before, a simulation can be run below 10000 hours. Compared to *ab initio* simulations, molecular dynamics ones can give insights on the kinetic effects during reactions but at the cost of the loss of some intrinsic properties. For example, using the Tersoff potential during a MD simulation, the melting point temperature for silicon is found around 2400 K [Marqués *et al.* 2001], well above the value found in the experiments, 1685 K [Mayer & Lau 1990]. This method is unfortunately unsuitable to compute processes applied on a whole transistor.

3.3 Monte Carlo methods

The Monte Carlo method is a group of algorithms that is broadly used to solve problems in several fields, Mathematics and Physics, among others. The Monte Carlo method was developed by Metropolis & Ulam [Metropolis & Ulam 1949] in the end of the 40's decade to investigate thermonuclear related problems. The name, Monte Carlo, comes from an area in Monaco famous for its casinos. The core idea of a Monte Carlo method is to solve a problem via a large set of random numbers, hence the relation with casinos. Although the Monte Carlo method regroups a wide number of algorithms, the most known are the Metropolis Monte Carlo [Metropolis *et al.* 1953] and the kinetic Monte Carlo [Young & Elcock 1966] also known as dynamic Monte Carlo. Metropolis Monte Carlo is used when the properties of the system are not known, meaning that the partition function of the system is not known *a priori*. In this case, using a Metropolis Monte Carlo can bring the system to its thermodynamical equilibrium.

In the kinetic Monte Carlo method, the different states constituting a system are known *a priori*. The system can therefore evolve between different states and states are separated by an energy barrier. The thermal vibrations brought by k_BT can make the system switch between states. The evolution between two states is called an event. An event could be an atomic jump, or an atom that is recrystallised. In the KMC method, all events are considered independent on previous events, and thus describe Poisson processes. Considering an event e_i, modelling a reaction with an activation barrier of E_a, the transition state theory can link the transition rate r_i with E_a:

$$r_i = A \times \exp\left(- \frac{E_a}{k_BT} \right) \tag{I.12}$$

where A is prefactor that is calibrated to mimic experimental data. Generalising to N independent Poisson processes with rates r_i, the problem reduces to a Poisson process with rate $R = \sum_i r_i$ with a mean time between rates of $< t >= 1/R$.

The kinetic Monte Carlo algorithm is as follows: among list of N events, an event e_n to be performed is chosen by a uniformly distributed random number s such as $R_n - 1 < sR \leqslant R_n$. The event is performed and the algorithm computes again the event list. Finally, to ensure a direct and unambiguous relationship between the Monte Carlo time and the real time [Fichthorn & Weinberg 1991], a random number u is used into the time increment calculation:

$$\Delta t = -\log(u)/R \tag{I.13}$$

where u is an uniform random number between 0 and 1.

The algorithm presented before is the Bortz, Kalos and Liebowitz algorithm [Bortz *et al.* 1975] and a schematic view of this algorithm can be seen in Figure I.24. Kinetic Monte Carlo simulations can hold several hundred thousand atoms and can simulate several hours. However, the method cannot give any physical insights of the reaction. The method needs in fact physical meaning as an input and thus often relies on *ab initio* and molecular dynamics methods to populate the possible events and their energies.

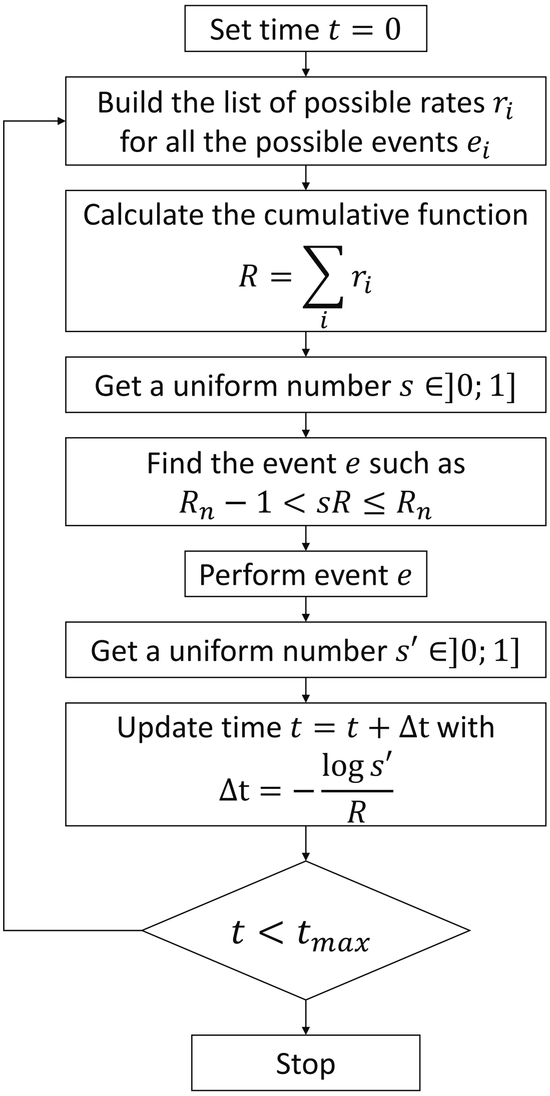

Figure I.24: Flow chart of the Bortz, Kalos and Liebowitz algorithm [Bortz *et al.* 1975] for Kinetic Monte Carlo simulations

4 Scope and aim of this thesis

This thesis aims to understand the SPER mechanisms that happen during the junction formation of a transistor following the 3D sequential integration and to model them into a kinetic Monte Carlo simulator. First, investigations of pure silicon SPER will be conducted in chapter II and chapter III. More precisely, chapter II will investigate silicon SPER with the kinetic Monte Carlo simulator that will be used in this work as well as some analyses with Molecular Dynamics calculations. The following chapter III will concentrate on the boron impact during silicon SPER. In a second part, the SPER of relaxed and strained SiGe alloys will be brought in chapter IV and chapter V, respectively. The aspect of amorphisation of materials will be not investigated throughout this work.

The investigations, models and calculations have been done with the help of two simulators. First, MMonCa, for Modular Monte Carlo, is a kinetic Monte Carlo simulator created by Dr. Ignacio Martin-Bragado. The simulator is written in `C++` and interfaced with `TCL`. The former language is used for the core model and its modules, the latter for the user-interactions. MMonCa has two different modules. First, a Lattice KMC (LKMC) that places all the atoms on their lattice sites and is used for phase-change reactions, such as SPER [Martin-Bragado & Moroz 2011]. Secondly, an Object KMC (OKMC) is an off-lattice simulator that can handle point and extended defect evolution [Martin-Bragado *et al.* 2013]. The random numbers are created by Mersenne Twister pseudorandom number generator [Matsumoto & Nishimura 1998]. Finally, the structure diagram of MMonCa can be seen in Figure I.25.

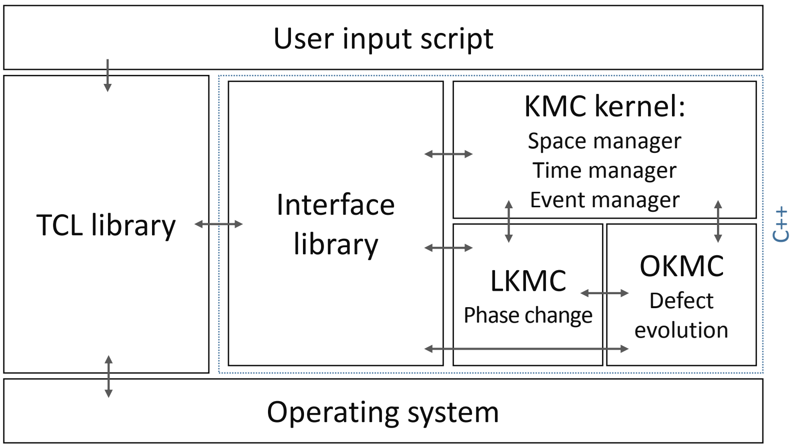

Figure I.25: Structure of MMonCa, the KMC simulator used in this work

Secondly, Molecular Dynamics calculations have been done. These computations were powered by `LAMMPS` [Plimpton 1995][4]. `LAMMPS`, for Large-scale Atomic/Molecular Massively Parallel Simulator, is a classical molecular dynamics simulator. In this work, `LAMMPS` has been used to investigate the SPER of silicon and silicon-germanium alloys, more particularly investigations on the substrate orientation dependence and the germanium content, respectively.

5 French summary — Résumé

L'industrie de la microélectronique est en constante évolution depuis le début des années 50, son démarrage. Cette évolution a été résumée par la maintenant célèbre loi de Moore. Toutefois, cette loi commence a être prise en défaut, comme peut le montrer le ralentissement de nouvelles lithographies par un des leader, Intel[5]. Même si la loi de Moore devient de plus en plus contraignante, on peut toutefois remarquer une autre amélioration

---

[4] `http://lammps.sandia.gov`

[5] `http://bit.ly/1LGd3ly`

constante. Koomey *et al.* [Koomey *et al.* 2011] ont en effet remarqué que l'efficacité energétique des processeurs est aussi en constante évolution et celle-ci ne parait pas diminuer, contrairement à la loi de Moore[6]. La Figure I.1 permet de voir cette progression de l'efficacité énergétique.

Du fait que les transistors ont maintenant une bonne efficacité énergétique, la mise en place d'un procédé d'intégration où deux transistors sont alignés verticalement est possible. Un tel procédé permet aux acteurs de la microélectronique de pouvoir poursuivre la loi de Moore. Ce procédé d'intégration est visible à la Figure I.5. Cependant, ce procédé, nommé CoolCube$^{\mathrm{TM}}$, possède des spécifications drastiques. En effet, pour éviter une détérioration du transistor du bas lors de la fabrication de celui du haut, ce dernier doit être fabriqué à faible budget thermique, soit au dessous de 500°C pendant un maximum de cinq heures.

Un procédé répondant à ces spécifications est la SPER, ou recroissance épitaxiale en phase solide. Son procédé est résumé à la figure Figure I.11 : la source et le drain sont amorphisés par implantation ionique, les dopants sont aussi implantés dans ces régions. Puis un recuit permet d'activer la réaction et les dopants sont finalement activés. Il est important qu'une graine de cristal existe, afin que lors de la SPER le réseau cristallin soit correctement recopié. Dans le cas où la graine cristalline n'existerait pas — via une amorphisation trop importante — le recuit donnerait place à une région polycristalline, ce qui doit être évité à tout prix, du fait de la faible performance d'un polycristal activé face à un monocristal activé. La Figure I.14 montre bien la différence entre a) la réaction de sper et b) la création d'un polycristal.

Dans le procédé CoolCube$^{\mathrm{TM}}$, à la place d'un silicium pur, un alliage de silicium-germanium (SiGe) est utilisé pour les jonctions P. L'alliage SiGe est utilisé ici car il permet une augmentation de la mobilité des trous dans la jonction, augmentation encore plus marquée si l'alliage est contraint. Le gain sur la performance finale d'un transistor à base de SiGe contraint par rapport à du silicium est visible à la Figure I.9.

La SPER est un phénomène complexe ayant de nombreuses dépendances. Premièrement, la vitesse de SPER , ou la vitesse à laquelle l'interface amorphe-cristal (interface α-c) avance, peut être modélisée par la loi d'Arrhenius. Soit v la vitesse de SPER, celle-ci peut être écrite comme :

$$v = v_0 \times \exp\left(-\frac{\Delta E^*}{k_B T}\right) \tag{I.14}$$

où v_0 est un facteur pré-exponentiel prenant en compte l'environement local du site de recristallisation, ΔE^* l'énergie d'activation de la réaction et $k_B T$ son sens usuel, la constante

---

[6] `http://bit.ly/2jw14ym`

de Boltzmann et la température. Pour le silicium, l'énergie d'activation extraite via des expériences est de 2,7eV. Pour le germanium, elle est de 2,17eV. Le cas singulier des alliages SiGe sera traité dans ce travail.

Deuxièmement, la vitesse est fortement dépendante de l'orientation du substrat. Cette dépendance est visible à la Figure I.19 pour le silicium et le germanium. Pour les alliages SiGe, cette dépendance n'a pas encore été investiguée. Il est intéressant de noter que même si la vitesse est fortement influencée par l'orientation du substrat, l'énergie d'activation reste la même dans toutes les orientations. Une courbe d'Arrhenius pour un substrat silicium est visible à la Figure I.18, montrant que, quelque soit l'orientation, l'énergie d'activation de la réaction reste la même.

Toisièmement, la SPER est aussi dépendante de la contrainte appliquée au système. Dans Equation I.14, ΔE^* est une simplification de l'enthalpie. Or, dans le cas où le système est soumis à une pression P, celle-ci intervient dans l'exponentielle. ΔE^* devient $\Delta E^* + P\Delta V^*$, où P est la pression et ΔV^* le changement de volume lorsque le cristal passe de la phase amorphe à cristalline.

Enfin, la présence de dopants, par exemple bore ou phosphore, augmente de manière significative la vitesse de SPER. La Figure I.21 montre bien une augmentation de la vitesse en fonction de la concentration de différents atomes dopants. Afin d'expliquer ce comportement, un modèle phénoménologique a été proposé dans la littérature. Il se nomme GFLS, pour déplacement de niveau Fermi généralisé. Ce modèle admet comme hypothèse qu'un défaut est responsable de la SPER et que la concentration de celui-ci influe au premier ordre la vitesse de la SPER. Or, lors de l'addition de dopants, la concentration de ce défaut augmente, du fait qu'il possède des états chargés dans la bande interdite et que le niveau de Fermi est déplacé.

Ces dépendances ont été investiguées antérieurement au travail proposé ici. Le lecteur intéressé peut être redirigé vers les travaux de Sklénard [Sklénard 2014]. Dans ces travaux, la SPER et ses dépendances ont été modélisées par une approche KMC, ou Monte Carlo cinétique. Le KMC est une méthode permettant de simuler des événements ayant des probabilités connues. Ainsi, le probabilité de recristallisation — l'événement — d'un atome à l'interface amorphe-cristal est connue par l'Equation I.14. La méthode considère tous les événements possibles et choisit un au hasard, d'où la relation stochastique.

Cependant, de nombreuses questions persistent du fait de l'introduction des alliages SiGe dans le procédé de fabrication proposé par CoolCube$^{\text{TM}}$. De plus, certains phénomènes apparaissant lors de la SPER du silicum ne sont toujours pas résolus. Le travail proposé ici reprend et étend les travaux de Sklénard. Premièrement, en reprenant le modèle de la SPER et en l'améliorant pour prendre en compte d'autres effets encore incompris, comme l'effet de la concentration de germanium lors de la SPER, dans les alliages contraints ou non, ou encore la saturation de l'augmentation de la vitesse de SPER à forte concentration de bore, comme il est possible de voir à la Figure I.21. Deuxièmement, en agrémentant les études KMC avec des études de la SPER en Dynamique Moléculaire, une autre méthode de simulation qui résoud les équations de Newton afin d'amener un système vers un point d'énergie plus faible. Ces études, utilisant une approche plus fondamentale que le KMC, permettent de s'assurer que les événements KMC introduits dans le simulateur sont plausibles.

Le travail proposé ici se décompose en ces chapitres suivants. Le chapitre II présente, dans un premier temps, le modèle KMC implémenté dans MMonCa, le simulateur KMC qui est utilisé tout au long de cette thèse. Dans un second temps, des investigations sur la SPER du silicium par des calculs de Dynamique Moléculaire sont montrés. Le chapitre III explore la saturation de l'augmentation de la vitesse de SPER lorsqe de fortes concentrations de bore sont présentes. Le chapitre IV propose un modèle KMC sur les effets de la concentration de germanium lors de la SPER d'alliage de SiGe relaxé. Enfin, le chapitre V investigue la SPER d'alliages de SiGe contraint.

Chapter II

Silicon and germanium SPER: LKMC and MD investigations

This chapter serves as an introduction to the Solid Phase Epitaxial Regrowth. First, the Lattice Kinetic Monte Carlo model implemented in MMonCa is presented. Prior to this thesis, the model was able to handle several SPER dependencies, such as substrate orientation, stress and dopant concentration. Only the handling of the substrate orientation in silicon and germanium is presented as it is the perfect introduction to the LKMC model. Secondly, the same SPER dependency is investigated on silicon with the scope of Molecular Dynamics simulations. Indeed, even if MD simulations of silicon SPER yield good agreement on <100> orientation, SPER rates of other orientations are far from experimental data. These investigations aim to find the cause of this.

Contents

1 MMonCa LKMC model: handling of the substrate orientation

A lattice Kinetic Monte Carlo model has been implemented in the LKMC section of MMonCa prior to this current work. This section will present the model implementation and its capabilities regarding the substrate orientation dependence of the silicon and germanium SPER. The model is a lattice model meaning that prior to the simulation beginning, all atoms are positioned onto their lattice sites. In the model, the differentiation between amorphous and crystalline atoms is made only by an internal flag on a lattice atom. Contrary to MD simulations, atoms are not moving, only their phase flags change upon a recrystallisation event.

As the SPER process is strictly located at the α-c interface, as discussed in section 2.3, the model is thus only focused at this interface. Atoms lying at the α-c interface are susceptible to recrystallise. According to the KMC algorithm applied to SPER, each atom must have its own recrystallisation probability:

$$r = r_0 \cdot \exp\left(\frac{-E_a}{k_B T}\right), \tag{II.1}$$

where r_0 is a prefactor depending on the atom surroundings and E_a the activation energy for the reaction.

The LKMC model follows the Drosd & Washburn phenomenological model [Drosd & Washburn 1982], stating that an atom is recrystallised when it forms two undisturbed bonds with crystalline atoms. An undisturbed bond is not stretched and has the nominal bond angle from one another. This phenomenological model can also be viewed as the reconstruction of a six-fold ring in the <110> orientation as seen in Figure II.1. The recrystallisation event leads to the recrystallisation of either one, two and three atoms on (100), (110) and (111) surfaces, respectively.

From the recrystallisation events of the Drosd & Washburn model emerges a simplification of the SPER reaction. Indeed, only three possible microscopic local configurations {100}, {110} and {111} at any α-c interface can be considered, as shown in Figure II.1. Therefore, in the LKMC model, three events ({100}, {110} and {111}) are present. To reflect the heavy dependency of the SPER rate on the substrate orientation, the pre-exponential factor r_0 is made dependent on the site orientation of the atom. To determine the local configuration, the local plane orientation thus has to be detected. To determine the local regrowth plane, the model relies on the list of first (1NN), second (2NN) and third (3NN) nearest neighbours for the atom considered for recrystallisation. In a diamond lattice material with a lattice parameter of a_0, any atom has 4, 16 and 24 1NN, 2NN and 3NN, at a distance of $a_0 \cdot \sqrt{3}/4$, $a_0 \cdot \sqrt{2}/2$ and $a_0 \cdot \sqrt{11}/4$, respectively. It has to

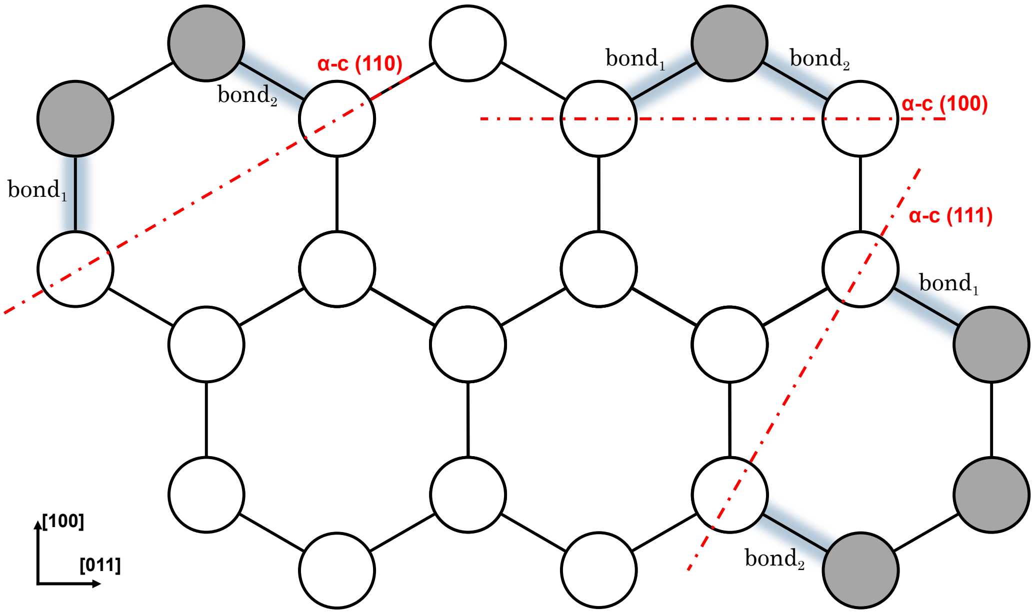

Figure II.1: Sketch of incomplete six-fold rings lying at the amorphous-crystalline interface. Amorphous atoms are coloured, crystalline ones in white. Highlighted bonds must be broken to recrystallise the whole six-fold ring

be emphasised that as the model is a lattice one, amorphous and crystalline atoms have the same number of nearest neighbours.

An amorphous atom is considered on a {100} local configuration when it has two or three crystalline 1NN ($c1NN$). If it has one crystalline 1NN, it can be in either a {110} or a {111} configuration. If the considered atom has an amorphous 1NN ($\alpha 1NN$) with one crystalline neighbour, then it is part of a {110} configuration. Otherwise the atom is part of a {111} configuration.

Furthermore, the model introduces the concept of lowly and highly coordinated {100} configurations, named $\{100\}_l$ and $\{100\}_h$, respectively. Indeed, if no distinction on the {100} configurations is made, the α-c interface will not be smooth [Martin-Bragado 2012]. Adding a differentiation in the {100} configurations allows a smoother α-c interface, closer to what it has been seen in experiments [Lohmeier *et al.* 1994], with a nominal roughness around 8 Å. The deciding tree that the algorithm is going through is depicted in Figure II.2.

Finally, especially on {111} orientations, experiments indicate the formation of defects during SPER [Csepregi *et al.* 1978, Drosd & Washburn 1982, Narayan 1982]. These defects have been undoubtedly distinguished as twin defects [Jones *et al.* 1988]. The twin defect is a natural consequence of the Drosd & Washburn model used in this LKMC model. Indeed, on {111} local configuration, the farthest atom from the interface possesses a certain degree of liberty, making it viable to be twisted by 60°. The structure is still a six-fold ring, however the overall periodicity is lost. Figure II.3 presents a {111} local configuration

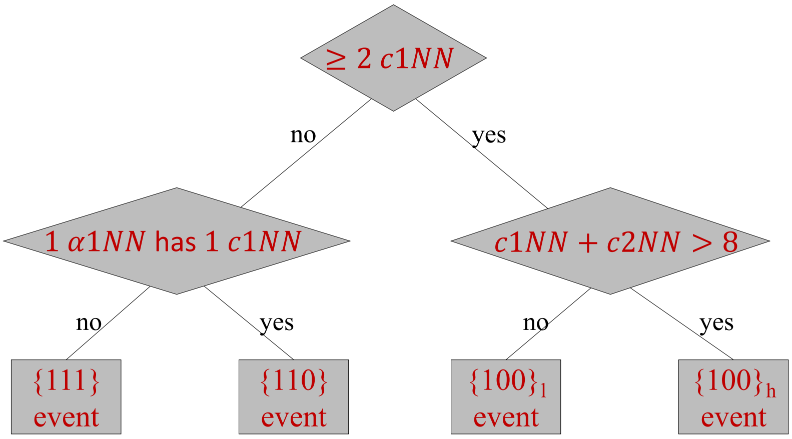

Figure II.2: Deciding tree for choosing the local configuration during SPER

and its twin defect. The amorphous atoms are coloured in red. As an analogy, the difference between a {111} local configuration and its twin defect is the same difference between the chair and boat conformation in cyclohexane, respectively. The inclusion of twinnig — twin defect generation — in the LKMC model is vital to correctly simulate the substrate orientation dependence of the SPER rate [Martin-Bragado 2012, Martin-Bragado & Sklénard 2012]. The twin defect probability has been defined to 10%. This means that 10% of all {111} local configurations that are recyrstallised during a SPER simulation harbour a twin defect. All parameters related to SPER are listed in Table II.1, where the germanium values are taken from [Darby *et al.* 2013].

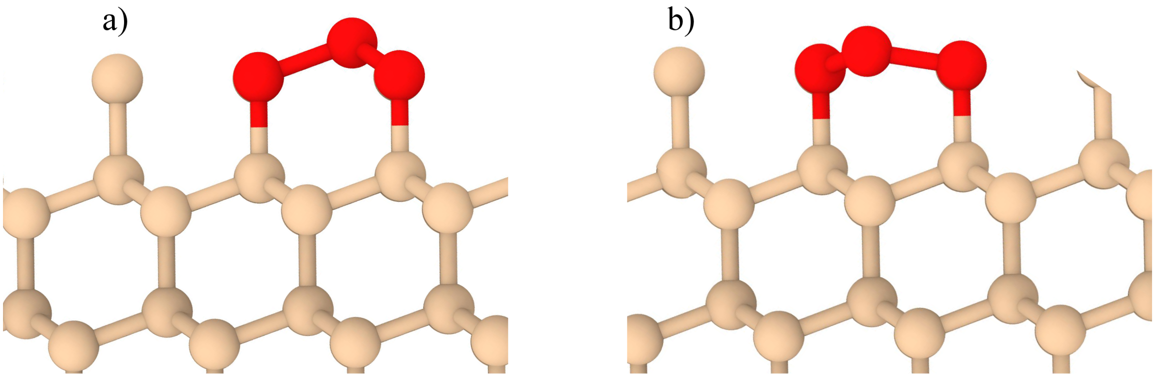

Figure II.3: A {111} local configuration (a) and its twin defect (b)

The equation Equation II.1 can be rewritten as:

$$r = K(n) \cdot \exp\left(\frac{-E_a}{k_B T}\right), \tag{II.2}$$

with $K(n)$ the substrate orientation dependent factor. The LKMC model has been used against a 60 nm×180 nm×$30\sqrt{2}a_0$ cell with periodic conditions along the z-axis. a_0 is the silicon or germanium lattice parameter. The α-c interface evolution is alongside the

Local config.	$K_{Si}(n)$ (s^{-1})	$K_{Ge}(n)$ (s^{-1})
$\{100\}_h$	7.425×10^{17}	2.35×10^{18}
$\{100\}_l$	3.094×10^{16}	1.08×10^{17}
$\{110\}$	1.325×10^{15}	1.65×10^{16}
$\{111\}$	8.10×10^{11}	1.50×10^{12}

(a) Local configuration prefactors

Material	E_a (eV)
Si	2.70
Ge	2.17

(b) Activation energies

Table II.1: Values used in the LKMC model

x-axis. The initial (100) plane is rotated from 0 to 90° around the $[0\bar{1}1]$ z direction to take into account all possible substrate orientations. Two cells, accounting for a rotation of $\theta = 0°$ and $\theta = 70°$, are presented in Figure II.4. The interface evolution is monitored away from the cell boundaries to avoid border effects. Indeed, as there is no periodic conditions along the y-axis, the interface grows following {111} facets near the boundaries. This can be clearly seen in Figure II.4a. The results of the LKMC simulations are shown in Figure II.5. As it can be seen, the LKMC model yields close agreement with experimental data for both silicon and germanium.

Figure II.4 shows valuable information about the LKMC model. First it is worth mentioning that the LKMC model outputs only atoms that are considered at an α-c interface. If the recrystallisation is lowly defective, the output cell has a thin interface, with only a few atomic layers, as in Figure II.4a. On the contrary, if the recrystallisation is highly defective, the interface is thick, as in Figure II.4b. Second, the effect of a twin defect can be seen in Figure II.4a, where defective silicon appears on a {111} plane due to the twin defects.

2 Molecular Dynamics SPER investigations

2.1 MD SPER background

The nature of the microscopical mechanism causing the SPER reaction has driven several investigations on the amorphous-crystalline interface. Molecular Dynamics simulations have been used to identify and understand the underlying mechanism of the SPER reaction. Several studies extensively investigated the growth mechanism with different potentials: Stillinger-Weber [Bernstein *et al.* 2000], Tersoff [Motooka *et al.* 2000], EDIP [Gärtner & Weber 2003], bond order potential (BOP) [Gillespie & Wadley 2009]. Under this variety of potentials, [Krzeminski *et al.* 2007] performed an in-depth investigation on the best suitable potential for SPER simulation. Their conclusion was that despite the high melting temperatures for crystalline (2391-2750K) and amorphous (2050K) [Marqués *et al.* 2004]

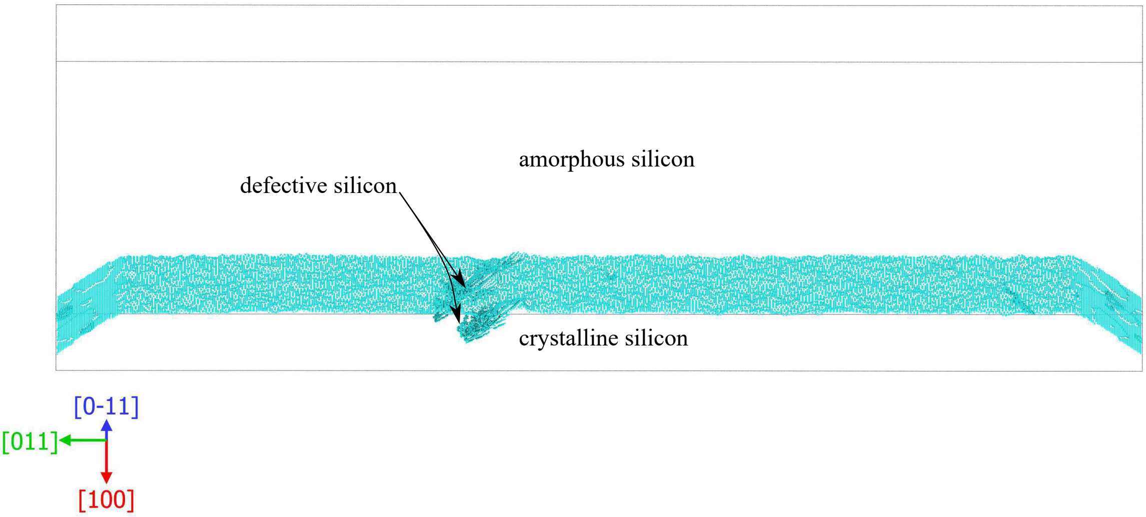

(a) Simulation cell after 10 nm recrystallisation at 550°C on a (100)silicon

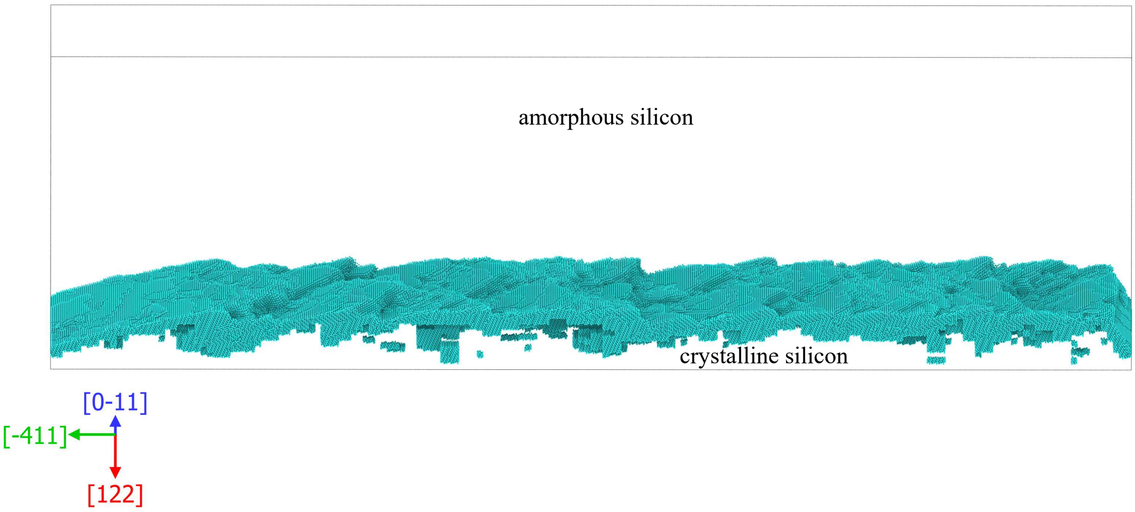

(b) Simulation cell after 10 nm recrystallisation at 550°C on a (122)silicon

Figure II.4: Simulation cells used to evaluate the substrate orientation dependence of the SPER rate. Only the (100) and (122) cells are presented, accounting for a rotation of $\theta = 0°$ and $\theta = 70°$

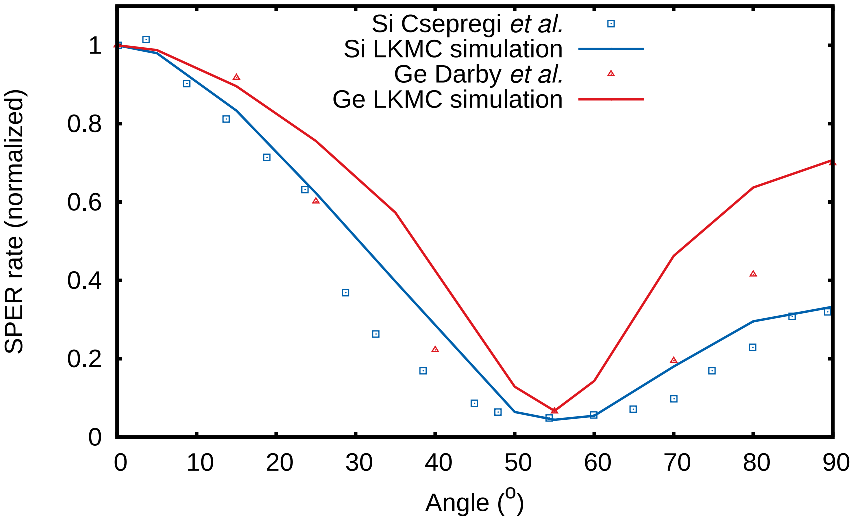

Figure II.5: Comparison between experiments and LKMC simulation of the SPER rate dependency of the substrate orientation. Experimental data from [Csepregi *et al.* 1978] and [Darby *et al.* 2013]

silicon compared to the experimental values, the Tersoff interactomic potential within its third parametrisation (T3) [Tersoff 1989] is the best potential for simulating the SPER reaction.

With the T3 potential, stress [Lai *et al.* 2012] and orientation [Lampin & Krzeminski 2009, Lai *et al.* 2011, Marqués *et al.* 2012] dependencies of silicon SPER have been investigated. From these works, molecular dynamics computations can only deliver a qualitative agreement with both of these dependencies. Indeed both activation volume and SPER ratios between <100> and <111> are found to differ from their experimental values.

2.2 Amorphous phase generation and characterisation

Prior to investigating the SPER reaction, the amorphous phase must be created. The design of a recipe to create an amorphous phase that corresponds to the experimental data is challenging. As said before in section 2.1.2, the amorphous phase does no longer have a long range order but still keeps its short range one. And here lies the difficulty of generating an amorphous phase. The algorithm must introduce a certain type of disorder into a crystalline lattice and randomness creation is not easily done with algorithms.

The first attempts were with hand built stick and ball systems of Polk & boudreaux [Polk & Boudreaux 1973]. However no recipe was provided *per se* as the amorphous-crystalline interface was perfected through computer optimisation. Later Spaepen [Spaepen 1978] and Saito & Ohdomari [Saito & Ohdomari 1981], tried simple construction rules to generate an amorphous-crystalline interface. The main focus of these rules was to restrain using the usual six-fold ring as the construction base.

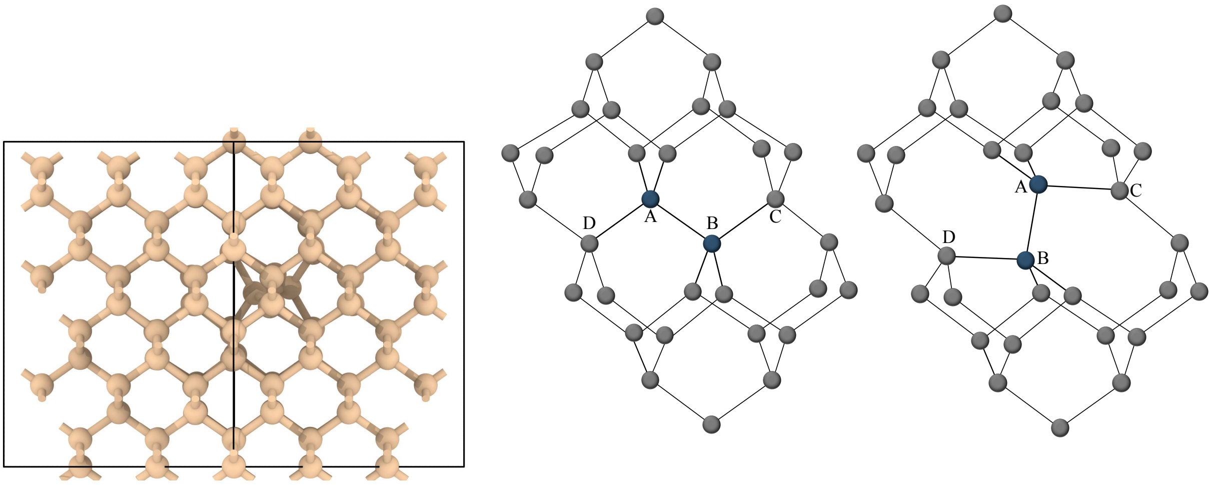

(a) <110> view of a unique bond defect in crystalline silicon. Relaxed position given by *ab initio* methods

(b) Schematic view of the bond defect generation. Atoms A and B are displaced. Adapted from [Cargnoni *et al.* 1998]

Figure II.6: The bond defect

Further attempts were done with the aid of computer programs. Wooten,Winer and Weare (WWW) [Wooten *et al.* 1985] introduced a bond rearrangement that if repeated enough would shatter the long range order of a crystalline lattice, thus making the phase amorphous. Finally, thanks to the emergence of Molecular Dynamics, the melt-quenching method [Biswas *et al.* 1987] was created. This method is based on a melting of the crystalline phase using high temperatures and is followed by a quench with a fast temperature ramping. The result is a solid phase with no more long range order but only close range order, as expected for an amorphous phase.

More recently, a topological defect called the bond defect has been identified using MD and *ab initio* investigations. This bond defect, as shown in Figure II.6, consists of two five-fold rings and two seven-fold rings packed together. This defect is closely related to the crystalline to amorphous transition under irradiation [Motooka 1994, Motooka *et al.* 1995, Stock *et al.* 2000, Marqués *et al.* 2003]. Indeed, during an ion implantation, pairs of interstitial-vacancy, called IV pairs, are created due to cascades. Tight-binding MD simulations calculations of Tang *et al.* [Tang *et al.* 1997] reported that under a certain condition, the IV-pair creates a metastable defect structure with an annihilation energy of 1.1eV. *Ab initio* investigations of Cargnoni *et al.* [Cargnoni *et al.* 1998] confirmed this energy barrier as well as the link between the IV-pair defect and the bond defect.
As the bond defect has a closer physical meaning with the junction process used in this work, the method of amorphous generation with bond defects has been chosen. To create a bond defect, two atoms must be displaced. First, the relaxed positions of these two atoms have been characterised using DFT methods. The result of this computation can

be seen in Figure II.6a. The displacement vectors of the two atoms from their original positions to their positions in the relaxed metastable defect are recorded. To take into account all the possible symmetries, the displacement vectors are expressed according to a third non-moving atom. In the schematic in Figure II.6b, the third non-moving atom could be either C or D.

To create an amorphous phase, three crystalline neighbour atoms are randomly chosen and two of them are displaced according to the displacement vectors. A bond defect is thus created and the two atoms that have been displaced are not considered crystalline anymore and cannot be chosen again for displacement. An amorphous phase created by the quenching method has also been created using the following parameters:

- $12a_0 \times 12a_0 \times 12a_0$ containing 13824 atoms
- periodic boundary conditions along all directions
- the simulation is done in the canonical ensemble NVT
- 3500K anneal during 50ps
- a quench using a temperature ramp of 3.5×10^{15}K/s

Several bond defect concentrations — the number of atoms that will be displaced during amorphisation — have been investigated to yield a true amorphous phase, as seen in Figure II.7 and Figure II.8. From these figures, the amorphous phase generated with 25% of bond defect is chosen as the way to create amorphous phases in all the Molecular Dynamics calculations shown in this work.

2.2.1 Amorphous crystalline interface extraction

The characterisation of an amorphous or crystalline atom is also a challenging topic. It is indeed rather difficult to declare an atom crystalline or amorphous at a α-c interface. Two methods have been used in the literature, and require the correlation between an atom and the perfect silicon crystalline atom. One method computes the dot product between the bond directions of an atom and the bond direction of the perfect silicon crystalline atom, χ [Bernstein *et al.* 2000]. The other method also computes a dot product, but between the position of an atom and a vector of the reciprocal lattice to the interface. This computation, yielding the structure factor is shown below:

$$S(x) = \left| \frac{1}{N_x} \sum_{x<x_i<x+dx} e^{j\vec{k}\cdot\vec{r_i}} \right| \tag{II.3}$$

where N_x is the number of atoms between x and $x+dx$, $r_i = \{x_i, y_i, z_i\}$ the position of an atom i and $\vec{k}$ is a vector of the reciprocal lattice parallel to the interface, thus depending

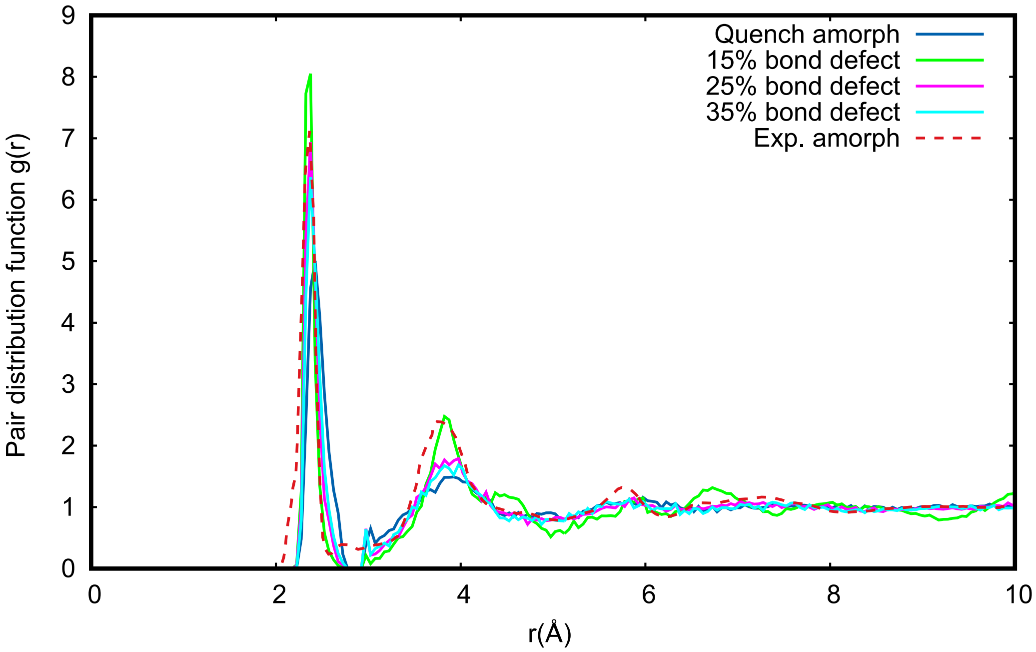

Figure II.7: Distribution function of several amorphous phases generated with different bond defect concentrations. Melt-quench generated amorphous phase is shown for comparison. Experimental data from [Laaziri *et al.* 1999]

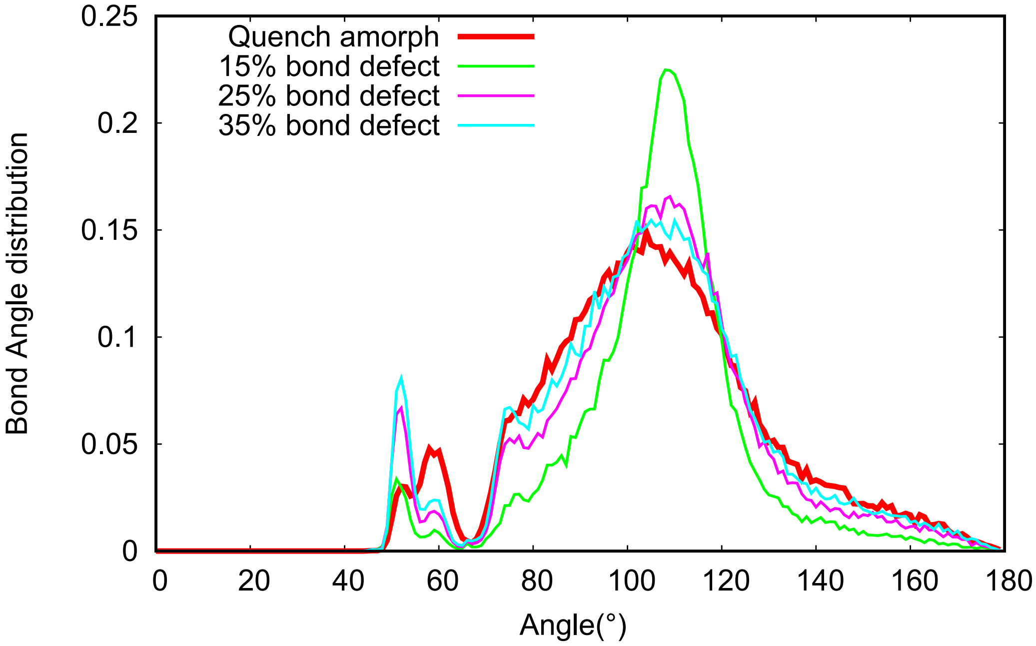

Figure II.8: Bond angle distributions of several amorphous phases generated with different bond defect concentrations. Melt-quench generated amorphous phase is shown for comparison

on the substrate orientation. In this case, the SPER process is along the x axis.

$$\vec{k_{100}} = \frac{2\pi}{a_0}(\vec{y} + \vec{z}) \tag{II.4}$$

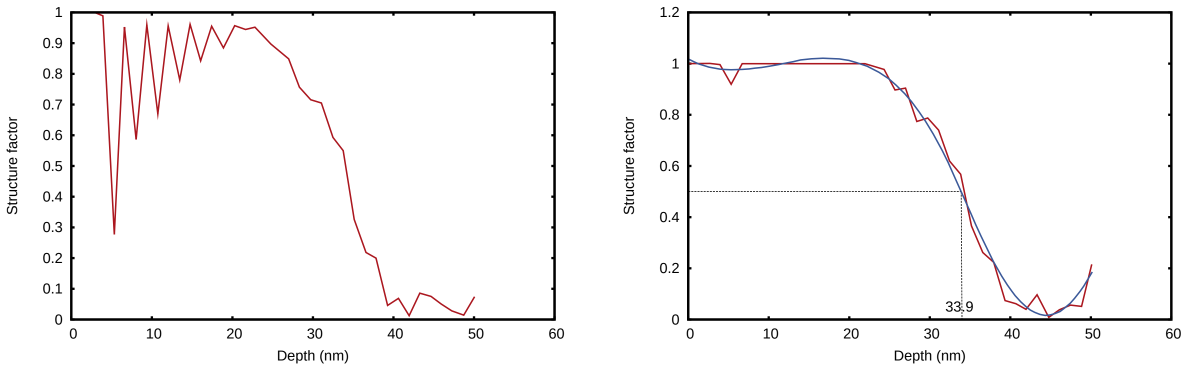

(a) Structure factor of a snapshot at high temperature. Due to thermal vibrations, the atoms are not in their lattice sites thus bringing the chiselling

(b) Structure factor of a snapshot brought to 0 K, the interpolated spline (in blue) and the extracted α-c interface. The chiselling disappears as all atoms are in their lattice sites

Figure II.9: Structure factor curves

$$\vec{k_{110}} = \frac{2\pi}{a_0}(\sqrt{2}\vec{y} + \vec{z}) \tag{II.5}$$

$$\vec{k_{111}} = \frac{2\pi}{a_0}(\sqrt{2}\vec{y} + \sqrt{6}\vec{z}) \tag{II.6}$$

The delta of the sum, dx, is chosen to be as little as possible.

- $dx = a_0/4$, for (100) orientation
- $dx = a_0\sqrt{2}$, for (110) orientation
- $dx = a_0\sqrt{2}$, for (111) orientation

This last method is used in the Molecular Dynamics calculations in this work due to the fact that it involves less computations for a similar result compared to the χ method. If the structure factor is applied on a snapshot taken from a Molecular Dynamics calculation, the result is not precise enough. As seen in Figure II.9a, the curve is chiselled in the crystalline phase. As the simulation cell is in a heat bath, the crystalline atoms are moving around their lattice points, thus giving this chiselling. To avoid this issue, all snapshots have to be brought to 0K where the atoms will be in their perfect lattice sites. After this manipulation, the structure factor is closer to the expectations. As it can be seen in Figure II.9b, the crystalline atoms yield a factor of `1` and amorphous ones of near `0`.

Finally, using `SciPy` [Jones *et al.* 01] methods, the structure factor is denoised, to avoid small peaks, and interpolated into a spline in order to provide a smooth curve. The result can be seen in Figure II.9b. From this smoothed curve, the α-c interface is extracted from the depth of when the curve goes below 0.5.

Furthermore, to evaluate the interface roughness, the extraction algorithm is not run on the whole system but on subdivisions of it, giving several α-c interface positions across the system, closely to [Mattoni & Colombo 2008] have done. This allows the extraction of an average α-c interface position as well as a standard deviation that will be interpreted as an interface roughness, as seen in Figure II.10.

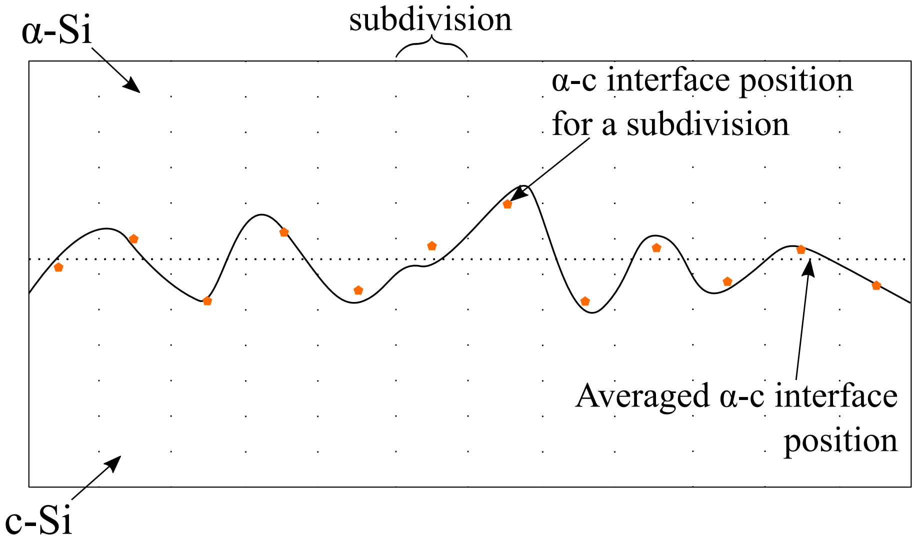

Figure II.10: Schematic of the interface roughness interpretation. The cell is divided into subdivisions, where the α-c interface position is extracted, giving access to the average and standard deviation values of the interface position

2.3 Simulation cell preparation

The simulation cells are always prepared with the same procedure. From a pure crystalline phase, as the one seen in Figure II.11a, 75% of the cell is amorphised following the bond defect generation seen in section 2.2. This manipulation yields Figure II.11b. It is worth noticing that the amorphous phase is less dense than the crystalline one, as the cell heights are different in Figure II.11. MD simulations were carried out with `LAMMPS` [Plimpton 1995][1] using a 1 fs timestep and periodic boundary conditions along the directions perpendicular to the α-c interface. The potential used is Tersoff interactomic potential within its third parametrization [Tersoff 1989], as stated previously in section 2.1. The bottom tenth of the simulation cell is frozen and serves as the seed for SPER. The cells do not expand in the parallel directions of the amorphous-crystalline interface due to the presence of this frozen seed. Next, the velocities of the non-frozen atoms are initialised with a Gaussian distribution around 300K. Finally, the simulation cell is placed into a heat bath of 500K for 0.5ns to further complete the initialisation. The thermostat used is a Nosé-Hoover thermostat [Nosé 1984, Hoover 1985] in the NVT canonical ensemble.

---

[1] `http://lammps.sandia.gov`

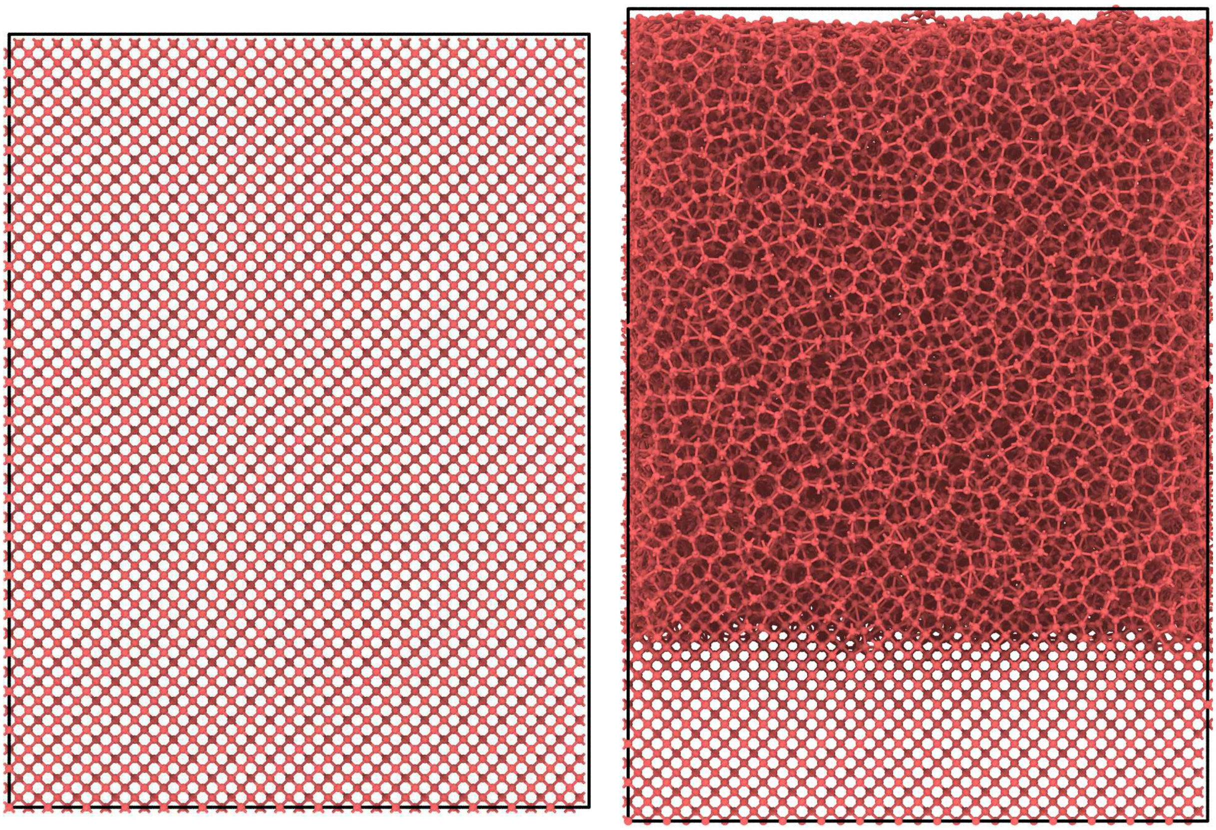

(a) <001> view of the crystalline cell before amorphisation

(b) <001> view of the crystalline cell after amorphisation

Figure II.11: Simulation cell preparation for MD calculations. Views generated by `OVITO` [Stukowski 2010]

From this preparation routine, only the temperature or the substrate orientation will change during this work.

2.4 <100> silicon SPER

Molecular Dynamics calculations have been performed on a cell with a size of $20a_0 \times 10a_0 \times 10a_0$, counting in total 36450 atoms. The α-c interface moves along a <100> direction. Several temperatures have been done, ranging from 1500K to 2000K with a 100K increment. To allow comparison, two experimental sets of data from Csepregi *et al.* [Csepregi *et al.* 1978] and Drosd & Washburn [Drosd & Washburn 1982] have been extrapolated to this temperature range. Furthermore, data issued from MMonCa simulations done with the same conditions as the MD simulations are also used for comparison. Amorphous-crystalline interfaces are extracted following the procedure detailed in section 2.2.1.

The extracted interface position versus time is plotted in Figure II.12. From this curve, a SPER rate is extracted via linear regression. To avoid discrepancies due to simulation initialisation, the regression is only done for times above 5 ns.

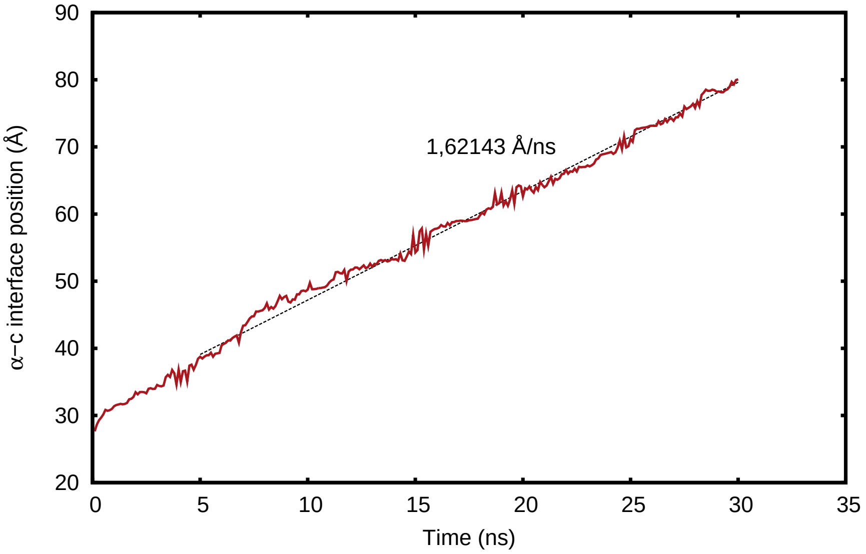

Figure II.12: Plot of the extracted α-c interface vs. time for MD calculations of <100> silicon at 1800K. The resulting extracted SPER rate is shown

The SPER rates of experimental and simulation data are plotted vs 1000/T in Figure II.13. The MD calculations agree very well with the KMC data extrapolations. However, they do not agree with either experimental data. The extrapolations are in fact causing these disagreements. These two experimental data agree within their experimental range of extraction (500-1000K). However a small deviation is this temperature gives huge differences at high temperatures. Hence the poor agreement with either MD or KMC data at high temperatures. The fitted prefactors and activation energies used for the extrapolations are listed in Table II.2.

However, the agreement is very good when we extrapolate the MD results to the low temperature range, as seen in Figure II.14. This is no surprise that MD simulations with Tersoff potential yields close agreement with experimental data, as it has been reported that this potential is best to simulate silicon SPER [Krzeminski *et al.* 2007].

Reference	Prefactor (/s)	E_a (eV)
[Csepregi *et al.* 1978]	3.52×10^{15}	2.35 ± 0.1
[Roth *et al.* 1990]	$8.22E\times10^{15}$	2.70 ± 0.02
[McCallum 1996]	1.81×10^{17}	2.7
KMC	3.65×10^{17}	2.70
MD	3.22×10^{17}	2.68

Table II.2: Simulation and experimental extractions of the prefactors and activation energies in pure silicon SPER

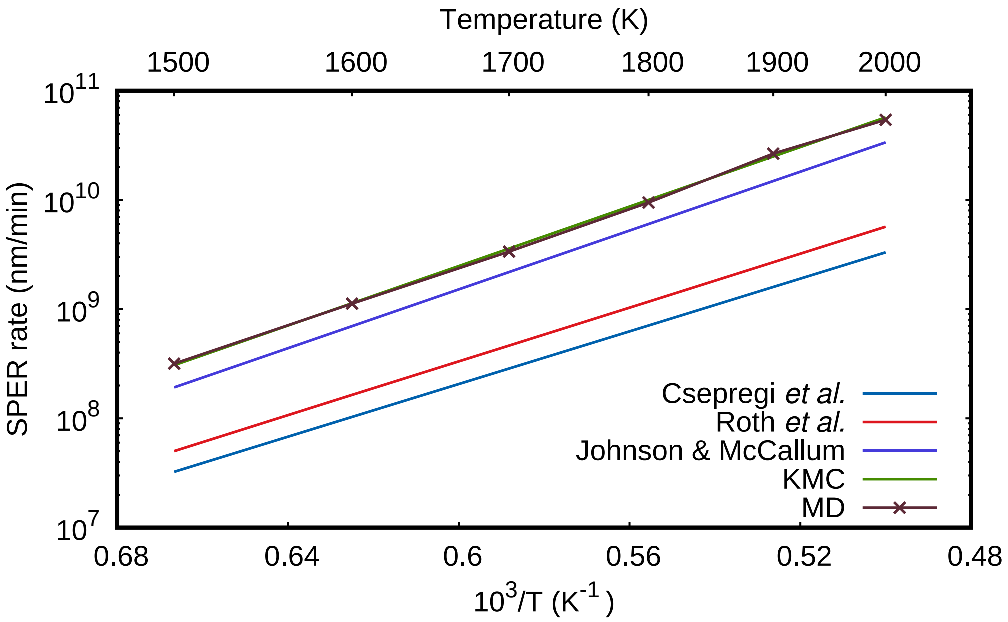

Figure II.13: Arrhenius plot of the SPER rates for the <100> silicon substrate orientation at MD temperatures. Extrapolations of experimental data from [Csepregi *et al.* 1978], [Roth *et al.* 1990] and [Johnson & McCallum 2007] are plotted, as well as KMC and MD simulations results

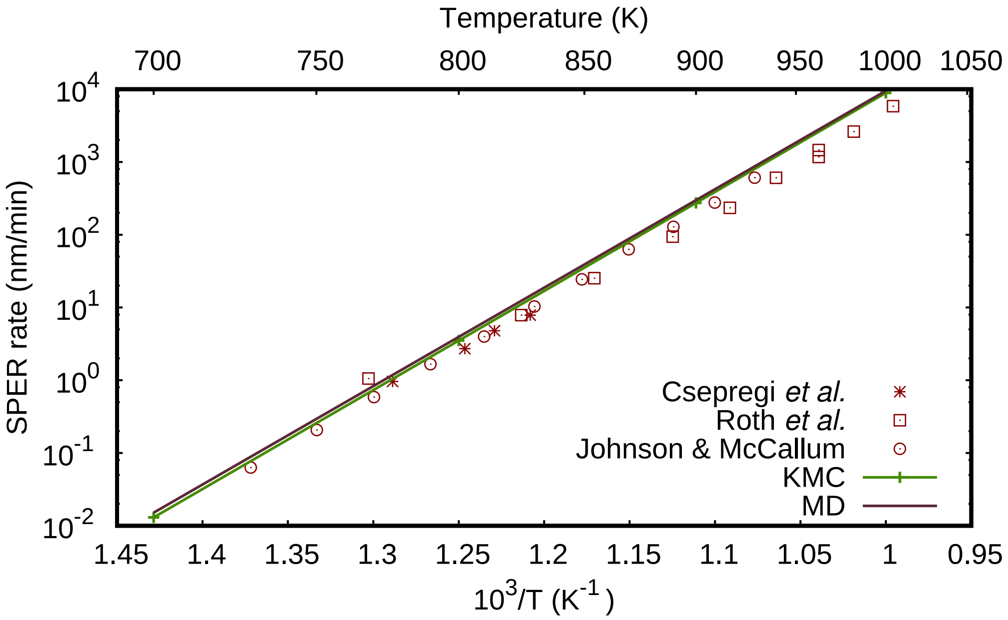

Figure II.14: Arrhenius plot of the SPER rates for the <100> silicon substrate orientation at process temperature. Extrapolations for MD simulations results are plotted. Experimental data from [Csepregi *et al.* 1978], [Roth *et al.* 1990] and [Johnson & McCallum 2007]

2.5 <111> silicon SPER

On the <111> substrate orientation, previous Molecular Dynamics simulations in the literature were less conclusive as they did not yield the expected SPER rate ratio with the <100> orientation. The experimentally found ratio between <111> and <100> SPER rates is around 1:20 [Csepregi *et al.* 1978]. Indeed, [Lampin & Krzeminski 2009, Krzeminski & Lampin 2011] and [Lai *et al.* 2011] simulations achived a ratio of 1:1.67 and 1:1.95, respectively. The simulation cell sizes used in the former publications are below 30000 atoms. However, Gärtner & Weber [Gärtner & Weber 2003] concluded that SPER rate is dependent of the simulation cell size. There has been no thorough investigations on the statement of Gärtner & Weber. In this section, investigations about the convergence of MD simulations regarding cell size and temperature will be done.

2.5.1 Cell size investigations

The dependence of the cell size on the SPER rate has been investigated on <111> SPER directions. Several cells have thus been created, following the same routine, cf. section 2.3. The cell sizes and number of atoms for each cell are gathered in Table II.3. All calculations have been performed at 1800K in order to have a relatively fast computation times.

Cell identifier	y(Å)	z(Å)	Growth area (Å^2)	Number of atoms
1	33.3	30.7	1.0×10^3	7280
2	66.5	57.6	3.8×10^3	27300
3	99.8	88.3	8.8×10^3	62790
4	133.1	115.2	1.5×10^4	109200
5	166.3	146.0	2.4×10^4	171900
6	199.6	172.9	3.4×10^4	245700
7	266.1	230.5	6.1×10^4	436000
8	399.2	345.7	1.4×10^5	989000

Table II.3: Cell sizes, growth areas and number of atoms.

From Figure II.15, it is undeniable that the extracted SPER rate is dependent on the surface growth. For small surfaces the SPER rate is heavily dependent. However, when the surface growth is higher than 3×10^4Å^2, further expansion does not bring a significant change to the SPER rate to counterbalance the computation load brought by the additional atoms.

The behaviour of the SPER rate versus the growth area could be explained by the onset of twin defects. As mentioned by Lampin *et al.* [Lampin & Krzeminski 2009], all <111> simulations resulted with the onset of twin defects. To follow on this remark, the twin defects appear close to the initial α-c interface, after the reconstruction of only one or two atomic layers. Figure II.16 points out this fact.

It can be hypothesised that the twin defect induces a short range dependence of the SPER rate. When the cell size is too small, this range overlaps and the SPER rate is very high. *A contrario*, when the cell size is large enough, twin defect ranges do not overlap and the overall SPER rate is diminished. Although the overall SPER rate is still higher

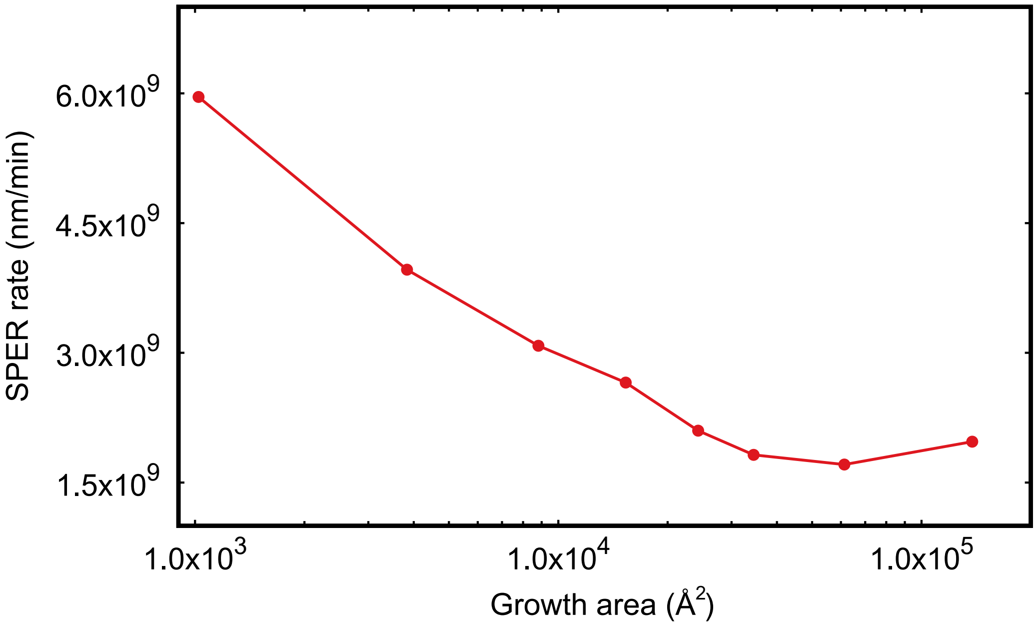

Figure II.15: Molecular Dynamics extracted SPER rate on <111> substrate orientation for different cell sizes

than expected, as the twin defects onset seems to be unavoidable. At this temperature, 1800K, the expected value for SPER rate is 3.828×10^8 nm/min. The minimum obtained here is 1.709×10^9 nm/min for 436000 atoms. Even if the SPER rate ratios has only been lowered from 1:1.95 — best obtained from literature data from [Lai *et al.* 2011] — to 1:5 between <100> and <111> direction by enlarging the surface growth area, the goal of finding the experimental ratio of 1:20 [Csepregi *et al.* 1978] is not yet attained.

2.5.2 Temperature investigations

As explained in the previous paragraph, the simulation cell has been optimised on the <111> direction. As said before, the onset of twin defects seems unavoidable for all cell sizes. However, this defect onset could be a high-energy event brought by the relatively high anneal temperature. In the following section, the temperature dependence of the SPER rate is investigated. The simulation cell has a size of 166.32Å×145.958Å×148.326Å, counting in total 172900 atoms for a surface growth of $2.43 \times 10^4 \text{Å}^2$. The simulated temperatures are {1500; 1550; 1600; 1700; 1800; 1900; 2000}K. Figure II.17 shows the extracted α-c interface over time for the simulated temperatures.

From these curves, the linear interpolation extraction of SPER rates is not straightforward. First, it seems that there is a transitory state for all simulations. The length of this transitory state varies with the applied temperature. For example, with a low temperature anneal, the timescale is about 10 to 20 ns, as it can be seen for the 1500K curve. The hotter the simulation, the smaller this transitory state is.

Second, along the y-axis, the issue deepens. For low temperatures, the interface position

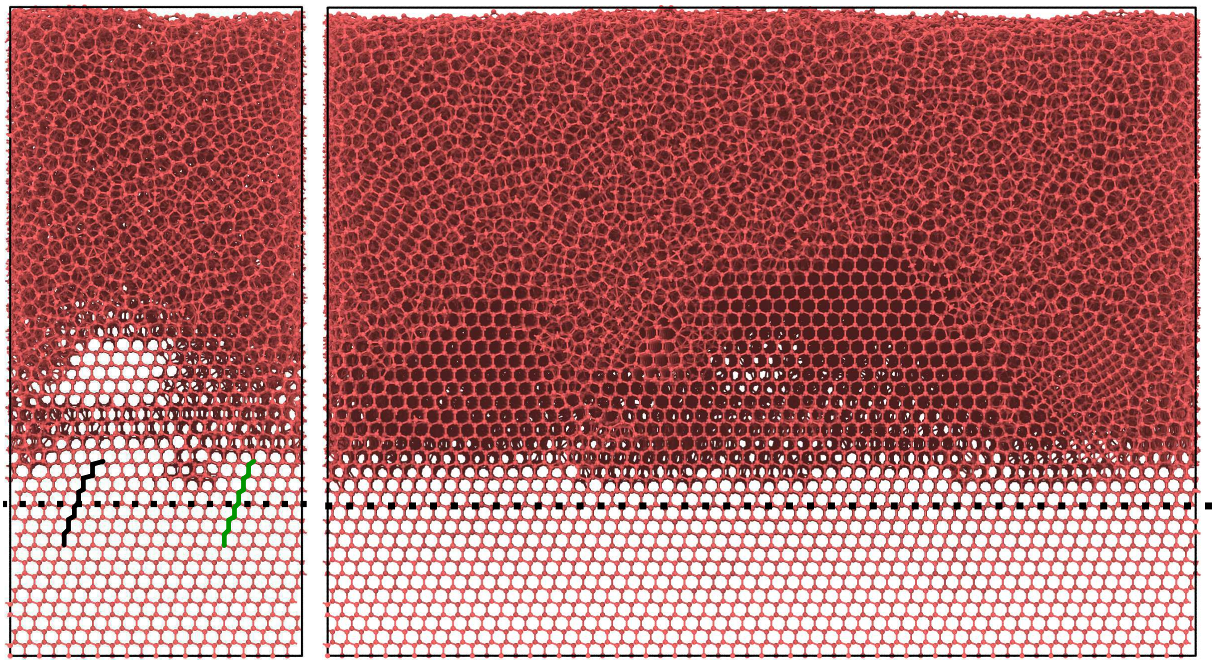

(a) Cell 2. The green line is a correct arrangement of atoms, whereas the black one has a twin defect

(b) Cell 6. On larger cells, twin defects appear only at certain locations in the cell, thus blocking the <110> channel

Figure II.16: <110> view of cell during <111> SPER. Twin defects are invariably situated after a few layers from the initial α-c interface (dotted line) for any growth area. Views generated by `OVITO`[Stukowski 2010]

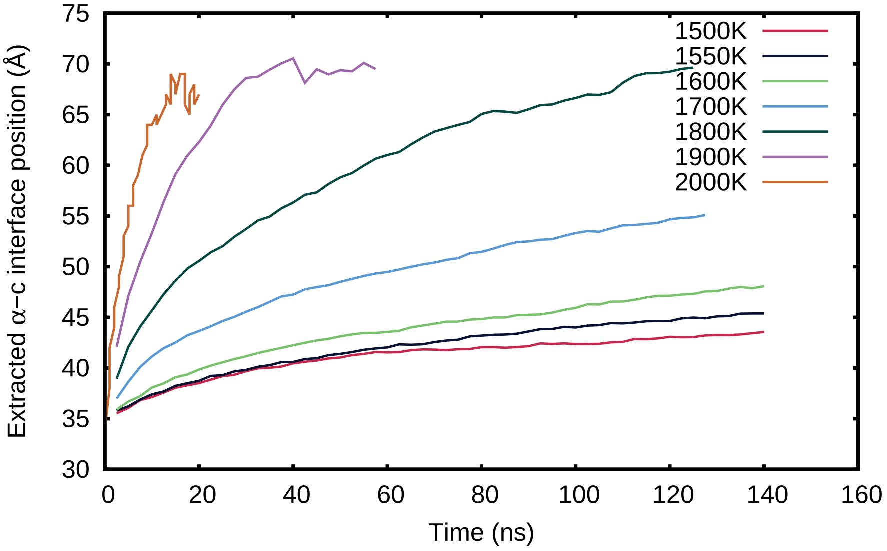

Figure II.17: MD simulations of the α-c interface evolution over time for several temperatures

range is not enough to be confident to extract a proper SPER rate. As an example, for the curve representing the 1500K anneal, if we choose to interpolate from 50 ns — to avoid the transitory state — to the end of the simulation, the interface has only moved 2 Å.

Third, for high temperatures, the apparition of random nucleation growth and crystallites in the amorphous phase as well as a rough interface distorts the extracted α-c interface position and the curve seems not to stabilise, as the curve for 1800K shows.

To circumvent these issues and extract the most correct SPER rate possible the linear interpolation is done far from the transitory state with an interface roughness less than 1nm. Table II.4 explicitely presents all data used in conjunction with Figure II.17 to extract SPER rates.

Temp. (K)	Time (ns)	Depth (Å)	SPER rate (nm/min)	Correlation coefficient
1500	70 - 140	41.82 - 43.55	1.514×10^{8}	0.974
1550	70 - 140	42.55 - 45.58	2.368×10^{8}	0.983
1600	70 - 140	44.37 - 48.06	3.356×10^{8}	0.990
1700	65 - 127	49.98 - 55.10	4.883×10^{8}	0.986
1800	20 - 82.5	50.55 - 65.35	1.409×10^{9}	0.993
1900	7.5 - 20	50.47 - 62.29	5.807×10^{9}	0.980
2000	2.5 - 9.5	46.50 - 64.22	1.452×10^{10}	0.983

Table II.4: The interpolation ranges and extracted SPER rates

To insure that the simulations are consistent against the growth area and cell size, another set of simulations have been performed with another cell. The second simulation cell has a size of 166.32Å × 134.435Å × 99.8937Å, counting in total 106750 atoms for a surface growth of 2.23×10^{4}Å^{2}. The SPER rates of these two cell sizes are plotted against expected data in Figure II.18.

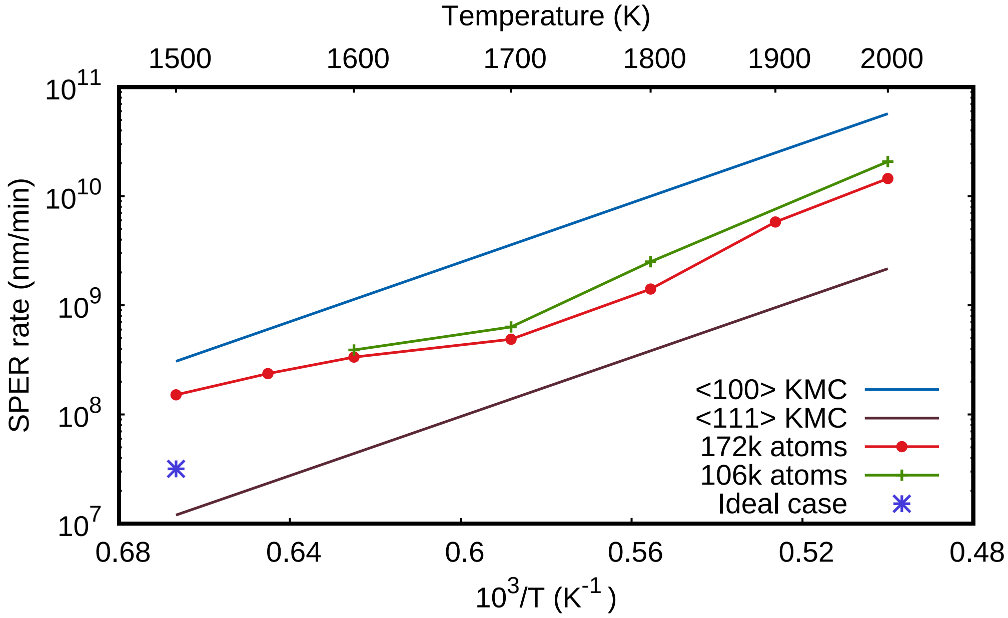

Figure II.18: Molecular Dynamics SPER rate on <111> substrate orientation for different temperatures

From Figure II.18, it seems that the temperature range between 1700-1800 yields the closest SPER rate to the expected rates. This is due to the issues discussed before. For low temperatures, not enough silicon layers have been recrystallised to yield a correct SPER rate. For high temperatures, the interface roughness is too prominent to also yield a correct SPER rate. *In fine*, the middle of the temperature range, as away as possible from these issues, generates the closest SPER rate to the expected rate. The SPER rate ratio between <100> and <111> extracted at 1700K is 1:7.35, less than a third of the experimental ratio.

2.5.3 Ideal case

The previous sections concluded that the SPER rate for <111> orientation is dependent on both the cell size and the temperature. One of the ideal simulation would be with a large cell and a very low temperature to limit the local effect of twin defect and the random nucleation growth in the amorphous phase. Such a simulation requires a huge amount of computing time. Therefore, this computation has only been done once. In this case, the simulation cell has a size of 133.056Å × 115.23Å × 244.661Å, counting in total 181200 atoms for a surface growth of 1.53×10^4Å^2. The anneal temperature is 1500K and the anneal time is close to 900 ns.

Figure II.19 presents the result of this simulation and highlights the transitory state aforementioned. If the SPER rate is extracted during the transitory state, the results are

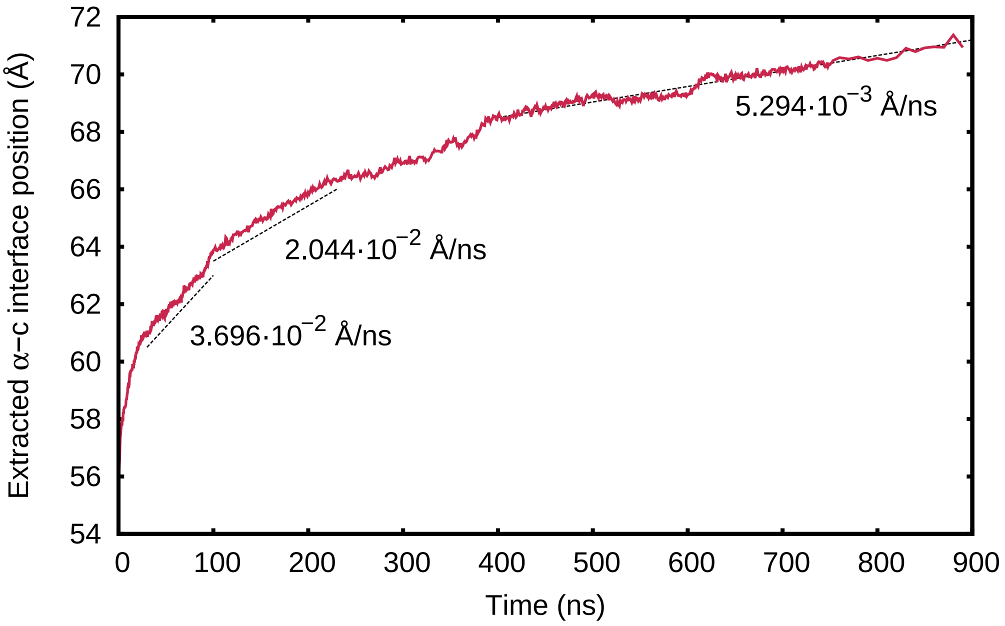

Figure II.19: α-c interface evolution over time for a 1500K anneal

not satisfactory. However, if extracted far from this state, the SPER rate is close to the expected rate. The ratio obtained with this simulation between <100> and <111> is 1:9.66, close to half the expected ratio. This value is plotted against previous results in Figure II.18. It could be hypothesised that with an even longer simulation time, the ratio would be closer to the expected one. Indeed, in Figure II.19, the curve does not seem stable yet. Moreover, the growth area is two times smaller than the recommended.

The case presented here is not yet the best possible, however this shows that the Tersoff potential in its third parametrisation can gives close agreement with the experimental data. However, this closeness appears to have a very high computational cost.

2.6 <110> silicon SPER

In the last part of the investigation of SPER substrate orientation dependence, the <110> substrate orientation is under scope. In this case, the simulation cell has a size of $25a_0 \times 35\sqrt{2}/2a_0 \times 40\sqrt{2}/2a_0$, counting in total 140000 atoms for a surface growth of $2.14{\times}10^4\text{Å}^2$. The simulation cell is prepared as before, seen in section 2.3. Figure II.20 presents a picture of the cell during an anneal. It is clear that {111} facets emerge during the SPER. This onset of {111} facets has been seen before on smaller cells [Lampin & Krzeminski 2009]. The fact that the SPER reaction seems to confirm the model of Csepregi *et al.* [Csepregi *et al.* 1978], where they stated that the growth is occurring via on {111} surfaces.

Figure II.21 shows the extracted SPER rate during these investigations. The optimisations performed during the last sections give good results against the expected SPER

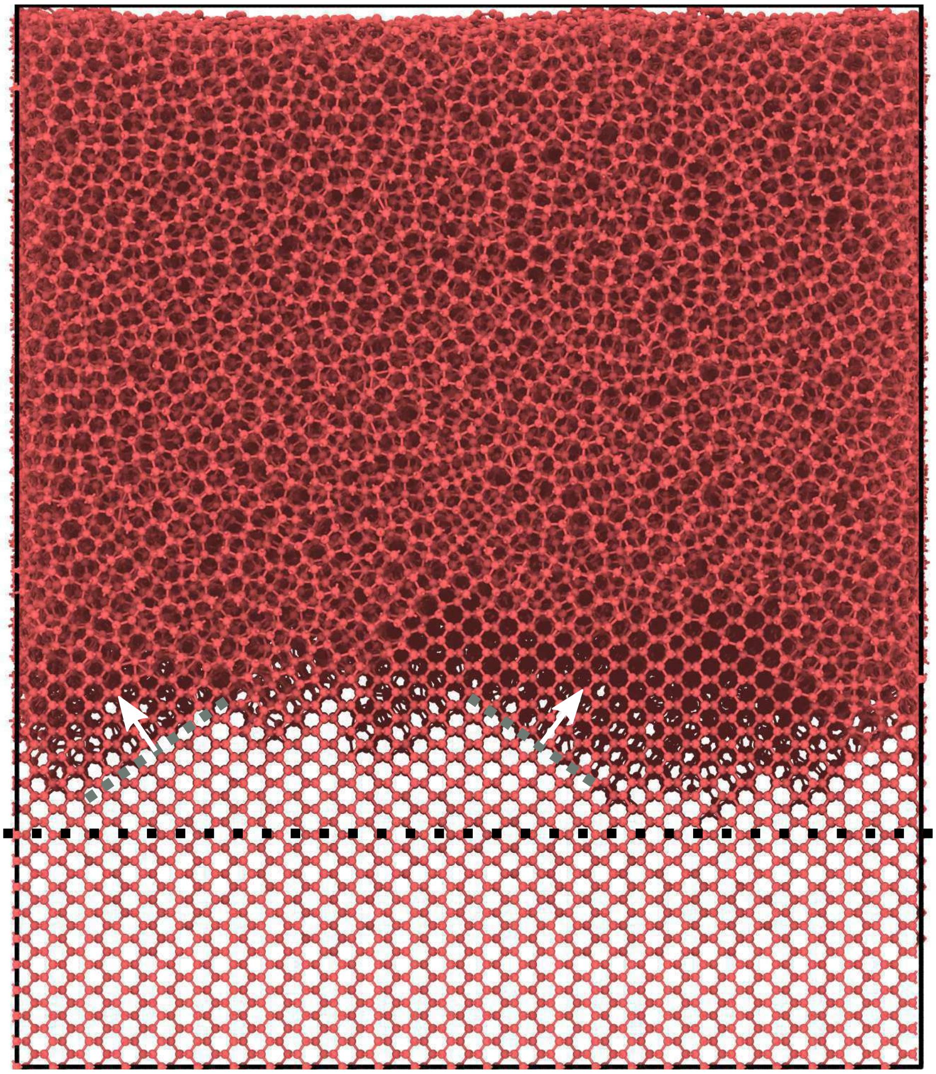

Figure II.20: State of the simulation cell after 141ns anneal at 1600K during a <110> substrate orientation MD calculation. The original α-c interface is plotted in dots. {111} interfaces are easily identifiable

rate. The ratio between <110> and <100> is 1:2.50, which is very close to 1:3 seen in experiments [Csepregi *et al.* 1978]. This ratio has to be compared with the best obtained in literature 1:1.76 at 1900K by [Lai *et al.* 2011]. KMC and MD simulated rates are here also compared to experimental data. In this case too, the extrapolation of experimental data to these temperatures cannot be straightforward compared to simulated data. Greater cell sizes, colder temperatures and longer simulation times could also be the key to match experimental and MD data.

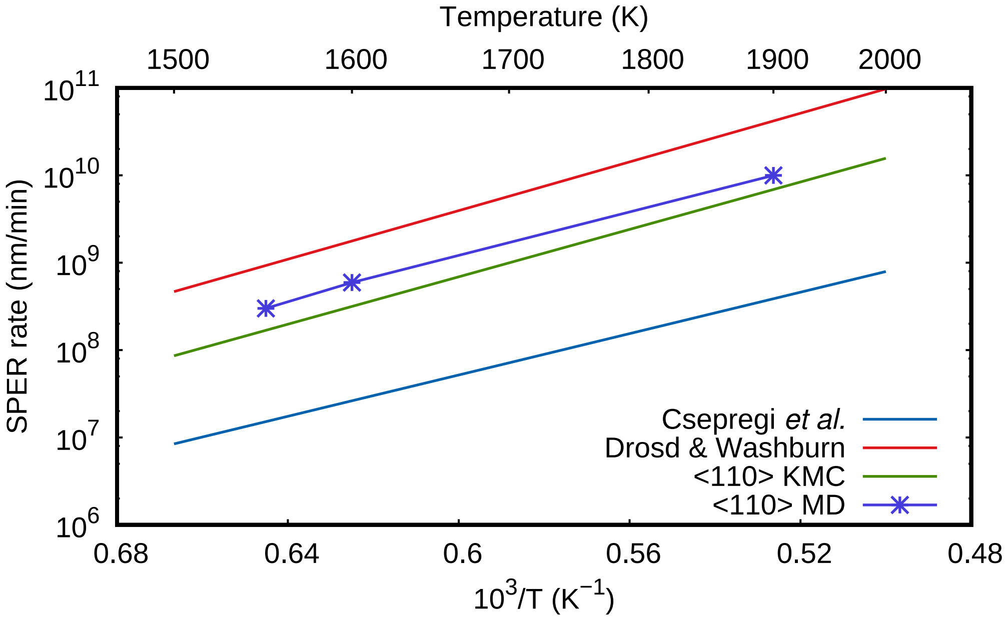

Figure II.21: Molecular Dynamics SPER rate on <110> substrate orientation for different temperatures. Experimental data from [Csepregi *et al.* 1978, Drosd & Washburn 1982]

3 Summary

In this chapter, the SPER model that has been implemented prior to this thesis has been presented. It is based on the phenomenological model of [Drosd & Washburn 1982]. Its gist is that the SPER reaction can be resumed into the reformation of crystalline six-fold rings, as seen in Figure II.1. The model implemented in MMonCa is a Lattice Kinetic Monte Carlo model, where all the atoms are positioned on the crystalline lattice and do not move during the reaction. The model focuses on the amorphous-crystalline interface where the SPER reaction is happening. The strong substrate dependency is handled by computing the local configuration around an atom. The prefactor of the Arrhenius law modelling the SPER rate, and the LKMC event probability, is determined by the local configuration. Furthermore, twin defects, as seen in Figure II.3, can appear on {111} local configuration, with a probability of 10%. This model, resumed in the Equation II.2, models with a close agreement the strong dependence of the SPER rate on the substrate orientation, for pure silicon and germanium, as it can be seen in Figure II.5.

In the second part, the silicon SPER has been investigated with the help of Molecular Dynamics simulations with the help of the Tersoff potential [Tersoff 1989]. The principal aim of this investigation is to find why, until now, the Tersoff potential could not bring the substrate orientation dependence seen in the experimental data. First, the amorphous phase is created by an accumulation of bond defects, seen in Figure II.6, which are closely related to the amorphous phases created by ion implantation. The position of the amorphous-crystalline interface is extracted via the structure factor, which yields a 1 when the phase is crystalline and near 0 when amorphous, as it can be seen in Figure II.9. The results cannot be directly compared to experimental values, as the extrapolations are made too far from the experimental temperature ranges. The results are therefore compared with the rates from the LKMC model. The results of the investigations are the following:

- Along <100> directions, the MD simulations yield very close SPER rates to the expected ones.
- Along <111> directions, the SPER rate is dependent of the growth area Figure II.15. This is possibly due to the onset of twin defects. The twin defect could have a short range effect that increases the SPER rate. With a small growth area, the twin defect ranges overlap on cause of anomalous increased SPER rate.
- Along <111> directions, simulating the SPER with low temperature seems to yield better results as the random nucleation growth of crystallites in the amorphous phase is lessened. However, this imposes a very high computational cost. The recrystallised layer needs also to be large enough to avoid poor SPER rate interpolation, as seen at low temperatures in Figure II.18.
- A single ideal simulation, with a low temperature anneal and a very long simulated time, has yielded a ratio of nearly 1:10 between <111> and <100> rates. This fact emphasise that the expected ratio of 1:20 is attainable with a large ceel and low temperature anneal and thus a consequent computational cost.
- Along <110> directions, the MD simulations give a ratio between <110> and <100> of 1:2.50, which is very close to 1:3 seen in experiments.

In conclusion, MD simulations with the Tersoff potential can give close results to the expected SPER rates and their ratios only if the simulations are done on a large enough cell with a sufficiently low temperature anneal. Further development should find the correct combination of cell size and anneal temperature that yields the expected ratio, especially on {111} orientation. Now that the ratio between the different SPER rates is accessible by the mean of MD simulations, further investigations on silicon-germanium alloys and germanium SPER with MD simulations could be attempted.

4 French summary — Résumé

Le modèle KMC de la SPER implémenté dans MMonCa est décrit dans ce chapitre. Dans MMonCa, tous les atomes sont déjà au préalable dans leur position cristalline, et la différence entre des atomes amorphes et cristallins n'est que logicielle. En effet, les atomes ne bougent pas lors de la recristallisation, seul leur état (amorphe ou cristallin) change. Le modèle est donc un KMC sur réseau ou LKMC en anglais, pour *Lattice Kinetic Monte Carlo*. Le modèle est basé sur le modèle phénoménologique de [Drosd & Washburn 1982], selon lequel un atome est considéré comme cristallin de nouveau lorsqu'il possède deux liaisons atomiques correctes, en terme de longueur et de distorsion, avec des atomes cristallins. Le fait de ne s'intéresser qu'à l'interface est légitime dans le sens où la SPER est très vraisemblablement un phénomène localisé uniquement à l'interface [Aziz 1992]. De ce modèle émergent naturellement trois configurations microscopiques possibles à l'interface, comme on peut le voir à la figure Figure II.1. Les atomes grisés sont considérés comme amorphes, les autres comme cristallins.
Microscopiquement, l'interface peut donc être résumée à une accumulation de trois configurations : $\{100\}$, $\{110\}$ ou $\{111\}$. Comme l'on sait que l'énergie d'activation de la SPER ne change pas avec l'orientation (Figure I.18), seul le facteur pré-exponentiel change en fonction de l'orientation microscopique. Pour le modèle, le facteur pré-exponentiel change donc en fonction de la configuration locale. Le modèle se base sur le nombre de premier et deuxième voisins de l'atome considéré afin de déduire la configuration locale de l'atome. De plus, la configuration $\{100\}$ est divisée en deux configurations distinctes, une fortement coordonnée et une faiblement coordonnée afin de garder une interface la moins rugueuse possible [Martin-Bragado 2012, Martin-Bragado & Sklénard 2012]. Les facteurs pré-exponentiels, calibrés sur des valeurs de la littérature, sont visibles dans la Table II.1. Enfin, lors de la recristallisation d'une configuration $\{111\}$, un défaut peut apparaitre. Ce défaut, nommé défaut d'empilement, est visible à la Figure II.3. Il est essentiel de tenir compte de ce défaut afin de s'approcher des valeurs expérimentales [Martin-Bragado 2012]. La probabilité qu'un site $\{111\}$ recristallise en formant un défaut d'empilement est fixé à 10%. D'un point de vue approche KMC, la probabilité qu'un atome se recristallise peut être écrite :

$$r = K(n) \cdot \exp\left(\frac{-E_a}{k_B T}\right) \tag{II.7}$$

où $K(n)$ est un facteur pré-exponentiel dépendant de la configuration locale autour dudit atome. Le modèle, confronté aux données expérimentales, est visible à la Figure II.5. Le modèle KMC est très proche des données expérimentales, particulièrement pour le silicium.

Dans un deuxième temps, la SPER du silicium est étudiée à travers des simulations de

Dynamique Moléculaire. Cette méthode de simulation atomistique calcule les équations de Newton sur chaque atome afin d'en extraire les forces et accélérations s'appliquant sur chacun d'entre eux. Cette méthode utilise des potentiels empiriques. De nombreux potentiels existent et peuvent être utilisés pour la simulation de la SPER du silicium. Une investigation rigoureuse de [Krzeminski *et al.* 2007] permit de révéler que le potentiel de Tersoff dans sa troisième itération [Tersoff 1989] est le potentiel le plus adapté pour étudier la SPER. Contrairement à l'approche KMC, ici les atomes bougent lors de la simulation.

La première étape est donc de créer une phase amorphe correcte. Le plus souvent, dans la littérature, la phase amorphe est créée par une trempe. En fondant puis en ramenant rapidement le système à 0K, il est ainsi possible de créer une phase amorphe. Celle-ci peut également être créée via l'accumulation d'un défaut généré par l'implantation ionique [Motooka 1994, Motooka *et al.* 1995, Stock *et al.* 2000, Marqués *et al.* 2003]. Il s'agit du défaut de liaison, *bond defect* en anglais, visible à la Figure II.6b. Ce défaut contient deux hexagones et deux heptagones et provient de l'annihilation échouée d'une paire lacune-interstitielle lors d'une implantation ionique. Pour créer ce défaut, deux atomes, A et B dans la Figure II.6b, doivent être déplacés selon des vecteurs spécifiques. Dans les simulations Dynamique Moléculaire, la phase amorphe est créée par accumulation de ce défaut de liaison : 25% des atomes dans la phase que l'on veut amorphiser sont déplacés, créant ainsi une phase amorphe.

Ensuite, pour étudier correctement la SPER, il convient de pouvoir extraire la position de l'interface amorphe-cristal. Pour cela, le facteur de structure est calculé. Celui-ci calcule le produit scalaire entre le vecteur de position d'un atome et celui du réseau réciproque. Plus le produit est proche de 1, plus l'atome se trouve dans sa position cristalline. Supposant que la recristallisation se produit selon un axe x, le facteur de structure est calculé suivant l'Equation II.3 avec les vecteurs du réseau réciproques donnés aux équations II.4, II.5 et II.6. Il est à noter que le système doit être ramené à 0K, car, dans le cas contraire les vibrations du réseau, du fait de la température, donnent un calcul du facteur de structure erroné, comme il est possible de voir à la Figure II.9a. Finalement, pour extraire la position de l'interface, le facteur de structure est calculé sur un système ramené à 0K puis interpolé par une cerce — *spline* — et enfin l'interface est extraite lorsque la *spline* atteint 0.5. Ces étapes sont visibles à la Figure II.9b.

La SPER du silicium est investiguée sur les trois orientations principales. Sur la direction <100>, le système simulé compte 36450 atomes. La vitesse de SPER est extraite par une régression linéaire de la position de l'interface en fonction du temps, comme il est possible de voir à la Figure II.12. Les températures simulées sont de 1500K à 2000K par pas de 100K. Les vitesses en fonction de 1000/T sont visibles à la Figure II.13. Il est impossible de comparer directement les résultats avec des résultats expérimentaux extrapolés, du fait de la plage de température trop élevée. Les résultats sont donc comparés avec des résultats issus de simulations KMC faits aux mêmes températures. Il est évident que la simulation Dynamique Moléculaire est en très bon accord avec la simulation KMC. Cette conclusion est logique dans le sens où le potentiel utilisé, Tersoff, est connu pour donner de bons résultats sur la SPER.

Sur la direction <111> les simulations en Dynamique Moléculaire n'ont jamais donné les résultats escomptés. En effet, il est attendu un ratio 1 :20 entre les vitesses de recristallisation du <111> et <100>. Or, jusqu'à présent, le meilleur ratio obtenu est de 1 :1,67 [Lampin & Krzeminski 2009]. La SPER sur cette direction est investiguée selon plusieurs paramètres.
Premièrement, selon l'aire du plan de recristallisation. En effet, la dépendance de la vitesse selon l'aire de recristallisation n'a jamais été investiguée. Plusieurs systèmes comprenant jusqu'à 989 000 atomes ont été utilisés. La température de recuit est de 1800K. La Figure II.15 montre indéniablement que la vitesse de SPER est en fonction de l'aire de la recristallisation du système étudié. Cette dépendance pourrait être expliquée par les défauts d'empilement, qui apparaissent invariablement sur tous les systèmes étudiés, voir Figure II.16. Ces défauts pourraient créer un champ local qui accélèrerait localement la SPER. Or, si ce champ se recouvre sur lui-même, dans le cas où le système est trop petit, la vitesse extraite s'en trouverait fortement augmentée. C'est ce que l'on peut voir sur les petites aires. Dans un second temps, sur les systèmes à grandes aires de recristallisation, même si les champs des différents défauts d'empilement ne se recouvrent plus, la vitesse de SPER est quand même globalement accélérée et ne diminue plus avec une autre augmentation de l'aire de recristallisation. En choisissant un système avec une aire conséquente, $6 \times 10^4 Å^2$, un ratio de 1 :5 entre les vitesses sur <111> et <100> est obtenu.

Deuxièmement, selon la température de recuit. En effet, l'apparition de défauts d'empilement est peut être due à la température de recuit très élevée des simulations. Des simulations avec des températures allant de 1500K à 2000K ont été faites, sur deux systèmes différents. Les positions des interfaces en fonction du temps sont données à la Figure II.17 pour un des deux systèmes. Les vitesses extraites en fonction de 1000/T sont représentées à la Figure II.18. D'après la figure, il semblerait que le milieu de gamme de température serait le plus adapté, car il donne les résultats les plus proches de ceux attendus. Or, le problème vient en fait des valeurs extrêmes. À faible température, l'interface ne s'est pas suffisamment déplacée (moins de 2 Åsur la Figure II.17), afin de pouvoir extraire correctement une vitesse. À forte température, des défauts d'empilement ainsi que d'autres phases cristallines apparaissent dans l'amorphe, rendant l'extraction difficile.

Finalement, en utilisant les conclusions des deux précédents paragraphes, selon un cas “idéal”. Cet “idéal” possède une large base de recristallisation, 1.53×10^4Å^2, la température de recuit faible pour éviter au plus les défauts d’empilement, 1500K, et un temps de simulation le plus grand possible, avoisinnant les 900ns. La Figure II.19 montre l’évolution de l’interface amorphe-cristal en fonction du temps. Elle permet de mettre en exergue l’existence d’un état transitoire au début de la simulation. Cet état transitoire permet aussi d’expliquer le fait qu’à faible température, les vitesses étaient trop élevées sur la Figure II.18. En extrayant le plus loin possible de cet état transitoire, entre 500 et 900 ns, la simulation donne de bons résultats, comme on peut le voir à la Figure II.18 où le point unique représente la vitesse extraite par cette simulation. Ce cas pourrait être amélioré en recristallisant encore plus mais aurait un temps de calcul extrêmement long, de plusieurs μs. Le ratio entre les vitesses sur les orientations <111> et <100> est de 1 :9.66, montrant définitivement que le potentiel Tersoff permet de bien reproduire la SPER du silicium, à condition d’utiliser les bonnes conditions de simulation.

CHAPTER III

Doped silicon SPER: The case of boron

THIS chapter will present the behaviour and the impacts of the boron inclusion in the layer during the SPER reaction. Boron has different behaviours in both crystalline and amorphous phases and also heavily modifies the SPER rate. This SPER rate modification has already been mentioned in section 2.3.3. However, the SPER rate enhancement possesses an upper limit that the current model is unable to explain. The chemical effects at the α-c interface during SPER have been until now dismissed. If the bond breaking model [Spaepen 1978, Spaepen & Turnbull 1979] is indeed considered as the main mechanism for SPER, the availability of sites where the bond can be broken should be taken into account. The following chapter will present a KMC model that takes into account chemical effects into the SPER rate calculation in order to explain this limit.

Contents

1 Experimental background

In crystalline silicon, boron diffuses via interstitials and, at high concentration, creates boron interstitials clusters (BICs) that hinder the activation. Further anneal leads to more boron deactivation as seen in several studies [Pawlak *et al.* 2004, Jin *et al.* 2002, Cristiano *et al.* 2004]. Strict control of the thermal budget is therefore important. In amorphous silicon, boron diffuses via dangling bonds [Mirabella *et al.* 2008] and also tends to form clusters [De Salvador *et al.* 2006]. These clusters are stable, immobile in both phases and do not disintegrate at the amorphous-crystalline interface during SPER [Mattoni & Colombo 2004]. Finally, boron also dramatically increases the SPER rate [Csepregi *et al.* 1977a], up to a certain point. Indeed, at high concentration, this increase is severely reduced, as it can be seen in several studies [Olson & Roth 1988, Park & Wilkins 2011, Gouyé *et al.* 2010].

These behaviours have been modelled separately in the literature. Firstly, the diffusion and clustering in amorphous silicon by [Martin-Bragado & Zographos 2011] and boron clustering in crystalline silicon by [Aboy *et al.* 2011]. Secondly, the impact of boron on SPER has been modelled through electrostatic and further strain effect corrections. The electrostatic correction is a phenomenological correction [Williams & Elliman 1983, Lu *et al.* 1991, Johnson & McCallum 2007], called Generalized Fermi Level Shifting (GFLS). It interprets the SPER rate increase due to the increase of the SPER-responsible defect concentration. However the saturation of SPER rate at high boron concentration cannot be predicted by the GFLS, even with the inclusion of the strain impact brought by the impurities [D'Angelo *et al.* 2008, Johnson *et al.* 2012].

2 Atomistic model

The atomistic model shown here is the union of point and extended defects reaction models and a refined SPER model. The point and extended defects reaction models are enclosed into the Object Kinetic Monte Carlo (OKMC) model, whereas the new SPER model is still implemented into the LKMC model.

2.1 Point and extended defect reactions: OKMC model

2.1.1 OKMC model presentation

The point and extended defect reactions are simulated in MMonCa with the OKMC model [Martin-Bragado *et al.* 2013]. This model is an off-lattice KMC model, meaning that the defects are not assigned to specific site positions inside the simulation cell, contrary to the lattice KMC model. The model can be resumed to the following: a defect can either migrate, react with another defect to form a bigger defect or break and form two smaller defects. There are two types of defects, point and extended defects. Points defects are for example silicon interstitials, vacancies or boron atoms. Extended defects can be {311} defects or clusters.

A point defect can migrate in three dimensions around its original position. The jump distance is set to 0.384 nm (the second neighbour distance in silicon). However, if another defect is closer than the jump distance, the two defects can interact. An extended defect can also migrate, catch a close defect and break up by emitting a point defect. These reactions are drawn in the schematic in Figure III.1.

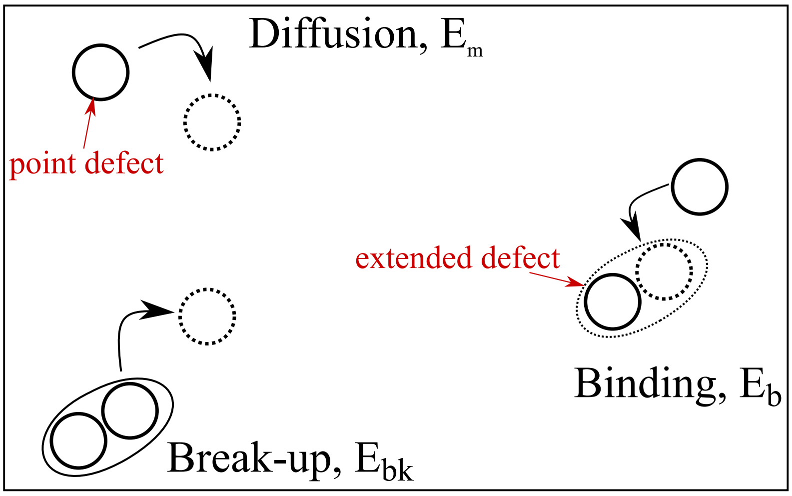

Figure III.1: Schematic of the possible reactions in the OKMC model: diffusion of a defect, binding of several defects and break-up of an extended defect

All of these possible reactions must have energy barriers to follow the KMC approach. There are two possibilities to obtain these energy barriers. From experimental data, migration energy can be directly derived. Binding and break-up energies can be indirectly derived with calibrating models. Another way is to use first principle methods where migration, binding and break-up energies can be directly computed. The binding energy — the energy barrier for two defects to overcome to be bound together (E_b) — is the difference between the constituent formation energies (E_f) from their isolated and bound forms. The formation energy of a defect can be described as the energy difference between a perfect crystal and a crystal hosting one defect. For a mobile boron-interstitial (BI), the binding energy can be calculated by:

$$E_b(BI) = E_f(B) + E_f(I) - E_f(BI) \tag{III.1}$$

For extended defects, the binding energy has the same definition. For example, to form a BIC with two interstitials and one boron (B_2I) from a mobile BI and a mobile I, the binding energy can be calculated by:

$$E_b(B_2I) = E_f(BI) + E_f(I) - E_f(B_2I) \tag{III.2}$$

Finally, the break-up energy — the energy barrier to release a defect from an extended defect (E_{bk}) — is the difference between the constituent formation energies from their isolated and bound forms plus the migration energy of the released defect. For a moving boron-interstitial (BI), the break-up energy is:

$$E_{bk}(BI) = E_f(B) + E_f(I) + E_{mig}(I) - E_f(BI) \tag{III.3}$$

These energy barriers are implemented in the KMC model to model point and extended defect reactions. The transition rate is computed as follows:

$$r = r_0 \cdot \exp\left(\frac{-E^*}{k_B T}\right), \tag{III.4}$$

where r_0 is a calibrated value to mimic literature data, and E^* the corresponding energy barrier for the reaction.

2.1.2 Reactions in the amorphous phase

In amorphous silicon, boron is known to diffuse [Duffy *et al.* 2004, Venezia *et al.* 2005] via dangling bonds [Mirabella *et al.* 2008]. Boron clustering is also reported in amorphous silicon [De Salvador *et al.* 2006]. The boron behaviour in amorphous silicon has been previously modelled with a KMC approach [Martin-Bragado & Zographos 2011], which was based on the ideas proposed by [Mirabella *et al.* 2008]. The model assumes two defects in amorphous silicon, which are dangling bonds (DB) and its counterpart floating bonds (FB). The former can interact with boron to enable diffusion via the B(DB) defect. The reaction of dangling bonds with floating bonds is an annihilation of both. The possible reactions in the amorphous phase are listed in Table III.1 and their associated parameters in Table III.2 and Table III.3. Prefactors have been calibrated in order that simulations reflect experimental data from [Mirabella *et al.* 2008]. The calibration cell had 170 nm$\times 130a_0 \times 130a_0$ as dimensions, where a_0 is the silicon lattice constant. The experimental as-implanted boron concentration were applied along the x-axis. The cell was entirely amorphised with an initial concentration of 9×10^{20} at/cm^3 floating bonds and dangling bonds. Furthermore, the initial dangling bond concentration is increased by 50% of the implanted boron concentration. Finally, the two thermal budgets from [Mirabella *et al.* 2008] were applied: 500°C-8h and 650°C-250s. Results of these calibrations can be seen in Figure III.2. Above a certain boron concentration, the boron is imprisoned in BICs and do not diffuse. Below this threshold, boron diffuses via interaction with dangling bonds.

$$\begin{array}{rcl}
\mathrm{DB} + \mathrm{FB} & \longrightarrow & \varnothing \\
\mathrm{B} + \mathrm{DB} & \longleftrightarrow & \mathrm{B(DB)} \\
\mathrm{B(DB)} + \mathrm{B} & \longleftrightarrow & \mathrm{B_2(DB)} \\
\mathrm{B(DB)} + \mathrm{B(DB)} & \longleftrightarrow & \mathrm{B_2(DB)_2} \\
\mathrm{B_2(DB)} + \mathrm{B(DB)} & \longleftrightarrow & \mathrm{B_3(DB)_2} \\
\mathrm{B_2(DB)_2} + \mathrm{B(DB)} & \longleftrightarrow & \mathrm{B_3(DB)_3}
\end{array}$$

Table III.1: Defect reactions in amorphous silicon

Defect	Mechanism	Prefactor	Energy (eV)	Ref.
DB	Diffusion	0.6 (cm^2/s)	2.6	[Mirabella*et al.* 2008]
FB	Diffusion	0.6 (cm^2/s)	2.6	[Martin – Bragado&Zographos 2011]
B(DB)	Binding	1.75 (/s)	0.2	[Martin – Bragado&Zographos 2011]
B(DB)	Diffusion	72 (cm^2/s)	2.8	[Martin – Bragado&Zographos 2011]

Table III.2: Point defect parameters for reaction in amorphous silicon

Defect	Energy (eV)
$B_2(DB)$	-0.4
$B_2(DB)_2$	-0.4
$B_3(DB)_2$	-1.9
$B_3(DB)_3$	-2.7

Table III.3: Potential energies for Boron-Dangling bonds complexes in amorphous silicon. Values from [Martin-Bragado & Zographos 2011]

2.1.3 Reactions in the crystalline phase

In crystalline silicon, boron has been extensively studied and is known to diffuse via interstitials and form Boron Interstitials Complexes (BICs). The point defect reactions and their prefactors and energies used in this work are listed in Table III.4 and Table III.5. The atomistic study of BICs was initiated by [Pelaz *et al.* 1999] and later completed by [Zechner *et al.* 2008] and [Aboy *et al.* 2011]. For clarity purposes, the exhaustive BICs reactions and potential energies are listed in Appendix A. Only the point defect reactions are listed in Table III.4.

Finally, due to changes in the Fermi level caused by boron doping, the point defects can change their charge in crystalline silicon. The energy levels in the band gap are listed in Table III.6. More details about point defects diffusion under Fermi level shift can be found in Martin-Bragado *et al.* [Martin-Bragado *et al.* 2005].

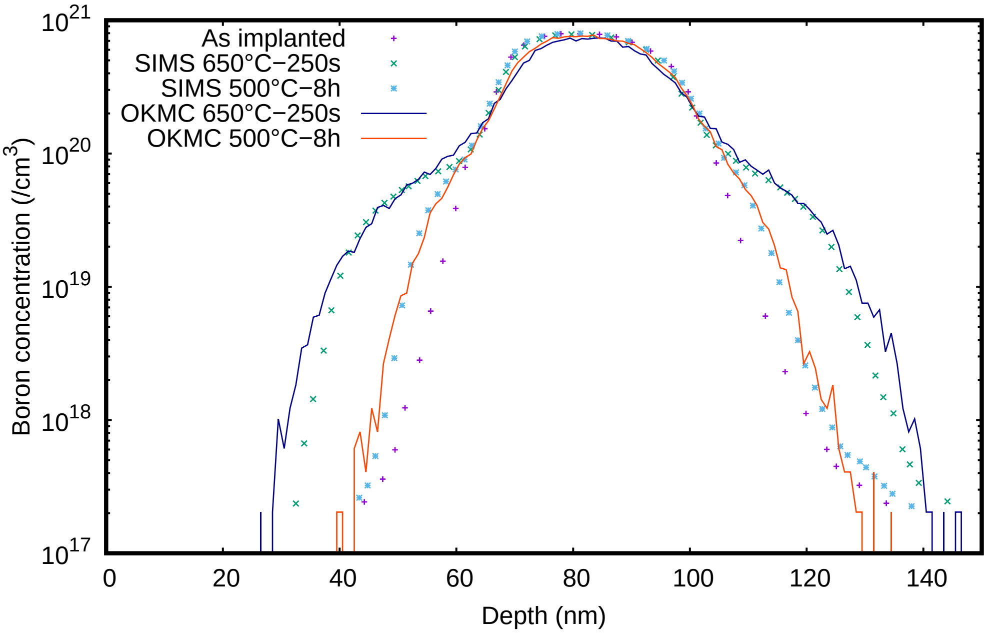

Figure III.2: Comparison between experimental data [Mirabella *et al.* 2008] and OKMC simulations for boron diffusion and clustering in amorphous silicon

$$\begin{array}{rcl} \mathrm{B} + \mathrm{I} & \longleftrightarrow & \mathrm{BI} \\ \mathrm{B} + \mathrm{BI} & \longleftrightarrow & \mathrm{BIC} \\ \mathrm{BI} + \mathrm{BI} & \longleftrightarrow & \mathrm{BIC} \end{array}$$

Table III.4: Point defect reactions in crystalline silicon

Defect	Mechanism	Prefactor	Energy (eV)
BI	Binding	3771.2 (/s)	0.50
BI	Diffusion	1.0×10^{-3} (cm^2/s)	0.2
BI$^-$	Diffusion	1.0×10^{-3} (cm^2/s)	0.36
BI$^+$	Diffusion	1.0×10^{-3} (cm^2/s)	1.1
I	Diffusion	5.0×10^{-3} (cm^2/s)	1.0
I$^-$	Diffusion	5.0×10^{-3} (cm^2/s)	1.0
I$^+$	Diffusion	5.0×10^{-3} (cm^2/s)	1.0

Table III.5: Parameters used for binding and diffusion of point defects in crystalline silicon. Values from [Martin-Bragado *et al.* 2005]

Defect	Level	e_t(T=0K) (eV)
I$^-$	$e(0,-)$	1.0
I$^+$	$e(+,0)$	0.4
BI$^-$	$e(0,-)$	0.8
BI$^+$	$e(+,0)$	1.04

Table III.6: Defect energy level at T=0K for charge state transition in crystalline silicon. The valence band maximum is used as the reference. Values from [Martin-Bragado *et al.* 2005]

2.1.4 The amorphous/crystalline interface

The OKMC model also handles the phase transition from amorphous to crystalline. The BICs do not disintegrate during the phase transition [Mattoni & Colombo 2004]. Furthermore, the interface is permeable to boron atoms, and subsequently activate them in the crystalline phase. However, the interface acts as a sink for dangling bonds and floating bonds. Finally, the B(DB) mobile defect will be desorbed at the α-c interface, leaving an activated boron atom in the crystalline phase. Reactions are listed in Table III.7. These reactions are neither considered as a LKMC event nor an OKMC one due to the fact that they have no energy barriers.

$$\begin{array}{rcl} \mathrm{DB} & \longrightarrow & \varnothing \\ \mathrm{FB} & \longrightarrow & \varnothing \\ \mathrm{B(DB)} & \longrightarrow & \mathrm{B} \\ \mathrm{B}_x\mathrm{(DB)}_y & \longrightarrow & \mathrm{B}_x\mathrm{I}_y \end{array}$$

Table III.7: Defect reactions at the α-c interface during SPER

2.2 Phase transition model: LKMC model refinement

2.2.1 Potential computation

As shown previously, within the Transition State Theory approximation and without any external stress or impurities, the silicon SPER rate for an atom lying at the α-c interface can be written as follow:

$$r = K(n) \cdot \exp\left(\frac{-E_a}{k_B T}\right) \tag{III.5}$$

Where $K(n)$ is a local configuration dependency that brings the orientation dependence, and E_a an activation energy. However, in presence of doping impurities, the SPER rate exponentially increases. This phenomenon has been previously studied and modelled [Williams & Elliman 1983, Lu *et al.* 1991, Johnson & McCallum 2007, Johnson *et al.* 2012], although never implemented into an atomistic simulator. The Generalized Fermi Level Shifting (GFLS) is a phenomenological correction postulating that the SPER is mediated by a defect, with positively and negatively charged counterparts, and thus its concentration. The defect concentration is modified with the concentration of doping impurities. In the case of acceptor impurities, the SPER rate increase, or GFLS factor, can be written as [Williams & Elliman 1983, Lu *et al.* 1991, Johnson & McCallum 2007, Johnson *et al.* 2012]:

$$\nu_{GFLS}(\mathrm{V}) = \frac{r_d}{r_i} = \frac{1 + g^+ \exp\Big(\beta(e(+,0) - e_F)\Big)}{1 + g^+ \exp\Big(\beta(e(+,0) - e_{Fi})\Big)} \tag{III.6}$$

With $\beta \equiv 1/k_BT$, g^+ is the defect degeneracy and $e(+,0)$ is the defect energy level. e_F and e_{Fi} are the Fermi level under doped and intrinsic conditions, respectively. The parameters used in this study are $g^+ = 3/2$ and $e(+,0) = 0.31$ eV. The maximum of the valence band is considered as the reference energetic level, giving:

$$\begin{cases} e_F - e_c = \mathrm{V} - e_g \\ e_v - e_F = -\mathrm{V} \end{cases}$$

Where e_v is the maximum of the valence band, e_c is the minimum of the conduction band and e_g the band-gap on silicon. It has to be noted that the band-gap temperature dependence is taken into account with the band-gap narrowing model of Varshni with the parameters from Alex *et al.* [Alex *et al.* 1996].

To obtain V, the non-linear Thomas-Fermi approximation for carrier densities is solved self-consistently with Poisson's equation:

$$\epsilon \Delta \mathrm{V}(x,y,z) = -4\pi \left[\rho(x,y,z) + \sum_i Q_i[N_i^Q] \right] \tag{III.7}$$

Where V is the electrostatic potential, Δ is the Laplacian, ϵ is the dielectric constant, $[N_i^Q]$ is the density of activated dopants i of charge Q. Only the dopants that are in substitutional position are considered activated. Finally, ρ is the carrier density given by:

$$\rho = N_C \mathcal{F}_{1/2}\Big[\beta(e_F - e_c)\Big] - N_V \mathcal{F}_{1/2}\Big[\beta(e_v - e_F)\Big] \tag{III.8}$$

Where N_C and N_V are the effective density of states in conduction and valence band, and $\mathcal{F}_{1/2}$ is the Fermi integral of order one half. Complete details of the Poisson solver can be seen in Sklénard's work [Sklénard 2014]. With the GLFS correction, Equation III.5 can be rewritten as:

$$r = \nu_{GFLS} \cdot K(n) \cdot \exp\left(\frac{-E_a}{k_BT}\right) \tag{III.9}$$

Theoretically, this potential computation should be solved each time a six-fold ring is recrystallised, in order to have the correct potential at the α-c interface. However, the computation is expensive as a three-dimensional Laplacian must be solved. This time-consuming routine could be economized by calling the solver less often. A convergence study has thus been done to find an update criterion that minimizes the computation work but still gives coherent results for the GFLS factor. The study compares the potential at the interface versus the potential in the bulk, in the absence of BIC formation, thus focusing only on SPER rate increase. A ratio of 1 means that the interface sees the same potential as the bulk thus giving the correct GFLS factor. The result of the study can be seen in Figure III.3. The Poisson solver is therefore called each 10^3 LKMC reaction.

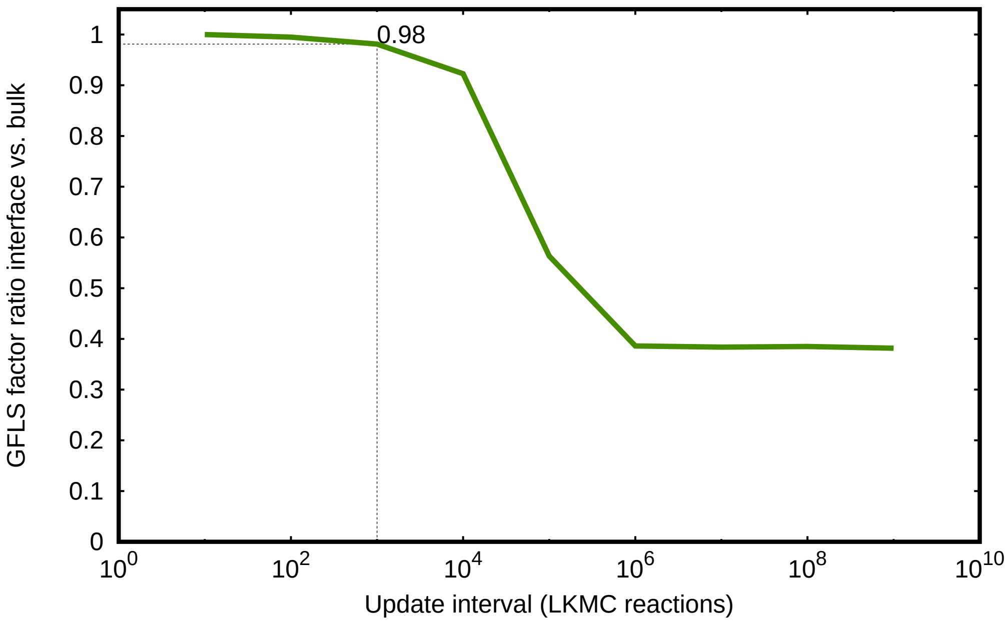

Figure III.3: Convergence study on the update criterion to yield correct GFLS factor with a minimum computation impact for the cell size used in these investigations

2.2.2 Cluster influence

The BICs lying at the α-c interface should also have an impact on the SPER rate. As mentioned by [Mattoni & Colombo 2004], the BICs do not seem to disintegrate during the phase transition. Furthermore, the KMC model presented here supposes that bonds have to be broken in order to allow the recrystallisation mechanism. However, it can be hypothesised that the BICs will not participate to the recrystallisation mechanism as it would be energetically detrimental to the BIC to bend and break bonds inside itself. For the model, this means that the lattice atoms around the BICs are deactivated for SPER, as the bonds around them cannot be broken. The model thus computes the distance between a lattice atom that might be recrystallised and the BICs it its vicinity. If the distance is lower than 0.384 nm, the SPER rate equals 0. It is worth noting that this distance is also the capture distance for point defect reaction in the OKMC model. A boolean $\mathcal{B}$ is hence added to take into account that some recrystallisation sites are deactivated due to the presence of a BIC. As some atoms at the interface are hence deactivated for SPER, the interface naturally creates <111> planes. The interface behaviour is schematised in Figure III.4. The Equation III.5 can now be written as:

$$r = \mathcal{B} \cdot \nu_{GFLS}(\mathrm{V}) \cdot K(n) \cdot \exp\left(\frac{-E_a}{k_B T}\right) \tag{III.10}$$

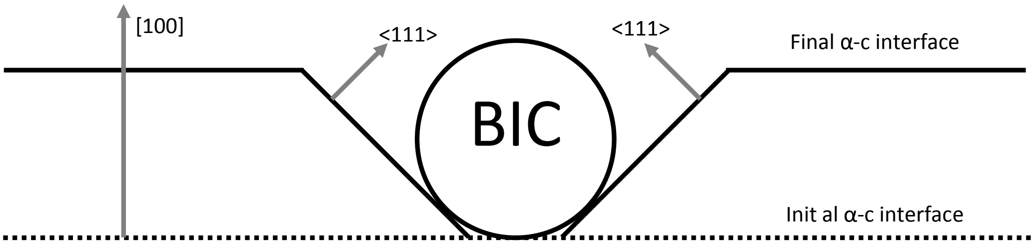

Figure III.4: Sketch of the amorphous-crystalline interface during SPER. As the BIC does not take place in SPER reaction, slow recrystallising <111> fronts appear around it.

3 Results and observations

For the simulations presented below, the initial conditions are the following: the amorphous phase has an initial concentration of 9×10^{20} at/cm^3 floating bonds and dangling bonds. Furthermore, the initial dangling bond concentration is increased by 50% of the implanted boron concentration, closely following the γ parameter of [Mirabella *et al.* 2008], where they used an increase of 100% regarding the boron concentration. This parameter represent the surplus of dangling bonds due to the implantation of boron. The crystalline silicon is considered perfect and the defects caused by ion implantation are not taken into account.

3.1 Carrier concentration after anneal

Firstly, to assess that boron is correctly activated and the potential thus correctly computed during the anneal, the model is tested against the experimental data from [Solmi *et al.* 1990]. The simulation cell is a 220 nm$\times 50a_0\times 50a_0$ where a_0 is the lattice constant of silicon. The amorphous phase lies from the free-surface to 200 nm.

As it can be seen in Figure III.5, the model yields a correct maximum of activated boron, between 3 to 5×10^{20} at/cm^3, which is in agreement with other experimental data [Jin *et al.* 2002, Cristiano *et al.* 2004] that shows a maximum at 3×10^{20} at/cm^3. The clustering phenomenon is clearly limiting the maximum activated boron, especially for the high dose implant around the boron profile peak (∼70nm) where it can be seen that the overall hole density decreases from 5×10^{20} to 3×10^{20}. The potential computation is correct in view of these results.

3.2 Model behaviour vs. a δ-profile

Secondly, the model is applied on a simulation (100) silicon cell of 60nm$\times 50a_0\times 50a_0$. The amorphous phase is set between 55 nm below the surface and the surface. The doped

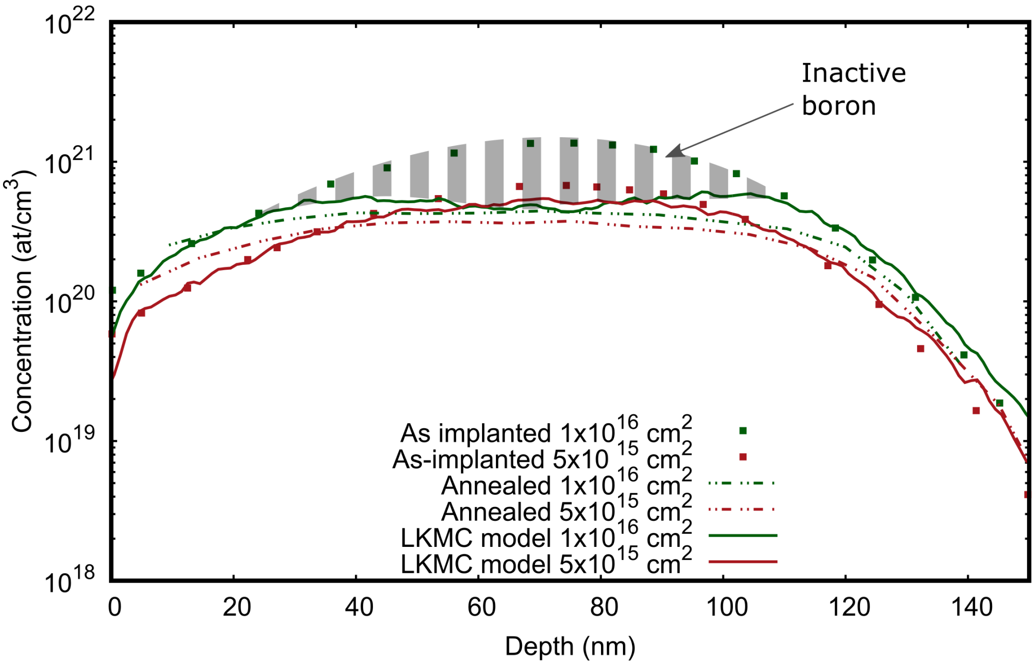

Figure III.5: 20 keV as implanted boron concentration profiles for two different doses and hole densities after 900°C anneal during 10 s for two different implant doses. Experimental data from [Solmi *et al.* 1990]. The hashed part represents the boron inactivated by the clustering reaction

region consists of a δ-layer doped between 50 and 20 nm from the surface. The SPER rate is extracted from 30 to 20 nm from the surface in order to have a correct Fermi level shift during the whole extraction. The model is tested against several data [Gouyé *et al.* 2010, Johnson *et al.* 2012, Park *et al.* 1988]. To emphasize the incremental improvements of the model, two more curves are plotted. First, only the GFLS correction is considered without reactions in the amorphous or crystalline silicon, meaning that all the inserted boron atoms are activated. This is the curve named `GFLS_0`. Secondly, reactions are activated thus boron can be deactivated via clustering. However, clusters do not hinder the SPER rate, meaning that Equation III.9 is taken and not Equation III.10. The curve resulting of this simulation is named `GFLS_1`. Finally, the curve named `LKMC model` possesses all the improvements: point and extended defects reactions in both amorphous and crystalline phases that brings the apparition of BICs as well as the deactivation of lattice sites for SPER due to presence of BICs at the α-c interface, i.e. Equation III.10 is taken for rates calculation.

The results of the simulations can be seen in Figure III.6. As expected, the three experimental curves show a saturation – or beginning of it – around 5×10^{20} at./cm^3. The LKMC model is in close agreement with experimental data, especially in concentrations that are technologically relevant, *i.e.* above 5×10^{20} at./cm^3. The incremental improvements of the original GFLS correction are easily identified. First, as the BICs are taken into account, the activated boron concentration lowers, giving thus a lower SPER rate

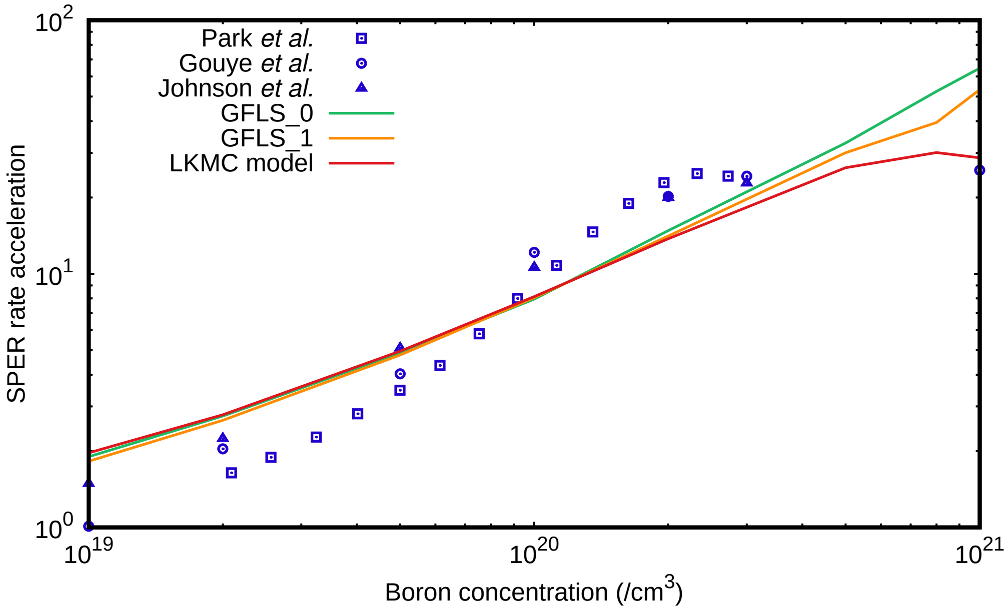

Figure III.6: SPER rate increases for a 500°C anneal. Experimental data from [Park *et al.* 1988, Gouyé *et al.* 2010, Johnson *et al.* 2012]. GFLS_0 and GFLS_1 show the incremental refinement of the LKMC model

increase. However, this correction is not enough to bring the saturation. The fact that the BICs themselves are hindering the SPER rate by bringing slower recrystallisation planes must be included. Indeed, a BIC could be compared to a sphere at the α-c interface that cannot be recrystallised. To continue the recrystallisation, the crystalline phase must be rebuilt around this sphere, hence bringing <111> planes to be recrystallised, as schematized in Figure III.4. As <111> planes are known to be the slowest planes to recrystallise [Csepregi *et al.* 1978], this phenomenon greatly hinders the overall SPER rate, thus giving the SPER rate saturation seen at high boron concentrations.

3.3 Model behaviour vs. a gaussian profile

The gradient of concentration is also known to have an impact on the SPER rate. Several studies have shown that the SPER rate mimics the increase and decrease of the boron concentration [Olson & Roth 1988, Park *et al.* 1988, Jeon *et al.* 1989]. Simulations were carried out to test the model behaviour against an implanted boron profile. Figure III.7 shows the results of the simulation. The KMC model can indeed mimic the experimentally seen behaviour as the simulated SPER rate increases and decreases as the boron concentration does. However it seems that the model overestimates the SPER rate acceleration during the boron concentration increase, between 225 and 100 nm depth. This is certainly due to the fact that in simulation, the damages done by ion implantation during amorphisation are not taken into account. The α-c interface is thus too perfect whereas experimentally it is rough with defects that decrease the SPER rate. This is confirmed by the fact that as soon as defects begin to appear during the simulation, *i.e.* BICs related defect around $1{\times}10^{20}/\mathrm{cm}^3$ boron concentration at 100 nm, the experimental and simulated SPER rates are close.

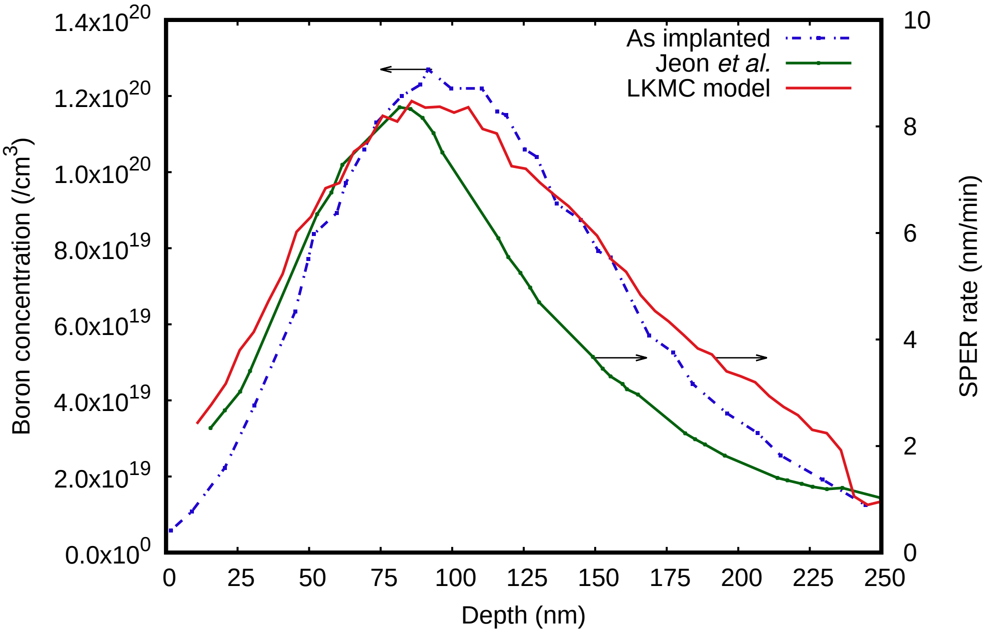

Figure III.7: SPER rate versus a boron profile at T=500°C. Data from [Jeon *et al.* 1989]. The KMC model yields good agreement with experimental data for the SPER rate versus the boron concentration.

3.4 Interface roughness

Furthermore, as <111> planes appear during a high boron concentration SPER, it can be hypothesised that the interface will be rougher than during intrinsic silicon SPER. This hypothesis is confirmed by the work of [Barvosa-Carter *et al.* 2004], where the α-c interface becomes rough when entering the boron-implanted region and the maximum of the roughness appears around the maximum of the boron profile. Moreover, the interface roughens when the boron concentration is increasing and flattens when the boron concentration is decreasing. This behaviour has been modelled by [Elliman & Wong 1996]. In their model, the interface roughness increase is due to the gradient of atoms that enhance the SPER rate.

This α-c interface roughening can now be atomistically explained within the framework presented in this work. As the interface is sweeping through a region with increased boron concentration, the possibility to encounter a BIC, which creates <111> planes and thus roughens the interface, is also increasing. On the other hand, when the boron concentration is decreasing, less and less BICs are encountered at the interface and the interface thus flattens again. The fluctuation of the interface roughness can be assessed by viewing the Figure III.8 and Figure III.9. Views `a)` and `c)` are taken away from the boron profile whereas view `b)` is taken near the maximum of the implanted profile. The inset shows at what point of the concentration profile the snapshots are taken.

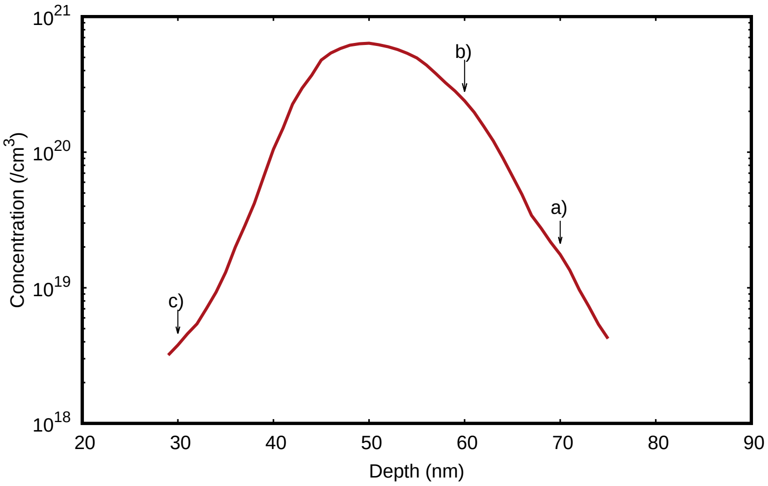

Figure III.8: Boron concentration profile used to investigate interface roughness in presence of boron and the positions of the α-c interface where snapshots were taken

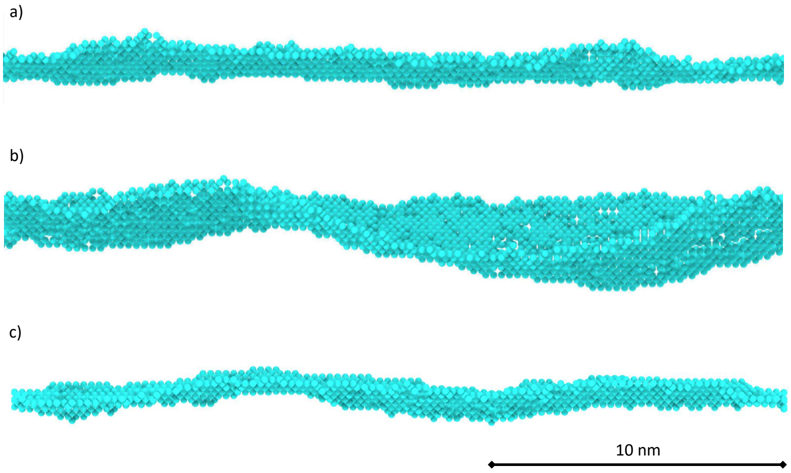

Figure III.9: 2D cross-section views of atoms at the α-c interface at three different boron concentration levels. Views generated with Ovito [Stukowski 2010]

3.5 Further observations

Finally, one might wonder if the model presented here could be extended to other impurities. Several impurities, both doping and non-doping, can be redistributed during the sweep of the α-c interface. An example can be seen in Figure III.10, where it is clear that the phosphorus is pushed back to the free surface during the SPER. The model keystone is its focus on the availability of recrystallisation sites at the interface during SPER. In another way, the SPER rate saturation is brought by the chemical effects at the α-c interface. As arsenic [Demenev *et al.* 2012] and phosphorus [Ruffell *et al.* 2005, Simoen *et al.* 2009] are known to aggregate and be redistributed during SPER, very high concentration of atoms can therefore be found at the α-c interface and could probably also hinder SPER rate. An extended KMC model should handle both a segregation model to correctly handle these impurities and a moving interface, making the model much more complex. A KMC segregation model indeed requires all possible reactions to be written, with associated energy barriers.

Another example emphasising the importance of the chemical effects is the case of carbon during silicon SPER. Carbon presents no clustering nor redistribution during SPER [Strane *et al.* 1996] and its inclusion will create a tensile in-plane strain, which is not known to hinder SPER rate [Sklénard *et al.* 2013]. The only remaining factor that could modify the SPER rate is the Si-C bond breaking value. Adapting the bond breaking value has been recently successful to explain the activation energy behaviour in silicon-germanium alloys [Payet *et al.* 2016b]. Thus, in addition to the electrostatic and strain effects, the chemical effects, site availability and bond breaking value at the α-c interface, must also be taken into account in order to fully explain SPER rate with presence of impurities.

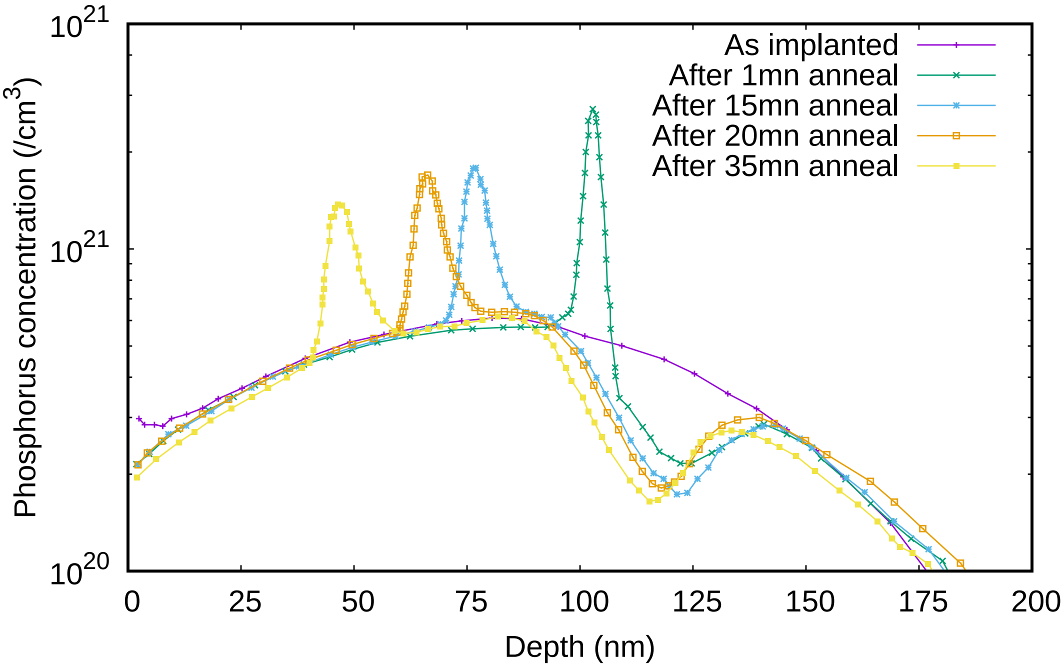

Figure III.10: Example of dopant redistribution during SPER. P profiles at different times are shown during a RTA at 350°C. Original α-c interface at 220 nm. The free surface at 0 nm. Data from [Simoen *et al.* 2009]

4 Summary

This chapter has investigated the SPER rate in presence of boron. Boron, as well as other doping impurities, enhances the SPER rate as seen in Figure I.21. A phenomenological model, called GFLS, has been introduced to take into account this enhancement. This model is based on the assumption that the SPER rate is proportional to the concentration of the defect responsible for the SPER. This concentration is increased by the shift in the Fermi level caused by the inclusion of doping impurities.

However this model cannot take into account the saturation of the SPER rate increase at high boron concentrations. With high boron concentrations, boron can create cluster in the amorphous and crystalline phase. Boron can indeed agglomerate into boron-interstitial complexes, or boron-dangling bonds complexes, in crystalline and amorphous phase, respectively. Furthermore, the presence of boron complexes at the amorphous-crystalline interface has been taken into account. As the complexes do not disintegrate during the SPER, the SPER reaction is blocked in their vicinity. A model of SPER combining point and extended defect reactions with SPER in presence of boron has been implemented in MMonCa. Its results against several experimental data are resumed:

- The model can simulate the saturation of the SPER rate increase due to the handling of boron complexes at the interface. These complexes locally stop the SPER and force the emergence of {111} planes that are twenty times slower to recrystallise than {100} ones. The SPER rate increase is close to experimental values except for low boron concentration where the model overestimates the SPER rates, as it can be seen in Figure III.6.

- As the SPER rate increase is directly linked to the Fermi level at the interface, the SPER rate increase and decrease regarding a boron profile. The model can mimic this behaviour as seen in Figure III.7.

- As the boron complexes at the amorphous-crystalline interface causes the rise of {111} planes, the interface roughens and flattens according to the local boron concentration. This behaviour, seen in experiments, is handled by the model as seen in Figure III.9.

Further development in this direction should take into account more dopants (phosphorus, arsenic ...) as well as non-doping impurities (C). Handling more impurities would enrich the KMC model, by adding more reactions that can happen at the α-c interface, such as segregation, diffusion or capture. Including the handling of phosphorus and arsenic in the KMC model could be technologically relevant as these impurities are also used in the modern junction fabrication processes.

5 French summary — Résumé

La présence de bore ou d'autres atomes accélère fortement la vitesse de recristallisation, comme on peut le voir sur la Figure I.21. Cette accélération a été expliquée de la manière suivante : la vitesse de recristallisation dépend de la concentration d'un défaut à l'interface amorphe-cristal. Or, ce défaut possède des états charges dans la bande interdite. Lorsque les dopants sont activés dans la phase cristalline, le niveau de Fermi à l'interface se meut vers la bande de conduction ou de valence, suivant le dopant. Le modèle développé par [Williams & Elliman 1983, Lu *et al.* 1991, Johnson & McCallum 2007, Johnson *et al.* 2012] permet de relier l'accélération de la vitesse de SPER au niveau de Fermi. Dans le cas où le dopant actif est un accepteur, l'accélération ν s'écrit :

$$\nu_{GFLS}(\mathrm{V}) = \frac{r_d}{r_i} = \frac{1 + g^{+} \exp\Big(\beta(e(+,0) - e_F)\Big)}{1 + g^{+} \exp\Big(\beta(e(+,0) - e_{Fi})\Big)} \tag{III.11}$$

où $\beta \equiv 1/k_BT$, g^{+} est la dégénérescence du défaut, e_F et e_{Fi} sont les niveaux de Fermi dopés et intrinsèques et $e(+,0) - e_{Fi}$ le niveau d'énergie du défaut par rapport au niveau de Fermi intrinsèque. Dans ce travail, on définit les différences d'énergies comme ceci : $e_F - e_c = \mathrm{V} - e_g$ et $e_v - e_F = -\mathrm{V}$, où e_v est le maximum de la bande de valence et e_g la bande interdite du silicium. Pour calculer V, l'équation non-linéaire de Thomas-Fermi est utilisée pourt calculer de manière auto-cohérente la densité des porteurs :

$$\epsilon \Delta \mathrm{V}(x,y,z) = -4\pi \left[\rho(x,y,z) + \sum_i Q_i[N_i^Q]\right] \tag{III.12}$$

où ϵ est la constante dielectrique du silicium, Δ, est le Laplacien et $[N_i^Q]$ la concentration de dopants de charge Q activés. Enfin, ρ, la densité de porteurs est déduite de :

$$\rho = N_C \mathcal{F}_{1/2}\Big[\beta(e_F - e_c)\Big] - N_V \mathcal{F}_{1/2}\Big[\beta(e_v - e_F)\Big] \tag{III.13}$$

où N_C and N_V sont les densités d'états électroniques dans les bandes de valence et de conduction et $\mathcal{F}_{1/2}$ l'intégrale de Fermi-Dirac.

Ce modèle, nommé déplacement du niveau de Fermi généralisé, ou *Generalized Fermi Level Shifting* GFLS en anglais, permet de simuler correctement cette accélération de la SPER. Ce modèle a été implémenté au préalable dans MMonCa, avec comme autre hypothèse que tous les atomes soient activés lorsqu'ils sont dans la phase cristalline. La probabilité d'un atome de recristallisation peut maintenant être écrite sous la forme :

$$r = \nu_{GFLS}(\mathrm{V}) \cdot K(n) \cdot \exp\left(\frac{-E_a}{k_BT}\right) \tag{III.14}$$

Le modèle de GFLS possède toutefois une lacune importante. En effet, il ne peut prédire la saturation de l'accélération de la vitesse, particulièrement visible lorsque la concentration du bore dépasse $3{\times}10^{20}\mathrm{cm}^{-3}$ dans la Figure I.21. Cette saturation a été confirmée par d'autres expériences, visibles à la Figure III.6 avec les courbes en pointillés bleues. Le modèle de GFLS, comme préalablement implémenté, donne la courbe nommée `GFLS_0`. Elle permet nettement de démontrer que le GFLS seul ne peut apporter la saturation à fortes concentrations de bore.

Un autre phénomène doit donc venir ralentir la SPER, et ainsi amener cette saturation. Plus particulièrement, un phénomène apparaissant en présence de fortes concentrations de bore, correspondant à celles utilisées dans les dispositifs microélectroniques actuels. Dans le cristal, il est connu que le bore forme des cluster bore-interstitiels ou BIC [Pichler 2004]. Ainsi, une partie du bore dans le cristal n'est pas activée du fait de cette clusterisation dans le cristal. En prenant en compte cet effet, le modèle donne la courbe nommée `GFLS_1` à la Figure I.21. Cette prise en compte n'est donc pas suffisante pour expliquer la saturation.

Plus récemment, il a été découvert que le bore peut aussi former des clusters dans la phase amorphe [De Salvador *et al.* 2006]. Or, il convient de se poser la question de ce qu'il advient de ces clusters — qui ne semblent pas bouger lors d'un recuit — lorsque l'interface amorphe-cristal arrive à leur niveau. En effet, comme l'a remarqué [Mattoni & Colombo 2004], les clusters de bore ne sont pas désintégrés par le passage de l'interface lors de la SPER. Dès lors, la présence de clusters, stables, à l'interface doit avoir un rôle détrimental sur la SPER. En effet, le modèle de SPER utilisé dans ce travail requiert que des liaisons soient cassées à l'interface afin d'initier la réaction de recristallisation [Spaepen 1978, Spaepen & Turnbull 1979]. Or, le BIC reste stable à l'interface, les atomes le composant sont donc inertes à la SPER. Ainsi, lors du passage de l'interface, la présence de BIC force celle-ci à le contourner, créant ainsi des plans de recristallisation $\{111\}$, qui sont vingt fois plus lents à recristalliser. Un schéma de ce modèle est visible à la Figure III.4.

D'un point de vue du modèle, certain atomes, même s'ils se trouvent à l'interface ne peuvent pas participer à la SPER, du fait qu'ils sont emprisonnés dans des clusters bore-interstitiels stables. On peut donc réécrire la probabilité de recristallisation d'un atome :

$$r = \mathcal{B} \cdot \nu_{GFLS}(\mathrm{V}) \cdot K(n) \cdot \exp\left(\frac{-E_a}{k_B T}\right) \tag{III.15}$$

où $\mathcal{B}$ est un bouléen qui vaut 1 si l'atome n'est pas dans un BIC ou 0 s'il l'est. En implémentant ce modèle, la courbe nommée `LKMC model` est obtenue à la Figure III.6, montrant ainsi que le nouveau mdoèle permet de simuler la saturation.

Le modèle permet aussi de prédire d'autres phénomènes dus à la présence de bore.

Premièrement, comme l'a vu [Olson & Roth 1988, Park *et al.* 1988, Jeon *et al.* 1989], si le profil de bore est gaussien, la vitesse augmente et diminue en suivant le profil de bore. Le modèle permet de bien simuler le comportement de la vitesse de SPER en fonction de la concentration de bore, comme on peut le remarquer à la Figure III.7.

Deuxièmement, la présence de bore a aussi comme autre effet d'augmenter la rugosité de l'interface [Barvosa-Carter *et al.* 2004], plus particulièrement, l'interface devient plus rugueuse lorsque la concentration augmente et inversement. Dans ce cas aussi, le modèle permet d'identifier atomistiquement les mécanismes de ce phénomène. Plus la concentration de bore augmente, plus grande est la chance qu'un BIC se forme, forçant ainsi l'apparition de plans $\{111\}$ sur une surface $\{100\}$, créant donc de la rugosité d'interface. Cette rugosité se résorbe lorsque la probabilité de rencontrer des BICs diminue, c'est-à-dire que la concentration de bore diminue. Les figures III.8 et III.9 met en exergue ce phénomène. Lorsque la SPER commence, au point `a)`, l'interface, symbolisée par les atomes colorés en bleus, est plate. Lorsque la SPER continue, l'interface arrive au point `b)` où l'interface devient plus rugueuse du fait de la forte concentration en bore, donc de la présence de BICs. Enfin, au point `c)`, la rugosité de l'interface s'est résorbée.

Chapter IV

Relaxed silicon germanium SPER

This chapter presents the Solid Phase Epitaxial Regrowth of relaxed SiGe alloys. Silicon-germanium alloys are widely used in the Semiconductors Industry especially as strain-induced mobility booster [Tezuka *et al.* 2003] and is therefore integrated in the source/drain regions. Compared to pure silicon, the SPER of SiGe alloys has not yet been thoroughly studied and presents new challenges on the comprehension of the SPER microscopic mechanism. Indeed, early experiments by [Lee *et al.* 1993] found that the activation energy in SiGe alloys is not a simple interpolation between silicon and germanium values, thus challenging the understanding of the SPER mechanism at that time. The following chapter will investigate this issue with the KMC and MD approaches.

Contents

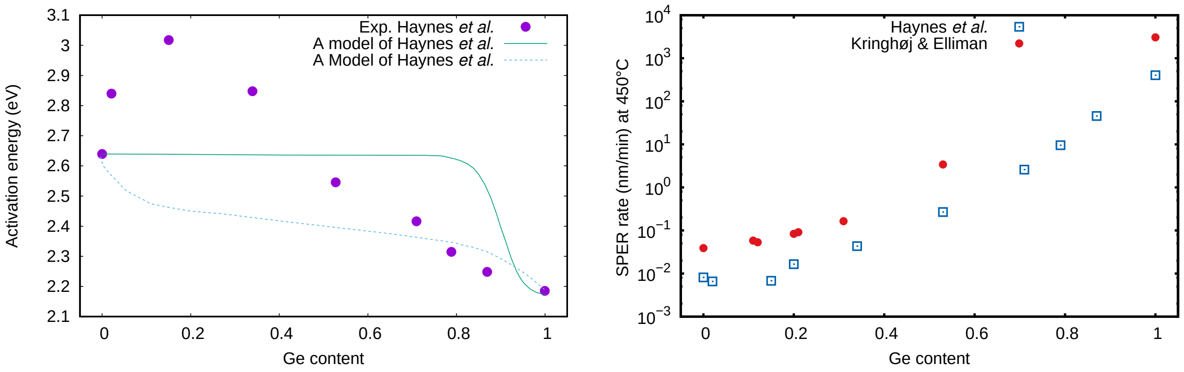

(a) Experimental values and continuous models (dashed and plain curves) of [Haynes *et al.* 1995]

(b) SPER rate in SiGe alloys. Data from [Haynes *et al.* 1995, Kringhøj & Elliman 1994]

Figure IV.1: SPER rates and activation energies in SiGe alloys

1 Germanium impacts on SPER velocities and activation energies

First investigated by [Lee *et al.* 1993], the extracted SPER activation energy of SiGe alloys does not vary linearly with germanium concentration from pure silicon to pure germanium. This fact was further asserted by the extensive investigations on the composition dependence of activation energy of SiGe SPER [Kringhøj & Elliman 1994, Haynes *et al.* 1995] [Kringhøj *et al.* 1995]. Few models have been derived from experiments and tried to explain this non-linear behaviour of the activation energy [Haynes *et al.* 1995, Kringhøj *et al.* 1995, Suh & Lee 1996]. As an example, Figure IV.1a presents the models developed by [Haynes *et al.* 1995].

2 LKMC model: refinement of the bond breaking model

The introduction of another fully miscible atom forces the previous model to take into account all the possible recrystallisation configurations, *i.e.* all the local configurations where an atom i can be recrystallised. Indeed, reasoning in two dimensions as in Figure II.1 can be misleading. For example, during the recrystallisation of two atoms on a {110} plane, if we look at a three dimension model, as in Figure IV.2, there are two recrystallisation configurations for atom 1, (i) recrystallising with atom 2 (1-2 recrystallisation) or, (ii) with atom 3 (1-3 recrystallisation). In pure elements there is no difference between 1-2 and 1-3 configurations. But in alloys, atoms 1, 2 and 3, as well as their first crystalline neighbours, can be different atoms in nature and consequently have different SPER rates that are to be included in the LKMC model, in order to keep a KMC approach, *i.e.* keep an exhaustive list of all the possible events.

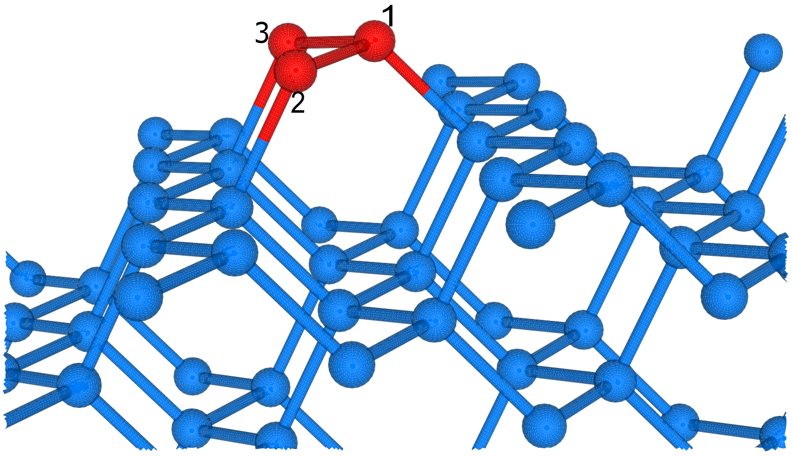

Figure IV.2: Two possible configurations for atom 1 to be recrystallised on a <110> interface: either with atom 2 or 3. As atom 2 or 3 can be different in an alloy, the configurations should yield different recrystallisation probabilities. Red atoms are amorphous, to be filled sites, and blue are crystalline.

Therefore, to differentiate between 1-2 recrystallisation and 1-3 recrystallisation, the chemical bond type between the crystalline and the amorphous atoms is introduced during the computation. These two particular bonds are highlighted in Figure II.1 for the three main interface orientations. We consider the bond type between the crystalline and the amorphous atoms as a differentiation between recrystallisation configurations on the grounds that the Spaepen & Turnbull bond breaking process [Spaepen 1978, Spaepen & Turnbull 1979] is the phenomenon responsible for the SPER. The bond breaking process is a phenomenon strictly bonded at the α-c interface. Only the bonds situated at the interface are thus focused on.

There are three possible bond types in a SiGe alloy: Si-Si, Ge-Ge and Si-Ge. Each bond type has its own activation energy and prefactor. As we focus for each recrystallisation configuration on two particular bonds, namely $bond_1$ and $bond_2$, linking the amorphous and crystalline phases, we define the activation energy for recrystallisation as an averaged energy between the two bonds to be broken (Equation IV.1). The prefactor is as well defined as a geometric mean between the prefactor of each bond (Equation IV.2). Activation energies and prefactors for each bond are gathered respectively in Table IV.1 and Table IV.2. The activation energy and prefactor values for the Si-Ge bond result from the calibration of the model with experimental data [Kringhøj & Elliman 1994, Haynes *et al.* 1995] on (100) substrate. There are no available data to calibrate the LKMC model on the (110) and (111) orientations. Nevertheless, the local configuration prefactors for silicon or germanium have been calibrated regarding the previous experimental and simulation results [Martin-Bragado 2012, Darby *et al.* 2013], and, approximatively, the same ratios are found between each local configuration. For example, the ratio between the

$\{100\}_h$ and the $\{100\}_l$ prefactors is around 20 for both Si-Si and Ge-Ge bonds. The same ratios have thus been applied between the prefactors of each local configuration for the Si-Ge bond.

$$E_a = 1/2 \cdot (E_{bond_1} + E_{bond_2}) \tag{IV.1}$$

$$K(n) = 10^{1/2 \cdot \left(log_{10}(K(n)_{bond_1}) + log_{10}(K(n)_{bond_2})\right)} \tag{IV.2}$$

Chemical Bond	SPER activation energy (eV)
Si-Si	2.7
Ge-Ge	2.17
Si-Ge	2.86

Table IV.1: SPER activation energies for each chemical bond used in the model

Local config.	$K_{Si-Si}(n)$ (s^{-1})	$K_{Ge-Ge}(n)$ (s^{-1})	$K_{Si-Ge}(n)$ (s^{-1})
$\{100\}_h$	7.425×10^{17}	2.35×10^{18}	4.02×10^{19}
$\{100\}_l$	3.094×10^{16}	1.08×10^{17}	1.81×10^{18}
$\{110\}$	1.325×10^{15}	1.65×10^{16}	2.32×10^{17}
$\{111\}$	8.10×10^{11}	1.50×10^{12}	3.00×10^{13}

Table IV.2: Local configuration prefactors for each chemical bond used in the model

Finally, a recrystallisation configuration can be found more than once, especially on {111} planes. In this case, the recrystallisation rate is multiplied by the number of times the recrystallisation configuration has been found. In conclusion, within the Transition State Theory, the recrystallisation rate for an atom at the interface can be described by this equation:

$$r = K(n) \cdot N_{config} \cdot \exp\left(-\frac{E_a}{k_B T}\right) \tag{IV.3}$$

where N_{config} is the number of times the same recrystallisation configuration has been found. In the case of different recrystallisation configurations, the rates are simply added.

3 Results and observations

3.1 Regrowth velocity

The former LKMC model has been used to study the evolution of the α-c interface during annealing. A (100)Si sample is considered, the dimensions of which were 60 nm$\times 90a_0 \times 60a_0$ in {x, y, z} respectively, where a_0 is the basic unit cell length (5.431 Å). A sketch of the used simulation cell is shown in Figure IV.3. Silicon atoms were randomly replaced by germanium atoms in order to build the wanted SiGe alloy. As the difference in bond length is not taken into account, the silicon lattice is preserved whatever is the germanium concentration. The basic unit cell length is therefore taken from the pure silicon value. Periodic boundary conditions were defined along in the y and z directions. The simulation domain was bonded by {100} planes in the x, y and z directions. A 55 nm thick amorphous layer with an atomically flat α-c interface has been studied for recrystallisation. A very short annealing is introduced in order to create an initial rough interface. The Figure IV.4 shows that the model yield close agreement to [Kringhøj & Elliman 1994] and a good agreement to the trend seen by [Haynes *et al.* 1995]. The figure thus shows that the calibration done for the prefactors and activation energy of the Si-Ge bond is correct.

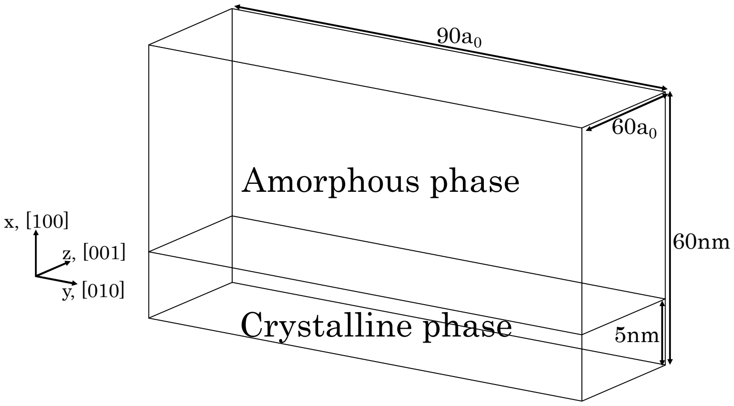

Figure IV.3: Schematic view of the simulation box used for SiGe SPER simulations.

The recrystallisation rates were calculated for several temperatures, ranging from 300 to 650°C, by measuring the time to recrystallise 20 nm of amorphous alloy. Macroscopic activation energies were extracted by a least-squared linear interpolation applied to the Arrhenius plot of the extracted recrystallisation rates. Corresponding disparities were found to be less than 10^{-4}. Upstream preparation and calibration have been done on the model so that it can yield the correct behaviours on pure elements SPER regarding the previous experimental and simulation results [Martin-Bragado 2012, Darby *et al.* 2013].

3.2 Extracted activation energy

Figure IV.4 shows the SPER rate at 450°C of SiGe alloys for the complete germanium fraction spectrum. A parabolic shape between the SPER regarding the germanium content is seen in both experimental and simulation results. The plot of the corresponding extracted activation energy versus the germanium fraction is presented in Figure IV.5 and underlines furthermore two distinct regimes. From 0 to 0.4, the activation energy is increasing from its pure silicon value (2.7 eV) to a maximum of 2.80 eV, and above 0.4, the

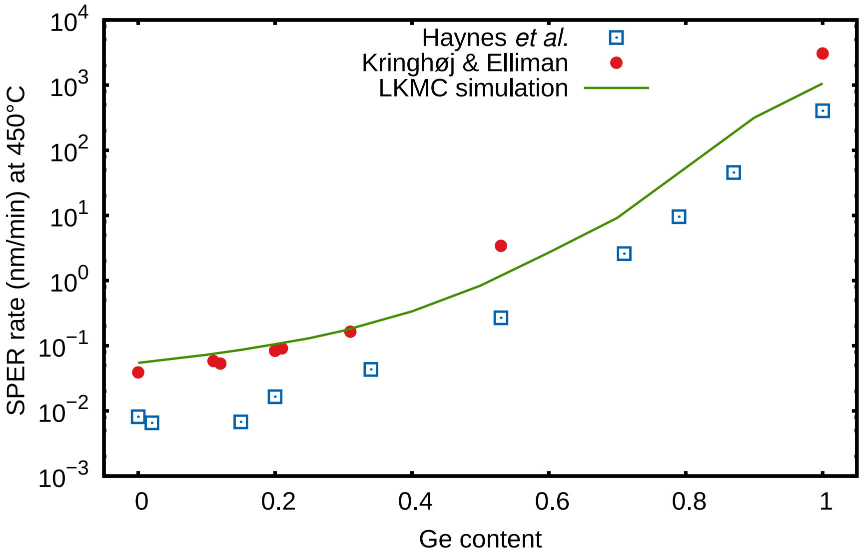

Figure IV.4: Composition dependence of the recrystallisation rate during SiGe SPER at 450°C. Experimental data from [Haynes *et al.* 1995] and [Kringhøj & Elliman 1994]

activation energy is decreasing from its maximum to its pure germanium value (2.17 eV). By taking into account a third activation energy, for the Si-Ge bond, the model yields a close agreement with the available experimental data.

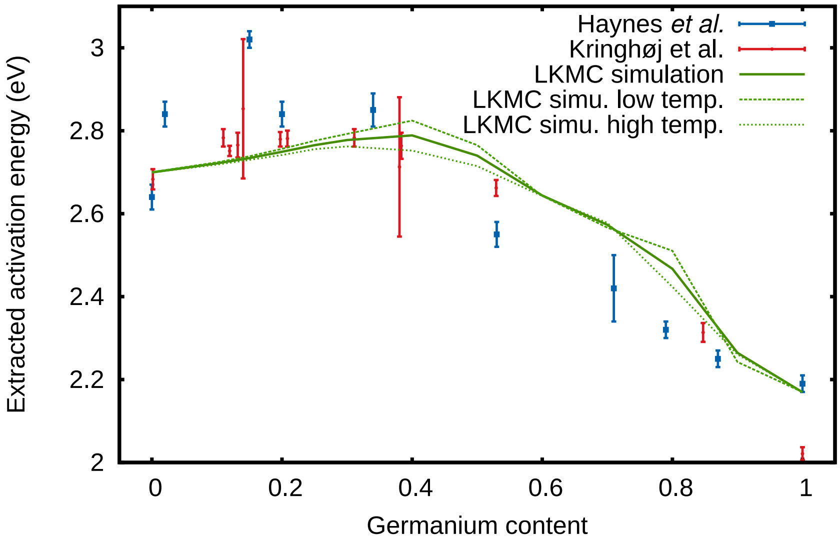

Figure IV.5: Composition dependence of extracted activation energy for SiGe alloys SPER. The activation energy presents a maximum for $Si_{60}Ge_{40}$. Activation energies extracted on limited temperature ranges are shown in dashed lines. Low temperature range: 300-450°C. High temperature range: 450-650°C. Solid line is the extraction on the whole temperature range. Experimental values from [Haynes *et al.* 1995] and [Kringhøj *et al.* 1995]

3.3 Observations

The fact that the SPER rate is monotonically increasing with the germanium fraction is misrepresenting the effects of germanium addition into SiGe alloys. Indeed, at a first glance at the Figure IV.4, one could be tempted to compare the extracted SPER activation energy with a linearly interpolated one, as Shiryaev *et al.* [Shiryaev *et al.* 1993] in the early stages of SiGe SPER investigations. Accepting the Spaepen & Turnbull bond breaking process [Spaepen 1978, Spaepen & Turnbull 1979], further confirmed by Aziz [Aziz 1992], as the microscopic mechanism of SPER, the activation energy for SPER in SiGe alloys should decrease linearly from 2.7 eV (pure silicon value) to 2.17 eV(pure germanium value). Indeed, first principles simulations done by Martins & Zunger[Martins & Zunger 1986] revealed that the cohesive energy in bulk $Si_{0.5}Ge_{0.5}$ is, at 0.01 eV/atom near, the mean of the cohesive energies for silicon and germanium bulk.

Exhaustive works however reveal a strongly non-linear activation energy regarding the germanium fraction [Kringhøj & Elliman 1994, Haynes *et al.* 1995, Kringhøj *et al.* 1995], as it can be seen in Figure IV.5. Several authors [Haynes *et al.* 1995, Kringhøj *et al.* 1995, Suh & Lee 1996] proposed continuous models to explain this non-linear behaviour.

However, continuous models lack the discernment of the microscopic competition that is happening during the SPER. In the model presented here, a recrystallisation rate is specifically appended for each recrystallisation configuration, depending on the α-c interface chemical bond types. As the energy for breaking a Si-Ge bond is, in our model, the highest, one could think that the maximum of the extracted activation energy should lie at $Si_{0.5}Ge_{0.5}$, where Si-Ge bond apparition probability is the highest. But due to microscopic competition, the maximum is shifted towards Si-rich SiGe alloys. Indeed, when the germanium fraction is higher than 0.5, the two main events that are competing have either a 2.86 or a 2.17 eV activation energy, and the latter event will most of the time be recrystallised, thus decreasing the extracted activation energy from 2.86 to 2.17 eV. Following the same reasoning, for Si-rich SiGe alloys, the two main competing events have either 2.7 or 2.86 eV. Here also, the extracted activation energy will be decreased from 2.86 to 2.7 eV. As the decreasing "force" is less in the Si-rich region than the Ge-rich region, the maximum is not attained at 0.5 but at 0.4 germanium fraction.

The addition, in our model, of a specific activation energy for Si-Ge bond can be put in comparison with the final sentence of the Haynes *et al.* [Haynes *et al.* 1995] discussion where they hypothesized that their model presented discrepancies due to the lack a an "intermediate rate term [...] for crystallization of the intermediate chemical configurations". Their hypothesis is therefore confirmed by the present work.

It can be hypothesised that the value of 2.86 eV is the addition of a linear interpolation between pure silicon and pure germanium SPER activation energy and a local strain due to the bond length difference in the alloy which increases the activation energy. Indeed, [Kringhøj *et al.* 1995] proposed a continuous model based on an activation energy correction due to bond length differences in the alloy. The bond length differences induce local strain that increases the activation energy for SPER. Their model yields close agreement with experimental results. In this model, the strain is not taken into account. However, this increase of activation energy due to local strain could have been emulated by taking a high value for Si-Ge bond breaking process. This local strain attains moreover its maximum for 0.5 germanium fraction, as seen by [Weidmann & Newman 1992], and thus giving us an additional confirmation of the bond strain role.

It is therefore more understandable to find a two-part behaviour in the SPER rate at Figure IV.5. However, as the activation energy is higher than pure silicon, the SPER rate should be slower than in pure silicon. The prefactor composition dependence is still lacking to complete the SPER rate composition dependence image. The prefactor values for SiGe alloys were also increased at higher rates than pure germanium or silicon as seen in Table IV.2. This leads to a prefactor extracted value that attains its maximum for 0.5 germanium fraction. As noted by [Kringhøj *et al.* 1995], this composition dependence could be linked to the entropy of mixing. Indeed, within the TST approximation, the change of entropy (ΔS) term is hidden in the prefactor $K(n)$ of Equation IV.3. The entropy of random ideal alloys, such as SiGe, is given by [Lewis & Randall 1961]:

$$S_{mix} = -k_B \left(x \cdot \ln(x) + (1-x) \cdot \ln(1-x) \right) \tag{IV.4}$$

where x is, in our case, the germanium fraction. It has to be noted that the Equation IV.4 reaches its extremum at $x = 0.5$, furtherly confirming the role of the entropy of mixing in the prefactor behaviour.

Ultimately, by combining both non linearities of the activation energy and prefactor, the SPER rate dependence on germanium content appears to vary monotonically from the pure silicon rate to the pure germanium one, as it can be seen in Figure IV.4.

Haynes *et al.* [Haynes *et al.* 1995] suggested a dependence of extracted SPER activation energy with the temperature to explain the differences found between the experimental values. By interpolating on two different temperature ranges, namely between 300 and 450°C or 450 and 650°C, the LKMC model is able to confirm this temperature dependence, as it can be seen in Figure IV.5. The model provides moreover an explanation to this unresolved question. In our model, the SPER is considered as a sequential phenomenon with several types of events that have their own recrystallisation probability and compete against each other. Therefore the global rate is limited by the events with the lowest recrystallisation probabilities, and the highest activation energies. During a low temperature SPER, these events have very low recrystallisation probabilities, and limit the SPER rate thus giving a high extracted activation energy. On the contrary, during a high temperature SPER, these events have higher recrystallisation probabilities compared to low temperature SPER. As they happen more frequently, they increase the overall SPER rate and lower the extracted activation energy. As this behaviour emerges from the conjunction between the existence of a rate limiting event and the event competition, only an atomistic model, which can simulate these two properties, is able to express this temperature dependence, as it can be seen in Figure IV.5.

3.4 Hypotheses on the orientation impact

Unfortunately, SiGe SPER has not been as widely investigated as Si and the effect of substrate orientation on SiGe SPER has not yet been studied. The model shown previously is used to hypothesize the behaviour of SiGe alloys during SPER on different substrate orientations than (100). A 60 nm×180 nm×$30\sqrt{2}a_0$ cell with periodic conditions on z-axis only is used. a_0 is the Si lattice parameter (5.431 Å). The α-c interface evolution is alongside the x-axis. The initial (100) plane is rotated from 0 to 90° around a [001] direction.

From the full Si cell, SiGe alloy is generated by randomly replacing Si atoms by Ge accounting for the specified Ge concentration. The bond distortion brought by the Ge presence is neglected. Initially, all atoms situated between 0 and 55 nm in the x-axis are considered amorphous and the SPER velocities, v, are extracted by a linear interpolation of the α-c interface position for different temperatures.

The results are shown in Figure IV.6, with SPER rates normalized to allow comparisons between the alloys, and in Figure IV.7 to complete the image of the Ge influence. Experimental data are plotted when available. This section will juggle between microscopic and macroscopic recrystallisations on several orientations. For the sake of clarity, the former recrystallisation will be preceded by μ and the latter by M, for each orientation.

On the other main orientations, the addition of Ge has the same effect as on (100) alloys. The SPER rate is indeed monotonically increased by the addition of Ge. However, this increase in not the same between the orientations. For (111) alloys, the increase is almost exponential across the whole Ge spectrum. However, the increase is not completely exponential for (100) alloys and they recrystallise almost at the same rate as (110) alloys, thus giving a rate ratio of almost 90% between these orientations, as it can be seen in Figure IV.7.

It can be concluded that, during $M(100)$ recrystallisation and especially in the Ge-rich region, the recrystallisation is slowed down by some mandatory $\mu(110)$ events, thus reducing the ratio between $M(100)$ and $M(110)$ SPER rates. The more the $\mu(110)$ events there are, the closer the ratio between $M(100)$ and $M(110)$ recrystallisation there will be.

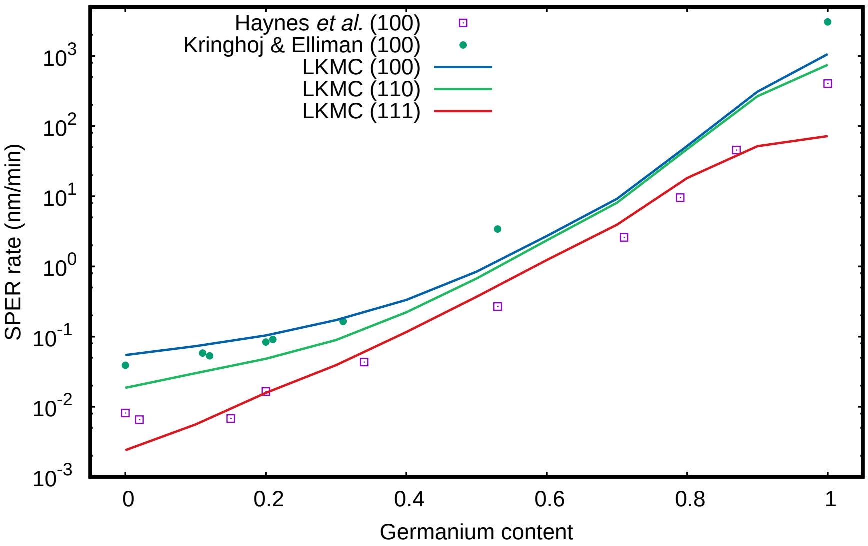

Figure IV.6: Experimental [Haynes *et al.* 1995, Kringhøj & Elliman 1994] and simulated SPER rates dependence on the germanium content on the main orientations during a 450°C anneal.

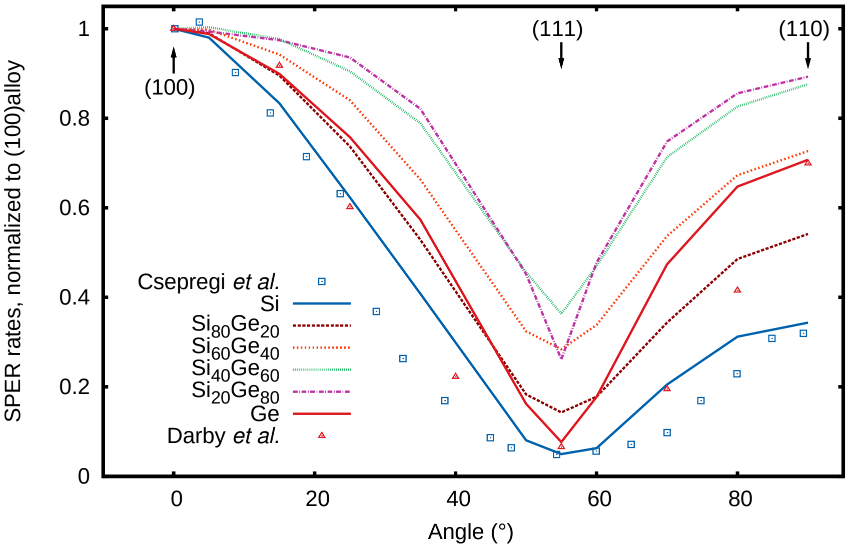

Figure IV.7: Available experimental [Csepregi *et al.* 1978, Darby *et al.* 2013] and simulated [Martin-Bragado 2012] normalized SPER rates dependence on substrate orientation during SiGe alloys recrystallisation

As $\mu(111)$ event is the slowest, a $M(111)$ recrystallisation cannot be furthermore slowed down, hence the quasi exponential rate increase. Figure IV.7 complements the Ge influence image. Due to the happening of slower events during $M(100)$ recrystallisation, the ratio between $M(100)$ and $M(110)$ or $M(111)$ SPER rates are not as strong as in pure Si or Ge. This is especially the case of Ge-rich alloys, e.g. SiGe 60% or 80%, where the ratio between (100) and (110) rates is close to 1:1.

3.5 Interface roughness

This Ge influence on the SPER rates and their ratios between orientations can also be explained by the competition between the events during SPER. This competition brings an inherent anisotropy at the α-c interface, where some sites have greater recrystallisation probabilities than others. This leads intrinsically to a rougher α-c interface in SiGe alloys than in pure elements. The model predicts this behaviour as it can be seen in Figure IV.8. This hypothesis, rose from the KMC calculations, has been tested against experimental data. Pure unstressed Si is known to keep a flat α-c interface during the recrystallisation process. The TEM images from references [Barvosa-Carter *et al.* 2004] and [Rudawski *et al.* 2008] show indeed relatively flat interfaces, of at most a few nanometers, after recrystallisation of several dozens of nanometers.

To compare pure elements to SiGe alloys, a relaxed SiGe 20% sample, grown on a graded buffer, has been implanted at room temperature with Ge^{+} ions at 80 keV, to yield 100 nm of amorphous SiGe. The sample was then annealed at 500°C during 7 hours in order to recrystallise 70 nm. The interface roughness is finally extracted via cross-sectional TEM image, and can be seen in Figure IV.9.

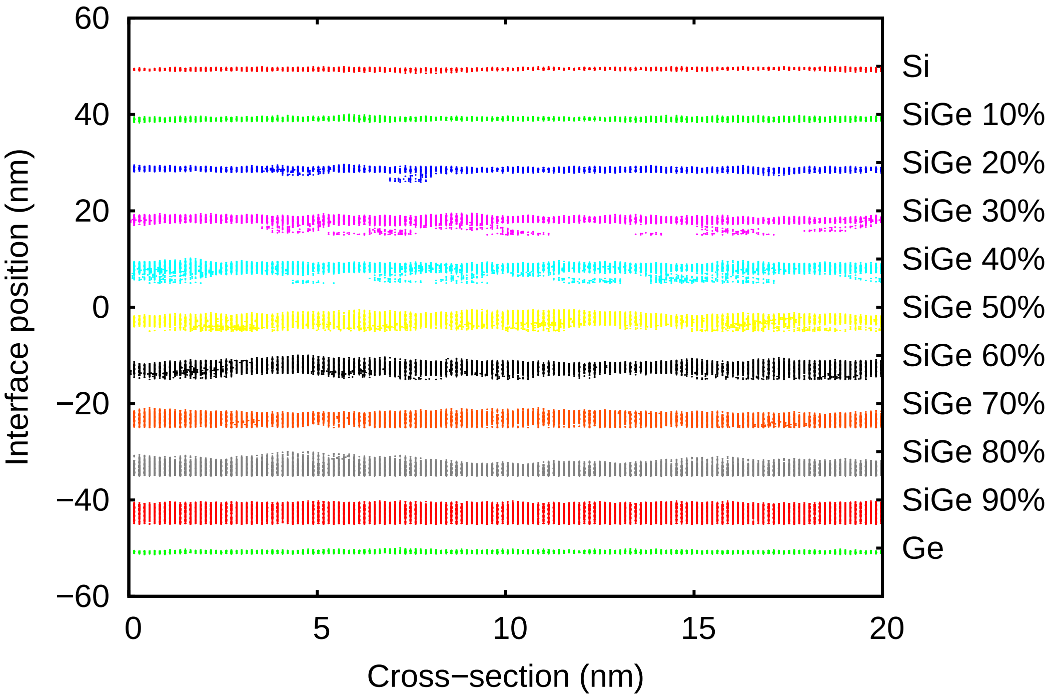

Figure IV.8: Cross-section of amorphous-crystalline interfaces after a 70 nm recrystallisation with the KMC model at 450°C. Interface are faced up and shifted by 10 nm each to allow comparison. The SiGe alloys exhibit rough interfaces, particularly in the Ge-rich region.

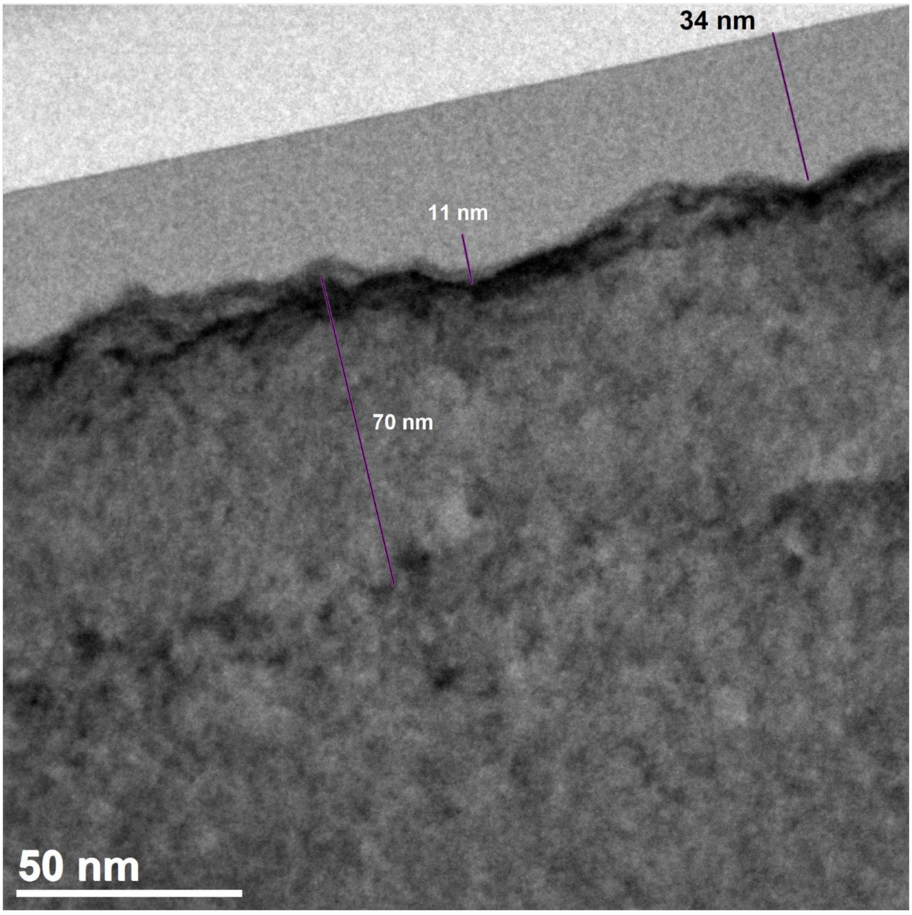

Figure IV.9: Bright-field cross-sectional TEM image of a SiGe 20% sample, grown on a graded buffer to avoid stress-related roughness, after a 70 nm recrystallisation at 500°C.

From Figure IV.9, it is clear that the roughness of the sample is larger than the roughness extracted from pure Si. Several authors have also shown that SiGe SPER exhibits a rougher α-c interface as the germanium content is increased [Elliman & Wong 1996, Corni *et al.* 1996, D'Angelo *et al.* 2007]. However, in these studies, the large roughness is due to the stress brought by the heteroepitaxy and can be explained by the model of [Sklénard *et al.* 2013]. In the case presented here, the alloy is grown on a graded buffer, therefore eliminating all possible stress. The roughness is thus only due to the local anisotropy brought by the competition between several events. The roughest interface is therefore seen on Ge-rich alloy, where there is a stronger competition between 2.86 and 2.17 eV events, as it can be noticed in Figure IV.8.

During a $M(100)$ SPER, the rougher the interface is, the more $\mu(110)$ recrystallisation sites there will be. This has been assessed by extracting from the KMC simulator the ratio of $\mu(100)$ and $\mu(110)$ sites that have been recrystallised during a $M(100)$ recrystallisation as a function of the Ge content, and can be seen in Figure IV.10. As hypothesized, the Ge-rich region yields more $\mu(110)$ events due to an increased roughness, thus explaining the low ratios between $M(100)$ and $M(110)$ SPER rates for Ge-rich alloys.

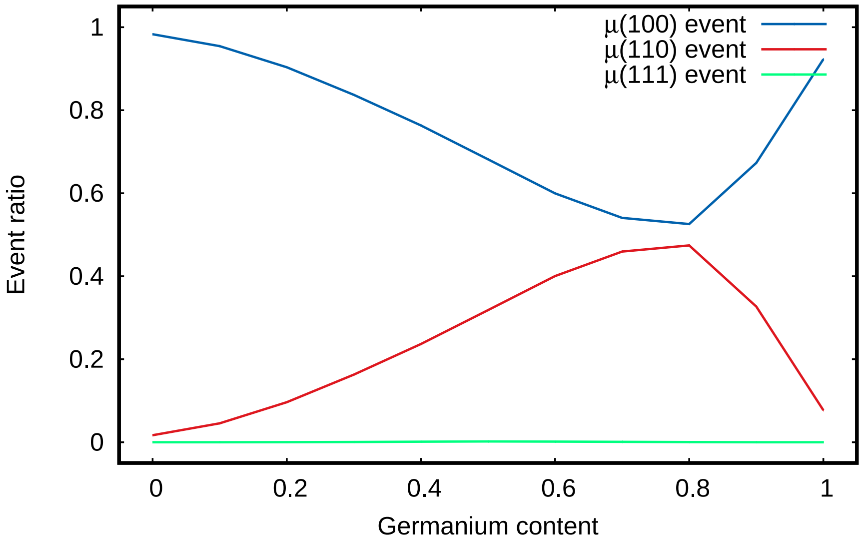

Figure IV.10: Ratio of performed events during a $M(100)$ recrystallisation. The local anisotropy brought by the competition between events leads to a rougher interface in Ge-rich alloys forcing more $\mu(110)$ recrystallisation events to be performed. This impacts the ratios between $M(100)$ and $M(110)$ SPER rates.

4 MD calculations

4.1 Simulation cell preparation

The simulation cell is prepared with the same procedure as in section 2.3 with silicon atoms randomly replaced by germanium ones to match the desired SiGe alloy concentration. In this case however, the used lattice constants are the ones corresponding to the SiGe alloy. Using a small cubic cell of 36450 atoms, the SiGe alloy has been relaxed in order to find the corresponding lattice constant with the Tersoff potential. The Tersoff potential lattice constant has been used in place of the experimental lattice constant in order to minimise the stress in the cell during simulation. The lattice constants found at 300K are plotted in Figure IV.11 against experimental data. It can be noted that the Tersoff potential used yields very close agreement with the experimental data.

4.2 Results

Figure IV.12 and Figure IV.13 show the simulation cells states after 30ns of anneal at 1700K and the extracted α-c interface over time during the same simulation, respectively. The crystalline phases are perfectly reconstructed with no apparition of defects on any SiGe alloy concentration. As expected, the more germanium content, the higher the SPER rate is.

The simulation is done for several temperatures in order to extract an activation energy for each germanium concentration. The results are compiled in Figure IV.14

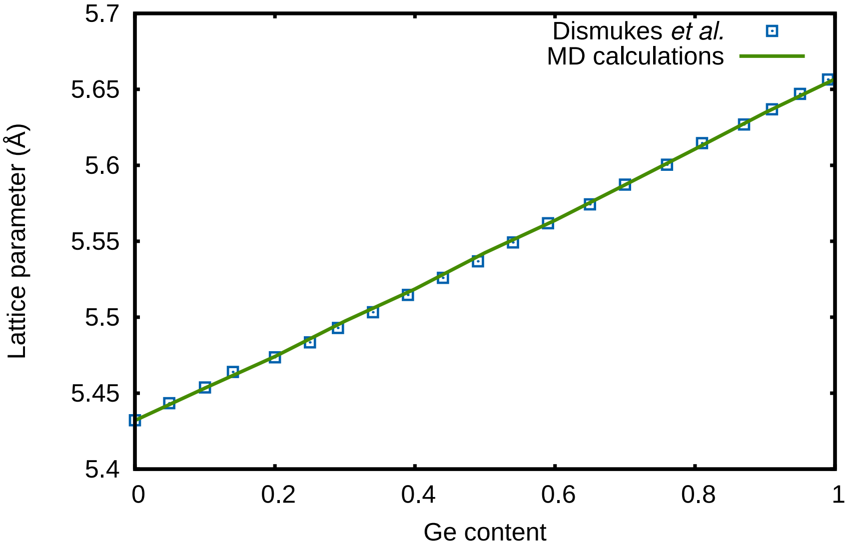

Figure IV.11: SiGe alloys lattice constants calculated at 300K with MD simulations. Experimental data from [Dismukes *et al.* 1964].

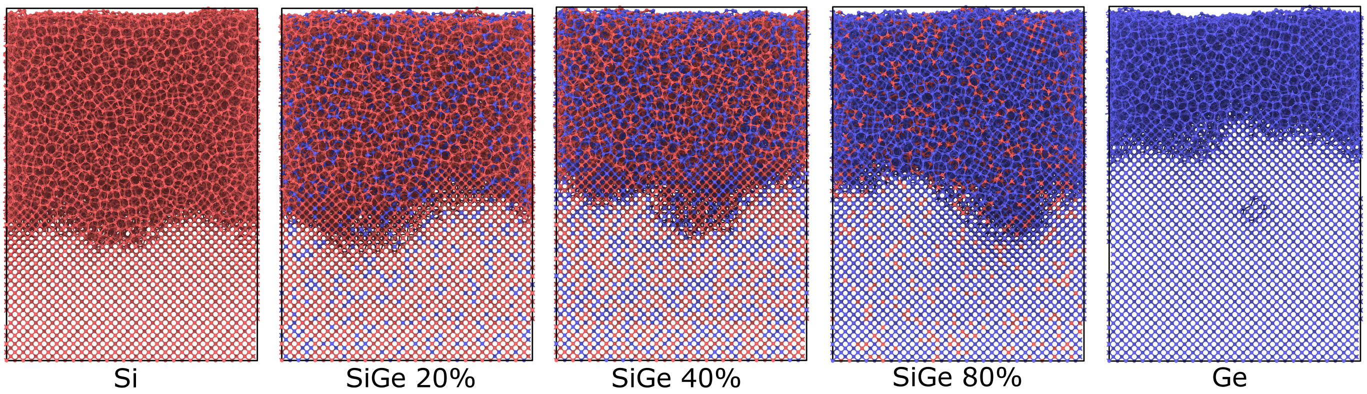

Figure IV.12: <010> view of MD simulation cell states for different germanium concentrations after a 30 ns anneal at 1700K. Views generated by `OVITO`[Stukowski 2010]

against LKMC and experimental data. The MD calculation show close agreement with both data. It has to be noted that with high germanium concentration, the anneal temperatures had to be reduced to avoid the amorphous phase to melt. The germanium concentration profiles were monitored at the beginning and the end of each simulation in order to evaluate a possible germanium snow-plough during the anneal. The profiles are plotted in Figure IV.15, where it can be seen that there is no visible germanium snow-plough, as the germanium content stays at their expected levels inside the alloys.

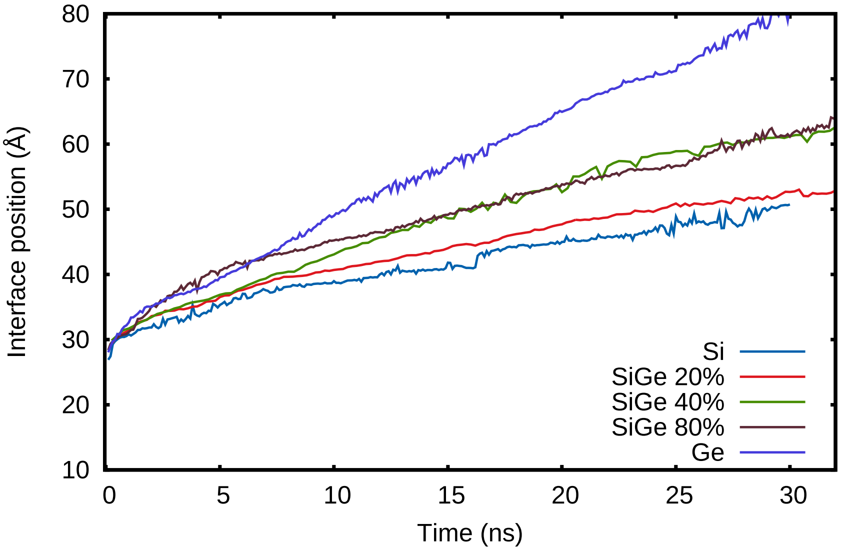

Figure IV.13: Interface evolution over time for several SiGe alloys by MD calculations

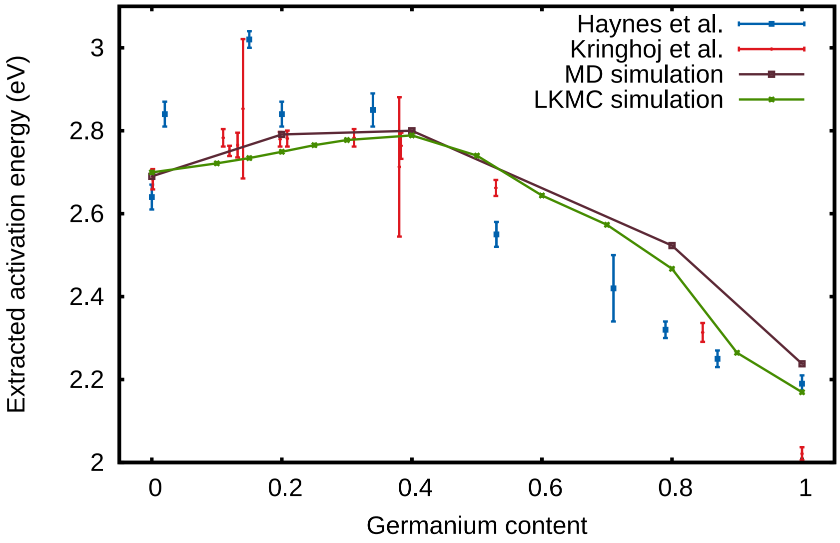

Figure IV.14: Extracted activation energies for SiGe alloys from several techniques: experimental data, LKMC model and MD calculations

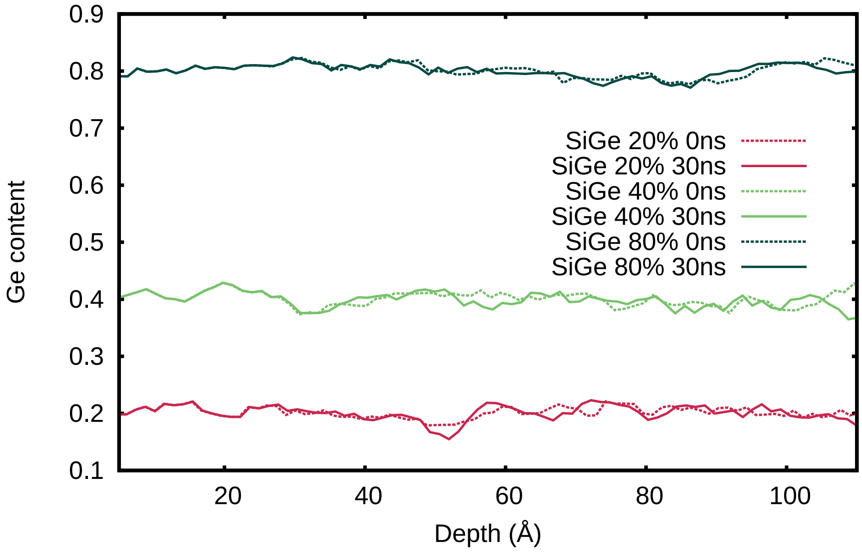

Figure IV.15: Germanium concentration profiles at 0 ns and 30 ns during SiGe alloys SPER

5 Summary

The SPER of relaxed silicon-germanium alloys has been investigated in this chapter. The SPER rates of these alloys increase exponentially regarding the germanium content. However, the activation energy does not decrease linearly between the silicon and germanium value. This behaviour was not yet understood atomistically.

The SPER model considered in this work is based on the bond breaking model, which states that the bonds have to be broken at the interface for the SPER to happen. In the case of SiGe alloys, there is a new bond Si-Ge that has to be taken into account. The activation energy for the to be broken Si-Ge bond has been calibrated to 2.86 eV. The new model, take the recrystallisation probability as the average of bonds to be broken at the recrystallisation site. The model, implemented in MMonCa give the following results:

- The model atomistically explains the behaviour of the extracted activation energy. As a higher energy has to be brought to break the Si-Ge bond than Si-Si or Ge-Ge ones, the extracted activation energy cannot be a linear function regarding the germanium concentration but has a maximum value around 40%, as seen in Figure IV.5.

- Even if the highest probability to find Si-Ge bond is at 50%, the maximum of the extracted activation energy is around 40%. This is due to averaging the bonds at the interface. At 50% of germanium, the average is between the three types of bonds, whereas at 40% the average is most of the time between Si-Si and Si-Ge bonds, hence a higher value at 40%.

- As sites have different recrystallisation probabilities regarding the atoms in their vicinity, the sites with the lowest recrystallisation probability recrystallise first. This brings a competition between the different recrystallisation sites at the interface.

- This competition brings an inherent anisotropy for recrystallisation at the interface, bringing the onset of numerous {110} planes at the interface during (100) recrystallisation. The interface is thus rougher in SiGe alloys than in pure silicon or germanium during SPER, as seen in Figure IV.8.

The model has been used to emits some hypotheses on the behaviours of (110) and (111)SiGe alloys during SPER.

- On the three main orientations, the SPER rate increase exponentially regarding the germanium content of the alloy, as it can be seen in Figure IV.6.

- Due to the onset of {110} planes during a (100) recrystallisation, the ratio between the rates of different substrates are heavily changed, as seen in Figure IV.7.

Finally, some Molecular Dynamics simulations have been carried out to confirm the behaviours of (100)SiGe alloys SPER. The activation energies extracted from MD calculations show the same behaviour regarding the germanium content, as seen in Figure IV.14. Regarding the investigations shown in the second chapter of this work, further development should address the lack of data of the SPER rates on different substrate orientations in SiGe alloys. With this type of investigations, the LKMC model could be refined with actual data for SPER rate on {110} and {110} substrate orientations.

6 French summary — Résumé

La SPER du silicium ou du germanium a été maintes fois investiguée dans la littérature. Toutefois, son alliage, le silicum-germanium, ou SiGe, n'a pas été autant sondé. Plus particulièrement, une question relative à la SPER du SiGe reste en suspens. Lorsqu'on extrait l'énergie d'activation de la SPER en fonction de la concentration en germanium de l'alliage, les expériences montrent que celle-ci n'est pas une simple interpolation linéaire entre les valeurs du silicium, et du germanium, 2,7 et 2,17 eV respectivement, comme on peut le voir sur la Figure IV.1a. Certains modèles continus ont été créés afin de modéliser ce comportement. Malheureusement, ils ne sont pas parvenus à expliquer le mécanisme microscopique sous-jacent.

Le modèle de SPER utilisé dans ce travail est basé sur celui de Spaepen & Turnbull [Spaepen 1978, Spaepen & Turnbull 1979], statuant que la réaction de recristallisation est initiée lorsque les liaisons chimiques entre la phase amorphe et cristalline sont cassées.

Or, dans le cas d'alliages SiGe, des liaisons Si-Ge doivent être prises en compte. Un nouveau modèle a ainsi été développé prenant en compte cette troisième liaison qu'est Si-Ge. Ce nouveau modèle impose une vision en trois dimensions lorsqu'il s'agit de l'interface amorphe-cristal. En effet, sur un plan {110} par exemple, il peut y avoir deux configurations pour recristalliser une configuration (110). Par exemple, à la Figure IV.2, l'atome 1 peut se recristalliser avec l'atome 2 ou 3. Le nouveau modèle prend aussi en compte ces différentes configurations qui n'étaient pas prises en compte auparavant. Dans les alliages SiGe, la probabilité de recristallisation a ainsi été modélisée dans le modèle LKMC par :

$$r = K(n) \cdot N_{config} \cdot \exp\left(-\frac{E_a}{k_B T}\right) \tag{IV.5}$$

où $K(n)$ est la dépendance de la SPER vis-à-vis de la configuration locale, comme vu au chapitre II et N_{config} prend en compte le nombre de configurations similaires rencontrées autour d'un atome. Si à la Figure IV.2, les atomes 2 et 3 sont identiques alors $N_{config} = 2$. Dans le cas contraire, $N_{config} = 1$ et les probabilités sont justes ajoutées. $K(n)$ est une moyenne logarithmique des facteurs pré-exponentiels et E_a une moyenne arithmétique des énergies des deux liaisons entre l'amorphe et le cristal. La valeur de l'énergie à fournir pour casser la liaison Si-Ge a été calibrée à 2,86 eV avec des valeurs expérimentales [Kringhøj & Elliman 1994, Haynes *et al.* 1995]. Les facteurs pré-exponentiels de la liaison Si-Ge ont aussi été calibrés. Plus précisément, seules leur valeurs {100} l'ont été, du fait qu'il n'existe pas de valeurs sur les autres orientations. Ainsi, les valeurs sur les autres orientations ont été déduites par rapport aux ratios entre les facteurs pré-exponentiels des différentes orientations dans le Si pur ou le Ge pur.

Le modèle permet d'expliquer de manière atomistique le comportement de l'énergie d'activation en fonction de la concentration en germanium, comme on peut le voir à la Figure IV.5. Il est à noter que le maximum n'est pas atteint pour 50% de germanium mais vers 40%, ce qui semble contradictoire. En effet, à 50% de germanium, la probabilité de trouver des liaison Si-Ge est plus importante qu'à 40 %. Or, du fait de l'introduction de plusieurs énergies d'activation dans le système, une compétition s'est créée. Dans les alliages riches en silicium, la compétition est entre des évènements ayant 2,7 et 2,86 eV, *i.e.* des liaisons Si-Si et Si-Ge. Dans les alliages riches en germanium, la compétition est entre des évènements ayant 2,17 et 2,86 eV, soit des liaisons Ge-Ge ou Si-Ge. C'est cette compétition qui fait qu'à 50% l'énergie d'activation extraite est plus faible qu'à 40%.
Cette compétition amène aussi un autre phénomène. En effet, comme certains sites sont d'une certaine manière privilégiés pour la recristallisation que d'autres, une certaine anisotropie apparait à l'interface. Si une telle anisotropie existe, une rugosité devrait être visible. Les interfaces obtenues par simulations LKMC à la Figure IV.8 montrent bien une

plus forte rugosité dans les alliages SiGe que dans les matériaux purs. Expérimentalement, la Figure IV.9 atteste d'une rugosité d'environ 11 nm après recristallisation d'un alliage SiGe avec 20% de germanium relaxé. Dans le silicium pur, les travaux de [Barvosa-Carter *et al.* 2004] et de [Rudawski *et al.* 2008] montrent des rugosités de quelques nanomètres. La rugosité est due à l'apparition de configurations {110} lors de la recristallisation sur un substrat (100). En effet, en surveillant quelles configurations microscopiques sont recristallisées lors de la SPER sur un substrat (100), de nombreuses configurations {110} apparaissent, particulièrement dans les alliages riches en germanium. Les résultats sont visibles à la Figure IV.10, où les courbes bleue, rouge et verte donnent la proportion de configurations {100}, {110} et {111} recristallisées, respectivement.

La modèle a été utilisé pour prédire le comportement et la vitesse de SPER sur les autres orientations. Sur les autres orientations principales, la vitesse de SPER augmente exponentiellement en fonction de la concentration de germanium, comme vu à la Figure IV.6. Il est notable que les vitesses (100) et (110) sont très proches dans les alliages riches en germanium. Ceci vient du fait de l'apparition de plans {110} lors de la recristallisation (100), ralentissant ainsi la vitesse (100) à la vitesse du (110). La Figure IV.7 résume toutes les vitesses, normalisées par rapport à leur alliage (100). Les ratios entre orientations sont fortement modifiés, particulièrement dans les alliages riche en germanium, du fait de cette apparition de plans {110} sur la recristallisation (110). Il doit être souligné que les vitesses et ratios montrés ici ne sont qu'hypothèses, dans l'attente de résultats expérimentaux venant confirmer ou infirmer ceux-ci.

La SPER d'alliages SiGe relaxés sur substrat (100) a aussi été sondée par des simulations en Dynamique Moléculaire. La méthode de travail utilisée dans ce cas est la même que montrée précédemment dans le chapitre II. Les atomes de silicium ont été replacés par des atomes de germanium afin de créer l'alliage voulu. La cellule de simulation contient 36450 atomes avec des dimensions de $15a_0 \times 15a_0 \times 20a_0$ Å^3, où a_0 est le paramètre de maille de l'alliage considéré à 300K. Le paramètre de maille utilisé est celui déterminé par dynamique moléculaire, afin d'avoir un alliage le plus relaxé possible lors de la simulation. Les paramètres de maille issus de l'expérience et de simulations Dynamique Moléculaire sont visibles à la Figure IV.11. Les simulations ne montrent aucun défaut lors de la SPER sur substrat (100), comme on peut le voir à la Figure IV.13, après 30 ns de recristallisation à 1700K. Les énergies d'activation extraites des simulations Dynamique Moléculaire sont visibles à la Figure IV.14. Ces simulations permettent de confirmer la validité du modèle LKMC.

Chapter V

Strained silicon germanium SPER

In the most advanced devices, transistors use SiGe alloys in a compressive state in order to reach the best hole mobility possible, as seen in section 1.3. However, the SPER of strained SiGe alloys has been even less studied than relaxed SiGe alloys. This chapter offers an investigation of strained SiGe alloy SPER thanks to *in situ* and *ex situ* experiments. The SPER was studied *in situ* with High-Resolution X-Ray Diffraction (HR-XRD) thanks to the high brilliance delivered by the European Synchrotron Research Facility (ESRF) at Grenoble (France). Following experiments, such as low brilliance XRD and Transmission Electron Microscopy, were carried out to complete the investigation. Germanium-rich SiGe alloys on silicon are shown to relax during SPER. However, the relaxation mechanism is revealed to be dependent of the anneal temperature.

Contents

1 Strained SiGe alloy fabrication

To prepare strained SiGe alloys, epitaxy is often used. Due to the lattice mismatch between silicon and the alloy, the resulting strain is contained into the deposited layer as an elastic energy. The thicker the deposit layer is, the higher the energy. However, the layer cannot contain indefinite amount of energy. Above a certain deposited thickness, called critical thickness, the layer will discharge the excess of energy via plastic relaxation. The plastic relaxation creates threading dislocations as it can be seen in region 1 of Figure V.1, where the authors wanted to create a relaxed SiGe layer (region 2). The onset of plastic relaxation is inherently connected with the germanium concentration, due to the fact that the higher germanium concentration means a higher lattice mismatch. The critical thickness h_c for epitaxially grown SiGe layers has been formally written by [People & Bean 1985, People & Bean 1986]. The values for h_c found by People & Bean are underestimated, as a later study has discovered [Hartmann *et al.* 2011]. This is certainly due to the omission of the surface roughening mechanism [Pidduck *et al.* 1992, Tersoff & LeGoues 1994] as a way of discharging elastic strain in the calculations of People & Bean.

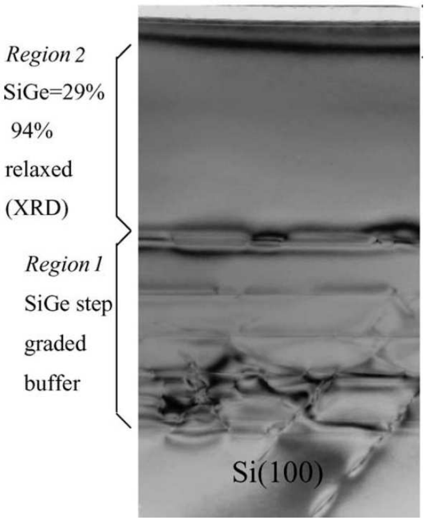

Figure V.1: TEM image of a SiGe layer epitaxially grown on silicon. Region 1 shows a highly defective layer with numerous threading dislocations due to the lattice mismatch. Region 2 is a relaxed SiGe layer. Adapted from [Harame *et al.* 2004]

Using Chemical Vapor Deposition (CVD), 40 nm thick strained SiGe layers with an uniform germanium content of either 12%, 22%, 32% or 42% have been grown on Si(100) wafers. The as-grown SiGe layer thicknesses were assessed by *in-situ* X-ray Reflectometry (XRR). The layers have been coherently grown and show a biaxial strain state induced by the heteroepitaxy. The strain has been confirmed by HR-XRD measurements.

To create an amorphous phase, deposited layers have been amorphised by germanium ion implantation with the following conditions: energy of 17 keV, dose of $1 \times 10^{15}/\text{cm}^2$ and flux of $1 \times 10^{15}/\text{cm}^2/\text{s}$. The implantation leads to a 35 nm amorphisation thus leaving 5 nm of crystalline SiGe seed. Upstream cleansing have been performed on the wafers to remove their native oxides in order to limit oxygen recoil in the amorphous layer.

2 *In-Situ* observations experimental setup

2.1 Background in X-ray diffraction

X-rays are electromagnetic radiations with a wavelength between 0.01 to 10 nanometres. They are very often used in crystallography in order to obtain the structure and characteristics of a crystal, as their wavelength range is close to a crystal lattice constant. When X-rays are applied to atoms, their electronic clouds respond to the incoming electromagnetic waves by oscillating with the same frequency. This creates a dipole between the non-moving nucleus[1] and the moving electronic cloud. A new electromagnetic radiation is created, with the same frequency as the incoming X-ray. The incoming X-ray is therefore scattered. A schematic representing the scattering of X-ray is shown at Figure V.2.

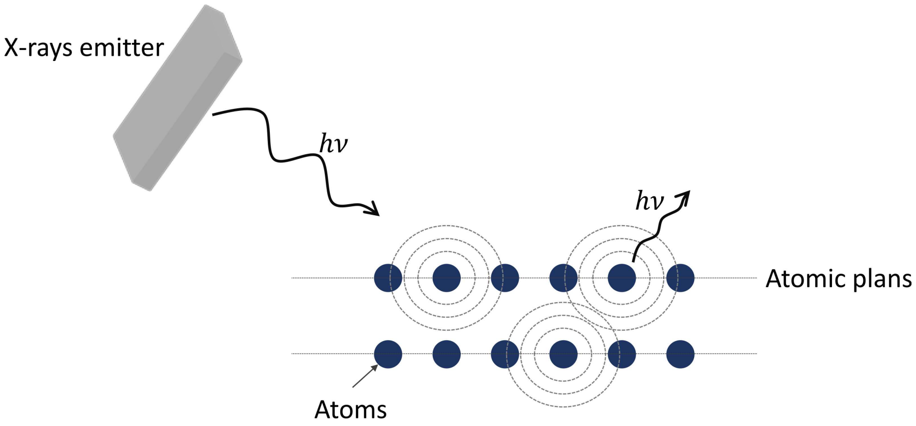

Figure V.2: Schematic of the atomic scattering happening when X-rays are applied to a crystalline structure

As the scattered waves are emitted isotropically around atoms, waves cancel one another through destructive interference. However, interferences are constructive on specific directions. On Figure V.3, the additional length travelled by incoming and emitting waves is $2d \sin\theta$. In order to have constructive interferences, this additional length must be proportional to the X-ray wavelength λ, giving the Bragg's equation:

$$n\lambda = 2d \sin\theta \tag{V.1}$$

---

[1] Compared to the electronic cloud, the nucleus has a higher mass and is negligently influenced by the incoming X-rays

where n is the order of diffraction.

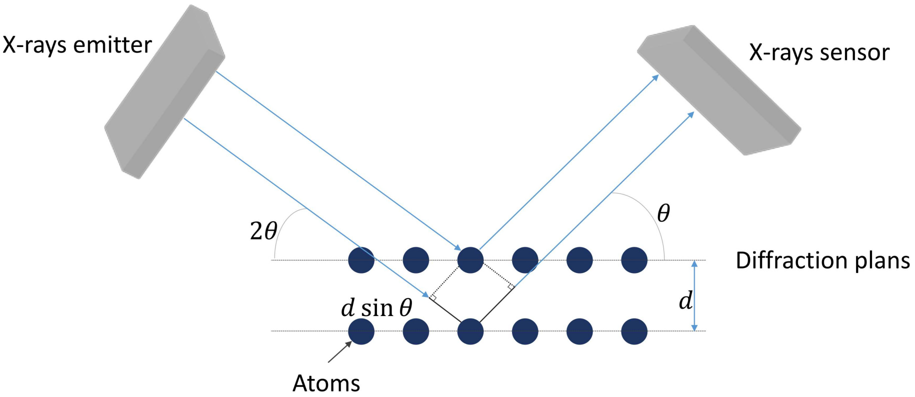

Figure V.3: Schematic of Bragg's law for diffraction in crystalline materials

Working with crystallography, it is often easier to work in the reciprocal space. From the crystalline space $\mathcal{R}_c = \vec{a}, \vec{b}, \vec{c}$, a new vectorial space can be created $\mathcal{R}_c^* = \vec{a^*}, \vec{b^*}, \vec{c^*}$ such as $\vec{a} \cdot \vec{a^*} = \vec{b} \cdot \vec{b^*} = \vec{c} \cdot \vec{c^*} = 1$. This new space, is called the reciprocal space. In this space, nodes corresponding to a linear combination of basis vectors of the reciprocal space. Each node is defined by the vector $\vec{h_{hkl}} = h\vec{a^*} + k\vec{b^*} + l\vec{c^*}$. A schematic of the reciprocal space map (RSM) for diamond silicon can be seen at Figure V.4. In the reciprocal space, the diffraction condition is written as: $\vec{h_{hkl}} = \vec{k_d} - \vec{k_l} = \vec{q}$ and Q can be defined as $Q = \frac{1}{d}$, where d is the distance between two diffraction planes.

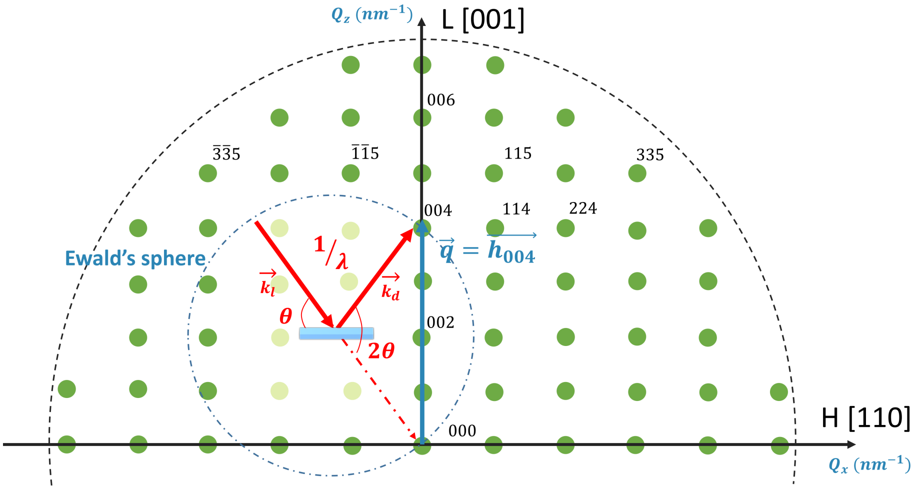

Figure V.4: Scheme of the reciprocal space map of a cubic structure and a vector representation of the diffraction conditions in the reciprocal space

The mapping of the reciprocal space give information of the structure of the epitaxial film and the substrate. Recording along Q_z around the (004) reflection allow the access to $a_\perp$, the interlayer spacing normal to the surface. However, in the case of relaxation, (004)RSM cannot directly evaluate the relaxation. In this case (224)RSM is mandatory to have access to $a_\parallel$ too. Figure V.5 shows the difference between $a_\perp$ and $a_\parallel$.

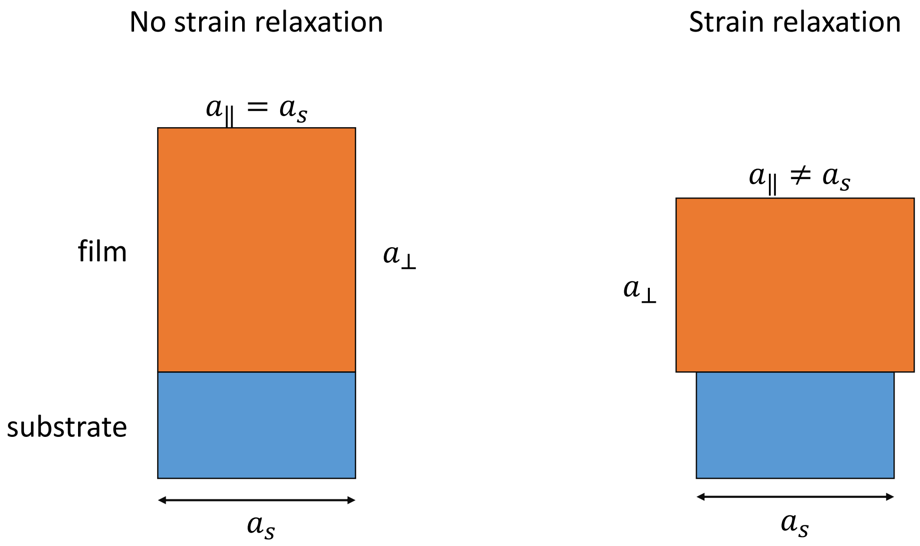

Figure V.5: Schematic showing the difference between strained and relaxed heteroepitaxial layers

A Q_z scan around the (004) reflection gives the curve seen in Figure V.6, a typical $\theta - 2\theta$ curve. The position of the different peaks and fringes allow access to several information, with the following equations:

$$t = \frac{1}{\sqrt{2\ln 2}\sigma} \tag{V.2}$$

$$t = \frac{3}{2\Delta Q_{z_2}} \tag{V.3}$$

$$t = \frac{1}{\Delta Q_{z_3}} \tag{V.4}$$

where t the thickness of crystalline SiGe, σ is the standard deviation of a Gaussian fit of the layer peak, ΔQ_{z_1} is difference between the substrate peak and the layer peak, ΔQ_{z_2} the difference between the layer peak and the peak of the first fringe and ΔQ_{z_3} the difference between fringe peaks. The different ΔQ_z are shown in Figure V.6. To find the position of the different layer peak and fringes, each peak can be approximated by a Gaussian curve.

2.2 The European Synchrotron Research Facility Experiment setup

On very thin films — less than 5 nm a crystal after implantation — a typical $\theta - 2\theta$ curve is usually done in several hours using laboratory X-rays equipment. However, the aim here is to follow in real-time the thickness of a SiGe layer, thus the SPER rate. Synchrotron radiations alleviate the issue by having a high brilliance, meaning a high X-

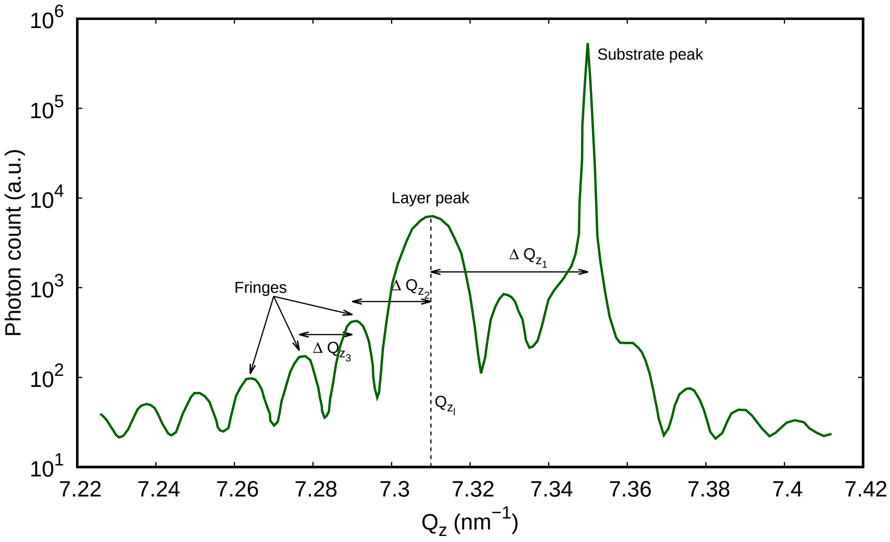

Figure V.6: Theoretical $\theta - 2\theta$ curve using a (004) reflection converted in a Q_z scan of a SiGe layer epitaxially grown on a Si substrate

ray flux, allowing the experiment. HR-XRD experiments were carried out at the European Synchrotron Research Facility (ESRF) at the beam line BM 32[2], specialised for surface and interface experiments. The beam had an energy of 12 keV. The experiment is installed as the following scheme:

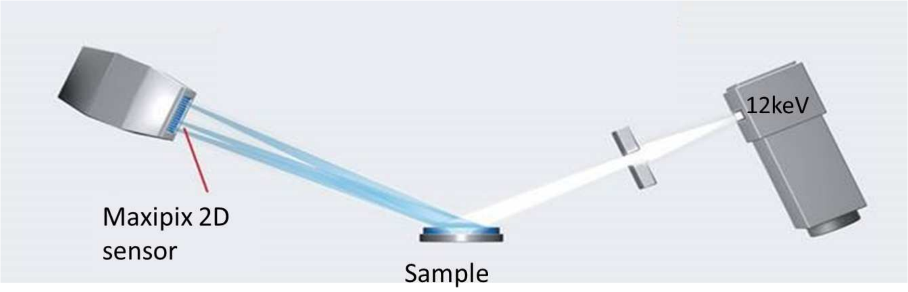

Figure V.7: Experimental installation for (004) HR-XRD carried out at the ESRF

The sample was heated with an oven at the wanted temperatures. Thermal budgets listed in Table V.1. The oven was filled with dinitrogen is order to experiment under inert atmosphere. Finally, the sensor was the Maxipix[3], a two-dimensional sensor. From the 2D-sensor to a $\theta - 2\theta$ curve, a complete workflow was created. Succinctly, the sensor records the diffraction peaks in the crystalline space. The workflow takes as input the different images from the sensor, transform them into a RSM and then apply a cut along Q_z in order to yield a $\theta - 2\theta$ curve. From $\theta - 2\theta$ curves, the thickness of crystalline SiGe layer can be extracted with the equations previously shown. The full extraction workflow

---

[2] `http://www.esrf.eu/UsersAndScience/Experiments/CRG/BM32`

[3] `http://www.esrf.eu/Instrumentation/DetectorsAndElectronics/maxipix`

can be found in Appendix B.

Layer	Temp (°C)	Time (min)
SiGe 12%	480	600
	500	100
	540	20
	560	15
SiGe 22%	460	520
	480	90
	520	60
	540	40
SiGe 32%	480	70
	500	41
	520	37
	540	30
SiGe 42%	420	540
	460	600
	500	35
	520	30

Table V.1: Thermal budgets applied during HR-XRD experiments

2.3 Results

Figure V.8 shows the θ-2θ curves for different SiGe alloys after SPER with their respective highest thermal budgets applied during this experiment. From these thermal budgets, the complete recrystallisation of the SiGe layer is expected. The theoretical positions of strained and relaxed layer peak are also shown. From these curves, it is clear that the 32% and 42% alloys are relaxed, as their relaxed peaks are higher than their strained ones. On the contrary, SiGe 12% seems to have kept its strain after the SPER. Finally, the SiGe 22% seems to be partially relaxed. Indeed, the relaxed peak is present but much smaller than the strained one. There is a drop of intensities to zero around $Q_z = 7.15$ due to the fact that the sensor does not have pixels at certain points. A direct view of the sensor at Figure B.1 during a diffraction confirm that there are some areas in the sensor where pixels are absent. This absence of pixels results into a drop of intensity at a certain Q_z point.

To qualitatively evaluate the relaxation, (004)RSMs are shown in Figure V.9. Theoretical positions of peaks are shown. As it can be seen, on the SiGe 22% sample, the relaxed peak is present but not prominent whereas on the other sample, the relaxed peak is prominent. The triangle shape around the strained peak in SiGe 22% sample denotes the presence of a certain gradient of $a_\perp$ inside the layer. This reinforces the idea that the

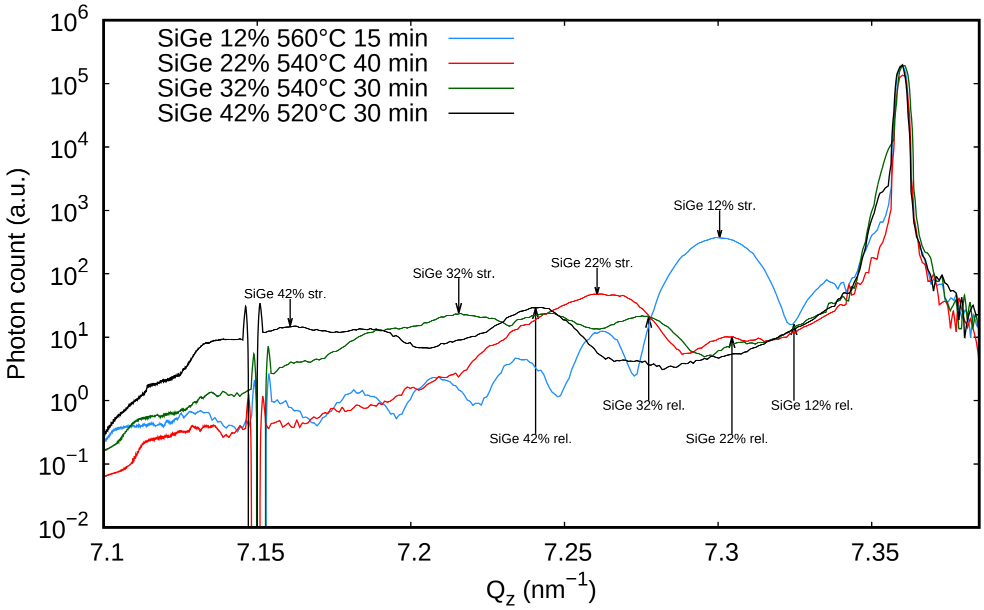

Figure V.8: θ-2θ curves converted in a Q_z scan of SiGe layers after SPER with the highest thermal budgets. Theoretical positions of the layer peaks for the strained and relaxed SiGe layers are shown

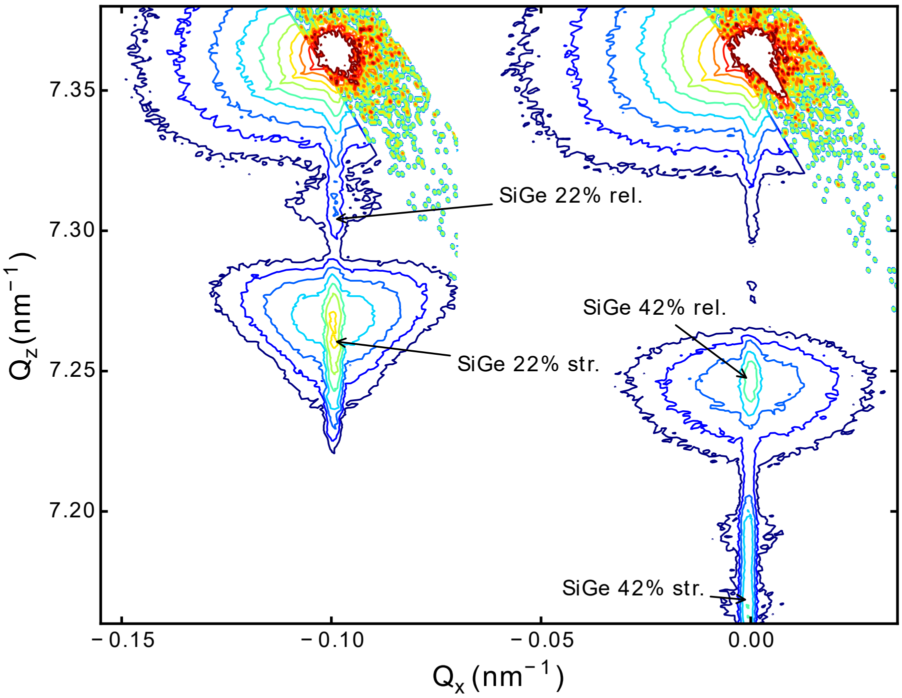

Figure V.9: Juxtaposed (004)RSMs of SiGe 22% and SiGe 42% showing partial relaxation and total relaxation. RSMs taken on samples with the highest thermal budget. RSM of SiGe 22% is shifted by -0.10 in Q_x, allowing comparison layer is partially relaxed.

As the experiments were in real-time, extraction of layer thickness over time was possible. However, such extraction was only possible on SiGe 12% and 22% samples. On higher germanium concentration samples, the relaxation made impossible the thickness extraction. Figure V.10 and Figure V.11 show the result of these extractions. Unfortunately, the SiGe 22% annealed at 480°C in Figure V.11 was not completely recrystallised at the end of the experiment. The Figure V.10 reveals the expected behaviour during SPER: the higher the anneal temperature is, the faster the layer recrystallisation is.

Figure V.11 however exhibits some peculiar behaviours. There is a clear difference between low temperature and high temperature anneal. During anneal at high temperatures, the layer thickness to some extent stopped around 28 nm whereas during low temperature anneal, this slow-down does not happen. Moreover after the slow-down at high temperature anneals, the thickness is increasing again but at another speed, since the slopes are different before and after the slow-down. This behaviour could betray the presence of interface roughness. Indeed, if the interface is rough, some parts of the interface could reach the free surface whereas other parts are still partially amorphous. At this point, the recrystallisation rate would be greatly hindered as the interface would have to recrystallise along <110> and <111> directions, which are very slow compared to the <100> direction. This behaviour is schematised in Figure V.12.

From these extractions, SPER rates and ultimately activation energies can be extracted. The extracted activation energies are listed in Table V.2 with available literature data. The value extracted for the SiGe 22% alloys in this work does not seem very precise due to the partial relaxation of the layers.

Reference	12	22
This work	3.11 eV	2.57 eV
[Paine *et al.* 1991]	3.2±0.1 eV	x
[Lee *et al.* 1993]	2.94-3.11 eV	x

Table V.2: Activation energies for strained SiGe layer SPER

As the temperature seems to have influence during the anneal on the relaxation, Figure V.13 shows the θ-2θ curves for the SiGe 22% samples at the same level of recrystallisation (either 20 nm or 30 nm layer thickness) but annealed with different temperatures. The positions of the strained and relaxed layer peaks as well as the position of the first fringe are given. The two anneal temperature curves are shifted to allow direct comparison. At 20 nm of layer thickness, both temperatures yield the same curve: presence of the first fringe and no sign of relaxation due to the absence of relaxed peak. At 30 nm, the relaxed peak appears for both anneal temperatures. However, at 30 nm, the high temperature anneal seems to portrait more relaxation. First, the strain peak is deteriorated as it cannot be longer approximated by a Gaussian curve. Second, the first fringe peak is

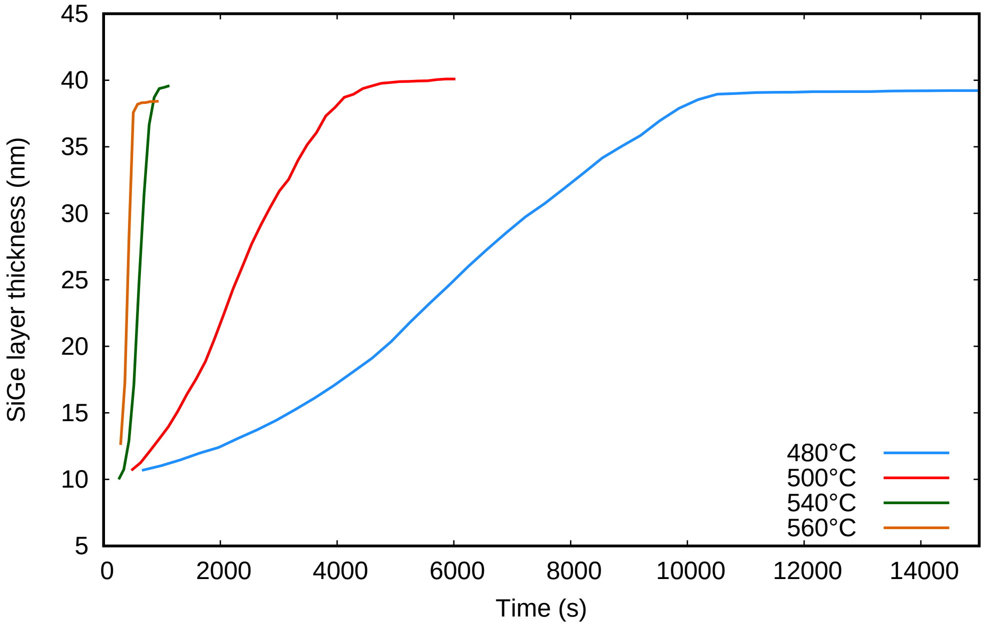

Figure V.10: SiGe layer thickness evolution during the SPER of strained SiGe 12% with several temperatures

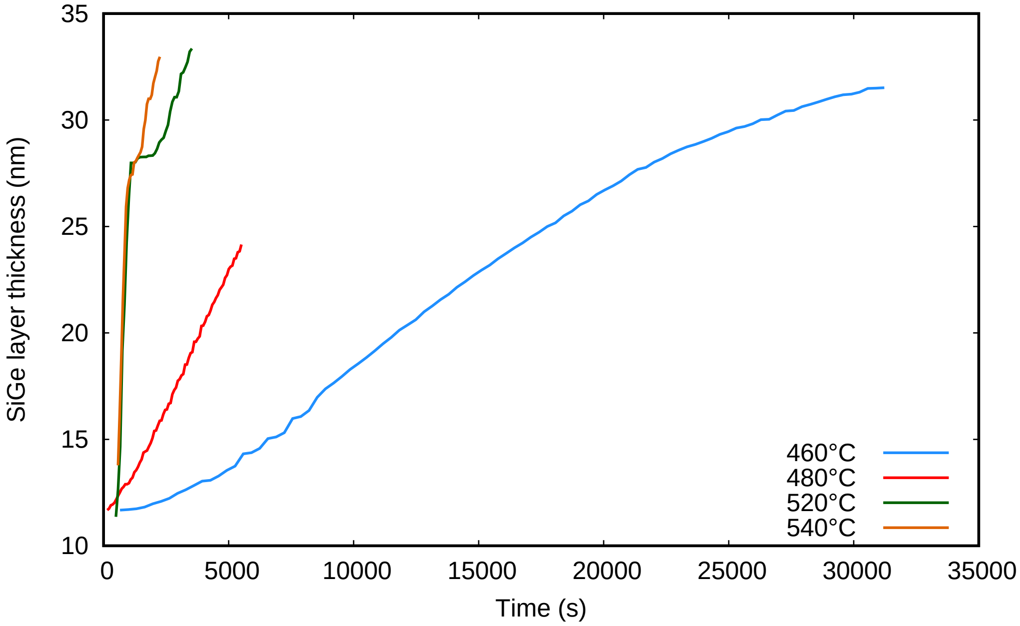

Figure V.11: SiGe layer thickness evolution during the SPER of strained SiGe 22% with several temperatures

also greatly deteriorated.

In conclusion, HR-XRD experiments on strained SiGe SPER with a thickness of 40 nm show that 32% and 42% alloys irremediably exhibit relaxation during SPER. SiGe 12% alloys do not seem to relax. Finally, SiGe 22% alloys seem to partially relax and the relaxation could be linked to the anneal temperature.

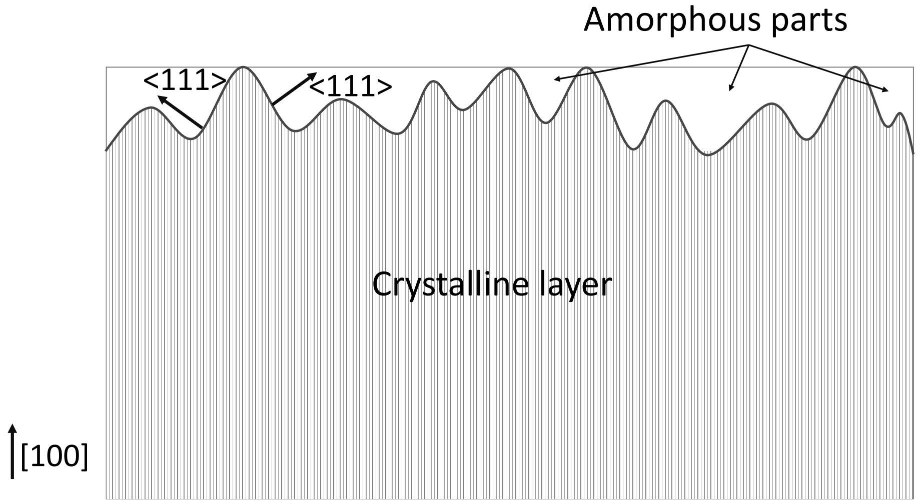

Figure V.12: Schematic of the end of a layer recrystallisation in case of a rough interface. As some parts are still amorphous they will be recrystallised along <111> direction, slower than the [100] direction

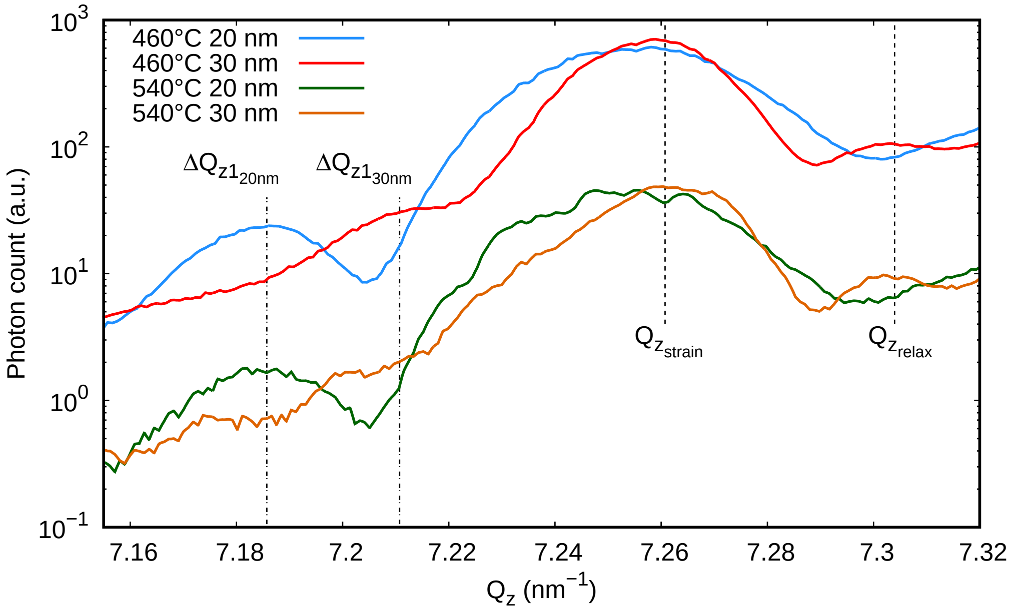

Figure V.13: θ-2θ curves for SiGe 22% with the same layer thickness but different temperatures. Positions of the important Q_z points are given

3 Further experimental observations

The previous section showed HR-XRD spectra along the (004) orientation. However, this type of experiment cannot give a conclusive answer to the hypothesis raised before: the anneal temperature seems to have an impact on the relaxation during SPER. In this section, (224) RSMs as well as TEM images are shown in order to draw a conclusion to the topic.

3.1 HR-XRD (224)RSM

HR-XRD extractions were performed on a Panalytical X'Pert Pro system. Copper Kα1 radiation was selected using a four-crystal Ge(220) Bartels monochromator and a 1D detector is used.

Figure V.14 and Figure V.15 show the results of the reciprocal space mapping for the two sample considered before in Figure V.13. The positions of the strained and relaxed peaks are shown in both figures. The relaxation line between the strained and relaxed SiGe layer positions are shown. Furthermore, are highlighted areas of the contour plots that share the same photon counts in both figures. This allow direct comparison of the relaxation level. Both maps were taken when the samples had a SiGe thickness of 32 nm. Both samples exhibit some stage of relaxation as the diffraction spot around the strained position spreads towards the relaxed position alongside the relaxation line. However, there is a subtle difference between the two thermal budgets. At 460°C, the diffraction spot — symbolised by the red ellipsoid — is centred close to the strained peak position. After the 540°C anneal, the diffraction spot as well as its centre are moved away along the relaxation line towards the relaxed peak position. In conclusion, the reciprocal space maps exhibit evident difference in term of relaxation between low and high temperature anneal.

3.2 TEM images

To visually estimate the relaxation, TEM images were done. With TEM images, there are two ways to assess the relaxation of a a layer. With cross-section TEMs, partial and threading dislocations can be seen. These type of defects clearly denote a relaxation of strain in the layer [Hong *et al.* 1992a]. Figure V.16 shows cross-section TEM images for the SiGe layers recrystallised at 460°C and 520°C. In both images, none of the strain relaxation defects such as partial and threading dislocations can be seen. However, hairpin dislocations appear. Figure V.17 clearly shows hairpin dislocations in the recrystallised layer. These dislocations appear in both samples. Finally, plan views of the annealed samples are shown in Figure V.18. Images were taken using several g vector in order to

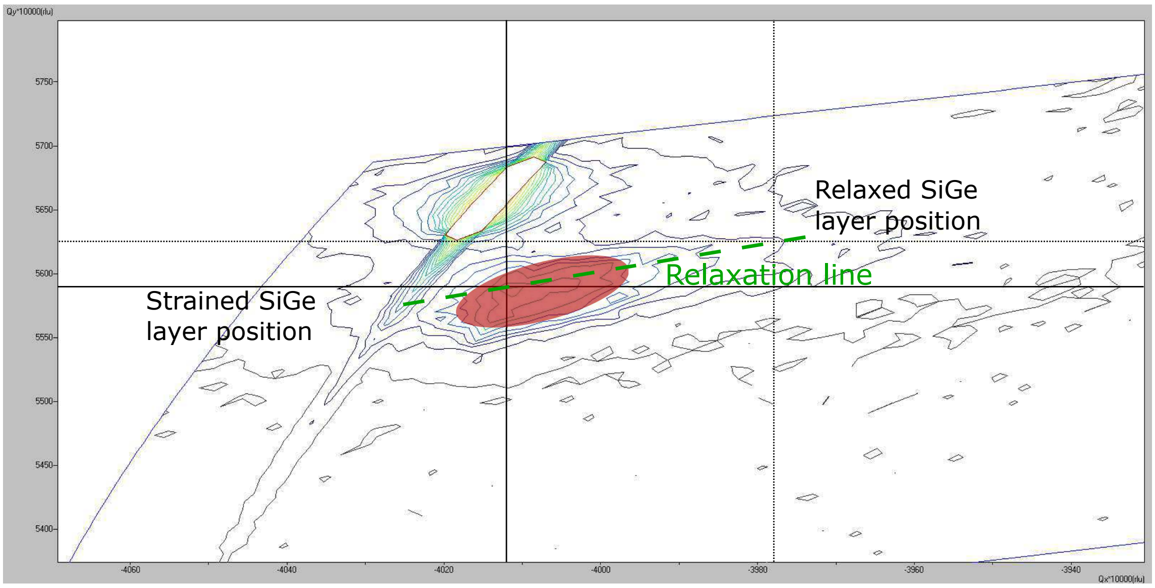

Figure V.14: (224)RSM for the sample SiGe 22% recrystallised at 460°C

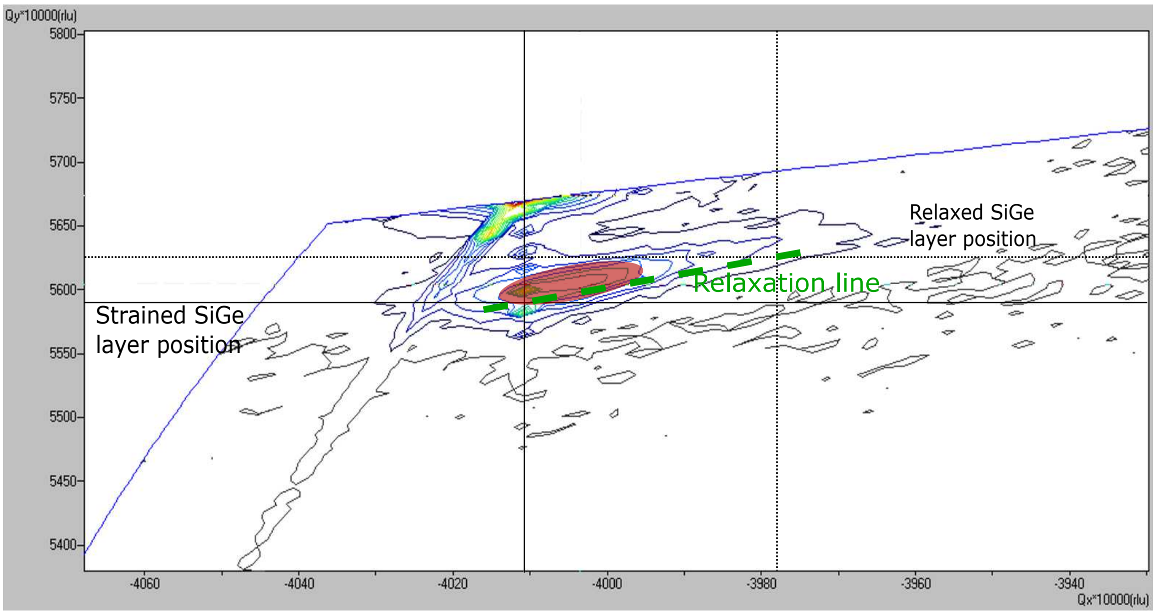

Figure V.15: (224)RSM for the sample SiGe 22% recrystallised at 540°C

see several types of hairpins. The images moreover show no signs of misfit dislocations, confirming that the layers are not completely relaxed.

3.3 Results and discussion

From the literature, it is known that only a certain thickness of strained layer can be recrystallized before the onset of strain relieving defects. These defects are extended defects in the form of stacking faults bounded by partial dislocations [Paine *et al.* 1990, Paine *et al.* 1991, Rodríguez *et al.* 1997] as well as threading dislocations [Hong *et al.* 1992b].

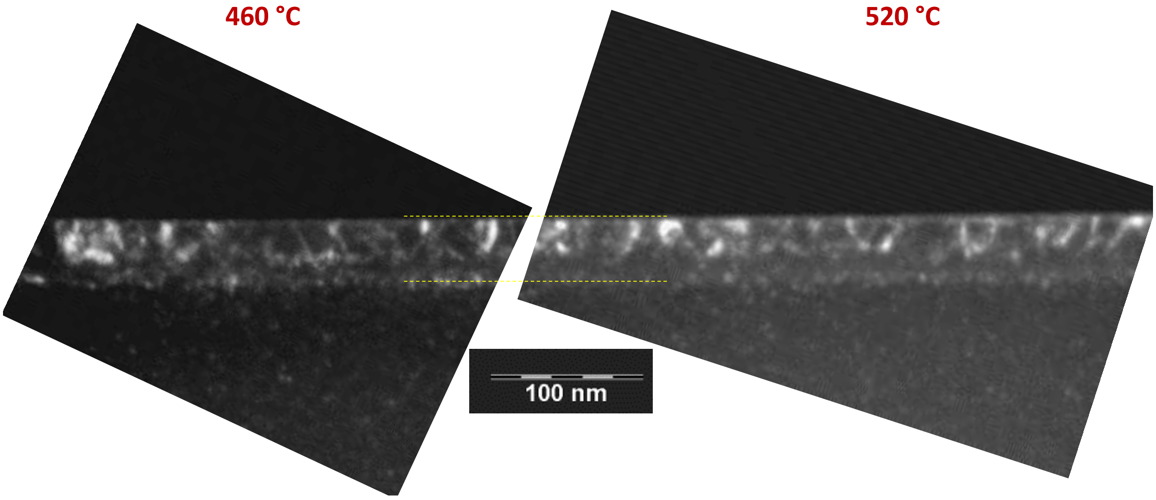

Figure V.16: Cross-section TEM images for SiGe layers recrystallised at 460°C and 520°C. Yellow lines symbolise the boundaries of the SiGe layer

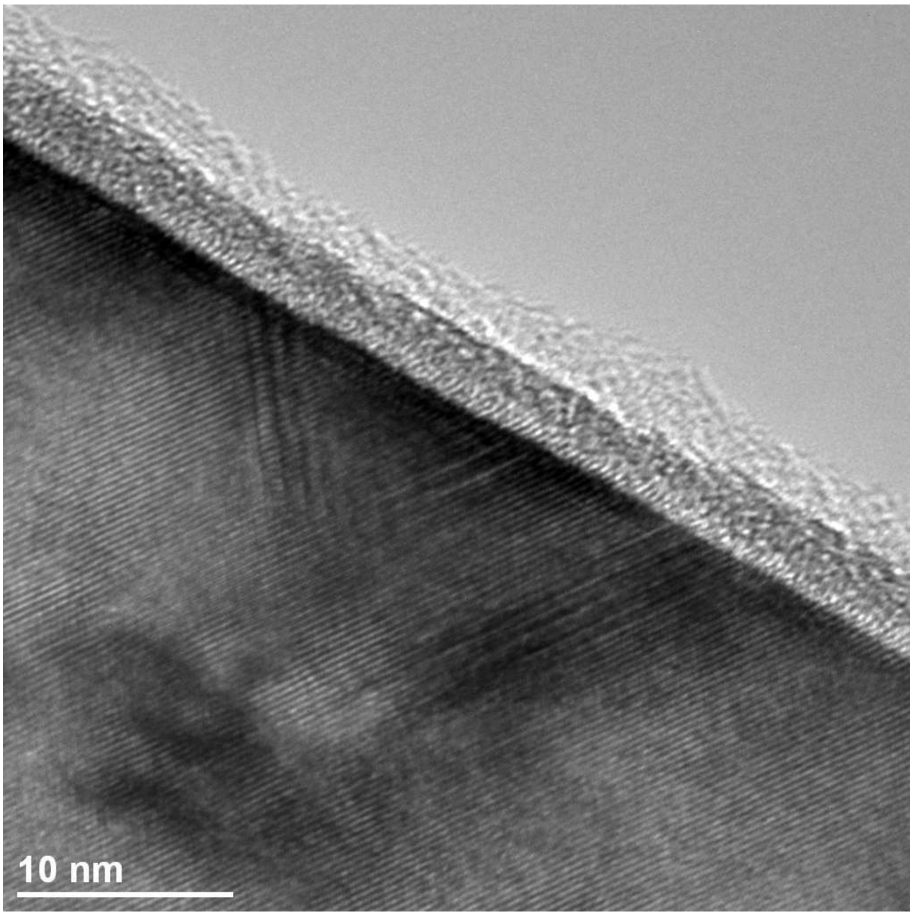

Figure V.17: High-resolution cross-section TEM image showing hairpin dislocations in a recrystallised SiGe 22% layer

After the nucleation of strain relieving defects, the SPER furthermore continues but the heteroepitaxial coherence is lost and the layer is recrystallising in a - at least - partially relaxed state. These results can directly be seen in Figure V.8, where the SiGe 32 and

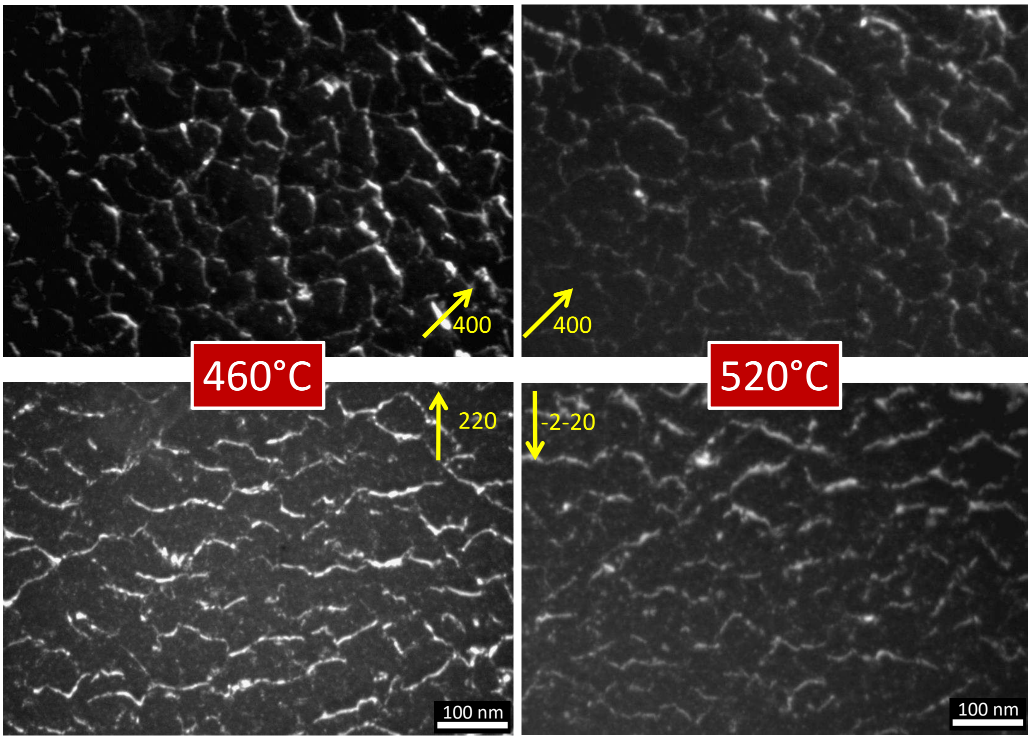

Figure V.18: Plan view TEM images for SiGe layers recrystallised at 460°C and 520°C. Diffraction g vectors are given

42% spectra are no longer centred at the strained peak but shift towards the relaxed peak. The more the layer germanium concentration, the more the spectrum will be shifted, indicating a greater relaxation. These results are coherent with [Chilton *et al.* 1989] and [Rodríguez *et al.* 1997] who also found that, for the same recrystallised thickness, the higher the germanium content there is in the layer, the higher the relaxation and the lower the critical thickness there are during SPER.

Similarly to the critical thickness on epitaxially grown SiGe layers, [Paine *et al.* 1990] derived an expression for the critical thickness during SPER by calculating the thickness above which it is energetically feasible to nucleate stacking faults at the α-c interface. The critical thicknesses derived from [Paine *et al.* 1990] for the layers used in this publication are gathered in Table V.3.

Ge content (%)	12	22	32	42
h_c (nm)	20	7	4	2

Table V.3: Critical thicknesses for the layers used in this work derived from [Paine *et al.* 1990] for the emergence of strain relaxation phenomenon during SPER

However, the critical thicknesses are inaccurate in this case, as the SiGe 12% layer shows no signs of relaxation as well as SiGe 22% layers are only partially relaxed. The derivation for [Paine *et al.* 1990] expression may have overlooked one parameter. As mentioned by [Cristiano *et al.* 1996], the hairpin dislocations are also a strain-relaxation related defect. The hairpins may be the first stages of a complete relaxation via the nucleation of misfit dislocations. During SPER, the hairpin dislocations can be related to the α-c interface roughness [Jones *et al.* 1988] and it is known to roughen during a strained SiGe layer SPER [Corni *et al.* 1996, D'Angelo *et al.* 2007]. Therefore, there could be a link between the roughness of the α-c interface and the anneal temperature.

4 MD simulations

In order to test the previous hypothesis, Molecular Dynamics simulations were carried out. Simulation cells with dimensions of $15a_0 \times 25a_0 \times 25a_0 \times$ containing 45450 atoms were created, where a_0 is the silicon lattice constant to simulate epitaxially grown SiGe on Si. Silicon atoms were randomly replaced by germanium ones to obtain a SiGe 40% alloy. The cells were partially amorphised using the method described in section 2.3. Anneal temperatures were {1600K, 1700K, 1800K, 1900K}. To assess the interface roughness, the method described in Figure II.10 is used.

The interface roughnesses are extracted after 3 nm recrystallisation from the cells seen in Figure V.20 and shown against the anneal temperature in Figure V.19. It is clear now that the temperature has a major role in the onset of hairpin dislocations. Indeed, at high temperature anneals, the interface is rough and thus nucleates more hairpin dislocations. At low temperature anneals, the interface is less rough hence less hairpin and subsequently less strain relaxation as it has been seen with the (224)RSMs.

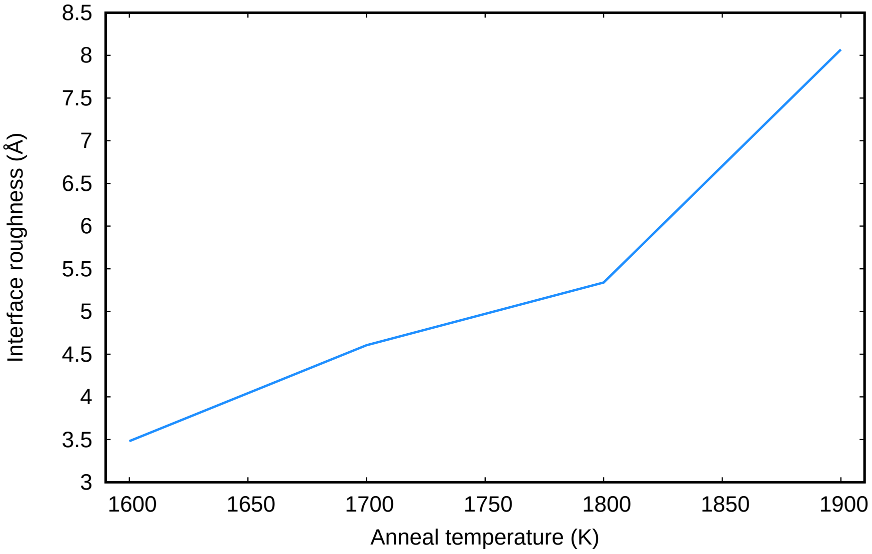

Figure V.19: α-c interface roughness from MD simulations after 3 nm recrystallisation of strained SiGe 40%

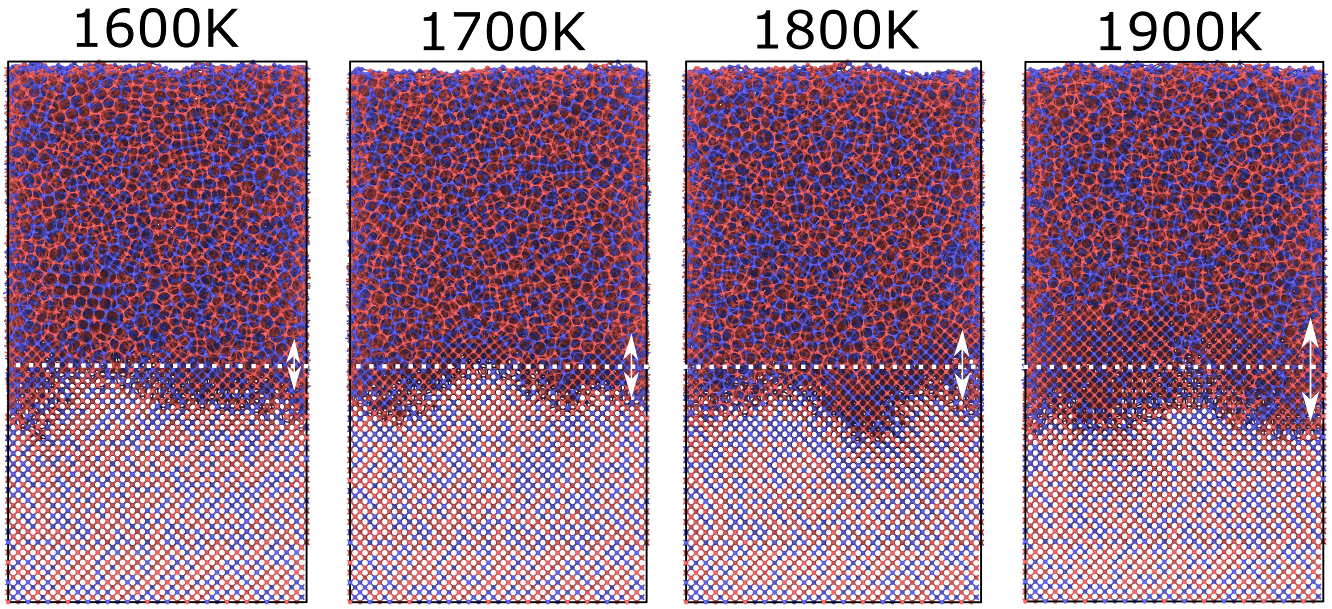

Figure V.20: <100> views of MD simulations after 3 nm recrystallisation of strained SiGe 40%. The extracted average α-c interface position and their standard deviations are shown

5 Summary

The SPER of 40 nm strained SiGe layers between 12 to 42% of germanium content has been investigated with experiments and MD simulations in this chapter. Experiments included (004) real time reciprocal space map (RSM), (224)RSM as well as TEM imaging. Real-time monitoring of SiGe SPER with X-ray diffraction (XRD) was enabled by synchrotron radiations. (004) RSMs hinted that some layers were partially relaxed after SPER. This is confirmed by (224)RSMs. The two XRD experimental results can be resumed as follows:

- 12% SiGe layers exhibited no strain relaxation.
- 32% and 42% SiGe layers showed clear strain relaxation as their diffraction spectra show two clear peaks, for a strained and a relaxed peak.
- 22% SiGe layers revealed a partial strain relaxation. 22% seems to be the upper limit of germanium concentration for a 40 nm layer.
- 22% SiGe layers furthermore exposed a difference between low temperature anneal and high temperature anneal where the strain is more conserved after a low temperature anneal.
- As real-time experiments were done, the SiGe layer thickness could be plotted over time. The thickness behaviours near the free surface show also a clear difference between low and high temperature anneals. This behaviour is hypothesised to be linked to the interface roughness.

Following XRD experiments, TEM images where done on 22% SiGe recrystallised layers that have seen different temperature anneals. TEM images revealed that none of the layers are completely relaxed due to the absence of threading dislocations. However, hairpin dislocations were seen in both layers. The hairpin dislocation is a minor strain relaxation defect. Their presence explain thus the partial relaxation of the layers seen in (224)RSMs. Furthermore, hairpin dislocations are linked to the interface roughness, linking the anneal temperature with the partial relaxation.
Using MD simulations on SiGe 40% layers, the surface roughness of the interface after a 3 nm recrystallisation is shown to be different regarding the anneal temperature. The higher the temperature is, the rougher the interface will be. These simulations confirm the link between anneal temperature and surface roughness.
The fact that the anneal temperature is related to the interface roughness and ultimately the strain relaxation could be technologically relevant and trigger investigations on junction fabrication using SPER with ultra low thermal budget. The work presented in this chapter could be enhanced with quantitative investigations on the strain relaxation during SPER.

6 French summary — Résumé

Les alliage silicium-germanium contraints sont utilisés dans les dispositifs avancés, du fait de leurs meilleures performances par rapport au silicium pur. La SPER de couches d'alliages SiGe contraints est investiguée dans ce chapitre par diffraction à rayons-X (XRD). La XRD permet entre autre d'obtenir la taille de la couche de SiGe cristalline mais nécessite un temps d'acquisition trop long par rapport au temps de recristallisation des couches étudiées. Ce problème d'acquisition est levé lorsqu'une source très brillante de rayons-X est utilisée. Des expériences de suivi en temps réel de la recristallisation des couches ont été réalisées à l'ESRF, *European Synchrotron Radiation Facility*, qui permet l'accès à une source de rayons-X très brillante et permet ainsi de réaliser des diffractions en quelques secondes.

Différentes couches de SiGe avec 12%, 22%, 32%, 42% de germanium ont été étudiées avec des différentes températures de recuit pour chaque couche. Les budgets thermiques sont visibles au tableau V.1. Les couches ont toutes été épitaxiées sur silicium afin d'obtenir 40 nm d'alliage contraint. Deux types de diffractions ont été faites. Premièrement, des cartographies de l'espace réciproque (RSM) selon l'orientation (004) permettent d'obtenir la distance inter-plan atomique normale au plan de recristallisation, ainsi que la taille de la couche cristalline. Cependant des RSMs selon l'orientation (004) ne permettent pas de conclure sur une éventuelle relaxation de la contrainte. Des mesures de diffraction après recristallisation ont été effectuées dans un second temps selon l'orientation (224) permettant ainsi de statuer sur une éventuelle relaxation.

Les RSMs selon l'orientation (004) ont permis l'accès aux courbes $\theta - 2\theta$ des couches recristallisées à la fin d'un recuit avec le budget thermique le plus haut. Ces courbes sont visibles à la Figure V.8. Sur ce graphe sont annotées les positions théoriques des pics de diffraction des couches contraintes et relaxées pour chaque concentration de germanium étudiée. De ce graphe, il parait clair que la couche SiGe 12% a recristallisé parfaitement, du fait de la présence de nombreux pics de diffraction secondaires. À l'inverse, les couches 32%, 42% semblent fortement dégradées du fait qu'il n'y ait pas un unique pic de diffraction mais deux et que ces deux pics soient centrés sur les positions contrainte et relaxée. Le fait qu'il y ait deux pics sur deux positions différentes est surement dû à une relaxation de la contrainte. Enfin, la couche SiGe 22% semble être à un point médian, où la relaxation de la contrainte commence à apparaitre.

Cette relaxation de la contrainte est visible sur la Figure V.9, qui montre côte-à-côte des cartes de l'espace réciproque des couches SiGe 22% et 42% citées dans le paragraphe précédent. Avec ces cartes, il est bien visible que la couche 42% a fortement perdu sa contrainte, la tache de diffraction autour du point relaxé étant majoritaire. Dans la couche SiGe 22%, la forme triangulaire autour du point contraint dénote une certaine mosaïcité de la relaxation dans la couche recristallisée.

Du fait que les RMSs en temps-réel issues des expériences menées à l'ESRF permettent aussi de suivre l'évolution de la taille de la couche SiGe en fonction du temps, dans le cas où la relaxation n'est pas trop importante. Ainsi, cette évolution n'a pas pu être suivie sur les couches 32%, 42%. Les Figure V.10 et Figure V.11 montrent cette évolution. Comme attendu, plus la température est élevée, plus la couche recristallise rapidement. Cependant, un autre phénomène apparait, et semble être lié à la température. En effet à forte température de recuit, la recristallisation semble ralentir lorsque l'interface est proche de la surface libre (40 nm). Ce phénomène est clairement visible dans la couche SiGe 22%. Ce ralentissement pourrait trahir la présence d'une rugosité d'interface importante lors de la SPER. Du fait de la rugosité, certaines parties de l'interface amorphe-cristal atteignent la surface libre et d'autres non, ce qui conduit à la création de plans {111} qui sont vingt fois plus lents à recristalliser. Ce phénomène est schématisé à la Figure V.12.

Continuant avec la température de recuit, elle semble aussi jouer un rôle dans la relaxation. Figure V.14 et Figure V.15 montrent des RSMs selon l'orientation (224) de couches SiGe 22% entièrement recristallisées avec deux températures de recuit différentes : 460°C et 540°C. Il y a une subtile différence de relaxation entre les deux échantillons. En effet, la tâche de diffraction de la couche de SiGe est plus centrée sur sa position contrainte théorique dans le cas 460°C, alors qu'à l'inverse, à forte température, la tâche s'est plus déplacée vers la position théorique relaxée.

Pour confirmer visuellement l'état de relaxation, des images TEM ont été effectuées. Les images TEM en coupe transverse, voir Figure V.16, ne montrent aucune relaxation complète sur aucune des deux couches par des boucles de dislocations. En haute résolution, voir Figure V.17, des dislocations en épingle — *hairpin dislocation* — apparaissent. Ces dislocations sont des défauts liés à une relaxation locale de la contrainte [Cristiano *et al.* 1996]. C'est donc la présence de *hairpins* qui relaxent partiellement la contrainte. De plus, ces dislocations ont été reliées à la rugosité de l'interface amorphe-cristal auparavant [Jones *et al.* 1988]. Ainsi, un lien est créé entre la température de recuit et la relaxation. Lorsque la température de recuit est élevée, l'interface est rugueuse, ce qui favorise l'apparition de *hairpins* qui vont relaxer la contrainte. Dans le cas d'une faible température de recuit, la rugosité d'interface et donc la contrainte est moins forte.

Des simulations en dynamique moléculaire ont été effectuées afin de confirmer le lien entre la rugosité de l'interface et la température de recuit. La dimension des cellules de simulation était de $15a_0 \times 25a_0 \times 25a_0 \times$ où a_0 est le paramètre de maille du silicium afin de simuler un alliage épitaxié sur silicium. Les atomes de silicum ont été aléatoirement remplacés par des atomes de germanium afin de créer un alliage SiGe de 40%. La rugosité d'interface après 3 nm de recristallisation avec différentes températures de recuit a été extraite des simulations. Pour cela, la cellule est divisée en sous-cellules et la position de l'interface est extraite dans chaque sous-celleule. La rugosité est considérée comme l'écart-type de toutes les positions extraites. Le schéma à la Figure II.10 montre ce procédé. La Figure V.19 montre bien un lien direct entre la température de recuit et la rugosité de l'interface amorphe-cristal lors de la SPER d'alliages SiGe contraints.

Le fait que des couches SiGe contraintes ne peuvent pas être recristallisées sans défaut est connu de la littérature. Il existe en effet un taille maximale de couche recristallisée avant que celle-ci ne se relaxe plastiquement via l'apparition de défauts étendus, tels que des dislocations. Cette taille maximale, *critical thickness* en anglais, a été déduite théoriquement par [Paine *et al.* 1990]. Pour les concentrations étudiées dans ce chapitre, le tableau V.3 donne les tailles critiques issues des travaux de [Paine *et al.* 1990]. Ces tailles semblent être erronées du fait que la couche de 40 nm de SiGe 12% recristallisée durant ces travaux ne présente pas de relaxation majeure. Les calculs de [Paine *et al.* 1990] ne prennent pas en compte l'apparition de dislocations *hairpin* du fait de la rugosité de l'interface. Or ces défauts pourraient relaxer suffisament la couche contrainte pour que des défauts majeurs tels que des boucles de dislocations n'apparaissent pas sur des alliages avec de faibles concentrations de germanium.

En conclusion, la SPER d'alliages de SiGe contraint a été étudiée dans ce chapitre. La contrainte peut être gardée dans le cas de faibles concentrations de germanium alors qu'elle est perdue par relaxation plastique dans des alliages ayant une forte concentration en germanium. Au point médian, la couche se relaxe partiellement via l'apparition de dislocations *hairpins*. Ces dislocations — et donc la relaxation de la couche — peuvent être liées à la température de recuit, qui favorise une interface amorphe-cristal rugueuse.

Chapter VI

Summary and further work directions

Contents

In this manuscript, the solid phase epitaxial regrowth (SPER) of silicon, germanium and silicon-germanium alloys has been explored with the help of Kinetic Monte Carlo (KMC) and Molecular Dynamics (MD) simulations. The SPER is used in advanced nodes for junction fabrication as it can yield highly doped region with a relatively low thermal budget. The fact that the SPER can be used with a low thermal budget is technologically relevant for the CoolCube$^{\mathrm{TM}}$ integration [Batude *et al.* 2015] where two transistors are sequentially processed one on top of another. The fabrication of the top transistor include a SPER process. This chapter will succinctly presents the work carried out in this work in order to understand the SPER mechanism in several cases, from the most generic — pure elements — to the closest from technological processes — strained SiGe SPER.

1 Summary

1.1 Silicon or germanium SPER

Prior to this work, a KMC simulator named MMonCa was able to take into account several dependencies of the silicon SPER rate. The substrate orientation, strain and — up to a certain concentration — dopant concentration dependencies were handled in MMonCa. chapter II presented the handling of the substrate orientation dependence in the Lattice KMC in MMonCa. The SPER model is based of the assumption that the SPER is localised at the amorphous-crystalline interface and a unique SPER reaction is initiated by a breaking a bond and is recrystallising a six-fold ring. From this assumption rises three microscopic configurations {100}, {110} and {111}, depending on how many atoms have to be recrystallised to form a crystalline six-fold ring. A recrystallisation probability is appended to each microscopic configuration. The probabilities follow an Arrhenius law, with the same activation energy but different prefactors. The model took also into account the fact that {111} configurations can recrystallise into a defect, called the twin defect. LKMC simulations were carried out on silicon and germanium substrate and show close agreement with available experimental data.

In a second part, chapter II held an investigation on the SPER rate dependence of the substrate orientation with MD simulations. In the literature, the Tersoff potential within its third parametrisation has been chosen to be the most suitable empirical potential to be used to simulate the SPER [Krzeminski *et al.* 2007]. However, the substrate orientation dependence was never achieved in MD simulations. This work focused on the cell size and anneal temperature in order to understand the absence of the dependence.
Firstly, the simulated cell size has an important role, as twin defects tend to appear during the MD simulations. The twin defect seems to have a local effect that increases locally the SPER rate. However, when the cell is too small, this local effect is applied on the whole cell, giving a increased SPER rate. Secondly, the anneal temperature can be directly linked to the onset of twin defects and crystallites in the amorphous phase during the MD simulations. Lowering the anneal temperature can also decrease the SPER rate. However, this greatly impacts the computational cost. Finally, to prove the two previous points, a single simulation has been carried out on a large cell at low anneal temperature during a long simulated time. This simulation nearly gave a ratio of 1:10 between <111> and <100> SPER rates, far better that the ones achieved in the literature data.

Chapter III focused on the peculiar case of the silicon SPER with presence of boron. As mentioned before, the previous LKMC model in MMonCa could handle the presence of doping impurities. However, there was no limiting process and the SPER rate increase was exponential against the boron concentration. However, at high boron concentration, the SPER rate has been experimentally seen to be at a maximum of 25 times the intrinsic SPER rate. To understand and model the mechanism behind this maximum, the SPER rate has been refined in several ways.
First, the point and defect reactions in amorphous and crystalline silicon has been taken into account. The boron atoms can indeed diffuse as well as agglomerate into clusters in both phases. This latter reaction, boron clustering, clearly hinders the SPER rate acceleration. Second, the newly formed clusters are known to be stable at the amorphous-crystalline interface, meaning that a cluster formed in the amorphous phase will be transferred into the crystalline phase upon recrystallisation. As the SPER model focuses on

breaking a bond at the amorphous-crystalline interface, the role of a stable defect at the interface had to be taken into account. As the cluster is considered stable at the interface, no bonds will be broken its vicinity. This forces the interface to move around the stable defect and creating along the way slower {111} planes. This is this onset of {111} planes that ultimately slows the SPER rate increase at high boron concentration.

1.2 Silicon-germanium SPER

The silicon-germanium (SiGe) alloy is used in the advanced junction formation processes as they offer a way to increase the junction performance. However, the SPER of SiGe alloys has been less studied than the SPER of pure elements.

The relaxed SiGe alloys SPER has been investigated in chapter IV. The SPER rate increase exponentially versus the germanium content of the alloy. However, the activation energy is not linear and possesses a maximum around 40% of germanium. This behaviour was not understood nor atomistically explained. The LKMC model focuses on the amorphous-crystalline interface and its bonds. In the case of SiGe alloys, a third bond — Si-Ge — appears. To follow the KMC formalism, the break of a SiGe bond must have an activation energy. This energy, when calibrated against experimental data is 2.86 eV, is higher than either the one to break a Si-Si bond (2.70 eV) or the Ge-Ge bond (2.17 eV). The LKMC model can thus explains why there is a maximum in the extracted activation energy in SiGe alloy by introducing this third energy. MD simulations have also been carried out to be compared to the results of the LKMC model. These simulations showed close agreement with the LKMC model.

The newly LKMC model has been used to draw hypotheses on SPER rates of SiGe alloys on other substrate orientations. The introduction of a third energy reaction at the interface brought a certain anisotropy to the interface, promoting certain sites to be recrystallised and not others. This anisotropy brings a inherent roughness to the SiGe SPER. Moreover, the anisotropy is stronger between reaction with high difference in their activation energies, especially in germanium rich SiGe alloys. This brings the <100> SPER rate close to the <110> one, and overall heavily change the ratios between SPER rates along the germanium spectrum.

Closer to technologically relevant process, the SPER of 40 nm strained SiGe alloys has been investigated in the chapter V with HR-XRD and TEM images. The layers exhibit strain relaxation depending on the germanium content: the higher, the more strain relaxation there is after SPER. However, the strain is kept on low germanium concentration. The layers with 22% of germanium revealed the beginning of the strain relaxation via the onset of hairpin dislocations. The strain relaxation is moreover linked to the anneal temperature. At the same level of recrystallisation, the same layer is more relaxed after a high temperature anneal than after a low temperature anneal. The link between temperature and strain relaxation was found to be the amorphous-crystalline interface. High temperature anneal creates a rough interface that promotes hairpin dislocation onset. Further MD simulations confirm this link between anneal temperature and interface roughness.

2 Directions for future work

Various aspects of the SPER reaction have been investigated during this PhD with the help of both KMC and MD simulation techniques. The KMC approach to atomistic simulations can be used to simulate a whole transistor processing, compared to MD or first principle methods. However, the principal issue with the KMC approach is that the events must correspond to actual atomistic phenomena, and most of them are still not clearly understood nor modelled. A perfect example would be the redistribution of certain dopants during the recrystallisation. As a consequence, further investigations of the microscopic mechanisms behind such phenomenon could be done. More precisely, the identification of mechanisms and extraction of energy barriers thanks to MD and first principle simulations seem necessary.

On the subject of MD simulations, it could be relevant to test the conclusions found in chapter II with other potentials. Finding simulation parameters that yield the correct ratios between SPER rates on silicon and germanium could be also relevant. Indeed, knowing that the SPER rates are correctly simulated for all substrate orientations on pure elements could trigger investigations on SiGe alloys and subsequent results could be incorporated in the KMC model where the prefactors for {110} and {111} rates in SiGe alloys are for now guesses.

Furthermore, the SPER of strained SiGe alloys with a KMC approach has not been mentioned in this PhD. As seen in the last chapter, the SPER involves numerous parameters. The handling of an atomistic strain and relaxation should be the key to a KMC model. Finally, to be as close as possible to junction fabrication processes, the effect of doping impurities during a strained SiGe SPER should be taken into account. This could be done by first investigating the dopant effect in relaxed SiGe alloy then with in presence of strain. A combination of first principle, MD and KMC simulations seems to be necessary. Finally, the investigation of *in-situ* doped epitaxy sources and drains would be technologically relevant, as this type of junction formation is also used in advanced CMOS devices. The *in-situ* doped epitaxy shares similarities with SPER such as segregation and clustering at the free surface, limited activation after junction formation and facets formation during the reaction. Such phenomena could be also included into the LKMC model.

Appendices

APPENDIX A

Formation energies for Boron-Interstitial complexes in silicon crystal

Defect	Energy (eV)
BI2	0.42
B2	-0.26
B2I	-0.384
B2I2	-0.652
B2I3	0.32
B3	-3.56
B3I	-1.9
B3I2	-2.1
B3I3	-1.54
BI3	6
BI4	8.1
BI5	10.2
BI6	12.3
BI7	14.3
BI8	16.3
BI9	18.3
B2I4	6.6
B2I5	9
B2I6	11.5
B2I7	14
B2I8	16.5
B2I9	19
B3I4	2.2
B3I5	4.4
B3I6	7.1
B3I7	10.3
B3I8	13.6
B3I9	16.8
B4	-0.7
B4I	-2
B4I2	-1.9
B4I3	-1.1
B4I4	0
B4I5	1.5
B4I6	3.6
B4I7	6.4
B4I8	9.8
B4I9	13.5
B5	-2.2
B5I	-1.6
B5I2	0.6
B5I3	0.2
B5I4	-0.6
B5I5	0
B5I6	1.6
B5I7	4
B5I8	7.4
B5I9	10.8
B6	-2.8
B6I	-3.4
B6I2	-2
B6I3	0.3
B6I4	-0.5
B6I5	-1
B6I6	-0.7
B6I7	2.2
B6I8	5.4
B6I9	8.8
B7	-3.6
B7I	-4.1
B7I2	-3
B7I3	-2.5
B7I4	-0.4
B7I5	-1.2
B7I6	-1.3
B7I7	-0.9
B7I8	2.2
B7I9	5.4
B8	-4.6
B8I	-5.1
B8I2	-4.8
B8I3	-3.6
B8I4	-2.7
B8I5	-1.6
B8I6	-2.4
B8I7	-1.5
B8I8	0.1
B8I9	3.3

Table A.1: Formation energies for Boron-Interstitial complexes in crystalline silicon

Appendix B

ESRF data analysis workflow

Raw 2D data from the Maxipic 2D-sensor have been converted into regular $\theta - 2\theta$ spectra by the following workflow.

First, the raw data from ESRF experiments are snapshots from the Maxipix sensor and the SPEC file. The snapshots are the photon counts on each pixel of the sensor. An example can be found at Figure B.1. Are visible also the ares where there are no pixels, hence the drop to zero in intensity seen in Figure V.8. The SPEC file contains all data related to each snapshot: position and rotation of each motor, time, oven temperature.

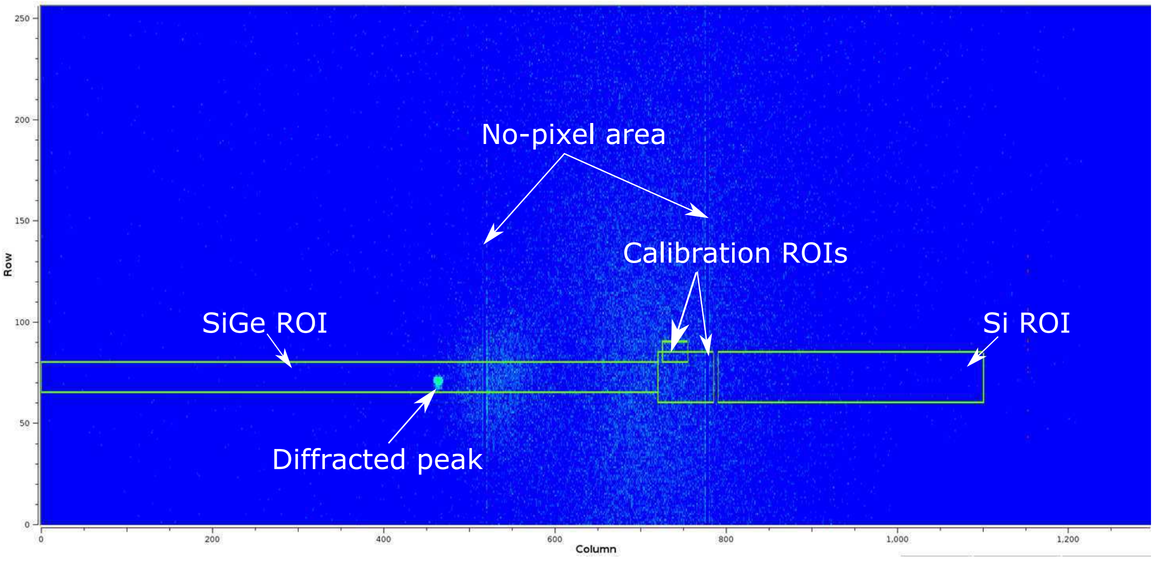

Figure B.1: A single snapshot of the Maxipix 2D sensor. Regions of interest and the diffracted peak are shown

To avoid noise during extractions, regions of interest (ROI) are created. The extraction will therefore only focus on these regions. Preceding the experiment, the direct beam from the X-ray source is calibrated in order to have the diffracted peaks always inside the ROIs. To emulate a linear detector instead of a 2D-detector, the intensities are integrated along the columns of the ROIs.

A regular $\theta - 2\theta$ spectrum — or a (004)RSM — is the accumulation of numerous snapshots, as a snapshot represents a unique angle. In a laboratory, one take of a snapshot can be as long as several minutes. However, thanks to the high brilliance of a synchrotron radiation, the snapshots done during this experiment are done in 0.3 s, giving a full spectrum in less than a minute, allowing the real-time monitoring of the SPER. Using X-ray utilities Python library [Kriegner *et al.* 2013], all the snapshots are concatenated, thus creating a (004)RSM for a unique time, considered as the average of all the snapshot time. The resulting RSM can be seen at Figure B.2.

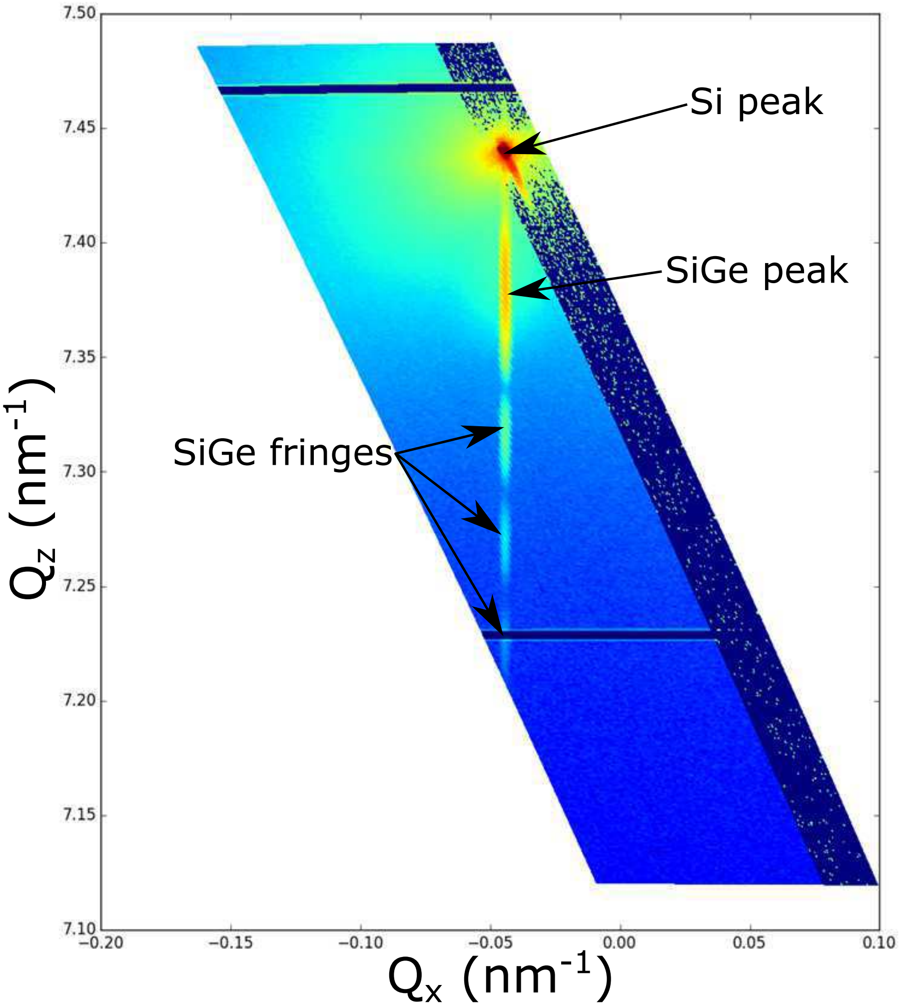

Figure B.2: (004)RSM resulting of a concatenation of transformation into reciprocal space of numerous snapshots during a XRD experiment

However, the previous RSM is not plotted in a cartesian grid but in the reciprocal space grid. The diffraction peaks and fringes are therefore striated as it can be seen in Figure B.3 `a)`. As the $\theta - 2\theta$ spectrum is taken from a Q_z cut, striated fringes and peaks are not wanted. Using in pipeline the `Gridder2D` and the `griddata` from X-ray utilities and Matplotlib respectively, the RSM is interpolated into a cartesian grid. The interpolated RSM is shown at Figure B.4.

After the interpolation, the silicon peak position is extracted, and the RSM is shifted to have the Si peak at $Q_x = 0.0$. Finally, a Q_z cut along $Q_x = 0.0$ yield the wanted $\theta - 2\theta$ spectrum. The process is summarised into the schematic in Figure B.5.

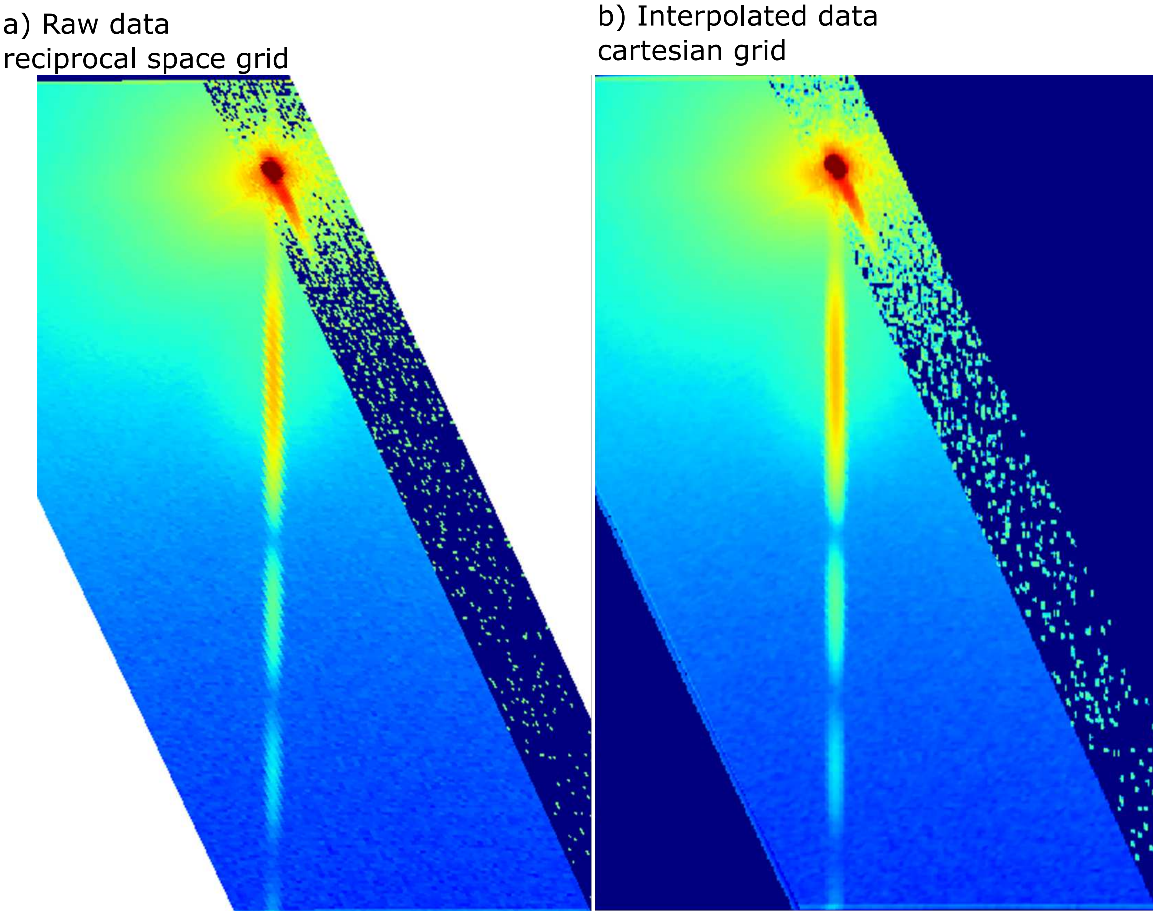

Figure B.3: Zoomed image of (004)RSMs before and after interpolation on a cartesian grid

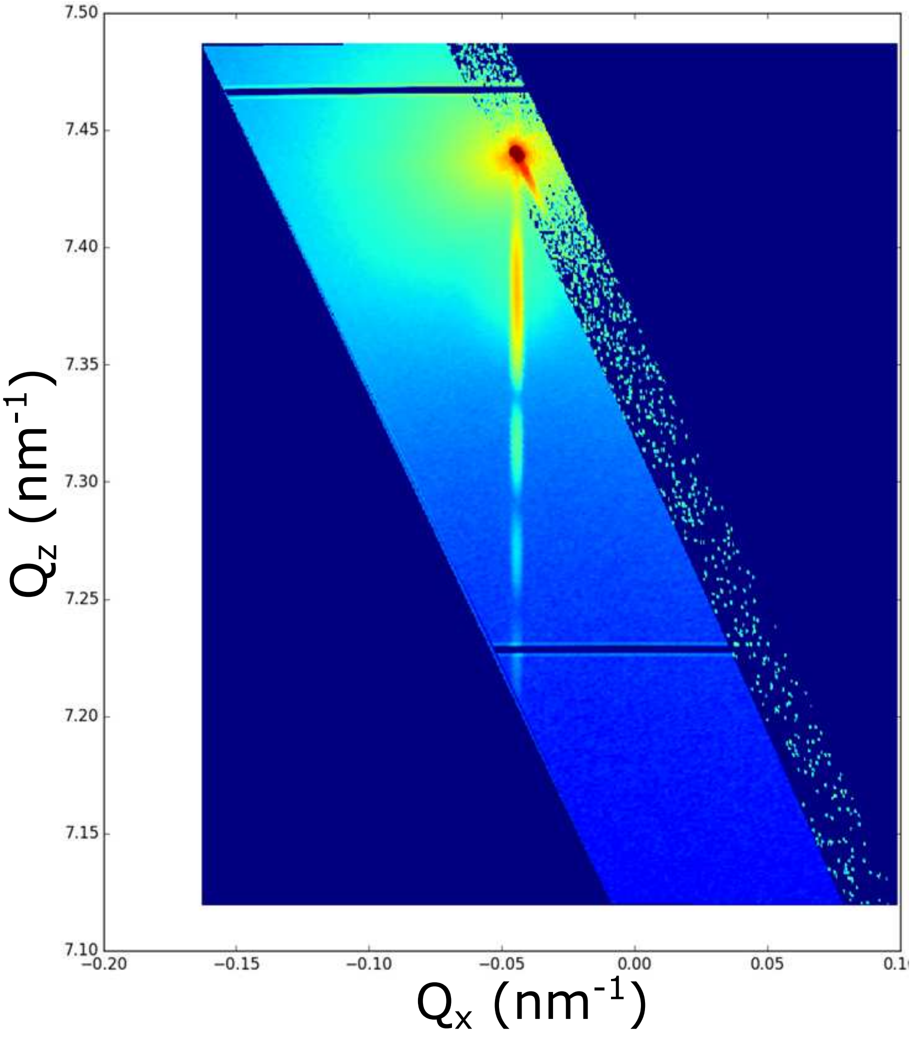

Figure B.4: Interpolated (004)RSM

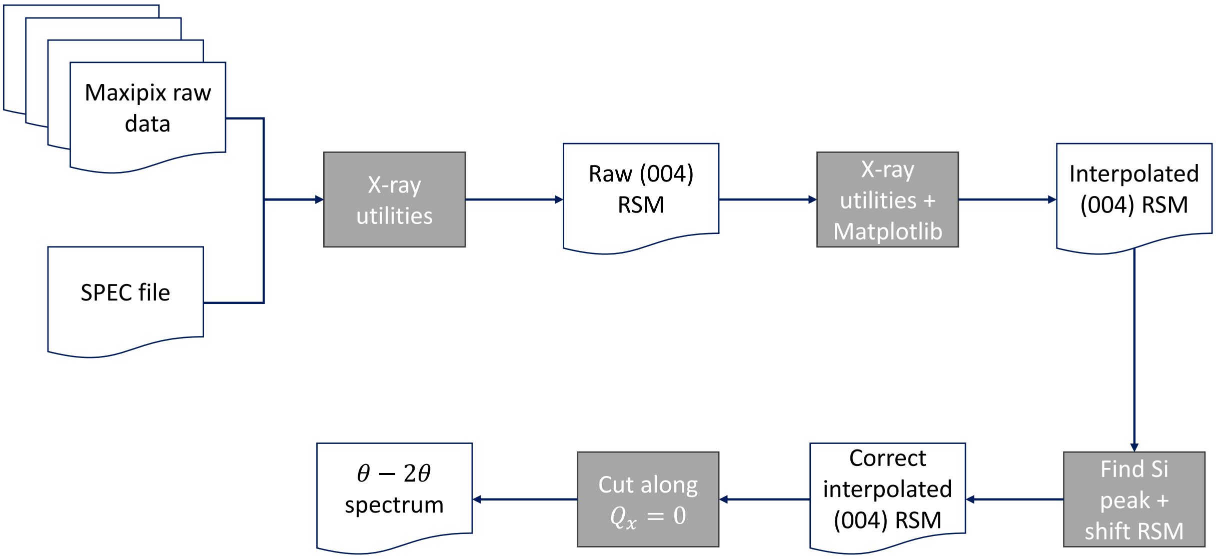

Figure B.5: Workflow of the analysis for the ESRF experiment data

Appendix C

List of communications

Journals

- Payet, A., Luce, F. P., Curfs, C., Mathieu, B., Sklénard, B., Barbé, J. C., ... & Guissi, S. (2016). Damage accumulation during cryogenic and room temperature implantations in strained SiGe alloys. Materials Science in Semiconductor Processing, 42, 247-250. doi: 10.1016/j.mssp.2015.07.059

- Payet, A., Sklenard, B., Barbe, J. C., Batude, P., Tavernier, C., Gergaud, P., & Martin-Bragado, I. (2016). An atomistic investigation of the composition dependence in SiGe alloys during Solid Phase Epitaxial Regrowth. Acta Materialia, 106, 290-294. doi: 10.1016/j.actamat.2016.01.022.

- Bonnevialle, A., Reboh, S., Le Royer, C., Morand, Y., Hartmann, J.-M., Rouchon, D., Pedini, J.-M., Tabone, C., Rambal, N., Payet, A., Plantier, C., Boeuf, F., Haond, M., Claverie, A. and Vinet, M. (2016), On the use of a localized STRASS technique to obtain highly tensile strained Si regions in advanced FDSOI CMOS devices. Phys. Status Solidi C. doi: 10.1002/pssc.201600028

Conferences

- Payet, A., Sklénard, B., Barbé, J. C., Batude, P., Licitra, C., Papon, A. M., ... & Martin-Bragado, I. (2016, September). Atomistic predictions of substrate orientation impact during SiGe alloys solid phase epitaxial regrowth. In Simulation of Semiconductor Processes and Devices (SISPAD), 2016 International Conference on (pp. 31-34). IEEE. doi: 10.1109/SISPAD.2016.7605141

- Pasini, L., Batude, P., Lacord, J., Casse, M., Mathieu, B., Sklenard, B., ... & Besson, P. (2016, June). High performance CMOS FDSOI devices activated at low temperature. In VLSI Technology, 2016 IEEE Symposium on (pp. 1-2). IEEE. doi: 10.1109/VLSIT.2016.7573407

Bibliography

[Aboy *et al.* 2011] Maria Aboy, Lourdes Pelaz, Elena Bruno, Salvo Mirabella and Simona Boninelli. *Kinetics of large B clusters in crystalline and preamorphized silicon.* Journal of Applied Physics, vol. 110, no. 7, 2011, doi: 10.1063/1.3639280. (Cited on pages 60 and 63.)

[Alder & Wainwright 1959] B. J. Alder and T. E. Wainwright. *Studies in Molecular Dynamics. I. General Method.* The Journal of Chemical Physics, vol. 31, no. 2, pages 459–466, 1959, doi: 10.1063/1.1730376. (Cited on page 22.)

[Alex *et al.* 1996] V. Alex, S. Finkbeiner and J. Weber. *Temperature dependence of the indirect energy gap in crystalline silicon.* Journal of Applied Physics, vol. 79, no. 9, pages 6943–6946, 1996, doi: 10.1063/1.362447. (Cited on page 66.)

[Arrhenius 1889] Svante Arrhenius. *On the reaction velocity of the inversion of cane sugar by acids.* J. Phys. Chem, vol. 4, page 226, 1889. (Cited on page 16.)

[Atkins 2009] Julio Atkins Peter ; de Paula. Physical chemistry. W. H. Freeman; 9th edition, 2009. ISBN-13: 978-1429218122 ISBN-10: 1429218126. (Cited on page 15.)

[Aziz *et al.* 1991] Michael J. Aziz, Paul C. Sabin and Guo-Quan Lu. *The activation strain tensor: Nonhydrostatic stress effects on crystal-growth kinetics.* Phys. Rev. B, vol. 44, pages 9812–9816, Nov 1991, doi: 10.1103/PhysRevB.44.9812. (Cited on page 18.)

[Aziz 1992] MichaelJ. Aziz. *The Mechanism of Solid Phase Epitaxy.* In S. Coffa, F. Priolo, E. Rimini and J.M. Poate, editors, Crucial Issues in Semiconductor Materials and Processing Technologies, volume 222 of *NATO ASI Series*, pages 465–476. Springer Netherlands, 1992, doi: 10.1007/978-94-011-2714-1“˙47. (Cited on pages 17, 55 and 85.)

[Barvosa-Carter *et al.* 2004] William Barvosa-Carter, Michael J. Aziz, A.-V. Phan, T. Kaplan and L. J. Gray. *Interfacial roughening during solid phase epitaxy: Interaction of dopant, stress, and anisotropy effects.* Journal of Applied Physics, vol. 96, no. 10, pages 5462–5468, 2004, doi: 10.1063/1.1790580. (Cited on pages 71, 77, 89 and 97.)

[Batude *et al.* 2011a] P. Batude, M. Vinet, B. Previtali, C. Tabone, C. Xu, J. Mazurier, O. Weber, F. Andrieu, L. Tosti, L. Brevard, B. Sklenard, P. Coudrain, S. Bobba, H. Ben Jamaa, P. E. Gaillardon, A. Pouydebasque, O. Thomas, C. Le Royer,

J. M. Hartmann, L. Sanchez, L. Baud, V. Carron, L. Clavelier, G. De Micheli, S. Deleonibus, O. Faynot and T. Poiroux. *Advances, challenges and opportunities in 3D CMOS sequential integration.* In 2011 International Electron Devices Meeting, pages 7.3.1–7.3.4, Dec 2011, doi: 10.1109/IEDM.2011.6131506. (Cited on page 4.)

[Batude *et al.* 2011b] P. Batude, M. Vinet, C. Xu, B. Previtali, C. Tabone, C. Le Royer, L. Sanchez, L. Baud, L. Brunet, A. Toffoli, F. Allain, D. Lafond, F. Aussenac, O. Thomas, T. Poiroux and O. Faynot. *Demonstration of low temperature 3D sequential FDSOI integration down to 50 nm gate length.* In VLSI Technology (VLSIT), 2011 Symposium on, pages 158–159, June 2011. (Cited on page 4.)

[Batude *et al.* 2013] P Batude, B Sklenard, C Xu, B Previtali, B De Salvo and M Vinet. *Low temperature FDSOI devices, a key enabling technology for 3D sequential integration.* In 2013 International Symposium on VLSI Technology, Systems and Application (VLSI-TSA), 2013. (Cited on page 4.)

[Batude *et al.* 2015] P. Batude, C. Fenouillet-Beranger, L. Pasini, V. Lu, F. Deprat, L. Brunet, B. Sklenard, F. Piegas-Luce, M. Cassé, B. Mathieu, O. Billoint, G. Cibrario, O. Turkyilmaz, H. Sarhan, S. Thuries, L. Hutin, S. Sollier, J. Widiez, L. Hortemel, C. Tabone, M. P. Samson, B. Previtali, N. Rambal, F. Ponthenier, J. Mazurier, R. Beneyton, M. Bidaud, E. Josse, E. Petitprez, O. Rozeau, M. Rivoire, C. Euvard-Colnat, A. Seignard, F. Fournel, L. Benaissa, P. Coudrain, P. Leduc, J. M. Hartmann, P. Besson, S. Kerdiles, C. Bout, F. Nemouchi, A. Royer, C. Agraffeil, G. Ghibaudo, T. Signamarcheix, M. Haond, F. Clermidy, O. Faynot and M. Vinet. *3DVLSI with CoolCube process: An alternative path to scaling.* In 2015 Symposium on VLSI Technology (VLSI Technology), pages T48–T49, June 2015, doi: 10.1109/VLSIT.2015.7223698. (Cited on pages vii, 5, 6 and 121.)

[Bazant & Kaxiras 1996] Martin Z. Bazant and Efthimios Kaxiras. *Modeling of Covalent Bonding in Solids by Inversion of Cohesive Energy Curves.* Phys. Rev. Lett., vol. 77, pages 4370–4373, Nov 1996, doi: 10.1103/PhysRevLett.77.4370. (Cited on page 22.)

[Bazant *et al.* 1997] Martin Z. Bazant, Efthimios Kaxiras and J. F. Justo. *Environment-dependent interatomic potential for bulk silicon.* Phys. Rev. B, vol. 56, pages 8542–8552, Oct 1997, doi: 10.1103/PhysRevB.56.8542. (Cited on page 22.)

[Bernstein *et al.* 2000] Noam Bernstein, Michael J. Aziz and Efthimios Kaxiras. *Atomistic simulations of solid-phase epitaxial growth in silicon.* Phys. Rev. B, vol. 61, pages 6696–6700, Mar 2000, doi: 10.1103/PhysRevB.61.6696. (Cited on pages 35 and 39.)

[Biswas *et al.* 1987] R. Biswas, Gary S. Grest and C. M. Soukoulis. *Generation of amorphous-silicon structures with use of molecular-dynamics simulations.* Phys. Rev. B, vol. 36, pages 7437–7441, Nov 1987, doi: 10.1103/PhysRevB.36.7437. (Cited on page 38.)

[Bortz *et al.* 1975] A.B. Bortz, M.H. Kalos and J.L. Lebowitz. *A new algorithm for Monte Carlo simulation of Ising spin systems.* Journal of Computational Physics, vol. 17, no. 1, pages 10 – 18, 1975, doi: 10.1016/0021-9991(75)90060-1. (Cited on pages viii, 24 and 25.)

[Brodsky & Title 1969] M. H. Brodsky and R. S. Title. *Electron Spin Resonance in Amorphous Silicon, Germanium, and Silicon Carbide.* Phys. Rev. Lett., vol. 23, pages 581–585, Sep 1969, doi: 10.1103/PhysRevLett.23.581. (Cited on page 13.)

[Brunet *et al.* 2016] L. Brunet, P. Batude, C. Fenouillet-Beranger, P. Besombes, L. Hortemel, F. Ponthenier, B. Previtali, C. Tabone, A. Royer, C. Agraffeil, C. Euvrard-Colnat, A. Seignard, C. Morales, F. Fournel, L. Benaissa, T. Signamarcheix, P. Besson, M. Jourdan, R. Kachtouli, V. Benevent, J. M. Hartmann, C. Comboroure, N. Allouti, N. Posseme, C. Vizioz, C. Arvet, S. Barnola, S. Kerdiles, L. Baud, L. Pasini, C. M. V. Lu, F. Deprat, A. Toffoli, G. Romano, C. Guedj, V. Delaye, F. Boeuf, O. Faynot and M. Vinet. *First demonstration of a CMOS over CMOS 3D VLSI CoolCube^{TM} integration on 300mm wafers.* In 2016 IEEE Symposium on VLSI Technology, pages 1–2, June 2016, doi: 10.1109/VLSIT.2016.7573428. (Cited on pages vii and 5.)

[Cargnoni *et al.* 1998] F. Cargnoni, C. Gatti and L. Colombo. *Formation and annihilation of a bond defect in silicon: An* ***ab initio*** *quantum-mechanical characterization.* Phys. Rev. B, vol. 57, pages 170–177, Jan 1998, doi: 10.1103/PhysRevB.57.170. (Cited on page 38.)

[Cheng *et al.* 2012] K. Cheng, A. Khakifirooz, N. Loubet, S. Luning, T. Nagumo, M. Vinet, Q. Liu, A. Reznicek, T. Adam, S. Naczas, P. Hashemi, J. Kuss, J. Li, H. He, L. Edge, J. Gimbert, P. Khare, Y. Zhu, Z. Zhu, A. Madan, N. Klymko, S. Holmes, T. M. Levin, A. Hubbard, R. Johnson, M. Terrizzi, S. Teehan, A. Upham, G. Pfeiffer, T. Wu, A. Inada, F. Allibert, B. Y. Nguyen, L. Grenouillet, Y. Le Tiec, R. Wacquez, W. Kleemeier, R. Sampson, R. H. Dennard, T. H. Ning, M. Khare, G. Shahidi and B. Doris. *High performance extremely thin SOI (ETSOI) hybrid CMOS with Sichannel NFET and strained SiGe channel PFET.* In Electron Devices Meeting (IEDM), 2012 IEEE International, pages 18.1.1–18.1.4, Dec 2012, doi: 10.1109/IEDM.2012.6479063. (Cited on pages vii, 6 and 7.)

[Cheng *et al.* 2015] S.-Y. Cheng, K.-T. Chen and S.T. Chang. *Impact of strain on hole mobility in the inversion layer of {PMOS} device with SiGe alloy thin film.* Thin Solid Films, vol. 584, pages 135 – 140, 2015. The 7th International Conference on Technological Advances of Thin Films & Surface Coatings (ThinFilms2014), doi: 10.1016/j.tsf.2015.01.047. (Cited on pages vii, 6 and 7.)

[Chevacharoenkul *et al.* 1991] Sopa Chevacharoenkul, John R. Ilzhoefer, Diego Feijóo and Ulrich Gösele. *Recrystallization of silicon amorphized by carbon implantation.* Applied Physics Letters, vol. 58, no. 13, pages 1434–1436, 1991, doi: 10.1063/1.105190. (Cited on page 20.)

[Chilton *et al.* 1989] B. T. Chilton, B. J. Robinson, D. A. Thompson, T. E. Jackman and J.-M. Baribeau. *Solid phase epitaxial regrowth of* $Si_{1_x}Ge_x/Si$ *strained-layer structures amorphized by ion implantation.* Applied Physics Letters, vol. 54, no. 1, pages 42–44, 1989, doi: 10.1063/1.100828. (Cited on page 114.)

[Christian 1965] JW Christian. *The Theory of Transformation in Metals and Alloys, International Series of Monographs on Metal Physics and Physical Metallurgy Vol. 7.* Pergamon, Oxford, vol. 7, pages 177–181, 1965. (Cited on page 15.)

[Claverie *et al.* 2010] A. Claverie, S. Koffel, N. Cherkashin, G. Benassayag and P. Scheiblin. *Amorphization, recrystallization and end of range defects in germanium.* Thin Solid Films, vol. 518, no. 9, pages 2307 – 2313, 2010. Proceedings of the {EMRS} 2009 Spring Meeting Symposium I: Silicon and germanium issues for future {CMOS} devices, doi: 10.1016/j.tsf.2009.09.162. (Cited on page 17.)

[Corni *et al.* 1996] F. Corni, S. Frabboni, R. Tonini, G. Ottaviani and G. Queirolo. *Stress and interface morphology contributions in the crystallization kinetics of a* $Ge_xSi_{1_x}$ *thin layer on (100) Si.* Journal of Applied Physics, vol. 79, no. 7, pages 3528–3533, 1996, doi: 10.1063/1.361404. (Cited on pages 90 and 115.)

[Cristiano *et al.* 1996] F. Cristiano, A. Nejim, B. de Mauduit, A. Claverie and P.L.F. Hemment. *Characterization of extended defects in SiGe alloys formed by high dose Ge+ implantation into Si.* Nuclear Instruments and Methods in Physics Research Section B: Beam Interactions with Materials and Atoms, vol. 120, no. 1, pages 156 – 160, 1996, doi: 10.1016/S0168-583X(97)80005-5. (Cited on pages 115 and 119.)

[Cristiano *et al.* 2004] F. Cristiano, N. Cherkashin, P. Calvo, Y. Lamrani, X. Hebras, A. Claverie, W. Lerch and S. Paul. *Thermal stability of boron electrical activation in preamorphised ultra-shallow junctions.* Materials Science and Engineering: B, vol. 114-115, pages 174 – 179, 2004, doi: 10.1016/j.mseb.2004.07.049. (Cited on pages 60 and 68.)

[Cristiano *et al.* 2016] F. Cristiano, M. Shayesteh, R. Duffy, K. Huet, F. Mazzamuto, Y. Qiu, M. Quillec, H.H. Henrichsen, P.F. Nielsen, D.H. Petersen, A. La Magna, G. Caruso and S. Boninelli. *Defect evolution and dopant activation in laser annealed Si and Ge.* Materials Science in Semiconductor Processing, vol. 42, Part 2, pages 188 – 195, 2016. E-MRS Spring Meeting 2015 Symposium Z: Nanomaterials and processes for advanced semiconductor {CMOS} devices, doi: 10.1016/j.mssp.2015.09.011. (Cited on page 6.)

[Csepregi *et al.* 1977a] L. Csepregi, E. F. Kennedy, T. J. Gallagher, J. W. Mayer and T. W. Sigmon. *Reordering of amorphous layers of Si-implanted with* ^{31}P*,* ^{75}As*, and* ^{11}B *ions.* Journal of Applied Physics, vol. 48, no. 10, pages 4234–4240, 1977, doi: 10.1063/1.323408. (Cited on page 60.)

[Csepregi *et al.* 1977b] L. Csepregi, R.P. Küllen, J.W. Mayer and T.W. Sigmon. *Regrowth kinetics of amorphous Ge layers created by 74Ge and 28Si implantation of Ge crystals.* Solid State Communications, vol. 21, no. 11, pages 1019 – 1021, 1977, doi: 10.1016/0038-1098(77)90009-6. (Cited on page 17.)

[Csepregi *et al.* 1978] L. Csepregi, E. F. Kennedy, J. W. Mayer and T. W. Sigmon. *Substrate-orientation dependence of the epitaxial regrowth rate from Si-implanted amorphous Si.* J. Appl. Phys., vol. 49, no. 7, pages 3906–3911, 1978, doi: 10.1063/1.325397. (Cited on pages viii, ix, xi, 16, 17, 18, 33, 37, 43, 44, 45, 46, 47, 51, 52, 53, 70 and 88.)

[Custer *et al.* 1994] J. S. Custer, Michael O. Thompson, D. C. Jacobson, J. M. Poate, S. Roorda, W. C. Sinke and F. Spaepen. *Density of amorphous Si.* Applied Physics Letters, vol. 64, no. 4, pages 437–439, 1994, doi: 10.1063/1.111121. (Cited on page 13.)

[Custer 1992] JS Custer. *The Amorphous Side of Solid Phase Epitaxy.* In Crucial Issues in Semiconductor Materials and Processing Technologies, pages 477–482. Springer, 1992. (Cited on pages viii, 17 and 18.)

[D'Angelo *et al.* 2007] D. D'Angelo, A. M. Piro, A. Terrasi, M. G. Grimaldi, S. Mirabella and C. Bongiorno. *Interface roughening and defect nucleation during solid phase epitaxy regrowth of doped and intrinsic* $Si_{0.83}Ge_{0.17}$ *alloys.* J. Appl. Phys., vol. 101, no. 10, pages –, 2007, doi: 10.1063/1.2732680. (Cited on pages 90 and 115.)

[D'Angelo *et al.* 2008] D. D'Angelo, L. Romano, I. Crupi, E. Carria, V. Privitera and M. G. Grimaldi. *Role of the strain in the epitaxial regrowth rate of heavily doped amorphous Si films.* Applied Physics Letters, vol. 93, no. 23, pages –, 2008, doi: 10.1063/1.3036899. (Cited on page 60.)

[Darby *et al.* 2013] B. L. Darby, B. R. Yates, I. Martin-Bragado, J. L. Gomez-Selles, R. G. Elliman and K. S. Jones. *Substrate orientation dependence on the solid phase epitaxial growth rate of Ge.* J. Appl. Phys., vol. 113, no. 3, 2013, doi: 10.1063/1.4776718. (Cited on pages viii, xi, 17, 18, 34, 37, 81, 83 and 88.)

[de Gironcoli *et al.* 1991] Stefano de Gironcoli, Paolo Giannozzi and Stefano Baroni. *Structure and thermodynamics of* $\mathrm{Si}_x\mathrm{Ge}_{1-x}$ *alloys from ab initio Monte Carlo simulations.* Phys. Rev. Lett., vol. 66, pages 2116–2119, Apr 1991, doi: 10.1103/PhysRevLett.66.2116. (Cited on page 11.)

[De Salvador *et al.* 2006] D. De Salvador, G. Bisognin, M. Di Marino, E. Napolitani, A. Carnera, H. Graoui, M. A. Foad, F. Boscherini and S. Mirabella. *Experimental evidence of B clustering in amorphous Si during ultrashallow junction formation.* Applied Physics Letters, vol. 89, no. 24, 2006, doi: 10.1063/1.2402905. (Cited on pages 60, 62 and 76.)

[Demenev *et al.* 2012] E. Demenev, D. Giubertoni, S. Gennaro, M. Bersani, E. Hourdakis, A. G. Nassiopoulou, M. A. Reading and J. A. van den Berg. *Arsenic redistribution after solid phase epitaxial regrowth of shallow pre-amorphized silicon layers.* AIP Conference Proceedings, vol. 1496, no. 1, pages 272–275, 2012, doi: 10.1063/1.4766541. (Cited on pages 19 and 73.)

[Dismukes *et al.* 1964] J. P. Dismukes, L. Ekstrom and R. J. Paff. *Lattice Parameter and Density in Germanium-Silicon Alloys.* The Journal of Physical Chemistry, vol. 68, no. 10, pages 3021–3027, 1964, doi: 10.1021/j100792a049. (Cited on pages xi, 11 and 92.)

[Dong *et al.* 2014] T. Dong, V. Dobrev, T. Kolev, R. Rieben, S. Tomov and J. Dongarra. *A Step towards Energy Efficient Computing: Redesigning a Hydrodynamic Application on CPU-GPU.* In 2014 IEEE 28th International Parallel and Distributed Processing Symposium, pages 972–981, May 2014, doi: 10.1109/IPDPS.2014.103. (Cited on pages vii and 2.)

[Donovan *et al.* 1985] E. P. Donovan, F. Spaepen, D. Turnbull, J. M. Poate and D. C. Jacobson. *Calorimetric studies of crystallization and relaxation of amorphous Si and Ge prepared by ion implantation.* Journal of Applied Physics, vol. 57, no. 6, pages 1795–1804, 1985, doi: 10.1063/1.334406. (Cited on pages 13, 14, 15 and 17.)

[Drosd & Washburn 1982] R. Drosd and J. Washburn. *Some observations on the amorphous to crystalline transformation in silicon.* J. Appl. Phys., vol. 53, no. 1, pages 397–403, 1982, doi: 10.1063/1.329901. (Cited on pages ix, 32, 33, 43, 53 and 55.)

[Duffy *et al.* 2004] R. Duffy, V. C. Venezia, A. Heringa, B. J. Pawlak, M. J. P. Hopstaken, G. C. J. Maas, Y. Tamminga, T. Dao, F. Roozeboom and L. Pelaz. *Boron diffusion in amorphous silicon and the role of fluorine.* Applied Physics Letters, vol. 84, no. 21, pages 4283–4285, 2004, doi: 10.1063/1.1751225. (Cited on page 62.)

[Elliman & Wong 1996] RG Elliman and WC Wong. *Kinetic roughening and smoothing of the crystalline–amorphous interface during solid phase epitaxial crystallization of GeSi alloy layers.* Applied Physics Letters, vol. 69, no. 18, pages 2677–2679, 1996, doi: 10.1063/1.117675. (Cited on pages 71 and 90.)

[Ferain *et al.* 2011] Isabelle Ferain, Cynthia A Colinge and Jean-Pierre Colinge. *Multigate transistors as the future of classical metal-oxide-semiconductor field-effect transistors.* Nature, vol. 479, no. 7373, pages 310–316, 2011. (Cited on pages 2 and 3.)

[Fichthorn & Weinberg 1991] Kristen A Fichthorn and W Hh Weinberg. *Theoretical foundations of dynamical Monte Carlo simulations.* The Journal of chemical physics, vol. 95, no. 2, pages 1090–1096, 1991. (Cited on page 24.)

[Gärtner & Weber 2003] K. Gärtner and B. Weber. *Molecular dynamics simulations of solid-phase epitaxial growth in silicon.* Nuclear Instruments and Methods in Physics Research Section B: Beam Interactions with Materials and Atoms, vol. 202, no. 0, pages 255 – 260, 2003, doi: 10.1016/S0168-583X(02)01866-9. (Cited on pages 35 and 46.)

[Ghani *et al.* 2003] T. Ghani, M. Armstrong, C. Auth, M. Bost, P. Charvat, G. Glass, T. Hoffmann, K. Johnson, C. Kenyon, J. Klaus, B. McIntyre, K. Mistry, A. Murthy, J. Sandford, M. Silberstein, S. Sivakumar, P. Smith, K. Zawadzki, S. Thompson and M. Bohr. *A 90nm high volume manufacturing logic technology featuring novel 45nm gate length strained silicon CMOS transistors.* In Electron Devices Meeting, 2003. IEDM '03 Technical Digest. IEEE International, pages 11.6.1–11.6.3, Dec 2003, doi: 10.1109/IEDM.2003.1269442. (Cited on page 6.)

[Gillespie & Wadley 2009] B.A. Gillespie and H.N.G. Wadley. *Atomistic examinations of the solid-phase epitaxial growth of silicon.* Journal of Crystal Growth, vol. 311, no. 11, pages 3195 – 3203, 2009, doi: 10.1016/j.jcrysgro.2009.02.050. (Cited on page 35.)

[Gillespie *et al.* 2007] B. A. Gillespie, X. W. Zhou, D. A. Murdick, H. N. G. Wadley, R. Drautz and D. G. Pettifor. *Bond-order potential for silicon.* Phys. Rev. B, vol. 75, page 155207, Apr 2007, doi: 10.1103/PhysRevB.75.155207. (Cited on page 22.)

[Gouyé *et al.* 2010] A. Gouyé, I. Berbezier, L. Favre, M. Aouassa, G. Amiard, A. Ronda, Y. Campidelli and A. Halimaoui. *Insights into solid phase epitaxy of ultrahighly doped silicon.* Journal of Applied Physics, vol. 108, no. 1, pages –, 2010, doi: 10.1063/1.3408556. (Cited on pages x, 19, 60, 69 and 70.)

[Harame *et al.* 2004] D.L Harame, S.J Koester, G Freeman, P Cottrel, K Rim, G Dehlinger, D Ahlgren, J.S Dunn, D Greenberg, A Joseph, F Anderson, J.-S Rieh, S.A.S.T Onge, D Coolbaugh, V Ramachandran, J.D Cressler and S Subbanna. *The revolution in SiGe: impact on device electronics.* Applied Surface Science, vol. 224, no. 1-4, pages 9 – 17, 2004, doi: 10.1016/j.apsusc.2003.08.086. (Cited on pages xi and 100.)

[Hartmann *et al.* 2011] J. M. Hartmann, A. Abbadie and S. Favier. *Critical thickness for plastic relaxation of SiGe on Si(001) revisited.* Journal of Applied Physics, vol. 110, no. 8, page 083529, 2011, doi: 10.1063/1.3656989. (Cited on pages 8 and 100.)

[Haynes *et al.* 1995] T. E. Haynes, M. J. Antonell, C. Archie Lee and K. S. Jones. *Composition dependence of solid-phase epitaxy in silicon-germanium alloys: Experiment and theory.* Phys. Rev. B, vol. 51, pages 7762–7771, Mar 1995, doi: 10.1103/PhysRevB.51.7762. (Cited on pages x, 17, 80, 81, 83, 84, 85, 86, 88 and 96.)

[Hohenberg & Kohn 1964] P. Hohenberg and W. Kohn. *Inhomogeneous Electron Gas.* Phys. Rev., vol. 136, pages B864–B871, Nov 1964, doi: 10.1103/PhysRev.136.B864. (Cited on page 22.)

[Hong *et al.* 1992a] Q. Z. Hong, J. G. Zhu, J. W. Mayer, W. Xia and S. S. Lau. *Solid phase epitaxy of stressed and stress-relaxed Ge-Si alloys.* J. Appl. Phys., vol. 71, no. 4, pages 1768–1773, 1992, doi: 10.1063/1.351212. (Cited on page 111.)

[Hong *et al.* 1992b] Stella Q. Hong, Q. Z. Hong and James W. Mayer. *Regrowth rates and dopant activation of Sb^+ implanted SiGe alloys.* Journal of Applied Physics, vol. 72, no. 8, pages 3821–3823, 1992, doi: 10.1063/1.352282. (Cited on page 112.)

[Hoover 1985] William G. Hoover. *Canonical dynamics: Equilibrium phase-space distributions.* Phys. Rev. A, vol. 31, pages 1695–1697, Mar 1985, doi: 10.1103/PhysRevA.31.1695. (Cited on page 42.)

[Hopstaken *et al.* 2004] M.J.P. Hopstaken, Y. Tamminga, M.A. Verheijen, R. Duffy, V.C. Venezia and A. Heringa. *Effects of crystalline regrowth on dopant profiles in preamorphized silicon.* Applied Surface Science, vol. 231-232, pages 688 – 692, 2004, doi: 10.1016/j.apsusc.2004.03.184. (Cited on page 19.)

[Jeon *et al.* 1989] Young-Jin Jeon, M.F. Becker and R.M. Walser. *Comparison of the Effect of Boron and Phosphorus Impurities on Solid Phase Epitaxial Regrowth of Amorphous Silicon.* MRS Proceedings, vol. 157, 01 1989, doi: 10.1557/PROC-157-653. (Cited on pages x, 70, 71 and 77.)

[Jin *et al.* 2002] Jian-Yue Jin, Jinning Liu, Ukyo Jeong, Sandeep Mehta and Kevin Jones. *Study of reverse annealing behaviors of p+/n ultrashallow junction formed using solid phase epitaxial annealing.* Journal of Vacuum Science & Technology B, vol. 20, no. 1, pages 422–426, 2002, doi: 10.1116/1.1424279. (Cited on pages 60 and 68.)

[Johnson & McCallum 2004] B. C. Johnson and J. C. McCallum. *Kinetics of arsenic-enhanced solid phase epitaxy in silicon.* Journal of Applied Physics, vol. 95, no. 8, pages 4427–4431, 2004, doi: 10.1063/1.1682672. (Cited on page 19.)

[Johnson & McCallum 2007] B. C. Johnson and J. C. McCallum. *Dopant-enhanced solid-phase epitaxy in buried amorphous silicon layers.* Phys. Rev. B, vol. 76, page 045216, Jul 2007, doi: 10.1103/PhysRevB.76.045216. (Cited on pages viii, ix, 16, 20, 45, 60, 65 and 75.)

[Johnson *et al.* 2008] B. C. Johnson, P. Gortmaker and J. C. McCallum. *Intrinsic and dopant-enhanced solid-phase epitaxy in amorphous germanium.* Phys. Rev. B, vol. 77, page 214109, Jun 2008, doi: 10.1103/PhysRevB.77.214109. (Cited on page 17.)

[Johnson *et al.* 2012] B. C. Johnson, T. Ohshima and J. C. McCallum. *Dopant effects on solid phase epitaxy in silicon and germanium.* Journal of Applied Physics, vol. 111, no. 3, pages –, 2012, doi: 10.1063/1.3682532. (Cited on pages x, 20, 60, 65, 69, 70 and 75.)

[Jones *et al.* 01] Eric Jones, Travis Oliphant, Pearu Peterson*et al.* *SciPy: Open source scientific tools for Python*, 2001–. [Online; accessed 2017-02-13]. (Cited on page 41.)

[Jones *et al.* 1988] K. S. Jones, S. Prussin and E. R. Weber. *A systematic analysis of defects in ion-implanted silicon.* Applied Physics A, vol. 45, no. 1, pages 1–34, 1988, doi: 10.1007/BF00618760. (Cited on pages 33, 115 and 119.)

[Justo *et al.* 1998] João F. Justo, Martin Z. Bazant, Efthimios Kaxiras, V. V. Bulatov and Sidney Yip. *Interatomic potential for silicon defects and disordered phases.* Phys. Rev. B, vol. 58, pages 2539–2550, Aug 1998, doi: 10.1103/PhysRevB.58.2539. (Cited on page 22.)

[Kaczmarski *et al.* 2005] M. Kaczmarski, O. N. Bedoya-Martínez and E. R. Hernández. *Phase Diagram of Silicon from Atomistic Simulations.* Phys. Rev. Lett., vol. 94, page 095701, Mar 2005, doi: 10.1103/PhysRevLett.94.095701. (Cited on page 10.)

[Kasper *et al.* 1995] E. Kasper, A. Schuh, G. Bauer, B. Holländer and H. Kibbel. *Test of Vegard's law in thin epitaxial SiGe layers.* J. Cryst. Growth, vol. 157, no. 1-4, pages 68 – 72, 1995, doi: 10.1016/0022-0248(95)00373-8. (Cited on page 11.)

[Knief & von Niessen 1999] Simone Knief and Wolfgang von Niessen. *Electron spin resonance signals in* $a-\mathrm{Si}:$ *Dangling versus floating bonds.* Phys. Rev. B, vol. 60, pages 5412–5416, Aug 1999, doi: 10.1103/PhysRevB.60.5412. (Cited on page 13.)

[Koomey *et al.* 2011] J. Koomey, S. Berard, M. Sanchez and H. Wong. *Implications of Historical Trends in the Electrical Efficiency of Computing.* IEEE Annals of the History of Computing, vol. 33, no. 3, pages 46–54, March 2011, doi: 10.1109/MAHC.2010.28. (Cited on pages vii, 2 and 27.)

[Kriegner *et al.* 2013] Dominik Kriegner, Eugen Wintersberger and Julian Stangl. *xrayutilities: a versatile tool for reciprocal space conversion of scattering data recorded with linear and area detectors.* Journal of Applied Crystallography, vol. 46, no. 4, pages 1162–1170, Aug 2013, doi: 10.1107/S0021889813017214. (Cited on page 130.)

[Kringhøj & Elliman 1994] P. Kringhøj and R. G. Elliman. *Solid-Phase Epitaxial Crystallization of Strain-Relaxed* $Si_{1_x}Ge_x$ *Alloy Layers.* Phys. Rev. Lett., vol. 73, pages 858–861, Aug 1994, doi: 10.1103/PhysRevLett.73.858. (Cited on pages x, 17, 80, 81, 83, 84, 85, 88 and 96.)

[Kringhøj *et al.* 1995] P. Kringhøj, R.G. Elliman, M. Fyhn, S.Y. Shiryaev and A. Nylandsted Larsen. *Recrystallisation of relaxed SiGe alloy layers.* Nuclear Instruments and Methods in Physics Research Section B: Beam Interactions with Materials and Atoms, vol. 106, no. 1-4, pages 346 – 349, 1995, doi: 10.1016/0168-583X(96)80028-0. (Cited on pages x, 80, 84, 85 and 86.)

[Krzeminski & Lampin 2011] C. Krzeminski and E. Lampin. *Solid phase epitaxy amorphous silicon re-growth: some insight from empirical molecular dynamics simulation.* The European Physical Journal B, vol. 81, no. 3, pages 283–290, 2011, doi: 10.1140/epjb/e2011-10958-7. (Cited on page 46.)

[Krzeminski *et al.* 2007] C. Krzeminski, Q. Brulin, V. Cuny, E. Lecat, E. Lampin and F. Cleri. *Molecular dynamics simulation of the recrystallization of amorphous Si layers: Comprehensive study of the dependence of the recrystallization velocity* *on the interatomic potential.* Journal of Applied Physics, vol. 101, no. 12, 2007, doi: 10.1063/1.2743089. (Cited on pages 35, 44, 56 and 122.)

[Laaziri *et al.* 1995] K. Laaziri, S. Roorda and J.M Baribeau. *Density of amorphous SixGe1â^'x alloys prepared by high-energy ion implantation.* Journal of Non-Crystalline Solids, vol. 191, no. 1, pages 193 – 199, 1995, doi: 10.1016/0022-3093(95)00310-X. (Cited on page 13.)

[Laaziri *et al.* 1999] Khalid Laaziri, S. Kycia, S. Roorda, M. Chicoine, J. L. Robertson, J. Wang and S. C. Moss. *High Resolution Radial Distribution Function of Pure Amorphous Silicon.* Phys. Rev. Lett., vol. 82, pages 3460–3463, Apr 1999, doi: 10.1103/PhysRevLett.82.3460. (Cited on pages vii, viii, 13, 14 and 40.)

[Lai *et al.* 2011] Haoyu Lai, Stephen M Sea, Harold Kennel and Scott T Dunham. *Molecular Dynamics Modeling of Stress and Orientation Dependence of Solid Phase Epitaxial Regrowth.* MRS Proceedings, vol. 1245, 02 2011, doi: 10.1557/PROC-1245-A16-13. (Cited on pages 37, 46, 47 and 52.)

[Lai *et al.* 2012] Haoyu Lai, Stephen M. Cea, Harold Kennel and Scott T. Dunham. *Molecular dynamics modeling of solid phase epitaxial regrowth.* Journal of Applied Physics, vol. 111, no. 11, 2012, doi: 10.1063/1.4721407. (Cited on page 37.)

[Lampin & Krzeminski 2009] E. Lampin and C. Krzeminski. *Molecular dynamics simulations of the solid phase epitaxy of Si: Growth mechanism and orientation effects.* Journal of Applied Physics, vol. 106, no. 6, pages –, 2009, doi: 10.1063/1.3211972. (Cited on pages 37, 46, 51 and 57.)

[Lee *et al.* 1993] C. Lee, T. E. Haynes and K. S. Jones. *Kinetics of solid phase epitaxial regrowth in amorphized Si0.88Ge0.12 measured by time-resolved reflectivity.* Applied Physics Letters, vol. 62, no. 5, pages 501–503, 1993, doi: 10.1063/1.108892. (Cited on pages 79, 80 and 108.)

[Lewis & Randall 1961] GN Lewis and Merle Randall. Thermodynamics; revised by pitzer, ks; brewer, l. 1961. (Cited on page 86.)

[Lietoila *et al.* 1982] A. Lietoila, A. Wakita, T. W. Sigmon and J. F. Gibbons. *Epitaxial regrowth of intrinsic, 31Pdoped and compensated (31P+11Bdoped) amorphous Si.* Journal of Applied Physics, vol. 53, no. 6, pages 4399–4405, 1982, doi: 10.1063/1.331222. (Cited on page 20.)

[Lohmeier *et al.* 1994] M. Lohmeier, S. de Vries, J. S. Custer, E. Vlieg, M. S. Finney, F. Priolo and A. Battaglia. *Interface roughness during thermal and ion-induced* *regrowth of amorphous layers on Si(001).* Applied Physics Letters, vol. 64, no. 14, pages 1803–1805, 1994, doi: 10.1063/1.111787. (Cited on page 33.)

[Lu *et al.* 1991] Guo-Quan Lu, Eric Nygren and Michael J. Aziz. *Pressure-enhanced crystallization kinetics of amorphous Si and Ge: Implications for point-defect mechanisms.* Journal of Applied Physics, vol. 70, no. 10, pages 5323–5345, 1991, doi: 10.1063/1.350243. (Cited on pages 14, 17, 18, 20, 60, 65 and 75.)

[Marqués *et al.* 2001] Luis A. Marqués, Lourdes Pelaz, Jesús Hernández, Juan Barbolla and George H. Gilmer. *Stability of defects in crystalline silicon and their role in amorphization.* Phys. Rev. B, vol. 64, page 045214, Jul 2001, doi: 10.1103/PhysRevB.64.045214. (Cited on page 23.)

[Marqués *et al.* 2003] Luis A. Marqués, Lourdes Pelaz, María Aboy, Lourdes Enríquez and Juan Barbolla. *Microscopic Description of the Irradiation-Induced Amorphization in Silicon.* Phys. Rev. Lett., vol. 91, page 135504, Sep 2003, doi: 10.1103/PhysRevLett.91.135504. (Cited on pages 38 and 56.)

[Marqués *et al.* 2004] Luis A. Marqués, Lourdes Pelaz, Maria Aboy and Juan Barbolla. *The laser annealing induced phase transition in silicon: a molecular dynamics study.* Nuclear Instruments and Methods in Physics Research Section B: Beam Interactions with Materials and Atoms, vol. 216, pages 57 – 61, 2004, doi: 10.1016/j.nimb.2003.11.020. (Cited on page 35.)

[Marqués *et al.* 2012] Luis A. Marqués, Lourdes Pelaz, Iván Santos, Pedro López and Ray Duffy. *Molecular dynamics simulation of the regrowth of nanometric multigate Si devices.* Journal of Applied Physics, vol. 111, no. 3, 2012, doi: 10.1063/1.3679126. (Cited on page 37.)

[Martin-Bragado & Moroz 2011] Ignacio Martin-Bragado and Victor Moroz. *Modeling of 311 facets using a lattice kinetic Monte Carlo three-dimensional model for selective epitaxial growth of silicon.* Applied Physics Letters, vol. 98, no. 15, pages –, 2011, doi: 10.1063/1.3580771. (Cited on page 26.)

[Martin-Bragado & Sklénard 2012] Ignacio Martin-Bragado and Benoit Sklénard. *Understanding Si(111) solid phase epitaxial regrowth using Monte Carlo modeling: Bi-modal growth, defect formation, and interface topology.* Journal of Applied Physics, vol. 112, no. 2, pages –, 2012, doi: 10.1063/1.4739733. (Cited on pages 34 and 55.)

[Martin-Bragado & Zographos 2011] Ignacio Martin-Bragado and Nikolas Zographos. *Indirect boron diffusion in amorphous silicon modeled by kinetic Monte Carlo.* Solid-

State Electronics, vol. 55, no. 1, pages 25 – 28, 2011, doi: 10.1016/j.sse.2010.08.008. (Cited on pages xiii, 60, 62 and 63.)

[Martin-Bragado *et al.* 2005] I. Martin-Bragado, P. Castrillo, M. Jaraiz, R. Pinacho, J. E. Rubio and J. Barbolla. *Physical atomistic kinetic Monte Carlo modeling of Fermi-level effects of species diffusing in silicon.* Phys. Rev. B, vol. 72, page 035202, Jul 2005, doi: 10.1103/PhysRevB.72.035202. (Cited on pages xiii, 63 and 64.)

[Martin-Bragado *et al.* 2013] Ignacio Martin-Bragado, Antonio Rivera, Gonzalo Valles, Jose Luis Gomez-Selles and María J. Caturla. *MMonCa: An Object Kinetic Monte Carlo simulator for damage irradiation evolution and defect diffusion.* Computer Physics Communications, vol. 184, no. 12, pages 2703 – 2710, 2013, doi: 10.1016/j.cpc.2013.07.011. (Cited on pages 26 and 60.)

[Martin-Bragado 2012] Ignacio Martin-Bragado. *Importance of twin defect formation created by solid-phase epitaxial growth: An atomistic study.* Scripta Materialia, vol. 66, no. 3-4, pages 186 – 189, 2012, doi: 10.1016/j.scriptamat.2011.10.036. (Cited on pages xi, 33, 34, 55, 81, 83 and 88.)

[Martins & Zunger 1986] José Luis Martins and Alex Zunger. *Stability of Ordered Bulk and Epitaxial Semiconductor Alloys.* Phys. Rev. Lett., vol. 56, pages 1400–1403, Mar 1986, doi: 10.1103/PhysRevLett.56.1400. (Cited on page 85.)

[Mastromatteo *et al.* 2010] M. Mastromatteo, D. De Salvador, E. Napolitani, F. Panciera, G. Bisognin, A. Carnera, G. Impellizzeri, S. Mirabella and F. Priolo. *Fluorine redistribution and incorporation during solid phase epitaxy of preamorphized Si.* Phys. Rev. B, vol. 82, page 155323, Oct 2010, doi: 10.1103/PhysRevB.82.155323. (Cited on page 19.)

[Matsumoto & Nishimura 1998] Makoto Matsumoto and Takuji Nishimura. *Mersenne Twister: A 623-dimensionally Equidistributed Uniform Pseudo-random Number Generator.* ACM Trans. Model. Comput. Simul., vol. 8, no. 1, pages 3–30, January 1998, doi: 10.1145/272991.272995. (Cited on page 26.)

[Matthews & Blakeslee 1974] J.W. Matthews and A.E. Blakeslee. *Defects in epitaxial multilayers: I. Misfit dislocations.* Journal of Crystal Growth, vol. 27, no. 0, pages 118 – 125, 1974, doi: 10.1016/S0022-0248(74)80055-2. (Cited on page 8.)

[Mattoni & Colombo 2004] A. Mattoni and L. Colombo. *Boron ripening during solid-phase epitaxy of amorphous silicon.* Physical Review B, vol. 69, 1 2004, doi: 10.1103/physrevb.69.045204. (Cited on pages 60, 65, 67 and 76.)

[Mattoni & Colombo 2008] A. Mattoni and L. Colombo. *Crystallization kinetics of mixed amorphous-crystalline nanosystems.* Phys. Rev. B, vol. 78, page 075408, Aug 2008, doi: 10.1103/PhysRevB.78.075408. (Cited on page 42.)

[Mayer & Lau 1990] James W Mayer and Sylranus S Lau. Electronic materials science: for integrated circuits in si and gaas. Prentice Hall, 1990. (Cited on page 23.)

[McCallum 1996] J. C. McCallum. *Kinetics of solid phase epitaxy in buried amorphous Si layers formed by MeV ion implantation.* Applied Physics Letters, vol. 69, no. 7, pages 925–927, 1996, doi: 10.1063/1.116945. (Cited on pages 16 and 44.)

[McCallum 1999] J.C McCallum. *The kinetics of dopant-enhanced solid phase epitaxy in H-free amorphous silicon layers.* Nuclear Instruments and Methods in Physics Research Section B: Beam Interactions with Materials and Atoms, vol. 148, no. 1-4, pages 350 – 354, 1999, doi: 10.1016/S0168-583X(98)00671-5. (Cited on page 19.)

[Metropolis & Ulam 1949] Nicholas Metropolis and Stanislaw Ulam. *The monte carlo method.* Journal of the American statistical association, vol. 44, no. 247, pages 335–341, 1949. (Cited on page 23.)

[Metropolis *et al.* 1953] Nicholas Metropolis, Arianna W Rosenbluth, Marshall N Rosenbluth, Augusta H Teller and Edward Teller. *Equation of state calculations by fast computing machines.* The journal of chemical physics, vol. 21, no. 6, pages 1087–1092, 1953. (Cited on page 24.)

[Mirabella *et al.* 2008] Salvatore Mirabella, Davide De Salvador, Elena Bruno, Enrico Napolitani, Emanuele F. Pecora, Simona Boninelli and Francesco Priolo. *Mechanism of Boron Diffusion in Amorphous Silicon.* Phys. Rev. Lett., vol. 100, page 155901, Apr 2008, doi: 10.1103/PhysRevLett.100.155901. (Cited on pages ix, 60, 62, 63, 64 and 68.)

[Momma & Izumi 2011] Koichi Momma and Fujio Izumi. *VESTA3 for three-dimensional visualization of crystal, volumetric and morphology data.* Journal of Applied Crystallography, vol. 44, no. 6, pages 1272–1276, Dec 2011, doi: 10.1107/S0021889811038970. (Cited on pages vii and 12.)

[Motooka *et al.* 1995] T. Motooka, Y. Hiroyama, R. Suzuki, T. Ohdaira, Y. Hirano and F. Sato. *Role of defects during amorphization and relaxation processes in Si.* Nuclear Instruments and Methods in Physics Research Section B: Beam Interactions with Materials and Atoms, vol. 106, no. 1, pages 198 – 205, 1995, doi: 10.1016/0168-583X(95)00704-0. (Cited on pages 38 and 56.)

[Motooka *et al.* 2000] T. Motooka, K. Nisihira, S. Munetoh, K. Moriguchi and A. Shintani. *Molecular-dynamics simulations of solid-phase epitaxy of Si: Growth mechanisms.* Phys. Rev. B, vol. 61, pages 8537–8540, Mar 2000, doi: 10.1103/PhysRevB.61.8537. (Cited on page 35.)

[Motooka 1994] Teruaki Motooka. *Model for amorphization processes in ion-implanted Si.* Phys. Rev. B, vol. 49, pages 16367–16371, Jun 1994, doi: 10.1103/PhysRevB.49.16367. (Cited on pages 38 and 56.)

[Narayan 1982] J. Narayan. *Interface structures during solid-phase-epitaxial growth in ion implanted semiconductors and a crystallization model.* Journal of Applied Physics, vol. 53, no. 12, pages 8607–8614, 1982, doi: 10.1063/1.330457. (Cited on pages 20 and 33.)

[Nosé 1984] Shūichi Nosé. *A molecular dynamics method for simulations in the canonical ensemble.* Molecular Physics, vol. 52, no. 2, pages 255–268, 1984, doi: 10.1080/00268978400101201. (Cited on page 42.)

[Olson & Roth 1988] G.L. Olson and J.A. Roth. *Kinetics of solid phase crystallization in amorphous silicon.* Materials Science Reports, vol. 3, no. 1, pages 1 – 77, 1988, doi: 10.1016/S0920-2307(88)80005-7. (Cited on pages 14, 16, 19, 60, 70 and 77.)

[Paine *et al.* 1990] DC Paine, DJ Howard, NG Stoffel and JA Horton. *The growth of strained $Si_{1_x}Ge_x$ alloys on (001) silicon using solid phase epitaxy.* Journal of Materials Research, vol. 5, no. 05, pages 1023–1031, 1990. (Cited on pages xiii, 112, 114 and 119.)

[Paine *et al.* 1991] David C. Paine, Neal D. Evans and Ned G. Stoffel. *A study of the effect of misfit-induced strain on the kinetics of solid phase epitaxy in the $Si_{1_x}Ge_x$ on 001 Si system.* Journal of Applied Physics, vol. 70, no. 8, pages 4278–4286, 1991, doi: 10.1063/1.349105. (Cited on pages 8, 108 and 112.)

[Pantelides 1986] Sokrates T. Pantelides. *Defects in Amorphous Silicon: A New Perspective.* Phys. Rev. Lett., vol. 57, pages 2979–2982, Dec 1986, doi: 10.1103/PhysRevLett.57.2979. (Cited on page 13.)

[Park & Wilkins 2011] Hyoungki Park and John W. Wilkins. *A topological point defect regulates the evolution of extended defects in irradiated silicon.* Applied Physics Letters, vol. 98, no. 17, pages –, 2011, doi: 10.1063/1.3585656. (Cited on page 60.)

[Park *et al.* 1988] Won Woo Park, M. F. Becker and R. M. Walser. *Precision measurements of the effect of implanted boron on silicon solid phase epitaxial re-*

growth. Journal of Materials Research, vol. 3, no. 2, pages 298–308, 03 1988, doi: 10.1557/JMR.1988.0298. (Cited on pages x, 69, 70 and 77.)

[Pawlak *et al.* 2004] B. J. Pawlak, R. Lindsay, R. Surdeanu, B. Dieu, L. Geenen, I. Hoflijk, O. Richard, R. Duffy, T. Clarysse, B. Brijs, W. Vandervorst and C. J. J. Dachs. *Chemical and electrical dopants profile evolution during solid phase epitaxial regrowth.* Journal of Vacuum Science & Technology B, vol. 22, no. 1, pages 297–301, 2004, doi: 10.1116/1.1643053. (Cited on page 60.)

[Payet *et al.* 2016a] A. Payet, F.P. Luce, C. Curfs, B. Mathieu, B. Sklénard, J.-C. Barbé, P. Batude, S. Joblot, C. Tavernier, B. Colombeau, S. Guissi, I. Martin-Bragado and P. Gergaud. *Damage accumulation during cryogenic and room temperature implantations in strained SiGe alloys.* Materials Science in Semiconductor Processing, vol. 42, pages 247–250, 2016, doi: 10.1016/j.mssp.2015.07.059. (Cited on page 10.)

[Payet *et al.* 2016b] Anthony Payet, Benoit Sklénard, Jean-Charles Barbé, Perrine Batude, Clément Tavernier, Patrice Gergaud and Ignacio Martin-Bragado. *An atomistic investigation of the composition dependence in SiGe alloys during Solid Phase Epitaxial Regrowth.* Acta Materialia, vol. 106, pages 290 – 294, 2016, doi: 10.1016/j.actamat.2016.01.022. (Cited on page 73.)

[Pelaz *et al.* 1999] Lourdes Pelaz, G. H. Gilmer, H.-J. Gossmann, C. S. Rafferty, M. Jaraiz and J. Barbolla. *B cluster formation and dissolution in Si: A scenario based on atomistic modeling.* Applied Physics Letters, vol. 74, no. 24, pages 3657–3659, 1999, doi: 10.1063/1.123213. (Cited on page 63.)

[People & Bean 1985] R. People and J. C. Bean. *Calculation of critical layer thickness versus lattice mismatch for* $Ge_xSi_{1_x}$*/Si strained-layer heterostructures.* Appl. Phys. Lett., vol. 47, no. 3, pages 322–324, 1985, doi: 10.1063/1.96206. (Cited on pages 8 and 100.)

[People & Bean 1986] R. People and J. C. Bean. *Erratum: Calculation of critical layer thickness versus lattice mismatch for GexSi1-x/Si strained-layer heterostructures [Appl. Phys. Lett. 47, 322 (1985)].* Applied Physics Letters, vol. 49, no. 4, pages 229–229, 1986, doi: 10.1063/1.97637. (Cited on page 100.)

[Pichler 2004] P Pichler. Intrinsic point defects, impurities, and their diffusion in silicon. Springer Vienna, Vienna, 2004. (Cited on pages 11 and 76.)

[Pidduck *et al.* 1992] A.J. Pidduck, D.J. Robbins, A.G. Cullis, W.Y. Leong and A.M. Pitt. *Evolution of surface morphology and strain during SiGe epitaxy.* Thin Solid

Films, vol. 222, no. 1, pages 78 – 84, 1992, doi: 10.1016/0040-6090(92)90042-A. (Cited on page 100.)

[Plimpton 1995] Steve Plimpton. *Fast Parallel Algorithms for Short-Range Molecular Dynamics.* Journal of Computational Physics, vol. 117, no. 1, pages 1 – 19, 1995. LAMMPS citing, doi: 10.1006/jcph.1995.1039. (Cited on pages 26 and 42.)

[Polk & Boudreaux 1973] D. E. Polk and D. S. Boudreaux. *Tetrahedrally Coordinated Random-Network Structure.* Phys. Rev. Lett., vol. 31, pages 92–95, Jul 1973, doi: 10.1103/PhysRevLett.31.92. (Cited on page 37.)

[Rodríguez *et al.* 1997] A. Rodríguez, T. Rodríguez, A. Kling, J. C. Soares, M. F. da Silva and C. Ballesteros. *Strain and defects depth distributions in undoped and boron-doped* $Si_{1_x}Ge_x$ *layers grown by solid phase epitaxy.* Journal of Applied Physics, vol. 82, no. 6, pages 2887–2895, 1997, doi: 10.1063/1.366121. (Cited on pages 112 and 114.)

[Roorda *et al.* 1991] S. Roorda, W. C. Sinke, J. M. Poate, D. C. Jacobson, S. Dierker, B. S. Dennis, D. J. Eaglesham, F. Spaepen and P. Fuoss. *Structural relaxation and defect annihilation in pure amorphous silicon.* Phys. Rev. B, vol. 44, pages 3702–3725, Aug 1991, doi: 10.1103/PhysRevB.44.3702. (Cited on page 15.)

[Roth *et al.* 1990] J. A. Roth, G. L. Olson, D. C. Jacobson and J. M. Poate. *Kinetics of solid phase epitaxy in thick amorphous Si layers formed by MeV ion implantation.* Applied Physics Letters, vol. 57, no. 13, pages 1340–1342, 1990, doi: 10.1063/1.103477. (Cited on pages viii, ix, 16, 44 and 45.)

[Rudawski *et al.* 2008] N. G. Rudawski, K. S. Jones and R. Gwilliam. *Kinetics and Morphological Instabilities of Stressed Solid-Solid Phase Transformations.* Phys. Rev. Lett., vol. 100, page 165501, Apr 2008, doi: 10.1103/PhysRevLett.100.165501. (Cited on pages viii, 18, 19, 89 and 97.)

[Ruffell *et al.* 2005] S. Ruffell, I. V. Mitchell and P. J. Simpson. *Solid-phase epitaxial regrowth of amorphous layers in Si(100) created by low-energy, high-fluence phosphorus implantation.* Journal of Applied Physics, vol. 98, no. 8, 2005, doi: 10.1063/1.2113409. (Cited on page 73.)

[Saito & Ohdomari 1981] Toshio Saito and Iwao Ohdomari. *A structural model for the interface between amorphous and (100) crystalline silicon.* Phil. Mag. B, vol. 43, no. 4, pages 673–687, 1981, doi: 10.1080/01418638108222166. (Cited on page 37.)

[Shiryaev *et al.* 1993] S. Y. Shiryaev, M. Fyhn and A. Nylandsted Larsen. *Solid phase epitaxy of relaxed, implantation-amorphized* $Si_{1_x}Ge_x$ *alloy layers grown on compositionally graded buffers.* Appl. Phys. Lett., vol. 63, no. 25, pages 3476–3478, 1993, doi: 10.1063/1.110125. (Cited on page 85.)

[Simoen *et al.* 2009] E. Simoen, A. Brugère, A. Satta, A. Firrincieli, B. Van Daele, B. Brijs, O. Richard, J. Geypen, M. Meuris and W. Vandervorst. *Impact of the chemical concentration on the solid-phase epitaxial regrowth of phosphorus implanted preamorphized germanium.* Journal of Applied Physics, vol. 105, no. 9, pages –, 2009, doi: 10.1063/1.3125459. (Cited on pages x and 73.)

[Sklénard *et al.* 2013] Benoit Sklénard, Jean-Charles Barbé, Perrine Batude, Pierrette Rivallin, Clément Tavernier, Sorin Cristoloveanu and Ignacio Martin-Bragado. *An atomistic investigation of the impact of in-plane uniaxial stress during solid phase epitaxial regrowth.* Applied Physics Letters, vol. 102, no. 15, pages –, 2013, doi: 10.1063/1.4802203. (Cited on pages viii, 19, 73 and 90.)

[Sklénard 2014] Benoît Sklénard. *Modélisation physique de la réalisation des jonctions FDSOI pour le noeud 20nm et au-delà.* PhD thesis, Grenoble, 2014. (Cited on pages 28 and 66.)

[Solmi *et al.* 1990] S. Solmi, E. Landi and F. Baruffaldi. *High-concentration boron diffusion in silicon: Simulation of the precipitation phenomena.* Journal of Applied Physics, vol. 68, no. 7, pages 3250–3258, 1990, doi: 10.1063/1.346376. (Cited on pages x, 6, 68 and 69.)

[Spaepen & Turnbull 1979] F. Spaepen and D. Turnbull. *Kinetics of motion of crystal-melt interfaces.* AIP Conference Proceedings, vol. 50, no. 1, pages 73–83, 1979, doi: 10.1063/1.31738. (Cited on pages 59, 76, 81, 85 and 95.)

[Spaepen 1978] Frans Spaepen. *A structural model for the interface between amorphous and crystalline Si or Ge.* Acta Metallurgica, vol. 26, no. 7, pages 1167 – 1177, 1978, doi: 10.1016/0001-6160(78)90145-1. (Cited on pages 17, 37, 59, 76, 81, 85 and 95.)

[Spinella *et al.* 1998] Corrado Spinella, Salvatore Lombardo and Francesco Priolo. *Crystal grain nucleation in amorphous silicon.* Journal of Applied Physics, vol. 84, no. 10, pages 5383–5414, 1998, doi: 10.1063/1.368873. (Cited on page 10.)

[Stillinger & Weber 1985] Frank H. Stillinger and Thomas A. Weber. *Computer simulation of local order in condensed phases of silicon.* Phys. Rev. B, vol. 31, pages

5262–5271, Apr 1985. Potential SW for MD, doi: 10.1103/PhysRevB.31.5262. (Cited on page 22.)

[Stock *et al.* 2000] D. M. Stock, B. Weber and K. Gärtner. *Role of the bond defect for structural transformations between crystalline and amorphous silicon: A molecular-dynamics study.* Phys. Rev. B, vol. 61, pages 8150–8154, Mar 2000, doi: 10.1103/PhysRevB.61.8150. (Cited on pages 38 and 56.)

[Strane *et al.* 1996] J. W. Strane, S. R. Lee, H. J. Stein, S. T. Picraux, J. K. Watanabe and J. W. Mayer. *Carbon incorporation into Si at high concentrations by ion implantation and solid phase epitaxy.* Journal of Applied Physics, vol. 79, no. 2, pages 637–646, 1996, doi: 10.1063/1.360806. (Cited on pages 20 and 73.)

[Stukowski 2010] Alexander Stukowski. *Visualization and analysis of atomistic simulation data with OVITO-the Open Visualization Tool.* Modelling and Simulation in Materials Science and Engineering, vol. 18, no. 1, page 015012, 2010. (Cited on pages ix, x, xi, 43, 48, 72 and 92.)

[Suh & Lee 1996] K. Y. Suh and Hong H. Lee. *Composition dependence of activation energy in solid phase epitaxial growth of* $Si_{1-x}Ge_x$ *alloys.* J. Appl. Phys., vol. 80, no. 12, pages 6716–6719, 1996, doi: 10.1063/1.363745. (Cited on pages 80 and 85.)

[Takeshi & Billinge 2012a] Egami Takeshi and Simon J.L. Billinge. *Chapter 1 - Structure of Complex Materials.* In Takeshi Egami and Simon J.L. Billinge, editors, Underneath the Bragg Peaks - Structural Analysis of Complex Materials, volume 16 of *Pergamon Materials Series*, pages 1 – 25. Pergamon, 2012, doi: 10.1016/B978-0-08-097133-9.00001-0. (Cited on page 13.)

[Takeshi & Billinge 2012b] Egami Takeshi and Simon J.L. Billinge. *Chapter 3 - The Method of Total Scattering and Atomic Pair Distribution Function Analysis.* In Takeshi Egami and Simon J.L. Billinge, editors, Underneath the Bragg Peaks - Structural Analysis of Complex Materials, volume 16 of *Pergamon Materials Series*, pages 55 – 111. Pergamon, 2012, doi: 10.1016/B978-0-08-097133-9.00003-4. (Cited on page 13.)

[Tang *et al.* 1997] Meijie Tang, L. Colombo, Jing Zhu and T. Diaz de la Rubia. *Intrinsic point defects in crystalline silicon: Tight-binding molecular dynamics studiesof self-diffusion, interstitial-vacancy recombination, and formation volumes.* Phys. Rev. B, vol. 55, pages 14279–14289, Jun 1997, doi: 10.1103/PhysRevB.55.14279. (Cited on page 38.)

[Tersoff & LeGoues 1994] J. Tersoff and F. K. LeGoues. *Competing relaxation mechanisms in strained layers.* Phys. Rev. Lett., vol. 72, pages 3570–3573, May 1994, doi: 10.1103/PhysRevLett.72.3570. (Cited on page 100.)

[Tersoff 1989] J. Tersoff. *Modeling solid-state chemistry: Interatomic potentials for multicomponent systems.* Phys. Rev. B, vol. 39, pages 5566–5568, Mar 1989, doi: 10.1103/PhysRevB.39.5566. (Cited on pages 22, 37, 42, 53 and 56.)

[Tezuka *et al.* 2003] T. Tezuka, N. Sugiyama, Tomohisa Mizuno and S. Takagi. *Ultra-thin body SiGe-on-insulator pMOSFETs with high-mobility SiGe surface channels.* Electron Devices, IEEE Transactions on, vol. 50, no. 5, pages 1328–1333, May 2003, doi: 10.1109/TED.2003.813249. (Cited on page 79.)

[Venezia *et al.* 2005] V.C. Venezia, R. Duffy, L. Pelaz, M.J.P. Hopstaken, G.C.J. Maas, T. Dao, Y. Tamminga and P. Graat. *Boron diffusion in amorphous silicon.* Materials Science and Engineering: B, vol. 124-125, pages 245 – 248, 2005. {EMRS} 2005, Symposium {DMaterials} Science and Device Issues for Future Technologies, doi: 10.1016/j.mseb.2005.08.079. (Cited on page 62.)

[Verlet 1967] Loup Verlet. *Computer "Experiments" on Classical Fluids. I. Thermodynamical Properties of Lennard-Jones Molecules.* Phys. Rev., vol. 159, pages 98–103, Jul 1967, doi: 10.1103/PhysRev.159.98. (Cited on page 22.)

[Weber *et al.* 2008] O. Weber, O. Faynot, F. Andrieu, C. Buj-Dufournet, F. Allain, P. Scheiblin, J. Foucher, N. Daval, D. Lafond, L. Tosti, L. Brevard, O. Rozeau, C. Fenouillet-Beranger, M. Marin, F. Boeuf, D. Delprat, K. Bourdelle, B. Y. Nguyen and S. Deleonibus. *High immunity to threshold voltage variability in undoped ultra-thin FDSOI MOSFETs and its physical understanding.* In 2008 IEEE International Electron Devices Meeting, pages 1–4, Dec 2008, doi: 10.1109/IEDM.2008.4796663. (Cited on page 2.)

[Weidmann & Newman 1992] Matthew R. Weidmann and Kathie E. Newman. *Simulation of elastic-network relaxation: The* $\mathrm{Si}_{1-x}\mathrm{Ge}_x$ *random alloy.* Phys. Rev. B, vol. 45, pages 8388–8396, Apr 1992, doi: 10.1103/PhysRevB.45.8388. (Cited on page 86.)

[Williams & Elliman 1983] J. S. Williams and R. G. Elliman. *Role of Electronic Processes in Epitaxial Recrystallization of Amorphous Semiconductors.* Phys. Rev. Lett., vol. 51, pages 1069–1072, Sep 1983, doi: 10.1103/PhysRevLett.51.1069. (Cited on pages 20, 60, 65 and 75.)

[Wooten *et al.* 1985] F. Wooten, K. Winer and D. Weaire. *Computer Generation of Structural Models of Amorphous Si and Ge.* Phys. Rev. Lett., vol. 54, pages 1392–1395, Apr 1985, doi: 10.1103/PhysRevLett.54.1392. (Cited on page 38.)

[Young & Elcock 1966] WM Young and EW Elcock. *Monte Carlo studies of vacancy migration in binary ordered alloys: I.* Proceedings of the Physical Society, vol. 89, no. 3, page 735, 1966. (Cited on page 24.)

[Zechner *et al.* 2008] Christoph Zechner, Dmitri Matveev, Nikolas Zographos, Wilfried Lerch and Silke Paul. *Simulation of dopant diffusion and activation during flash lamp annealing.* Materials Science and Engineering: B, vol. 154-155, pages 20 – 23, 2008. Front-End Junction and Contact Formation in Future Silicon/Germanium Based Devices, doi: 10.1016/j.mseb.2008.10.005. (Cited on page 63.)

Modélisation physique des procédés de fabrication de jonctions sur substrat FDSOI pour le nœud 10 nm et en-deçà

Résumé :

La fabrication de jonctions implique de nombreux défis technologiques à mesure que les dispositifs se rétrécissent. Afin de mitiger les problèmes liés à la diminution agressive des dimensions des transistors, des substrats SOI ainsi que du silicium-germanium (SiGe) contraint ont été introduits dans les nœuds avancés. Ces nœuds nécessitent toutefois une jonction abrupte fortement activée, qui est réalisable avec la recristallisation en phase solide (SPER) et un faible budget thermique (500°C-5h). Dans ce manuscrit, la SPER du silicium, germanium et d'alliages SiGe est étudiée avec des méthodes atomistiques telles que le Monte Carlo Cinétique (KMC) et la dynamique moléculaire (MD). Le modèle KMC de SPER se base sur une équation d'Arrhenius et distingue des configurations locales à l'interface amorphe-cristal pour simuler la dépendance de la vitesse de SPER par rapport à l'orientation de substrat. Les simulations en dynamique moléculaire montrent que la vitesse de SPER sur les orientations {111} est fortement dépendante de la taille de la cellule ainsi que de la température et du temps de recuit. Le modèle KMC est de plus étendu afin de considérer l'effet du bore pendant la SPER. Le bore peut en effet créer des complexes à la fois dans l'amorphe et le cristal et augmenter la vitesse de SPER. Cette augmentation est toutefois saturée lorsque le bore atteint de trop fortes concentrations. Un modèle de réaction de défauts traitant les complexes a été adjoint au modèle de SPER afin de correctement simuler la vitesse de SPER pour toutes les concentrations de bore.

Dans les alliages (100)SiGe relaxés, l'énergie d'activation de la SPER possède un maximum à 40% de concentration de Ge. Le modèle KMC doit introduire en plus des liaisons Si-Si et Ge-Ge, la liaison Si-Ge pour simuler correctement la recristallisation des alliages. Le modèle est également utilisé pour émettre des hypothèses sur la vitesse de SPER sur d'autres orientations. Les simulations en dynamique moléculaire confirment également le comportement de l'énergie d'activation dans les alliages SiGe. Des expériences de diffractions par rayons-X suivant en temps réel la recristallisation d'alliages de SiGe contraints ont été réalisées avec un rayonnement synchrotron. La contrainte est perdue dans les alliages riches en Ge et la température de recuit pourrait avoir un rôle sur la relaxation. La rugosité de l'interface pourrait être le lien entre la relaxation de la contrainte et la température, du fait que des simulations en dynamique moléculaires révèlent l'influence de la température de recuit sur la rugosité de l'interface et que les défauts relaxant la contrainte ont été associés à une interface rugueuse. En résumé, le SPER et ses diverses dépendances ont été étudiées dans ce manuscrit par des approches atomistiques. Les conclusions tirées améliorent la compréhension actuelle de la SPER, permettant ainsi une meilleure optimisation de la fabrication des jonctions.

Mots clés : Recristallisation en phase solide, Monte Carlo cinétique, Dynamique moléculaire

Physical modelling of junction fabrication processes on FDSOI substrate for the 10 nm node and below

Abstract:

The junction fabrication involves numerous technological challenges as the devices shrink. To alleviate issues brought by the aggressive device scaling, Fully Depleted SOI substrates as well as strained silicon-germanium (SiGe) have been introduced in advanced nodes. They however require a highly-activated abrupt junction achievable with solid phase epitaxial regrowth (SPER) and a low thermal budget (500°C-5h). In this manuscript, the SPER of silicon, germanium and SiGe alloys is investigated using Kinetic Monte Carlo (KMC) and Molecular Dynamics (MD) methods. The KMC model of SPER uses an Arrhenius equation and distinguishes local configurations at the amorphous-crystalline interface to simulate the SPER rate dependence on substrate orientations. In MD simulations, the SPER rate on {111} orientations is found to heavily depends on the cell size, anneal temperature and time. The KMC model is furthermore refined to consider the effect of boron during SPER. Boron is known to create complexes in both amorphous and crystalline phases and increase the SPER rate. This increase however saturates at high boron concentrations. A defect reaction model handling the complexes has been conjoined to the SPER model to correctly simulate the SPER rate behaviour for all boron concentrations. In relaxed (100)SiGe alloys, the SPER activation energy possesses a maximum at 40% of Ge concentration. The KMC model introduces in addition to Si-Si and Ge-Ge bonds, the Si-Ge bond to correctly simulate alloy recrystallisation. The model is also used to hypothesise the rates on other orientations. MD simulations also confirm the activation energy behaviour in SiGe alloys. Finally, X-ray diffractions following in real-time the recrystallisation of strained SiGe alloys are performed with synchrotron radiations. The strain is lost in Ge-rich alloys. The strain relaxation can be related to the anneal temperature. The interface roughness could be the link between the strain relaxation and the temperature, as MD simulations exhibit an influence of the anneal temperature on the interface roughness and strain relaxing defects are associated to a rough interface. In summary, the SPER and its several dependencies are investigated in this manuscript with atomistic approaches. The drawn conclusions increase the current understanding of SPER, allowing a better optimisation of junction fabrication.

Keywords: Solid Phase Epitaxial Regrowth, Kinetic Monte Carlo, Molecular Dynamics